Cranfield University

Vasiliki Loukodimou

Development of leak-before-break filament wound composite structures

School of Aerospace, Transport and Manufacturing

PhD
Academic Year: 2015 - 2019

Supervisor: Dr Alexandros A. Skordos
Industrial supervisor: Dr Mihalis C. Kazilas
Associate Supervisor: Dr Hamed Yazdani Nezhad
November 2019

Cranfield University

School of Aerospace, Transport and Manufacturing

PhD

Academic Year 2015 - 2019

Vasiliki Loukodimou

Development of leak-before-break filament wound composite structures

Supervisor: Dr Alexandros A. Skordos
Industrial supervisor: Dr Mihalis C. Kazilas
Associate Supervisor: Dr Hamed Yazdani Nezhad
November 2019

Abstract

A leak-before-break (LBB) concept was developed for composite pressure vessels (CPVs) to achieve a safe, predictable and controllable way of failure preventing the consequences of a catastrophic rupture. Artificial defects were introduced in the structure in prearranged patterns, acting as weak areas and enforcing failure initiation and propagation from these locations. A continuum damage constitutive model was developed through testing and simulation of tensile and compression specimens at $[0°]_8$, specimens under cyclic in-plane shear at $[\pm45°]_{2s}$, $[+45°]_8$ and $[\pm67.5°]_{2s}$ as well as out-of-plane specimens at $[0°]_{10}$ and $[0°]_{12}$. A methodology was established for the introduction of artificial defects in the composite material for its failure control considering fibre cuts and interfacial defects. The LBB concept was investigated through the simulation of the behaviour of CPVs including defects under internal pressurisation. The assessment of the LBB behaviour was based on the ability to discern between the occurrence of two leakages; the first associated to the leakage phenomenon for pressure relief in the case of over-pressurisation and the second corresponding to ultimate failure. The influence of size and degree of damage induced through the defects was investigated, as well as the use of local reinforcing patches to enhance the LBB behaviour. The most suitable design for the optimal function of the LBB behaviour involves a circular fibre cut defective area of 87.5% fibre cut damage which results in a clear separation between leak and damage by a pressure difference of about 280 bar. The selected case was used for the manufacturing of a closed-end loaded composite pipe to validate the concept. The results of the testing showed that leakage did not occur from the introduced weak points due to manufacturing defects; however, the prediction of the damage initiation from the introduced defects was accurately identified with a difference of 2% compared to the simulation results.

Keywords:

Composite pressure vessels; Internal pressurisation; Artificial defects; Leak-before-break; Damage model

Πλεύσε καρδιά μου σαν καράβι στ'ανοιχτά
κι αν σε χτυπήσουν οι φουρτούνες της ζωής, μη φοβηθείς,
άνοιξε όρτσα τα πανιά σου και σάλπαρε μαζί τους.

Acknowledgements

I would like to express my sincere gratitude to Dr Alexandros Skordos for his constant support, the guidance and the continuous effort towards the improvement of this work. I am also utterly grateful to Dr Mihalis Kazilas for his constant help and support throughout these years.

I would like to thank all members of Adhesives Composites and Sealants team for their moral and technical support as well as Mr Jim Hurley and Dr Hamed Yazdani Nezhad for always being willing to help.

I am deeply grateful to my parents Dimos and Anni, my siblings Giannis and Diamanto, as well as to Anurag for their patience, encouragement and moral support.

A sincere thank you to all my relatives and friends back in Greece as well as my friends in the UK for their continuous encouragement.

This work was made possible by the sponsorship and support of Lloyd's Register Foundation*, as well as of the UK Department for Business, Innovation and Skills (BIS) through its Regional Growth Fund (RGF), the Higher Education Funding Council for England (HEFCE) and Structural Integrity Research Foundation (SIRF) for their funding support to NSIRC.

**A charitable foundation, helping to protect life and property by supporting engineering-related education, public engagement and the application of research.*
www.lrfoundation.org.uk

Table of Contents

List of Figures

List of Tables

Notation

A. Nomenclature

Latin characters

A	Coupling factor between shear and transverse strains
A_{slave}	Slave nodal surface
B	Base of triangle in spiral wound pipe Stress transformation parameter Bending factor
B_a	Simplified stress transformation parameter
b	Coupling factor between shear and transverse damage Width Voigt elastic constant tensor
C	Pipe circumference
D	Inner diameter of pipe
d	Head displacement Distance inspiral wound pipe Damage variable
d_{tot}	Total tow-preg length
E	Young's modulus
E_D	Strain energy density
E_{11}^{y}	Nonlinear undamaged modulus under compressive loading
E_0	Modulus in the normal direction
$E_I^{'}$	Equivalent elastic modulus for Mode I
$E_{II}^{'}$	Equivalent elastic modulus for Mode II
F	Force Large displacement correction factor
G	Shear modulus
G_0	Modulus in the shear direction
G_{Ic}	Critical strain energy release rate for Mode I
G_{IIc}	Critical strain energy release rate for Mode II
H	Half laminate thickness
h_{cont}	Interface contact thickness
h	Half specimen thickness

L	Length
l_{ch}	Cohesive zone length
l_1	Distance from loading pin to the mid-plane of the specimen
l_2	Distance from loading pin to the edge of the loading block
m	Hardening law exponent Compliance calibration coefficient
N	Load block correction factor
P	Load Pressure
R	Yield stress
T_g	Glass transition temperature
t	Thickness Time
V_c	Fibre cut volume fraction
V_f	Fibre volume fraction
V_f'	Fibre volume fraction of defetive composite
V_m	Matrix volume fraction
W	Towpreg width
x	Coordinate Miscellaneous/uknown data
$\|x\|$	Absolute value
$\langle x_{ij} \rangle_+ = \begin{bmatrix} x_{ij} \text{ if } x_{ij} \geq 0 \\ 0 \text{ if } x_{ij} < 0 \end{bmatrix}$	Positive Heavyside function
$\langle x_{ij} \rangle_- = \begin{bmatrix} 0 \text{ if } x_{ij} > 0 \\ x_{ij} \text{ if } x_{ij} \leq 0 \end{bmatrix}$	Negative Heavyside function
Y	Damage evolution function
Y_{12}^0	Initial shear damage threshold
Y_{12}^c	Critical shear damage limit
Y_{12}^U	Shear damage fracture limit
Y_{22}^0	Initial transverse damage threshold
Y_{22}^c	Critical transverse damage limit
Y_{22}^U	Transverse damage limit
y	Coordinate

Z	Thermodynamic variable/force
z	Coordinate

Greek characters

α	Crack length Wrapping angle of prepreg
β	Hardening law multiplier
γ	Non-linear compression corrective parameter
Δ	Correction factor for rotation of DCB arms
δ	Displacement
ε	Strain tensor
ε^e	Elastic strain tensor
ε^p	Plastic strain tensor
$\bar{\varepsilon}^p$	Accumulated effective inelastic strain
θ	Fibre angle
$\frac{\vartheta}{\vartheta x}$	Partial derivative
v_{12}	Poisson's ratio
ρ	Density
σ	Stress tensor
$\tilde{\sigma}$	Effective stress tensor
$\bar{\sigma}$	Laminate average stress
σ_A	Axial stress
σ_H	Hoop stress
τ	Shear stress Time

Subscripts

c	Cut
f	Fibre
i	Counting index Initial value
j	Counting index
k	Counting index

m	Matrix
max	Maximum value
n	Normal direction Counting index
tan	Tangential direction
u	Ultimate value
I	Normal direction
II	Shear direction
1, 2, 3	Material direction

Superscripts

c	Compression
C	Critical value
f	Fibre direction
k	Counting index
t	Tension
0	Undamaged state Initial value
U	Ultimate value

B. List of Abbreviations

LBB	Leak-Before-Break
CPVs	Composite Pressure Vessels
CFRP	Carbon Fibre Reinforced Polymer
UD	Unidirectional
PTFE	Polytetrafluoroethylene
ETFE	Ethylene Tetrafluoroethylene
FEA	Finite Element Analysis
VPS	Virtual Performance Solution
CDM	Continuum Damage Mechanics
VCP	Visual Crash Program
NOPER	Number of Operations
ILAY	Layer Identification database
ANGPL	Angle Ply orientation

THKPL	Ply Thickness
IDPLY	Ply identification number
IDLAYER	Layer identification number
IORT	Orthotropic axis definition
IDMAT	Material identification number
OCTRL	Output parameters control
TCTRL	Time step control data
ERFOUTPUT	Contour and curve output
LAYPLOT	Layer plot output
NODPLOT	Node plot output
SHLPLOT	Shell plot output
DSYOUTPUT	Mesh plot output
THPOUTPUT	Time history plot output
SHLTHP	Shell time history output
DTUSER	User imposed initial time step
NODTSP	Nodal time step control
DTMASS	Dynamic mass scaling criterion time step
TIO2	Run termination time
LR	Lloyd’s Register
HEC	High Elongation Carbon fibre
NDT	Non Destructive Testing
XCT	x-ray computed tomography
DCB	Double Cantilever Beam
ENF	End Notched Flexure
NPC	Non-precracked
PC	Pre-cracked
CC	Compliance Calibration
CBT	Classical Beam Theory
ASTM	American Standard Test Method
SSE	Sum of Squared Error
VBA	Visual Basic for Applications
S.g.	Strain gauge

1 Introduction

1.1 Background

Composite materials have been increasingly utilised since the 1940s in high performance operations as critical parts for the Oil & Gas, offshore marine, aerospace, automotive, biomedical and nuclear industries. In these areas, the requirements of high mechanical properties combined with light weight and high environmental resistance need to be met. Composites excel in this field providing high strength-to-weight and stiffness-to-weight ratio as well as high resistance to environmental factors. Their superior properties led to the replacement of conventional materials such as steel, aluminium and titanium by polymer composites [1, 2].

Pipes and pressure vessels belong to the infrastructures in which polymer composites have been replacing metals as material of choice. Composite pressure vessels (CPVs) have unique advantages over metallic cylindrical structures, such as high strength, high stiffness, long fatigue life, low density and versatility based on the intended design and function of the cylindrical structure. The resistance over corrosion and wear as well as thermal and acoustic insulation, maintainability and serviceability are further benefits of CPVs. Since the introduction of the first composite pressure vessel in 1970s until now, these cylindrical structures have been a continuous area of study addressing the requirements of the industrial application in which they are used.

There are five main designs of pressure vessels [3–5]. The least expensive but heaviest tank is Type I, which is an all-metallic structure. Type II is a metallic vessel with fibre reinforcement in the hoop direction. The lighter design- Type III pressure vessel-involves a metallic liner fully wrapped with composite. Type IV consists of a composite overwrapped plastic liner and metallic bosses integrated in the design. In this type of pressure vessel, the loads are fully carried by the composite. The most recent development in the evolution of pressure vessels is the next generation Type V tank, manufactured entirely out of composites without the use of a liner.

CPVs are used for the storage and transportation of fluids typically at pressures significantly greater than ambient. They are closed, rigid containers which can store large amounts of energy as they operate under high pressure. These extreme operating conditions can deteriorate their structural integrity and lead to catastrophic failures. Many accidents have been reported over the last decades due to the failure of CPVs. One of these incidents involves the SpaceX Falcon 9 rocket explosion in Cape Canaveral in 2016 [6] (Figure 1.1) due to helium storage CPV failure during a routine filling operation [7]. Failure of CPVs usually occurs in an unpredictable and abrupt way that takes place through explosion incidents leading to injuries and fatalities and causing dramatic environmental and economic impact. The existence of leak that can provide prior warning is most of the times accompanied by burst, which leaves no margin for reaction. Fail-safe designs aim to predict and control the way of failure of CPVs avoiding their catastrophic consequences and providing a progressive, gradual manner of failure.

Figure 1.1 SpaceX Falcon 9 rocket explosion in Cape Canaveral due to helium storage CPV failure [6]

In this research work, the focus is on the development of a leak before break (LBB) concept in order to prevent catastrophic failures caused by CPVs and to provide a controlled failure. The requirement for light weight structures designed for applications in which the space each structure occupies needs to be optimally utilised leads to the rejection in using additional components such as safety valves as a potential LBB strategy. Therefore, in this work the generation of a leak is taking place under certain damage threshold, through a pre-designed and

prearranged pattern positioned at a certain location. In this way the system allows timely detection of the damage through drop of the internal pressure that occurs due to leakage as well as through visual inspection of the structure.

1.2 Aims and research hypotheses

The aim of this research work is to develop an LBB concept for filament wound composite structures for the accomplishment of a safer, more predictable and controllable way of failure and the prevention of its catastrophic events. In order to achieve this, weak regions/defects are introduced in the composite structure during manufacturing. The weak regions/defects are introduced in specific locations creating suitable patterns. Under certain loading conditions, the weak points/defects act as stress concentration points forcing failure initiation around these regions. Due to these imperfections and the continuous loading conditions, cracks propagate from the weak regions/defects and coalesce creating leak paths in the composite structure. The research hypotheses and questions that need to be addressed are expressed as follows:

1. The damage behaviour of composite structures can be simulated through the development of a constitutive model based on the Ladevèze damage material model.
2. The constitutive model can be used for the verification of a methodology for the control of failure of tensile specimens.
3. The Ladevèze-based constitutive model can be utilised for the development of LBB behaviour on pressurised composite cylindrical structures.
4. The damage behaviour of the composite pressure vessel can be predicted through the use of continuum damage mechanics and the Ladevèze-based constitutive model.

1.3 Thesis road map

This thesis is organised in 10 chapters. Chapter 2 reviews the failure of CPVs and relevant damage mechanisms, presents the state of the art on safe-fail design of CPVs that provide damage tolerant structures and describes work to

date on artificially introduced defects in composites. Chapter 3 describes the simulation methodology followed in this work, including the simulation environment, the modelling strategy and the chosen material models. Chapter 4 details the experimental details, methodology and procedures used for manufacturing and testing for composite specimens and CPVs. Chapter 5 is dedicated to the development and verification of the constitutive model and includes results from material characterisation, as well as the procedure for the identification of material model parameters and associated verification. Chapter 6 focuses on the introduction of defects for the development of LBB behaviour. Chapter 7 describes the results of the simulation of the LBB response of CPVs and the design of suitable defect patterns. Chapter 8 focuses on the assessment and validation of the LBB concept. Chapter 9 presents an overall discussion of the findings of this research work, whilst Chapter 10 summarises the main conclusions as well as recommendations for future development and studies.

2 Literature Review

2.1 Introduction

Fibre reinforced composite materials have been increasingly used in advanced industries, where precision on the estimation and prediction of the failure behaviour of the composite structure is required. Failure in carbon fibre reinforced polymer (CFRP) structures is a complex phenomenon. CFRP can often undergo abrupt failure whilst in-service due to the brittle nature of the reinforcement and matrix [8, 9]. Failure usually occurs as a combination of more than one failure mechanisms including fibre rupture, matrix microcracking, fibre/matrix debonding and delamination [10, 11]. The failure prediction and control of damage in composite laminates has been the focus of many research studies [12] through design methodologies [13, 14], failure criteria [15, 16] and simulation approaches validated through experimental studies [17–19].

This chapter is divided into three main sections. The first section is dedicated to the review of failure modes and failure mechanisms developing in CPVs. The second part of this chapter focuses on fail-safe design of composite structures. The third section focuses on the control of failure of structures through the introduction of artificial defects/weak points through fibre discontinuities and interlaminar weak bonding areas. The final section in this chapter links the reviewed state of the art to the developments carried out in this work.

2.2 Failure of composite pressure vessels

CPVs are widely used for the storage and transportation of various gaseous and liquid substances under high pressure. Due to their light weight, CPVs are widely used in industries such as aerospace in which high reliability and significantly low safety factors are required [20, 21]. Failure in CPVs can be developed due to various conditions. The most common causes of failure are internal pressurisation under hydrostatic [22, 23] or fatigue loading [24, 25], external pressurisation [26, 27], damage from impact [28–30], buckling [31–33], failure as a result of environmental degradation [34–36] and failure resulting from a combination of loadings [37–39]. In this work, the focus is set on the application

of internal pressurisation in Type IV and V CPVs through hydrostatic loading. In Type IV CPVs the polymeric liner is non-load sharing as it contributes with less than 5% to the overall design load bearing [40, 41]. In pipes, there are mainly three types of tests; under open-end, restrained and closed-end loading conditions [42–45], as illustrated in Figure 2.1. For open-end pressure tests the hoop to axial stress ratio is 1:0; the pipe is under pure hoop internal pressure loading being free to slide on 'O' ring seals. At the restrained-end loading with hoop to axial stress ratio of about 3.5:1, axial displacements along the length of the pipe are controlled. The closed-end pressurisation resembles the function of CPVs with a hoop to axial stress ratio of 2:1.

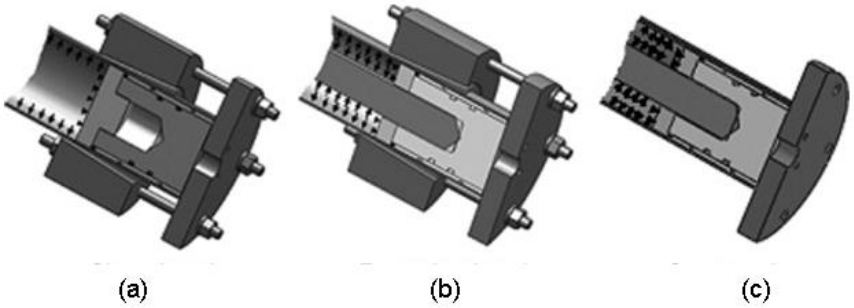

Figure 2.1 Pipe end loading conditions of (a) closed-end, (b) restrained-end and (c) open-end tubes [44]

2.2.1 Burst under internal pressure

Burst in CPVs undergoing internal pressurisation is classified as a structural failure and is characterised by strength loss [23], usually occurring due to excessive internal pressurisation from overfilling, overheating [46] or impact damage [47, 48]. The mechanisms developing from the damage initiation until the occurrence of ultimate failure are complex and have been studied experimentally and analytically for the understanding and prediction of rupture [49–51]. The failure mechanism that dominates burst failure is fibre damage which can lead to abrupt failure or explosion [23, 45, 52–54]. Burst usually takes place in composite cylinders enhanced with a polymeric liner that prevents the containing liquid from leaking [53]. Failure initiates typically as a small crack between the fibres and the matrix. The increase of the pressurisation leads to

propagation of the matrix cracking and the formation of fibre/matrix debonding. The effective stiffness degradation leads to redistribution of stresses to the neighbouring fibres and plies, initiating the formation of fibre breakages and interlaminar failure in the form of delamination. Burst in composite pressure vessels occurs as the accumulation of a large scale of fibre breakage. Two failure modes of burst exist in CPVs, the safe and unsafe mode [50]. The safe mode is accompanied by failure taking place in the Type IV cylindrical structure, whilst the metallic bosses are moved into the vessel creating rapid contraction in the axial direction. This case initiates various failure mechanisms, such as fibre breakage, matrix cracking, out-of-plane damage and interlaminar shear damage. However, the dominant failure mechanism that leads to burst is fibre breakage of plies in the hoop direction. In the unsafe failure mode, failure is initiated at one of the domes/ curved ends of the CPV due to matrix cracking and leads to the ejection of the metallic boss. In this mode the failure mechanism that leads to burst is fibre breakage at helical plies. Therefore, matrix cracking on the domes is the mechanism determining whether the mode is going to be safe or not. For both safe and unsafe modes, burst comes as a result of the load transfer from the broken fibres to their surrounding, while matrix cracking results in the progressive degradation of the structure. Under internal pressure, static or cyclic, the fibres of the composite cylinder are only subjected to tensile loading which, at the fibre level, is equivalent to a unidirectional (UD) composite, loaded in the fibre direction [55, 56]. Damage initiates from random fibre defects leading to fibre rupture. Due to a local load increase, the matrix cannot isolate the damage and fails under shear accompanied by fibre/matrix debonding. The damage accumulates affecting neighbouring intact fibres and leads to clusters of fibre breakages. The increase of the fibre damage over a critical damage threshold leads to the instability and catastrophic failure of the CPV.

The orientation of the fibres plays a significant role in the failure behaviour of CPVs with respect to their burst pressure. Netting analysis indicates the fibre winding angle that provides the highest values of burst pressure which is at 54°44’ [53, 57, 58]. In this analysis, it is assumed that fibres are the only load carrying feature without taking into account the matrix stiffness or any interaction between

the fibres [57]. This optimum fibre angle is ideal for a closed-end pipe or CPVs loaded under internal pressure corresponding to a hoop to axial stress ratio of 2:1. In the case of open-end cylinder the optimum winding angle is at 75°, whilst in the axial compressive case under 3:1 hoop to axial stress ratio this is at 85° [45]. Experimental and analytical investigations on closed-end pipes with liner at winding angles of $[\pm 45°]_s$, $[\pm 55°]_s$, $[\pm 60°]_s$, $[\pm 75°]_s$ [23] and $[\pm 88°]_s$ subjected to internal pressurisation confirm that highest burst pressure occurs using winding angle of 55° [59]. All cases apart from the cylinder with winding angle of $[\pm 75°]_s$ undergo failure caused from burst. In the case of use of circumferential 90° fibres in combination with angled layers, the burst pressure of the vessel increases for angles from 0° up to 55°, whilst for angles of 55° and higher the use of angle plies has an insignificant effect [60].

The loading conditions, rate and thermal conditions in the interior and exterior of the composite cylinders play a significant role in the failure behaviour and burst pressure. Pipes wound at $[\pm 60°]_3$ loaded under hoop to axial stress ratio of 7:1, 1:0, 2:1 and 12:1, exhibit catastrophic burst performance [43]. In all cases except for 12:1, the sudden burst creates catastrophic failure leaving the pipe in two halves as illustrated in Figure 2.2 [43]. The global failure is associated with fibre fracture in a broom-like effect. For the 12:1 case the burst failure occurs locally in the form of two helical cracks.

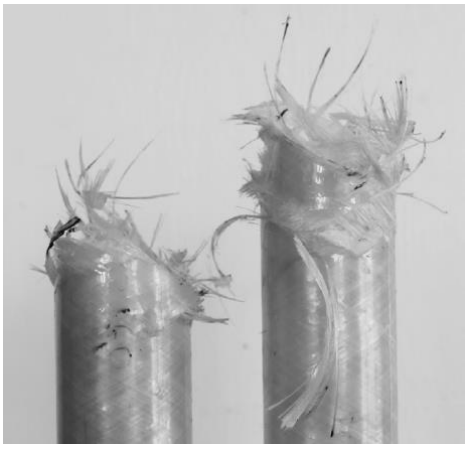

Figure 2.2 Catastrophic failure of $[\pm 60°_3]_T$ open-end pipe under 1:0 hoop to axial stress ratio [43]

The increase of the loading rate in cylindrical structures leads to higher burst pressures, whilst low rates are related to accumulation of matrix cracks under transverse tension which is related to a formation of a leakage [51, 61, 62]. Simulation [51] and experimental [63] investigations in Type IV pressure vessels indicate that at ambient temperature, high loading rates are related to liner rupture and matrix cracking development under transverse tension through the thickness; a phenomenon mostly related to failure due to leakage. Low loading rates are associated with no damage on the liner [51]. The damage is transferred to the overwrap and burst occurs with predominant the mechanism of fibre breakage. Open-end fatigue pressurisation tests on $[\pm 75°]_2$ filament wound pipes without liner indicate that under high loading rates the incidents of leakage and burst coincide, in contrast to low loading levels in which leakage occurs first [64]. This implies the predominant nature of fibre breakage in high pressure rates, whilst matrix damage is the principal failure mechanism that leads to failure of the cylinder. Pressurised Type IV vessels subjected to fire can burst due to external structural deterioration [34]. In closed-end composite cylinders with liner, investigation of the winding angles between $[45/-45/45/-45]_2$, $[55/-55/55/-55]_2$, $[60/-60/60/-60]_2$, $[75/-75/75/-75]_2$ and $[88/-88/88/-88]_2$ at temperatures of -2°C, 25°C, 60°C and 80°C shows that maximum burst pressure is obtained using orientation of 55° at all temperatures with the highest being at 25°C [65].

2.2.2 Leakage under internal pressure

Leakage is a functional failure that occurs when the composite cylinder can no longer serve its primary purpose of containing fluids. The failure mechanism that governs leakage is matrix cracking [23, 66, 67]. It is expected that when the composite structure suffers from increasing loads, matrix microcracks due to manufacturing or voids between the liner and the composite can accumulate and lead to the creation of weepage paths and initiation of leakage [50]. Weepage is the result of joining transverse cracks and can be observed in places where decolouration and crazing have previously occurred parallel to the fibres. The difference between weepage and leakage is that the latter occurs at higher internal pressure and appears as jets of fluid penetrating the laminate.

The failure behaviour of composite cylinders can vary depending on the loading conditions, the winding angle as well as the temperature [68–73]. Analysis of CPVs without liner under internal pressurisation shows that for fibre orientations lower than ±50°, failure occurs due to matrix shear damage, whilst for winding angles higher than ±55° failure occurs due to matrix transverse damage [74]. Composite pipes with winding angle of ±60° with respect to the axial direction of the cylinder when loaded under closed-end conditions undergo rotation of their orientation to the optimum ±55° [67]. Closed-end composite cylinders under 2:1 hoop to axial stress ratio and cyclic loading usually show transverse matrix cracking leading to strips of decolouration parallel to the orientation of the fibres and the formation of droplets on the cylindrical surface through weepage [43]. Also, a small degree of structural damage occurs. Fatigue internal pressurisation tests on closed-end composite pipes without the use of liner at winding angle of 54°44’ show that failure initiation occurs through matrix shear cracking, which at high pressures progresses into fibre/matrix debonding in the structure [53, 57, 70, 72]. Strips of decolouration appear parallel to the fibres which progress and increase in number with the rise of pressure. Weepage is initiated in the form of droplets forming lines parallel to the fibre direction. Ultimately, burst occurs through the failure mechanism of fibre breakage. In the case of composite pipes with $[\pm 75^{0}]_{4}$ layup without use of liner functional failure occurs, as illustrated in Figure 2.3, followed by structural failure in the hoop direction close to the location of leakage [23]. The same failure behaviour is observed in composite tubes with liner at winding angle of $[\pm 75^{0}]_{4}$. The failure in the hoop direction is caused by the inability of the cylinder to withstand loads in the axial direction. The non-load sharing liner is subjected to the increased axial loading, which results to its failure in the hoop direction. In the case of pure tensile axial loading under 1:1 hoop to axial stress ratio, transverse matrix cracking occurs parallel to the fibre reinforcement [68, 70]. Elongation in the transverse direction takes place and the composite wall thickness can be reduced significantly [68]. The elongation occurs due to deformation of a helical crack at the exterior layer of the pipe which extends along the gauge length under elevated axial deformations [43]. This is followed by fibre breakage perpendicularly to the crack, realignment of the fibres of the

cracked area and delamination due to fibre pull out [75]. Strips of decolouration/whitening form on the pipe and leakage in the form of jets of water occur [43, 68]. Pipes subjected to high hoop loading conditions 1:0 (open-end) and 4:1 fail under leakage through well-defined jets due to the development of interlaminar shear stresses. In open-end composite pipes with no liner at winding angle of 54°44' undergoing fatigue internal pressurisation matrix damage is the dominant failure mechanism [57, 76]. Isolated decolouration strips are observed parallel to the fibres and weepage occurs. The increase of the pressure leads to the creation of sudden jets of the containing fluid and the development of delamination in adjacent layers, which subsequently leads to bending. The ultimate structural failure of the pipe takes place through a fibre rupture mechanism. In open-end composite cylinders of $[\pm 75^0]_2$ layup without liner the application of low pressure loading can lead to formation of decolouration (matrix crazing) and matrix microcracks which lead to leakage [64]. Leakage occurs due to coalescence of matrix microcracks, which when they reach a certain level can be penetrated by fluid and form a leakage path (pin hole). Eventually, the cylinder reaches catastrophic failure through burst due to abrupt fibre breakage. Based on experimental investigations the optimum angle for internal pressure loading at a hoop to axial stress ratio of 2:1 is ±55°, whilst for the loading cases of 1:1 and 4:1, the preferable winding angles are ±45° and ±63°, respectively [68]. Combinations of winding angles can provide a beneficial failure behaviour compared to single winding angles [69, 73]. The use of multiaxial tubes in various biaxial conditions results in an increase of the pipe strength as their use enhances their functional and structural failure behaviour. Pressurised Type IV vessels under elevated temperatures due to fire fail as a result of leakage through heat transfer which affects the liner [34, 77].

The quantification of leakage [77] in cylindrical structures can be carried out through (a) visual inspection, (b) electrical resistance measurement on the surface for leakage detection , (c) fluid volume loss monitoring to assess the amount of fluid that penetrated the material through matrix cracks and (d) computation based on Darcy's law taking into account the material permeability and the dependence of fluid viscosity on temperature.

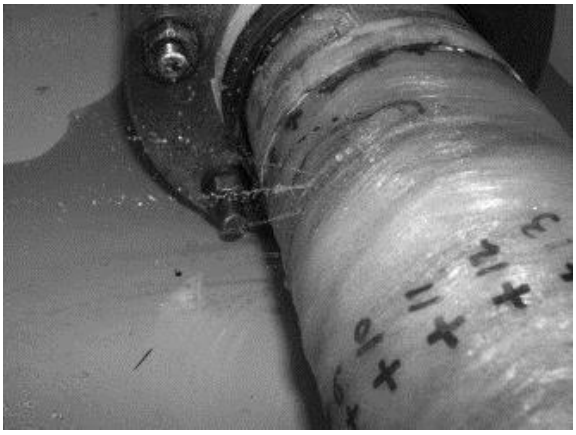

Figure 2.3 Functional failure of pipe at $[\pm 75°]_4$ [23]

2.3 Fail-safe designs for composite cylindrical structures

Apart from their light weight, high strength and stiffness, composites have been used as energy absorbing components to provide safe failure when undergoing damage [78, 79]. The development of fail-safe designs is based on the development of damage tolerant structures that can maintain certain strength levels and continue to operate, allowing partial damage, until its detection prior to the occurrence of ultimate structural failure [80]. The mechanisms leading to damage can develop due to existent imperfections of the structure that can be triggered under certain loading conditions or due to installation or in-service incidents, such as impacts and environmental conditions. Safe crack propagation can be achieved through structural redundancy by sizing the structure, thus delaying the formation of large size cracks and providing timely detection prior to ultimate rupture. Structures designed at adequately low stress levels facilitate the detection of large defects during an inspection. Fail-safe structures often comprise multiple elements that enable crack arrest and energy absorption, as well as load paths that can contain the crack thus acting as sacrificial features.

The energy absorption characteristics of composite cylinders enhance their ability to withstand damage and fail in a progressive and controlled manner. The crashworthiness of composite tubes undergoing crash, external [81] or internal pressurisation and combinations of those [82, 83] is a characteristic highly dependent on the energy absorption capability of composites [84]. A structure

undergoing crash is subjected to axial compressive loading. Energy absorption can be ensured by the selection of suitable types of constituents including toughened epoxies, types of fibres with ductile-like type of failure and nanoparticle fillers [85–91], as well as fibre orientation [92, 93], fabrication method [94, 95] and optimum design geometries [96–99]. Collapse triggers can also be utilised in order to provide progressive failure in crash incidents avoiding abrupt catastrophic failure [100, 101]. This is based on the introduction of high stress locations from which damage occurs and is propagated to the surrounded material. Triggers can be external comprising metallic parts [102–105], plug-type initiators [106] or internal chamfered ends [107–109], notches [110, 111], embedded ply-drops [101, 112, 113] and tulip [104] or crown shaped features [114] located at one or both ends of the tube for the crash testing of fibre and hybrid reinforced composites as well as sandwich structures.

Failure in thin fibre reinforced composite structures usually occurs in a brittle way due to the nature of the fibre reinforcement. In order to avoid sudden, catastrophic collapse of the structure a more progressive ductile/plastic-like failure mode is required. Two progressive types of collapse exist in composite cylinder undergoing compression, progressive folding and crashing. Progressive folding is associated with lamina buckling, hinge formation and brittle fracture. The four failure modes of the tube undergoing progressive crashing comprise transverse shear, lamina bending, brittle fracture and local buckling. The failure mechanisms involved in these failure modes are fibre and matrix damage, fibre-matrix debonding, delamination and bending [84, 85, 115–120].

Composite cylindrical structures have been investigated in order to examine their sensitivity to imperfections [121–128] and for the improvement of knockdown factors [129–131]. Sensitivity to composite internal, outer and liner surface cracks under internal pressurisation has been investigated [41, 132–139] and in some cases focuses on the performance of fail-safe leak-before-break behaviour with and without defects [40, 139–141]. The increase of the depth-to-thickness ratio of the crack leads to decrease of the strength of the cylinder. The continuous increase and decrease of pressure due to fatigue loading leads to decolouration due to fibre/matrix debonding, which is accompanied by matrix cracking and

interlaminar shear damage, related to Mode I and Mode II, developed at the area underneath the artificial surface crack. Eventually, as the delamination propagates (under Mode II), leakage failure occurs which is followed promptly after by burst.

Cutouts and hole imperfections exist often in the structures due to inspection or electric line installation thus interrupting the smooth distribution of loads [142]. Unreinforced cutouts and holes subjected to buckling can cause failure under global collapse, failure due to high stress concentration around the cutouts or unstable local buckling through interlaminar failure at the area near the cutout due to high deformation [143–148]. Unreinforced cutouts in the circumferential direction cause an additional 8% reduction of buckling load compared to its respective value in the axial direction [149]. Experimental and numerical investigations indicate that depending on threshold ratios of the cut length to the radius of the cylinder the buckling load of the structure is affected either by the size of the square, rectangular or circular (Figure 2.4) cutout defect or by initial imperfections of the structure or combination of those [149, 150]. The increase of diameter can reduce the buckling load [146]. Apart from the hole diameter, the pipe diameter, the perforation pattern and circumferential hole spacing play a significant role in the compressive behaviour of composite tubes [151, 152]. The buckling load can be increased by the increase of the hole spacing and tube diameter and the reduction of the hole diameter. Cylindrical shells subjected to internal pressure and axial compression show increase of the buckling load and delay of the deformation of the surrounding area of the cutout [153, 154].

Cutout reinforcement can consist of additional layers attached on top of the square-shaped cutout and its thickness, size and fibre orientation can vary [144]. The reinforced cutouts mostly cause high resistance to buckling accompanied by stable post-buckling behaviour until ultimate failure occurs. Overall, the buckling behaviour of the structure is enhanced as the size and thickness of the reinforcement increases. Grid stiffeners can be utilised to improve the buckling behaviour of cylindrical shells [142, 155]. The use of grid reinforcement in a configuration that smoothly transmits the loading improves the buckling behaviour of the composite cylindrical structure. Circular cutouts show ultimate

damage at a higher load compared to square cutouts due to higher stress concentration in the latter. The increase of circumferential stiffness is feasible by fibre steering through advanced fibre placement and provides buckling load higher by 17% compared to the unreinforced pipe [156].

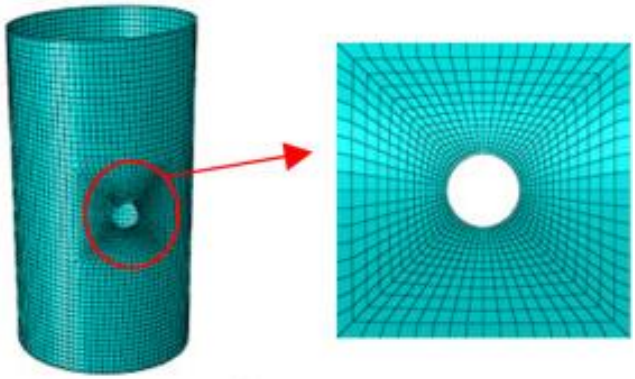

Figure 2.4 Mesh of circular cutouts in composite cylinder [150]

2.4 Artificially introduced defects in composite structures for the control of their failure

The control of the way of failure of composite structures through the control of the failure mechanisms and location of damage, whilst it is in its inception, is of prime interest and importance. This has been the focus of experimental and analytical [157, 158] investigations. In this section, the focus is on the introduction of fibre discontinuities and interlaminar weak bond areas as defects for the control of failure in composite structures.

2.4.1 Fibre discontinuities

The introduction of slits/fibre cuts in the structure and ply drops can be used for the creation of discontinuous fibres for the study of their effect in composite structures. The cuts are introduced, mainly in an automated way, by the use of tangential knives [159], paper cutters [160] and laser [161]. Curing by hot pressing, in particular in combination with compression moulding, can lead to transverse and axial stretching of the slits [162]. After curing, resin rich areas are created around the slits which can be potential stress concentration points

initiating the development of progressive failure mechanisms [163]. This can be advantageous for the control of crack initiation location and its subsequent propagation [164]. The larger these regions are the higher the fracture toughness of the material, since they lead to a gradual failure mode [163]. However, the overall tensile strength decreases by approximately 15% irrespectively of the number of the introduced ply cut defects [165]. The failure starts with microcracks at the fibre ends leading to their debonding from the matrix [166, 167]. The failure continues as a matrix crack to the neighbouring fibres following an oblique angle with respect to the fibre orientation.

Fibre cut-outs can be introduced vertically or at an angle to the direction of the fibres. In the former case, when the fibre orientation is arranged in a 0° UD arrangement and loaded under tension, the failure starts around the slits, between them and the continuous fibres [168], as illustrated in Figure 2.5. The material follows pseudo-ductile behaviour demonstrating a non-linear and predictable stress-strain response through progressive failure of the interlaminar regions where the slits have been introduced [169, 170]. If the slits are alternatively distributed not only in the width but also in the thickness direction, the failure is caused due to delamination at the points where the slits have been introduced [168]. In the case the slits are successively staggered, splitting at the slit ends leads to the final failure of the sample. The failure stress in the case of alternatively distributed defects is higher than the strength in the case the slits coincide. For centrally located discontinuities of different thicknesses on UD laminates debonding occurs at the cut ends, accompanied by non-linear strain response [171]. With further loading, delamination is formed at the cut ends and the final breakage occurs. Thicker discontinuous layers are linked to lower stress requirement for the initiation and propagation of damage. A discontinuous carbon/glass fibre reinforced hybrid composite can behave as a pseudo-ductile material [170]. The failure is initiated by stable pull out of the centrally located carbon layers from the glass layers accompanied by a wide pseudo-ductile strain plateau until the formation of delamination and the final failure of the samples. In the presence of a resin rich region between the discontinuities, matrix cracking

occurs at this point before the initiation of delamination at the interface between the cut and continuous plies [172].

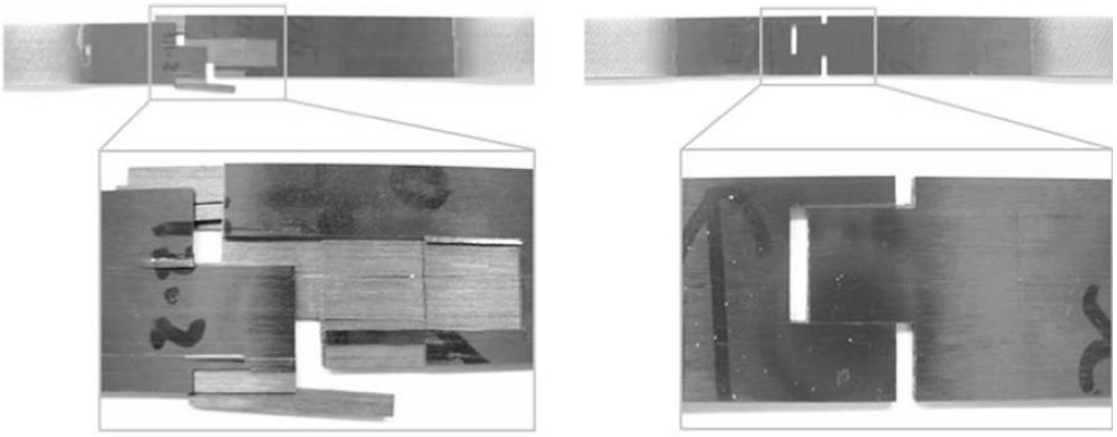

(a) (b)

Figure 2.5 Schematic representation of tested tensile coupons with slits (a) dispersed in various layers and (b) through the thickness [168]

In the case of quasi-isotropic laminates, delamination is the mechanism leading to catastrophic failure. Failure starts with the generation of transverse cracks in the structure, whilst some areas of delamination are formed at the points where the slits have been inserted due to shear stress concentration. The slits in 0° layers fail first, followed by matrix cracking in 90° layers, and then failure of ±45° plies [173]. As the material continues bearing the load, significant delamination occurs connecting the damaged regions. For increasing loading the delamination propagates in both the length and width direction. For star pattern defects consisting of superimposed cuts as the strain increases the cuts open thus creating high strain concentrations at the surrounding area and particularly around the slits [174]. Cracks are initially formed and high strain occurs at a band area around the cuts. The strain in the load direction of 0° plies is mainly affected. The combination of slits with other inserts introduced in the composite structure controls the failure mode as well as the strength [159]. In quasi-isotropic lay-ups the placement of a thermoplastic interlaminar layer between the layers during manufacturing can lead to rapid or slow delamination effects depending on the adhesion properties between the insert and the main material. If these interlaminar inserts are placed only onto the slits delamination occurs. Another

pattern that has been investigated involves the manufacturing of composites with slits in the central upper half and no slits in the lower half; the two halves bonded together whilst a layer of release film is induced just underneath the cut area [175, 176]. Laminates with resin pockets located between the slits are obtained in this manner. If an artificial sharp crack is introduced at the resin rich region, the delamination initiates at the introduced sharp crack. In both cases, the fracture toughness is statistically the same and delamination is the dominant failure mode. Introduction of flaws in composites allows control of the development of interlaminar cracks under Mode I and through-thickness crack accumulation through branching for the development of progressive failure [177]. The introduced defects consist of either 'crack branch flaws'; a combination of ply drops-small gaps on a layer- and delamination inserts or delamination flaws through the introduction of insert films or ply gaps. The introduction of 'crack branch flaw' provides control of failure but also a high stress reduction under loading in the fibre direction, in contrast to transverse loading in which control of damage takes place through delamination flaws. Ply gaps with and without delamination inserts promote a controllable failure for 45° ply configurations.

Fibre cut-outs can also be introduced in the composite layers at an angle to the fibre orientation. As in the case of perpendicular slits their pattern can be staggered, bi-angled or continuous [160, 173, 178]. Even though continuous angled slits are easier to introduce, they appear to decrease the tensile strength compared to non-continuous slit patterns. In cross-ply orientations, the damage initiation and progression involves matrix cracks along the slit length, splitting at the slit ends in the 0° layers and transverse matrix cracking in the 90° layers. Ultimately, all these damage points interconnect with each other and lead to interlaminar failure. For large angles crossing points of the slits are the weakest locations with high stress concentration causing transverse cracking [179]. For smaller angles delamination occurs in the reverse way, with delamination starting at the corners of the slits and moving towards the crossing centre [178]. The angle of the slits affects the tensile strength of the composite demonstrating higher values for angles between 11° and 31° [180]. In these cases fibre breakage is the dominant damage mode as delamination is depressed [181].

2.4.2 Interlaminar weak bond areas

This section focuses on the introduction of interfacial defects for the formation of weak bonding areas in composite structures and the generation of delamination and debonding for the development of predictable and controlled damage. Standardised tests such as Mode I [182] and Mode II [183] for the measurement of the fracture toughness of composites are the most representative case of introduction of weak bond areas in composites by using polytetrafluoroethylene (PTFE) films. The main purpose of their use is the generation of an artificial defect through this weak bond area within the composite layers, which acts as a starter for the propagation of delamination.

Inserts used for control of delamination can be interlayer films of PTFE [184], ethylene tetrafluoroethylene (ETFE) [177] and interlayers with polyamide particles [185]. Apart from the type of the interlaminar defect, its amount, size and location can play a significant role in the way the structure will react under loading. More specifically depending on the dimensions of the weak bond defect, the strength of the structure can be reduced by about 40 to 90% [184]; however, a progressive way of failure can be achieved by improvement of the delamination fracture toughness [186–188]. Elliptical [189] rectangular [190], circular [191] and other shapes [192] of films embedded in the structure can be used. Based on analytical models delamination is initiated under compression from these points only after the interlaminar film and surrounded layers buckle. The delamination subsequently propagates due to the stable compressive loading and/or due to the stored strain energy changes caused by the delamination length growth.

The introduction of an interlaminar weak bond area in the structure can affect the integrity of the structure depending on the location of the introduced defect. In the case of sandwich composites an interlaminar defect can be introduced through the width at the midsurface of the two face sheets between 0° plies [184]. Four point bending testing of these structures shows that the failure can be initiated at the interlaminar crack tip of the compressive face as a result of interlaminar fracture. The significant reduction of strength is related to the decrease in stiffness due to buckling. Under compression loading, the position of PTFE film through the thickness does not affect the maximum failure load and failure takes

place just below the global buckling load [193] due to delamination growth, whilst undelaminated samples break under compression and buckling.

Interlaminar defects can be introduced in more than one places in and between plies with different orientation away from the mid-surface [194]. For flat laminates under compression, the existence of more than one PTFE films through the thickness can affect the strength in a more drastic way. It is expected that delamination and buckling are initiated at the longer defect. As the load increases the delamination propagates and when it reaches the boundary, the second artificial delamination starts propagating. However, it is possible that multiple delaminations can initiate and propagate together due to buckling within the sublaminates [195]. The compression strength is also affected by the position of the longer delamination [192]. Examining the shape of a delamination that affects the compressive strength of a sample through the width strips have more significant influence compared to circular and peanut shaped defects. If the biggest delamination is introduced in the centre of the specimen the compression strength is higher and therefore the material is more compression resistant than in the case the longest delamination is towards the surface of the specimen. Compared to control samples, the compression strength reduction in the latter case can be 60% for a maximum delamination length of 40 mm, whilst for a 30 mm delamination [196] the maximum compression load can be reduced by 80%. As far as the buckling behaviour of the material is concerned, a triangle shape pattern with the longest delamination close to the surface shows higher buckling resistance than one with the longest delamination in the middle [192]. This is because for a large delamination introduced next to the surface of the material, propagation is stable and leads to early local buckling [197]. In the case of large delamination close to the mid surface, the sublaminates are stiffer and can sustain the applied load. Local buckling is restrained compared to delamination next to the surface. However, when it occurs, during their post-buckling event, the laminate cannot support the applied load and unstable delamination occurs which leads to an early ultimate buckling failure. Consequently, the location of the longest delamination determines the response of the material under compression or buckling loading.

2.5 Modelling of progressive damage evolution

Damage phenomena are a complex process due to the heterogeneity and anisotropic nature of these materials [198]. Extensive damage simulation studies have been carried out utilising as foundation the work of Kachanov [199] and Rabotnov [200]. A series of benchmarking studies called the World Wide Failure Exercise (WWFE) [201–203] have been conducted to examine damage modelling and failure prediction in composites. In this section the focus is on the models that can be utilised for the simulation of progressive damage evolution in composites. Damage processes can be modelled within the framework of continuum damage mechanics (CDM), based on which, damage evolution occurs through material degradation translated into stiffness reduction (strain softening) and inelastic response with permanent strains upon unloading due to sliding friction phenomena by employing damage parameters and model constants [204]. These factors are identified through experimental investigation based on the mechanisms of damage and are incorporated in the CDM models. Damage modelling focuses on two damage modes; intralaminar and interlaminar. CDM models are primarily used to simulate intralaminar damage and are linked to the microscale, mesoscale and macroscale.

Microscale damage models investigate the interaction between the constituents; the fibre, the matrix and the fibre-matrix interface [198, 205]. They can be utilised for accurate prediction of the onset of damage; however, they cannot be used for the simulation of progressive damage in the laminate due to the representation of only local phenomena, which cannot characterise the entire material [206]. The area of multiscale modelling has been investigated by bridging scales in order to further comprehend and predict the evolution of damage from its development in the lower scale to the final fracture at higher scales. Two approaches have been identified for multiscale modelling; the hierarchical and concurrent [205, 207]. The hierarchical approach uses homogenisation techniques based on which material properties are calculated at lower scales and are employed in their homogenised form at higher scales [208–214]. This usually requires the simulation of all deformation dependent material parameters which is accompanied by computationally expensive solutions [207]. Concurrent multiscale methods are

used for the simulation of nonlinear behaviour of composites. FE^2 is a widely used concurrent multiscale method based on mathematical equations to describe the composite constituents in the microscale using representative volume elements (RVEs) [215]. Higher level models are obtained through execution of FE analyses of a volume element utilising intricate averaging processes. The computational costs of the concurrent approach have led to the investigation of more efficient solutions making use of FE approaches in combination with hierarchical methodologies [216, 217].

Progressive damage modelling in composites has been extensively studied in the mesoscale or at ply level [198, 205]. Ply level models consider the laminated composite consisting of several individual orthotropic plies in which matrix and fibres are treated as a homogeneous material. Intralaminar damage is treated using CDM mesomodels, whilst interlaminar damage is expressed through discrete failure approaches [205]. The plies/layers are treated as perfectly bonded if no elements are assigned in adjacent layers to simulate the interface as well as phenomena developed therein, such as delamination. Mesoscale damage models have been extensively studied throughout the years and have been utilised representing a wide range of reinforcing morphologies subjected to various loading conditions. There are two approaches to describe damage growth in composites; through physically based continuum damage mechanics [218–222] and through thermodynamics of irreversible phenomena. In this work the focus is on the latter. A generalised damage theory was developed in the 1980s at LMT-Cachan by Ladevèze [223–226]. This model considers that the laminate can be represented by the ply and the interface elementary units. The Ladevèze model is expressed through state variables that describe stiffness degradation, as well as irreversible thermodynamic forces. It has been utilised for the simulation of intralaminar damage including matrix microcracking, fiber/matrix debonding and fibre breakage, as well as interlaminar damage using cohesive interfaces. Additionally, this mesomodel accounts for inelastic phenomena due to friction from fibre pull out during the development of matrix damage. The Ladevèze mesomodel has been implemented in the commercial software Pam-Crash™ [198] and can be used to simulate delamination due to impact and crash

phenomena [79, 227–230], as well as in other commercial software such as Abaqus implementing the damage and the cohesive material models through the VUMAT subroutines [231] and SAMCEF [232]. The ability of the Ladevèze model to predict intralaminar and interlaminar progressive damage in combination with the simple in plane and out-of-plane quasi static testing required for the identification of the model parameters renders this mesomodel a robust and reliable solution for the simulation of intricate engineering problems [79]. However, in some cases the coupling between the matrix microcracking and delamination is not captured. This has been resolved through the development of enhanced cohesive interface models by linking state variables that correspond to both ply and the cohesive material [231].

The Talreja mesomodel is based on irreversible thermodynamic phenomena which are expressed through internal variables [233–236]. It considers that damage comprises two stages; the development of multiple matrix microcracks and the propagation state that leads to delamination. Additionally, damage occurs as the accumulation of multiple cracks under various failure modes and the development of damage follows certain orientations that facilitate its propagation. A strain evolution law is included in the constitutive equations to describe damage development in the principal directions using second order tensors. The identification of the internal variables requires the execution of an experimental investigation, whilst certain constants are extracted through analytical equations. The most recent development of the Talreja model suggests a procedure for the analytical identification of the majority of the damage material parameters in UD composites, whilst the ones remaining can be identified through experimental or numerical investigation [237].

The damage mesomodel proposed by Matzenmiller, Lubliner and Taylor (MLT) [238] followed the work of Talreja suggesting the implementation of two damage variables for the principal directions and one which corresponds to damage due to shear. The MLT model uses the expressions of effective stresses [239] and a Weibull distribution to account for damage growth [240–243]. The MLT model has been utilised in LS-DYNA [244] to model damage evolution due to impact [245, 246]. In the case of crash events a coupled plasticity method is incorporated in

the MLT mesomodel in order to account for inelastic phenomena and energy absorption [247]. The law accounting for the inelastic behaviour of the material is based on a perfect plasticity flow rule where no hardening or softening take place, thus minimising the model parameters required without compromising the accuracy of the results.

A constitutive model based on thermodynamics of irreversible phenomena was suggested by Maimi and Camanho [19, 248–250]. The damage model accounts for longitudinal and transverse damage under multiaxial loading. It takes into consideration the closure of transverse cracks by introducing variables differentiating damage due to tension from compression loading based on the sign of the stress tensor. The inelastic behaviour under shear loading is represented through in-plane uncoupled isotropic plasticity and linear stiffness softening damage. The mesomodel has been utilised in combination with cohesive elements for the prediction of damage under impact phenomena indicating predictability [251–253]. The majority of the damage material properties are extracted through testing; however, certain constants need to be acquired through solving intricate analytical equations. The model has been implemented in Abaqus making use of the UMAT or VUMAT user-subroutines [254].

The challenge associated with the use of ply-scale models is that, in some cases, the damage behaviour in each ply of the laminate is considered to be independent of the neighbouring plies and therefore the interaction between them as well as with the interface is not captured. This interaction has been studied through the development of enhanced cohesive models to simulate interlaminar phenomena which are used in combination with CDM mesomodels to capture intralaminar damage [231, 255]. Another approach is associated with the use of discrete failure approaches to simulate intraply matrix microcracks and delamination, whilst fibre damage is modelled using CDM [255, 256]. The use of cohesive elements and virtual crack closure technique (VCCT) can be used to couple intralaminar and interlaminar effects [257–260]. However, an a priori knowledge of the matrix crack pattern is required for these non-predictive discrete mechanisms. Discrete methodologies that do not require prior awareness of

matrix cracks in the structure and can be applied arbitrarily are the extended FE method (X-FEM) [261, 262], the phantom node method (PNM) [263, 264], the augmented finite element method (AFEM) [265, 266] and the floating node method (FNM) [267, 268]. The use of these models can accurately account for the interaction between intralaminar matrix cracking and delamination, nevertheless, certain integration and calculation complications might arise due to inaccurate element partition [269] as well as from the introduction of boundary conditions on the fractured surfaces [269, 270].

Macroscale damage models focus on the simulation of large scale structures. Using this scale of simulation, information of the overall behaviour of the structure is acquired; however, details in the layer level, as well as their interaction cannot be captured. The utilisation of stack of elements, known as sublaminates can lead to simulation and prediction of effects in the layer level, whilst retaining the numerical efficiency of a macroscale model. The COMposite DAMage Model (CODAM) belongs to this category [219]. It has been implemented in LS-DYNA as a strain-based user material module. The initial versions of this model focused on two damage modes; fibre breakage and matrix microcracking/delamination. This macroscale damage model has been studied for the simulation of initiation and progression of damage during impact and crush loading [271, 272] as well as for open-hole composite laminates subjected to tensile and compressive loading [273, 274] refining the initial model through implementation of a cohesive tie-break law to account for delamination. The calibration of this model requires the performance of standard tests for the extraction of elastic constants and the stress-strain response of the material, as well as data regarding its strain softening behaviour. Fracture energy and the crack length are extracted from compact tension tests to identify the energy absorption of the system, as well as the damage zone size. The sublaminate approach has been also studied using the Ladevèze mesomodel and cohesive elements to simulate delamination in the commercial software Abaqus using the VUMAT subroutine [231] as well as in Pam-Crash™ through the respective implemented modules [275].

2.6 Summary of literature review and gaps identified

The application of internal pressurisation in CPVs is related to burst and leakage failure phenomena. Burst is developed as a structural failure occurring as a result of fibre breakage, whilst leakage is a functional failure caused by matrix damage. Cylindrical structures involving liners are usually associated with burst, whilst leakage occurs almost always in cylinders without liners. However, high loading rates in pipes without liner can lead to burst phenomena.

Fail-safe design development is necessary for structures used in applications in which safety is a major concern and their failure can lead to catastrophic events. The approach adopted uses mechanisms under which progressive failure occurs through energy absorption and safe crack propagation. This is based on the enhancement of the design through selection of toughened constituents that tend to fail in a ductile-like manner, thus providing progressive failure. Reinforcement on imperfections can usually function as feature for the controlled failure of structures.

The simulation of progressive damage evolution in composite structures is required for the identification of the damage mechanisms taking place in the structure as well as of their interaction that can lead to final failure. The framework of CDM is utilised to account for intralaminar damage in the microscale, mesoscale and macroscale level. Based on the literature survey that was carried out, the most suitable approaches reflecting reasonable accuracy of the damage phenomena occurring in the lamina and numerical efficiency are considered to be the ply-level and sublaminate methodologies. Within the damage models studied, the Ladevèze damage material model is chosen in this work for the simulation of progressive damage modelling. This well-established and robust model has been extensively used in Abaqus through the use of subroutines and Pam-Crash^{TM} as a built-in module. Additionally, the determination of the model parameters through simple experiments renders this mesomodel convenient in its implementation. The Ladevèze damage model is used in combination with cohesive/delamination models to account for interlaminar damage usually considering the coupling between matrix microcracking and delamination through suitable state variables.

This research focuses on the development of a LBB concept on CPVs undergoing internal pressurisation in order to ensure their graceful failure performance. As failure in these structures has been found to occur in an abrupt and unpredictable way through the incident of leakage accompanied by burst, a design methodology needs to be followed for their gradual and safe failure. This behaviour reflects the operation of fail-safe structures as the cylindrical structure is relieved through leakage occurrence in the case of over-pressurisation and at the same time it is able to withstand the induced damage and be gradually and progressively led to its failure. The occurrence of leakage that can contribute to the LBB can be established by artificially introduced defects which act as mechanisms that drive the initiation and propagation of damage and control the way of failure of the structure. Being mostly dependent on matrix cracking the leakage can be developed through the use of fibre discontinuities and interlaminar weak bond areas. Investigation of the location, dimensions and pattern of the defects can determine their level of contribution to the occurrence of leakage. The investigation can be simplified by focusing on closed-end composite pipes as their loading under a hoop to axial stress ratio of 2:1 resembles the behaviour of CPVs. The use of liner is usually associated with the occurrence of abrupt burst incidents. Therefore, exclusion of liners from the interior of pipes can ensure that the likelihood of leakage development is higher compared to a burst.

The identified gaps in the literature are the following:

- Currently there are no methodologies for defect introduction for the control of failure on flat laminates. This is developed based on experimental and simulation investigation in Chapter 6 through the development of a strategy for the introduction of fibre cut defects and interlaminar weak bond areas.
- Cylindrical structures have only been examined for their sensitivity to composite internal, outer and liner surface cracks due to notches and only to initial design criteria for defects for the development of LBB. In this work, Chapter 7 is dedicated to gradually distributed defects introduced in the composite structure through the thickness to provide fail-safe LBB through investigation of the damage introduced by defects.

- No developed and validated methodology for LBB concept has been identified in the literature. This is presented in Chapters 7 and 8 through simulation of defect concepts using fibre cut defects, interlaminar weak bond areas, as well as combination of those. Defects shapes, locations and reinforcing solutions were also examined.

3 Simulation methodology

3.1 Simulation environment

Finite Element Analysis (FEA) was carried out using the Virtual Performance Solution (VPS) solver program from ESI Group utilising the module of Pam-Crash™ [275]. The Pam-Crash™ module was selected as it is suitable for the examination of crash and impact phenomena. Furthermore, the Ladevèze damage material model that was chosen for the damage simulation is implemented in Pam-Crash™ as a built-in option. The FE models were built in the Visual-Environment graphical user interface. The composite structure was simulated utilising multi-layered shell elements. These are widely used for the modelling of thin composite structures, such as pipes, in contrast to solid elements which are preferred for thick structures and are computationally expensive. The multi-layered shell element type refers to the material type 131 in Pam-Crash™ and allows the selection of the type 1, UD composite global ply, which corresponds to the Ladevèze material model for damage simulation. The occurrence of delamination was addressed through cohesive/tied interfaces through the selection of material type 303. The numerical analysis was performed using the explicit solver of Pam-Crash™. High speed dynamic impact, blast and crash [276] phenomena are time-dependant and require the solution of the model in the time domain taking into account inertia effects, contact treatment and nonlinearities of the material [205]. Small time steps are used to obtain stable numerical solution. The calculations taking place during an explicit analysis are based on the current state of the system using direct rather than iterative solvers; hence, explicit analysis is considered as computationally efficient. On the other hand, implicit analysis is usually preferred to model time-independent phenomena during static or quasi-static loading scenarios, where acceleration effects are negligible due to the slow application of the loads on the structure. In order to solve nonlinear problems, the implicit solver calculates the solution for the current state of the system iteratively taking into account previous states. Implicit solvers can use large time steps whilst retaining their numerical stability and accuracy. However, convergence issues might be present and high

computational effort in the case of severe nonlinearities. Hence, an explicit solver was chosen in this research work as the preferred numerical scheme.

3.2 Modelling strategy

A modelling strategy was formulated to represent the response of characterisation UD coupons using continuum damage mechanics [227, 277]. This was addressed through the Ladevèze damage material model. This damage model is based on the development of a constitutive model that takes into account damage and inelastic phenomena for the computation of the damage state of the composite laminate at any instant during complex loading. This is achieved through mechanical modelling incorporating thermodynamics of irreversible processes by introducing state variables [278] based on the local state method. According to the local state method, state variables that include observable and internal variables and their associated thermodynamic forces need to be estimated in order to express the thermodynamic state of a medium at a certain point and instant. In this work, the observable and internal variables consist of elastic strains (ε^e) for reversible phenomena and inelastic strains (ε^p), damage and hardening variables for irreversible phenomena respectively [278].

The Ladevèze model relies on the mesoscale, an intermediary scale operating between micromechanics and the laminate level [279, 280]. The laminate comprises two constituents at the mesoscale level: the ply in which fibres and matrix are considered as one medium and the interface, which is a surface that connects two adjacent plies. The mesoscale damage theory uses the assumption that the damage is uniform throughout the thickness of individual layers of the composite allowing for the damage to vary from layer to layer [204, 223]. This is the basic principle based on which the LBB concept was estimated and quantified in this work. The LBB concept considered to occur as a result of sufficient damage of percentage over 50% applied in adjacent elements through the thickness.

The Ladevèze model considers that the damageable ply is at a state of plane stress. Effective stresses are developed to resist the forces that act over the damaged area. Considering the principle of strain equivalence [278], the deformation behaviour of a damaged material is expressed by the constitutive

laws for the virgin material by replacing the stress with the effective stress. Based on the principle of strain equivalence, the degradation of the elastic moduli is calculated in terms of damage parameters, which are derived from functions of associated thermodynamic forces serving as damage evolution parameters.

The degradation of elastic moduli in combination with the inelastic strains describe the ply damage state. Following classical plasticity, the inelastic strain in the mesoscale damage theory is described by an elastic domain that depends on the current effective stress and the accumulated inelastic strains for all the previous instants up to the present [204]. Inelastic strains are associated with matrix damage, whilst the fibres are considered to have an elastic response. Inelastic strains can occur in a laminate when the maximum inelastic stress is exceeded. The nonlinear response of the material is expressed through hysteresis during unloading of the laminate. The Ladevèze model approximates the non-linear unloading and subsequent loading response to linear elastic (Figure 3.1).

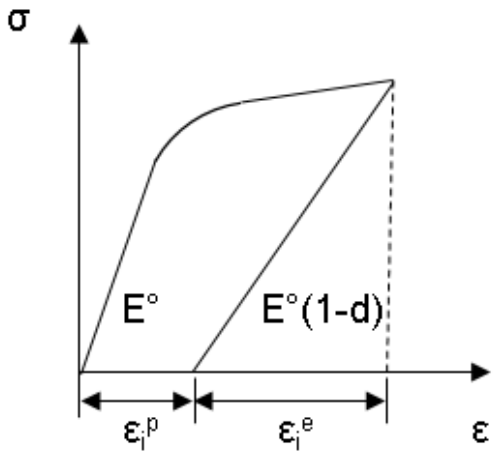

Figure 3.1 Approximation of non-linear elastic response of damaged composites

Based on the Ladevèze [226] and Pickett model [230] the simulation of delamination is carried out considering damage in the idealised interfacial layer between adjacent layers. The crack propagation at the interface is calculated combining fracture and damage mechanics considering a linear elastic damage stress-strain relation [230]. Delamination specimens were modelled as two composite shells connected through a damageable interface. Considering this

principle, in this work the interface of adjacent layers was modelled to provide idealised, strong or weak bonding for the establishment of the most effective design pattern for the development of the LBB concept.

Material properties, damage factors and thermodynamic variables were determined using experimental results on carbon fibre specimens. The experimental investigation consisted of tensile tests at $[0°]_8$ fibre orientation, compression tests at $[0°]_8$ fibre orientation and cyclic tensile tests at $[\pm45°]_{2s}$, $[+45°]_8$ and $[\pm67.5°]_{2s}$. The selection of these fibre layup sequences was determined based on the material properties and constants required for the Ladevèze damage material model. The $[\pm45°]_{2s}$ layup accounts for the examination of shear damage and the associated inelastic phenomena, whilst $[+45°]_8$ and $[\pm67.5°]_{2s}$ layups are utilised due to the optimal coupling between shear and transverse damage [204]. The cyclic tests consisted of 5 load-unload curves for the identification of the moduli degradation and the damage occurring after each cycle as well as for the determination of shear and transverse coupling parameters. Delamination samples for Mode I and II at $[0°]_{10}$ and $[0°]_{12}$ fibre orientation, respectively were also prepared for the acquisition of the strain energy release rates as well as the normal and shear stresses for the initiation and propagation of delamination.

3.3 Material models

3.3.1 Material type 131

Material type 131 [275] is appropriate for the simulation of multi-layered and multi-material shell elements (Figure 3.2). The layers can consist of materials modelled as:

- Elastic damage fibre-matrix composite (bi-phase or global)
- Elastic-plastic with damage

The representation of a shell element is at the mid-surface of the multi-layered shell, which is shown as a grey rectangle in Figure 3.2. The UD layers are stacked up from the bottom ($z=-\frac{t}{2}$) to the top ($z=\frac{t}{2}$) side across the thickness (t) of the

shell. Each layer corresponds to one integration point through the shell thickness, located within the shell in the centre of each ply. This position of integration is automatically chosen in Pam-Crash™ so that the most accurate result can be achieved, based on the numerical integration scheme.

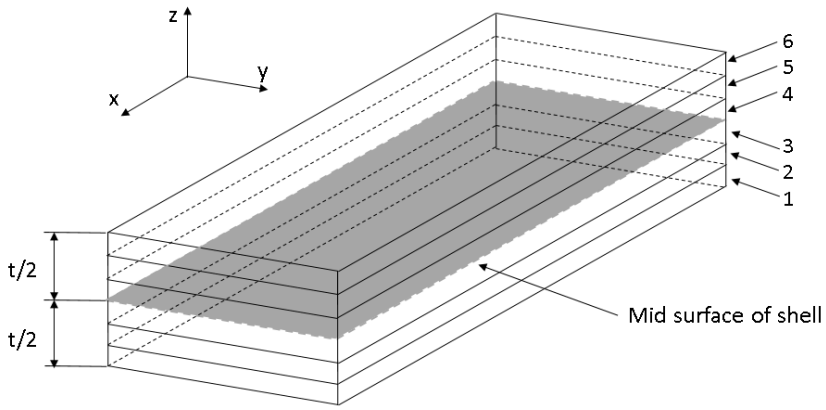

Figure 3.2 Multi-layered shell element

3.3.2 Unidirectional composite global ply

The material model used in this research work is the UD composite global ply model, also found as Ply type 1 in Pam-Crash™. This material model represents the Ladevèze damage material model [224, 279]. It is one of the most widely used Continuum Damage Mechanics (CDM) models due to its effective performance and robustness with regard to the simulation of the mechanical response and prediction of damage evolution of composites under in-plane loading conditions [204].

The Ladevèze damage material model is used for the simulation of UD continuous fibre reinforced composite materials and corresponds to a homogenised, global description of the fibre and matrix phases. The two phases of fibres and matrix are not treated separately but as one medium and the composite ply is described using homogeneous CDM. The types of damage (Figure 3.3) that can be described by the Ladevèze damage material model are:

- Fibre fracture: It is the most catastrophic failure mechanism since the fibre works as the primary load carrying component in composites. It occurs

when the maximum allowable axial tensile stress or strain has been exceeded. It is the result of tensile or compressive loading.

- Matrix microcracking: It involves the deterioration of the matrix by the creation of small cracks which can propagate and intersect with other cracks. This type of damage appears parallel to the fibre direction under shear forces or transverse to the fibres under tensile loading. However, in the Ladevèze damage material model matrix microcracking parallel to the fibre direction is related only to transverse damage.
- Fibre/matrix debonding: It refers to the separation of the two components known also as interface failure. It occurs due to shear loading.

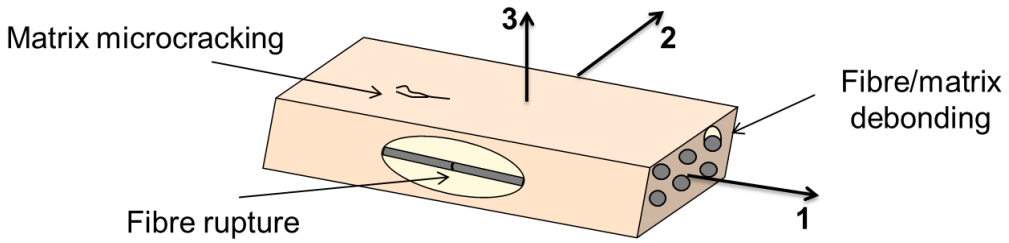

Figure 3.3 Types of damages described by the Ladevèze damage material model

3.3.2.1 Constitutive law

Laminae fall in the category of orthotropic materials in which the mechanical properties are direction dependent and are different in three mutually perpendicular planes. The analysis of laminated composite plates uses a plane stress assumption, based on which the stress components in the through the thickness normal and out-of-plane shear direction are zero. Components of strain in the through the thickness normal and out-of-plane direction are not necessarily zero. The constitutive law for this state is expressed as follows:

$$\begin{bmatrix} \varepsilon_{11} \\ \varepsilon_{22} \\ 2\varepsilon_{12} \\ 2\varepsilon_{23} \\ 2\varepsilon_{13} \end{bmatrix} = \begin{bmatrix} \frac{1}{E_{11}} & -\frac{v_{12}}{E_{11}} & 0 & 0 & 0 \\ -\frac{v_{12}}{E_{11}} & \frac{1}{E_{22}} & 0 & 0 & 0 \\ 0 & 0 & \frac{1}{G_{12}} & 0 & 0 \\ 0 & 0 & 0 & \frac{1}{G_{23}} & 0 \\ 0 & 0 & 0 & 0 & \frac{1}{G_{12}} \end{bmatrix} \begin{bmatrix} \sigma_{11} \\ \sigma_{22} \\ \tau_{12} \\ \tau_{23} \\ \tau_{13} \end{bmatrix} \quad (3.1)$$

Here, ε_{11}, ε_{22}, $2\varepsilon_{12}$, $2\varepsilon_{23}$ and $2\varepsilon_{13}$ are the elastic strains in the principal material coordinate system and similarly σ_{11}, σ_{22}, τ_{12}, τ_{23} and τ_{13} the stresses in the material coordinate system. Directions 11 and 22 represent the normal strain and stress components, whilst 12, 23 and 13- directions correspond to shear components. Parameters E_{11}, E_{22}, G_{12}, G_{23} and G_{13} are the Young's moduli in the material coordinate system. E_{11} is the modulus in the fibre (axial) direction, E_{22} is the transverse modulus, G_{12}, G_{23} and G_{13} are the shear moduli in 12, 23 and 13- directions respectively. Factor v_{12} is the Poisson's ratio in the 12-direction. The elastic strain incorporates an axial component due to the applied force and a transverse component due to Poisson's effects. Macroscopically the difference in behaviour between damaged and undamaged material is addressed through the implementation of internal variables for the description of the deteriorated state of the material [278]. The concept of damage over an area leads to the definition of the effective stresses developed by Rabotnov [239] as follows:

$$[\tilde{\sigma}] = \begin{bmatrix} \frac{\langle \sigma_{11} \rangle_+}{(1-d_1)} + \langle \sigma_{11} \rangle_- \\ \frac{\langle \sigma_{22} \rangle_+}{(1-d_2)} + \langle \sigma_{22} \rangle_- \\ \frac{\tau_{12}}{(1-d_{12})} \end{bmatrix} \quad (3.2)$$

where:

$$\langle \sigma_{ij} \rangle_+ = \begin{bmatrix} \sigma_{ij} \text{ if } \sigma_{ij} \geq 0 \\ 0 \text{ if } \sigma_{ij} < 0 \end{bmatrix} \quad \text{and} \quad \langle \sigma_{ij} \rangle_- = \begin{bmatrix} 0 \text{ if } \sigma_{ij} > 0 \\ \sigma_{ij} \text{ if } \sigma_{ij} \leq 0 \end{bmatrix} \quad (3.3)$$

Here, $\tilde{\sigma}$ is the effective stress whilst, d_1, d_2 and d_{12} are the damage parameters which represent the state of the damage in the 11, 22 and 12-directions and are based on experimentally observed damage phenomena. Factor d_1 is related to damage due to fibre breakage, d_2 to damage occurring during matrix microcracking parallel to the fibre direction and d_{12} is related to damage occurring during debonding between fibres and matrix. The Ladevèze damage material model damage factors d_2 and d_{12} are implemented to describe transverse and shear matrix damage respectively. The value of damage parameters is 0 in the undamaged state and 1 in the fully damaged case leading to ultimate failure of the lamina. The bracket notation in Equation (3.4) is used to distinguish the effects of normal tensile $\langle\sigma_{ij}\rangle_+$ and compressive $\langle\sigma_{ij}\rangle_-$ loading. In the case of normal tensile loading as the damage, which consists of microcracks and microvoids, increases the effective normal tensile stresses increase, whilst in the case of normal compressive loading, microcracks and microvoids tend to close and hence the effective stress does not increase. The effective shear stress is considered to be independent of the sign. Subscript i corresponds to the direction which is normal to the plane of interest and j to the direction of the applied stress. Normal components are described by i=j, whilst i≠j represents shear components. Based on the principle of strain equivalence, the deformation behaviour of a damaged material is described by the constitutive laws of the pristine, undamaged material in which the stress value is replaced by the effective stress value [278]. Therefore, the uniaxial linear elastic law for a damaged material is expressed as follows:

$$\varepsilon=\frac{\tilde{\sigma}}{E} \tag{3.4}$$

Utilising Equations (3.2) and (3.4), the constitutive law for a damaged orthotropic material in plane stress is defined as follows:

$$\begin{bmatrix}\varepsilon_{11}\\ \varepsilon_{22}\\ \varepsilon_{12}\end{bmatrix}=\begin{bmatrix}\dfrac{\langle\sigma_{11}\rangle_{+}}{E_{11}^{0}(1-d_1)}+\dfrac{\langle\sigma_{11}\rangle_{-}}{E_{11}^{0}}-\dfrac{v_{12}^{0}}{E_{11}^{0}}\sigma_{22}\\ \dfrac{\langle\sigma_{22}\rangle_{+}}{E_{22}^{0}(1-d_2)}+\dfrac{\langle\sigma_{22}\rangle_{-}}{E_{22}^{0}}-\dfrac{v_{12}^{0}}{E_{11}^{0}}\sigma_{11}\\ \dfrac{\tau_{12}}{2G_{12}^{0}(1-d_{12})}\end{bmatrix} \tag{3.5}$$

Here, superscript 0 corresponds to undamaged state. The response of a damaged layer can be expressed at any loading state based on Equation (3.5) through the elastic moduli degradation defined in terms of the undamaged values of moduli and the respective damage factors.

3.3.2.2 Matrix transverse and shear damage evolution

The description of the state of a material at a certain point and instant is described through the expression of the strain energy density E_D as follows [223, 281, 282]:

$$E_D=\frac{1}{2}\left[\frac{\langle\sigma_{11}\rangle_{+}^{2}}{E_{11}^{0t}(1-d_1^{ft})}+\frac{\langle\sigma_{11}\rangle_{-}^{2}}{E_{11}^{\gamma}(1-d_1^{fc})}-\frac{2v_{12}^{0}}{E_{11}^{0t}}\sigma_{11}\sigma_{22}+\frac{\langle\sigma_{22}\rangle_{+}^{2}}{E_{22}^{0}(1-d_2)}+\frac{\langle\sigma_{22}\rangle_{-}^{2}}{E_{22}^{0}}+\frac{\tau_{12}{}^{2}}{G_{12}^{0}(1-d_{12})}\right] \tag{3.6}$$

Parameter v_{12}^{0} is the undamaged Poisson's ratio in the 12-direction and d_1^{ft}, d_1^{fc} are the damage parameters for tensile and compressive fibre damage respectively. Subscripts t and c refer to tensile and compression loading respectively. Factor E_{11}^{γ} is the nonlinear undamaged modulus under compressive loading. The partial derivatives of the strain energy density (Equation (3.6)) with respect to the damage parameters d_1, d_2, d_{12} lead to the determination of the thermodynamic forces Z_{11}, Z_{22} and Z_{12} of a damaged layer (Equations (3.7)-(3.8)). The thermodynamic forces are analogous to strain energy release rates as they govern the damage evolution in a composite ply and they represent the dissipation of energy during the occurrence of matrix damage in the transverse and shear directions. Z_{22} and Z_{12} are the thermodynamic forces that are responsible for the development of matrix damage in a composite ply and E_{22} and G_{12} are the only moduli with degraded values [204, 223]. The ply modulus in the fibre direction is only degraded when fibre breakage occurs. Therefore, Z_{11}

is not taken into account for the evolution of damage in a composite ply. The thermodynamic forces Z_{22} and Z_{12} are calculated as follows:

$$Z_{22}=\frac{\vartheta E_D}{\vartheta d_2}\Big|_{\tilde{\sigma},d_{11},d_{12}} = \frac{1}{2}\cdot\frac{\langle\sigma_{22}\rangle_+^2}{E_{22}^0\cdot(1-d_2)^2} \tag{3.7}$$

$$Z_{12}=\frac{\vartheta E_D}{\vartheta d_{12}}\Big|_{\tilde{\sigma},d_{11},d_{22}} = \frac{1}{2}\cdot\frac{\tau_{12}^2+\tau_{13}^2}{G_{12}^0\cdot(1-d_{12})^2} \tag{3.8}$$

Here, $\frac{\vartheta E_D}{\vartheta d_2}$ and $\frac{\vartheta E_D}{\vartheta d_{12}}$ are the partial derivatives of strain energy density with respect to damage in the transverse and shear direction respectively, whilst the effective stress and damage in 11 and 12-direction for the transverse case and 11, 22-direction for the shear case are held constant. The thermodynamic forces are directly connected to the damage evolution functions, which are defined as follows:

$$Y_{22}(t)=\max_{\tau\le t}\left(\sqrt{Z_{22}(\tau)}\right) \qquad \text{Transverse damage} \tag{3.9}$$

$$Y_{12}(t)=\max_{\tau\le t}\left(\sqrt{Z_{12}(\tau)+bZ_{22}(\tau)}\right) \quad \text{Shear damage} \tag{3.10}$$

The damage evolution functions represent the maximum values of thermodynamic forces throughout the load history from time 0 up to the current moment t. This is motivated by the fact that propagation of damage occurs only when the previous maximum value of the thermodynamic forces is exceeded for additional damage to occur. Parameter b is a coupling factor between shear and transverse damage. The damage parameters for matrix damage evolution can be obtained through:

$$d_2=\begin{bmatrix}\dfrac{\langle Y_{22}(t)-Y_{22}^0\rangle_+}{Y_{22}^C} & \text{If } d_2<d_{max}, Y_{22}(t)<Y_{22}^U \text{ and } Y_{12}(t)<Y_{12}^U \\ d_{max} & \text{otherwise}\end{bmatrix} \tag{3.11}$$

$$d_{12}=\begin{bmatrix}\dfrac{\langle Y_{12}(t)-Y_{12}^{0}\rangle_{+}}{Y_{12}^{C}} & \text{If } d_{12}<d_{max}, Y_{22}(t)<Y_{22}^{U} \text{ and } Y_{12}(t)<Y_{12}^{U}\\ d_{max} & \text{otherwise}\end{bmatrix} \tag{3.12}$$

Here, parameters Y_{22}^{0} and Y_{12}^{0} denote the initial transverse and shear damage threshold values respectively. The critical transverse and shear damage limit are represented by Y_{22}^{C} and Y_{12}^{C} respectively. Parameter Y_{22}^{U} denotes the brittle transverse damage limit of the fibre-matrix interface and Y_{12}^{U} the shear damage fracture limit. Damage parameter d_{max} defines the maximum allowed value for d_2 and d_{12}.

3.3.2.3 Inelastic damage law

The permanent inelastic strains that occur when a lamina is unloaded, after the stress limit has been exceeded, can be described through a Hill-type inelastic criterion as follows [275]:

$$f(\tilde{\sigma},R)=\sqrt{\left[\frac{\tau_{12}}{(1-d_{12})}\right]^{2}+a^{2}\left[\frac{\langle\sigma_{22}\rangle_{+}^{2}}{(1-d_{2})}+\langle\sigma_{22}\rangle_{-}\right]^{2}}-R(\bar{\varepsilon}^{p}) \tag{3.13}$$

$$R(\bar{\varepsilon}^{p})=R_{0}+\beta(\bar{\varepsilon}^{p})^{m} \tag{3.14}$$

The inelastic damage law is defined with respect to the effective stresses ($\tilde{\sigma}$) and the accumulated effective inelastic strain ($\bar{\varepsilon}^{p}$) from the beginning of loading up to the present instant. The system exhibits hysteresis during unloading. In Pam-Crash™ solver the unloading and loading slopes of the material are approximated as linear elastic. Parameter $a^2=A$ denotes a coupling factor between shear and transverse plastic strains, R_0 represents the initial yield stress on the onset of inelasticity, β the hardening law multiplier which defines gradient of the hardening curve and m the hardening law exponent.

3.3.2.4 Fibre damage

In the Ladevèze damage material model, fibre damage is described through threshold strain criteria, governed by variables that treat separately tension and compression [275]. There are three regions that describe the damage state of the fibres stressed under tensile loading: subcritical, critical and post critical. The subcritical region designates the undamaged state of the fibre and is characterised by the threshold strain region in which the strain (ε_{11}) does not exceed the initial longitudinal fibre tensile damage threshold strain (ε_i^{ft}). As the fibres continue to undergo deformation under tensile loading, the tensile damage d^{ft} increases linearly between the damage threshold strain region and the ultimate longitudinal fibre tensile damage strain (ε_u^{ft}). When the ultimate value of strain is reached, the tensile damage reaches its ultimate value ($d_u^{ft} \cong 1$). The evolution of the tensile Young's modulus based on the damage threshold strain region is as follows:

$$E_{11}=E_{11}^{0t}\left(1-d^{ft}\right)=\begin{bmatrix} d^{ft}=0 & \text{if } \varepsilon_{11}<\varepsilon_i^{ft} & \text{Subcritical} \\ d^{ft}=d_u^{ft}\dfrac{\varepsilon_{11}-\varepsilon_i^{ft}}{\varepsilon_u^{ft}-\varepsilon_i^{ft}} & \text{if } \varepsilon_i^{ft}\leq\varepsilon_{11}<\varepsilon_u^{ft} & \text{Critical} \\ d^{ft}=1-(1-d_u^{ft})\dfrac{\varepsilon_{11}}{\varepsilon_u^{ft}} & \text{if } \varepsilon_u^{ft}\leq\varepsilon_{11}<\infty & \text{Post-critical} \end{bmatrix} \tag{3.15}$$

During compressive loading the fibre compressive damage is related to fibre misalignment and fibre micro-buckling phenomena which follow non-linear behaviour. The non-linear fibre compressive behaviour is expressed as:

$$E_1^{\gamma}=\frac{E_1^{0c}}{1+\gamma E_1^{0c}|\varepsilon_{11}|} \tag{3.16}$$

Here, factor γ is introduced in the equation of the nonlinear compressive Young's modulus to describe the reduction of the longitudinal modulus with strain under compression. Parameter E_1^{0c} is the initial value of the compressive Young's modulus in the fibre direction.

The compressive fibre damage is expressed through the subcritical, critical and post critical threshold strain regions, similarly to tensile fibre damage. The subcritical region represents the undamaged state of the fibre under compressive loading in which the strain (ε_{11}) does not exceed the initial longitudinal fibre compressive damage threshold strain (ε_i^{fc}). The critical region is described by the linear increase of the compression damage d^{fc} between the damage threshold strain region and the ultimate longitudinal fibre compressive damage strain (ε_u^{fc}). In the post-critical region, when the ultimate longitudinal fibre compressive damage strain is reached, the compressive damage obtains its ultimate value ($d_u^{fc} \cong 1$) and the material fails completely. The calculation of the compressive Young's modulus in the fibre direction based on the damage threshold strain region is as follows:

$$E_{11}^{c} = E_{11}^{y}\left(1-d^{fc}\right) = \begin{bmatrix} d^{fc}=0 & \text{if } |\varepsilon_{11}|<\varepsilon_i^{fc} & \text{Subcritical} \\ d^{fc}=d_u^{fc}\dfrac{|\varepsilon_{11}|-\varepsilon_i^{fc}}{\varepsilon_u^{fc}-\varepsilon_i^{fc}} & \text{if } \varepsilon_i^{fc}\leq|\varepsilon_{11}|<\varepsilon_u^{fc} & \text{Critical} \\ d^{fc}=1-\left(1-d_u^{fc}\right)\dfrac{|\varepsilon_{11}|}{\varepsilon_u^{fc}} & \text{if } \varepsilon_u^{fc}\leq|\varepsilon_{11}|<\infty & \text{Post-critical} \end{bmatrix} \quad (3.17)$$

The subcritical, critical and post-critical regions for fibre damage under tensile and compressive loading are displayed in Figure 3.4. The two graphs illustrate stress-strain and damage-strain evolution respectively.

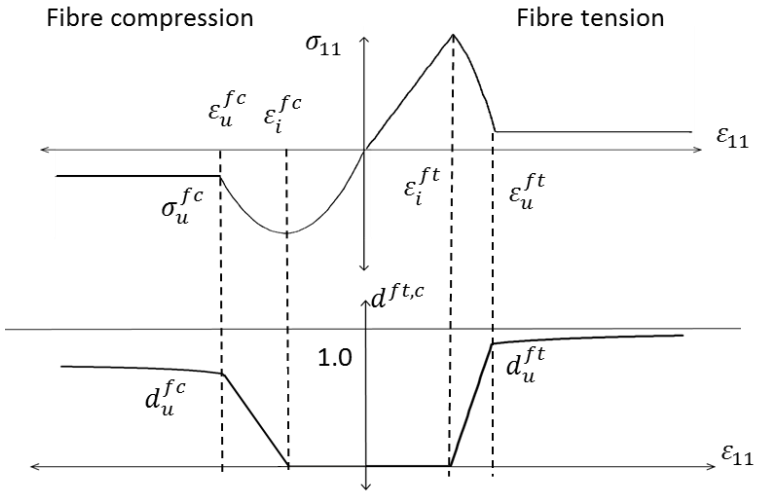

Figure 3.4 Fibre tensile and compressive damage

3.3.3 Material type 303

Material type 303 is used in Pam-Crash™ to simulate tied interfaces between adjacent plies of a composite laminate, as well as delamination under out-of-plane loading. The tied interfaces consist of the slave node and the master segment (Figure 3.5). These are connected using a penalty method, according to which the applied forces are computed based on the deformation and the spring stiffness. The penalty deformation is applied to adjacent interface elements and refers to the relative displacement of the slave node from the actual to the ideal position with respect to the master segment, which can be expressed as normal displacement δ_I and shear displacement δ_{II} for Mode I and Mode II respectively [227, 230]. The calculation of the sliding crack displacements δ_I and δ_{II} is based on the beam theory for DCB geometry corresponding to Mode I [283–285] and ENF geometry for Mode II [286–288] respectively. The equations are developed with respect to the original crack taking into account the summation of the deflection of the cracked part, the displacement at the crack tip and the deflection at the end of the uncracked beam due to rotation at the crack tip. The sliding equations are:

$$\delta_I = \frac{3d}{\alpha^3}\left[\frac{\alpha(\alpha-\alpha_0)^2}{2} - \frac{(\alpha-\alpha_0)^3}{6}\right] \tag{3.18}$$

$$\delta_{II} = -\frac{8d\alpha^3 h}{3\alpha^3+2L^3}\left[\frac{3\alpha_0^2}{\alpha^3} - \frac{3}{\alpha}\right] \tag{3.19}$$

Here, d is the head displacement, α is the crack length and α_0 the initial crack length. Parameters h and L represent half the specimen thickness and the total length of the specimen respectively. The strains occurring due to normal and shear displacements are:

$$\begin{bmatrix}\varepsilon_I \\ \varepsilon_{II}\end{bmatrix} = \frac{1}{h_{cont}}\begin{bmatrix}\delta_I \\ \delta_{II}\end{bmatrix} \tag{3.20}$$

Here, h_{cont} is the distance between a slave node and master segment which corresponds to the interface thickness. The penalty spring stiffness is calculated based on the stresses applied on the node in the normal and shear direction. This is described as:

$$\begin{bmatrix} \sigma_n \\ \sigma_{tan} \end{bmatrix} = \begin{bmatrix} \sigma_I \\ \sigma_{II} \end{bmatrix} = \begin{bmatrix} E_0 & 0 \\ 0 & G_0 \end{bmatrix} \begin{bmatrix} \varepsilon_I \\ \varepsilon_{II} \end{bmatrix} \tag{3.21}$$

Here, E_0 is the modulus in the normal direction and G_0, the modulus in the shear direction. Moduli E_0 and G_0, depend on the energy dissipation occurring at the tied interface when damage takes place. The calculation of the normal and shear moduli is carried out through the slope at the elastic region of the stress-strain curves from Mode I and Mode II tests respectively.

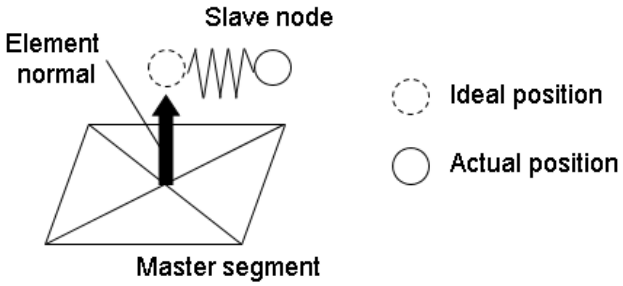

Figure 3.5 Tied interface, slave node and master segment

The forces applied at the interface are a function of the normal and shear stresses and the slave nodal surface, also known as spring area. This is expressed as:

$$\begin{bmatrix} F_n \\ F_{tan} \end{bmatrix} = \begin{bmatrix} F_I \\ F_{II} \end{bmatrix} = A_{slave} \begin{bmatrix} \sigma_I \\ \sigma_{II} \end{bmatrix} \tag{3.22}$$

Here, the slave nodal surface (A_{slave}) is expressed by the area of the element the slave node belongs to, multiplied by ¼ for linear quadrilateral elements or ⅓ for linear triangular elements. This is calculated as follows:

$$A_{slave} = {}^1/_4 \sum_{i=1}^{nquad} Area_i + {}^1/_3 \sum_{i=1}^{ntriangle} Area_i \tag{3.23}$$

The critical strain energy release rate (G_{Ic}) is used to describe the energy dissipation due to the resistance of the material to the propagation of an existing crack. The simulation of crack propagation can be achieved by combining fracture and damage mechanics for the development of a linear elastic stress-strain damage relation:

$$\sigma_I=(1-d_I)E_0\varepsilon_I \tag{3.24}$$

$$\sigma_{II}=(1-d_{II})G_0\varepsilon_{II} \tag{3.25}$$

The linear elastic stress-strain damage relation can be described through a triangular curve based on Pickett's approach [230] (Figure 3.6). Point A corresponds to the initiation of damage (σ_i^{max}). After the stress has reached its maximum value, damage starts occurring until the ultimate failure of the material at Point B. The damage is described through the damage factors d_i, where i=I or II for Mode I and II respectively, the value of which vary from 0 for the undamaged state to 1 for ultimate failure as follows:

$$d_i=\begin{bmatrix}\dfrac{\varepsilon_i-\varepsilon_{iA}}{\varepsilon_{iB}-\varepsilon_{iA}} & \text{if } \varepsilon_i\geq\varepsilon_{iA}\\ 0 & \text{otherwise}\end{bmatrix} \tag{3.26}$$

The strain energy release rates for the initiation (G_i^0) and propagation of the damage until ultimate failure (G_u^0) can be acquired from the area under the triangular stress-displacement curve. The evolution of strain energy in the elastic and damaging region is calculated as follows:

$$G_i^0=\frac{1}{2}\cdot\sigma_i^{max}\varepsilon_{iA}h_{cont} \tag{3.27}$$

$$G_u^0=\frac{1}{2}\cdot\sigma_i^{max}\varepsilon_{iB}h_{cont} \tag{3.28}$$

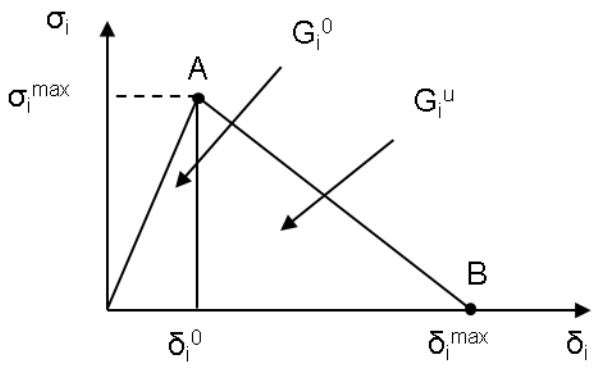

Figure 3.6 Stress-displacement linear elastic damaging graph (i=I or II for Mode I and II respectively) [230]

3.4 Finite element implementation

The core procedure for the model development is described in this section. An FEA model was developed for the simulation of composite structures. The pre-processing took place in Visual-Mesh and Visual-Crash Pam. The explicit analysis of the model was performed through the VPS Solver, whilst the post-processing was carried out in the Visual-Viewer. The model development process is presented in Figure 3.7. Specific characteristics for the simulation of different scenarios will be introduced in following chapters (Chapters 5-7).

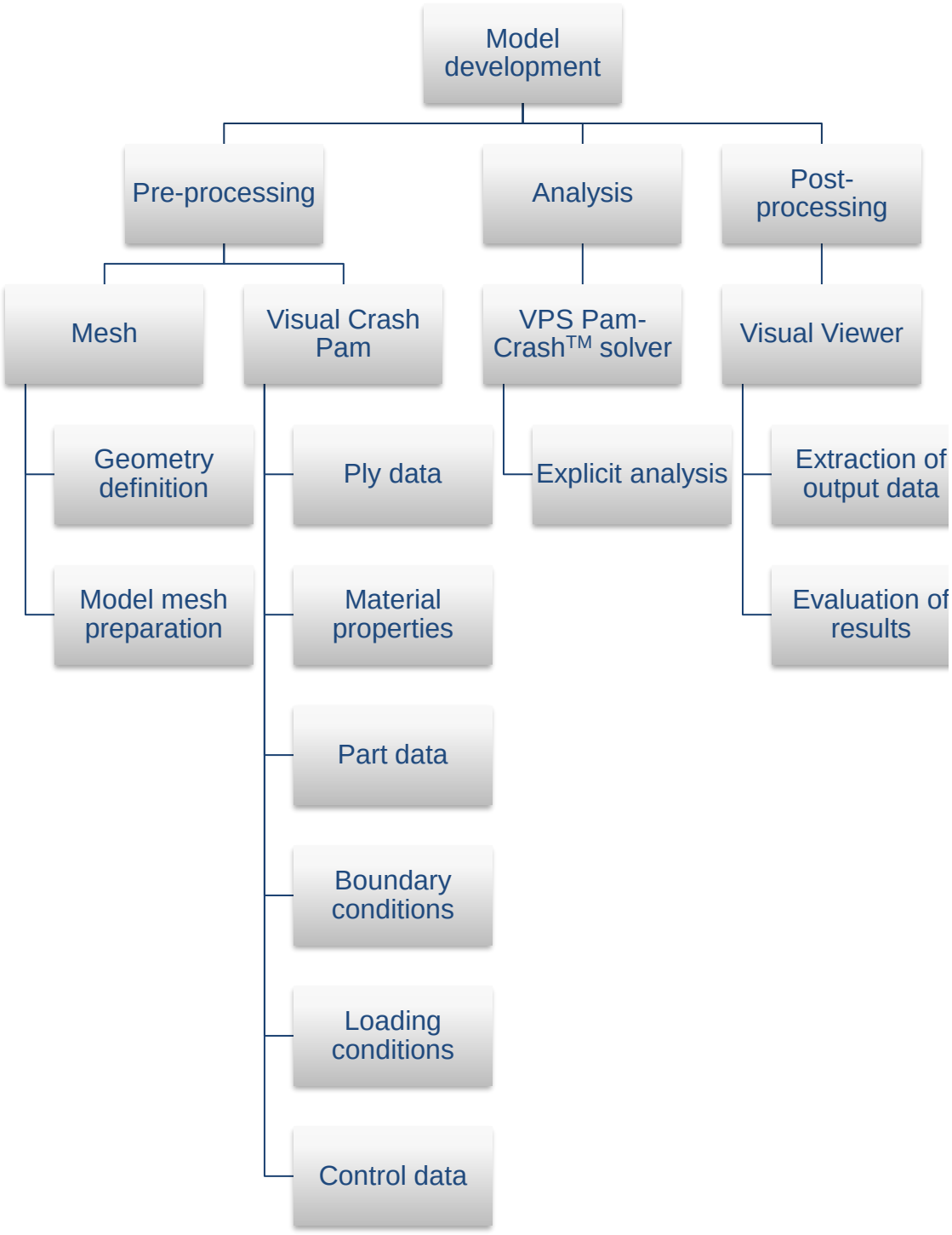

Figure 3.7 Model development process

In the pre-processing, Visual-Mesh was used for the generation of the geometry of the model and its mesh. The geometry was formed through the creation of circumferential nodes or curves in the xyz global coordinate system. Quadrilateral shell elements were used to mesh the two-dimensional surface providing highly accurate results for structured grids compared to triangular elements.

The definition of the model data was carried out on the Visual-Crash Pam pre-processor, of the Visual Crash Program (VCP). In this module the ply, material, part, control data as well as loads and boundary conditions were assigned on the model. The ply data was defined through a composite ply panel from which the Ply type 1 (ITYP=1) Global Ply UD composite was selected. The homogenised material properties contained in the ply data card are summarised in Table 3.1, where ρ is the density of the composite. The data was acquired through experimental investigation (Chapter 5.1).

Table 3.1 Ply data for multi-layered shell element

Type of material properties	Symbol
Tensile	E_{11}^{0t}, ε_i^{ft}, ε_u^{ft}, d_u^{ft}
Compressive	E_{11}^{0c}, ε_i^{fc},ε_u^{fc}, d_u^{fc}, γ
Shear	G_{12}^{0}, Y_{12}^{0}, Y_{12}^{C}, Y_{12}^{U}, R0, β, m
Transverse	E_{22}^{0t}, Y_{22}^{0}, Y_{22}^{C}, Y_{22}^{U}
Shear and transverse	A, b, dmax
Miscellaneous	ρ, v_{12}

Material data were assigned to the model on a definition card from which the 131-Multilayer Orthotropic Bi Phase material type was selected for the simulation of the multi-layered orthotropic shell. In this card the total number of layers of the composite material were defined through the number of operations (NOPER) alongside a layer identification database (ILAY=1). This option allows the acquisition of additional information about the individual layers as output in

combination with the control cards. In the material card, the orientation of each angle ply (ANGPL) was defined, as well as the absolute ply thickness (THKPL) at a constant 0.3 mm. Ply identification (IDPLY) data determined in the ply card were assigned to the material card for each layer of the layer identification (IDLAYER) dataset. Shell element information used as output for post-processing was specified through an auxiliary output section. The shell properties were selected by introducing the ply identification number and the respective reference number of the required property. The defined auxiliary variables included stress and strain properties in the three material directions, shear and transverse, plastic transverse strain ($\varepsilon_{22}^{plastic}$), shear plastic strain ($2\varepsilon_{12}^{plastic}$) and strain rate ($\dot{\varepsilon}$). Table 3.2 summarises the output auxiliary variables that were selected.

Table 3.2 Auxiliary variables of material type 131 saved for plots

Reference number	ITYP=1
1	ε_{11}
2	ε_{22}
3	ε_{12}
4	ε_{23}
5	ε_{13}
6	σ_{11}
7	σ_{22}
8	σ_{12}
9	σ_{23}
10	σ_{13}
11	d_{12}
12	d_2
13	$\varepsilon_{22}^{plastic}$
14	$2\varepsilon_{12}^{plastic}$
15	$\dot{\varepsilon}$

Additional shell element properties were specified through a part data panel. The element thickness and the orthotropic axis were defined in this panel. The

definition of the orthotropic axis (IORT=0) and hence of the reference fibre orientation was established through the global coordinate system frame with respect to a vector (1, 0, 0). Material identification (IDMAT) data were also assigned to the part data panel.

The three-dimensional structure was constrained through appropriate boundary conditions. Translational and rotational displacements were defined in the global frame. Loading conditions were applied through the definition of concentrated loads and face pressures. Features where the loads were applied, were selected and loading curves were assigned to them. The loading curves used in this work include displacement, force and pressure.

The preparation of the model was completed by defining the control data. This data enables the efficient analysis of the model providing the desired output information. Control data comprises optional and standard data. The optional data included the selection of the latest version of the Pam-Crash^{TM} solver and definition of the type of the analysis which was set to explicit. The standard data panel included information about the output parameters control (OCTRL), explicit time step control data (TCTRL) and end of run definition (RUNEND). An overview of the standard control data can be found on Figure 3.8. The output parameters control comprised the output type, contour plot variables, output frequency and time history plot. The output type (ERFOUTPUT) was set to provide both contour and curve data. Contour plot variables were selected to be obtained from the analysis including plot output for the layers (LAYPLOT), nodes (NODPLOT) and the shell element (SHLPLOT). The output frequency was set to provide mesh plot intervals (DSYOUTPUT) of 0.025 s and 1000 time history plot points (THPOUTPUT). Time history output for the shell element (SHLTHP) were also defined.

The explicit time step control data comprised user imposed initial time step (INITIAL), nodal time step control (NODAL) and dynamic mass scaling control (DYNA_MASS_SCALE). The user imposed initial time step value (DTUSER) was set to 0 ms. The nodal time step control option (NODTSP) was activated to include delamination phenomena and a minimum time step of 0.0001 ms for the

dynamic mass scaling criterion (DTMASS) was specified, whilst keeping the increase mass per node constant to 0.

Standard control data was completed through the definition of the run termination time (TIO2) for the specification of the duration of the analysis. This was driven by the time dependent loading curves applied to the model during the definition of the loading conditions. The duration of the loading was set to be the same to the end of run definition. This value was different for each modelling case, accommodating the individual loading requirements.

The model analysis was carried out on the VPS Pam-Crash^{TM} solver and its results were evaluated on the Visual-Viewer. Data previously defined in the pre-processing were obtained as output on the Visual-Viewer.

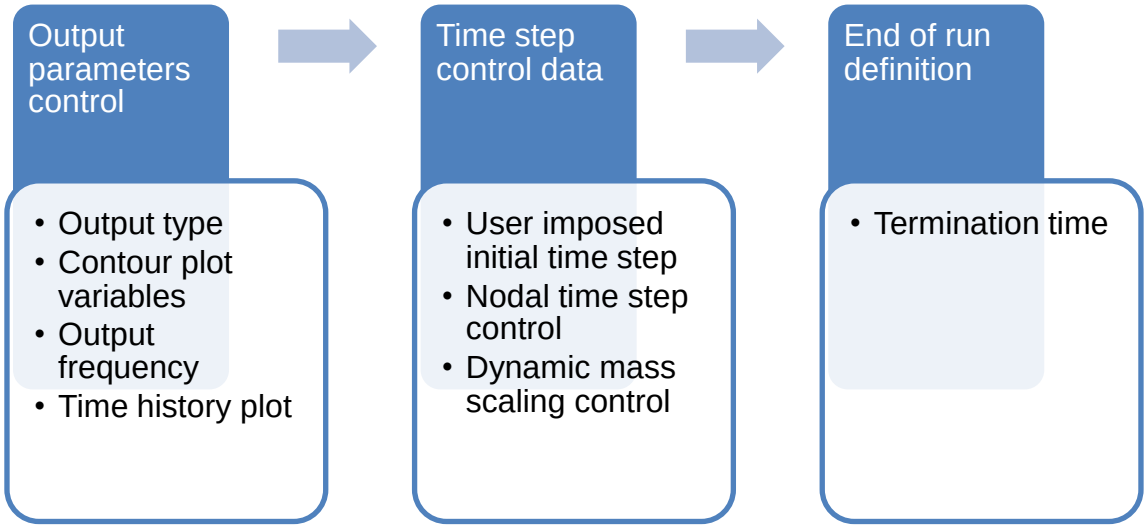

Figure 3.8 Standard control data

4 Materials and experimental methods

This chapter reports the materials, manufacturing processes and test protocols used in this research work. Carbon prepreg was selected for the manufacturing of composite plates and pipes. The experimental work involved in-plane and out-of-plane tests for the estimation of material properties and damage parameters used in simulation. Hydrostatic burst tests were also performed on intact pipes and pipes with defects for the assessment of the LBB concept.

4.1 Materials

The materials that were used in this research work consisted of carbon fibre prepreg for the manufacturing of composite plates and pipes and miscellaneous materials that assisted the manufacturing process. The materials used are specified in more detail in the following paragraphs.

4.1.1 Carbon fibre prepregs

A high quality UD carbon fibre prepreg with the commercial name SE84LV [289] was selected for the development of the LBB concept through the execution of an extensive experimental campaign on laminates and cylindrical structures for the acquisition of material and damage parameters used for the development of a constitutive model. This material, which is certified by Lloyd's Register (LR), was acquired from MarineWare. This prepreg system has T_g of 115°C and comprises high elongation carbon fibre (HEC) with 300 g/m^2 aerial weight as well as epoxy resin system SE84LV with 33% resin content by weight. The use of HEC fibre provides high strain and relatively high stress and Young's modulus, suitable for the development of the LBB concept on composite pipes as leakage is expected to occur through failure in the matrix, in a slow manner from layer to layer. This toughened UD carbon prepreg system is widely used in heavily loaded components such as yacht hulls and spars. The nominal mechanical properties of SE84LV are summarised in Table 4.1 [289]. The supplied SE84LV carbon prepreg roll was kept in a freezer at -18°C. The SE84LV prepreg roll has eight

weeks life out of the freezer when being in ambient temperature between 18-22°C or two years at -18°C.

Table 4.1 Mechanical properties of SE84LV [289]

Property	Unit	Value
Aerial weight	g/m^2	300
Fibre volume fraction	%	55
Tensile strength	MPa	2458
Tensile modulus	GPa	134
Tg	°C	115

An epoxy prepreg system with the commercial name RP507 [290] was acquired and used for preliminary experimental investigation of the defect modelling strategy for the development of the LBB concept. This material was supplied by PRF Composite Materials Laminates. This prepreg system comprised UD, high strength carbon fibre with 150 g/m^2 aerial weight as well as epoxy resin system RP507 with 38% resin content by weight and medium tack. The prepreg system has a glass transition temperature (T_g) of 121°C. RP507 is a medium temperature cure resin system with curing temperatures varying between 90°C to 160°C. RP507 can be used in applications in aerospace, automotive, marine and defence. The nominal mechanical properties for this UD material are summarised in Table 4.2 [290]. The RP507 carbon fibre prepreg was supplied in a roll and was kept in the freezer at -18°C. Its outlife was specified by the manufacturer as one month at 20°C or twelve months at -18°C.

Table 4.2 Mechanical properties of RP507 [290]

Property	Unit	Value
Aerial weight	g/m^2	150
Fibre volume fraction	%	55
Tensile strength	MPa	2212
Tensile modulus	GPa	131
T_g	°C	121

4.1.2 Miscellaneous

4.1.2.1 6082T6 Aluminium tooling plate

An aluminium alloy tool/mould was used for the manufacturing of flat CFRPs. The aluminium tool was used as part of the oven system for the curing of the composite laminates. The dimensions of the aluminium tool were 450x450x4 mm^3 in order to accommodate the composite laminates that were manufactured, as well as the sealing product at the edges of the tool without interfering with the composite panel.

4.1.2.2 Chemlease® PMR-90 EZ Release agent

A semi-permanent release agent was used for mould releasing of the composite laminates. The commercial name of this material is Chemlease® PMR-90 EZ [291], supplied by Chemtrend. Chemlease® PMR-90 EZ was used in order to provide multiple releases and high slip and therefore to enhance productivity. It was also used to provide protection of the part and its surface quality, as well as extension of the tool life.

4.1.2.3 VACsealY-40 Tacky tape

A high quality sealant tape was used for vacuum bag sealing during the manufacturing process. VACsealY-40 [292] was supplied by VAC Innovation.

This material was used to provide good adhesion as well as quick release. This material can be used under elevated temperatures of up to 205°C in conventional and autoclave ovens.

4.1.2.4 Bleeder Lease® B Peel ply

A coated nylon peel ply sheet with nominal thickness of 0.114 mm was placed on each side of the composite laminate. Bleeder Lease® B [293] was supplied by Airtech and was used for easy release of cured composite laminates. The easy release is achieved due to a silicone release agent that Bleeder Lease® B is coated with. The use of Bleeder Lease® B enables the application of vacuum conditions which eventually leads to the reduction of voids and air bubbles. A textured surface is produced when the peel ply was peeled off the cured laminate due to the tightly woven nature of Bleeder Lease® B. The texture surface improves the adhesion of the part for further processing such as bonding and painting.

4.1.2.5 A4000 Perforated release film

A perforated release film with the commercial name A4000 [294] and thickness of 0.025 mm was used on top of the peel ply at the upper side of the laminate. This high performance fluoropolymer release film was supplied by Airtech. It incorporates perforations following the P3 perforation style [295], which corresponds to nominal hole diameter of 0.381 mm and nominal open area of 0.14%. The existence of perforation enables controlled release of excess resin from the laminate while it also enhances the application of vacuum conditions for the reduction of voids and air bubbles. The maximum operating temperature of this material is 260°C.

4.1.2.6 Airweave® N-4 Breather

A medium weight conformable breather was selected to ensure adequate evacuation and air channelling throughout the vacuum bag. The material was supplied by Airtech Advanced Materials Group. The use of Airweave® N-4 [296] provides high quality vacuum bagging and also protects the vacuum bag from any sharp edges of the composite structure. Bridging can be avoided due to its

flexible nature and conformability to complex shapes. Airweave® N-4 is made of non-woven polyester and has white colour. Its nominal areal weight is approximately 140 g/m^2. Being able to absorb the excess resin of resin rich systems under curing, Airweave® N-4 can be also used as a bleeder.

4.1.2.7 Ipplon® WN1500 Vacuum bag

A high temperature nylon vacuum bag, supplied by Airthech, was used in order to create a uniform compressive force over the structure that was under vacuum conditions. Ipplon® WN1500 [297] has a maximum operating temperature of 246°C and can be used under high pressure. The thickness of this material is 0.05 mm and its colour is blue. Ipplon® WN1500 can achieve high elongation of 375% and has a tensile strength of 62 MPa.

4.1.2.8 Non stick Polytetrafluoroethylene (PTFE)

The Mode I and II out-of-plane tests require the incorporation of non stick Polytetrafluoroethylene (PTFE) crack starting films [298] in the middle of the composite structure during manufacturing. This material was supplied by Goodfellow and its thickness is 13 μm. Its low coefficient of friction renders it ideal to provide negligible bonding on adjacent surfaces. Its maximum operating temperature is 260°C.

4.1.2.9 Glass fibre tabs

The preparation of composite specimens for testing involved the attachment of continuous E-glass fibre reinforced polymer matrix materials as tabs. A $[0/90]_{2s}$ epoxy glass fibre plate with 1.5 mm thickness was supplied by Croylek. The plate was then cut at a 45° fibre orientation with respect to the force direction in order to provide a smooth transition of the force from the tab to the specimen. Also, the use of tabs on the composite samples protects it from the grips of the test equipment.

4.1.2.10 Loading blocks

Aluminium blocks were used for load introduction in Mode I testing. The purpose of the blocks is to introduce and sustain the applied loading without any damage

on the CFRP specimens to occur. The material used for blocks was Grade 2014A aluminium. The blocks were manufactured and supplied by Machinepart Engineering Ltd. The width of the loading blocks was governed by the width of the composite specimens. The rest of the dimension were specified based on the standard for Mode I testing [299]. The blocks dimensions are presented in Figure 4.1.

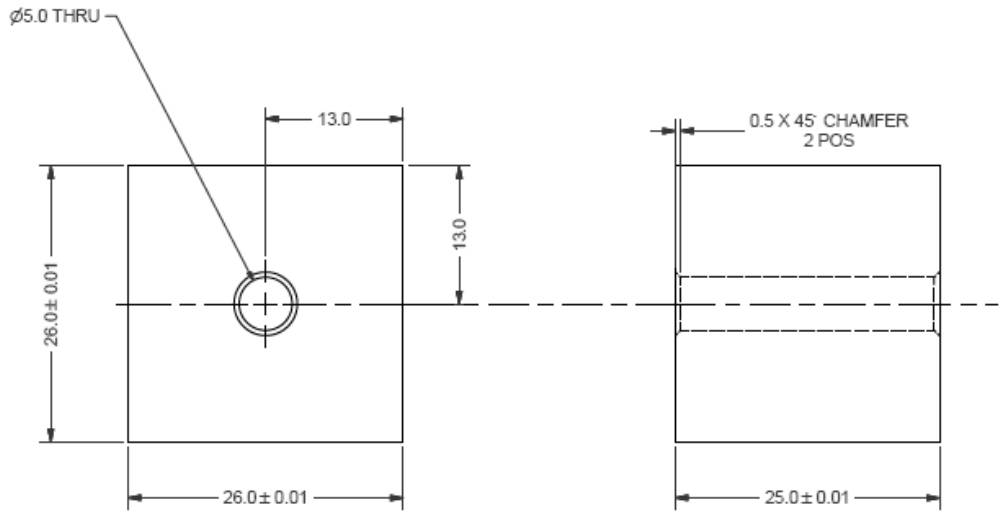

Figure 4.1 Loading blocks drawings (dimensions in mm)

4.1.2.11 Araldite 2014-1

The bonding of tabs on the test specimens was performed with the use of Araldite® 2014-1 [300] supplied by RS components Ltd. This epoxy adhesive system consists of two parts, which when mixed produce a thixotropic paste adhesive with high strength. Lap shear strength of 10 MPa and above can be achieved after 20 minutes at 60°C. Araldite 2014-1 can also provide resistance against high temperature and chemical substances.

4.1.2.12 3M Scotch-Weld™ DP760

A 3M Scotch-Weld™ epoxy adhesive system was used for the bonding of end caps on composite pipes. This adhesive system was supplied by RS components

Ltd. DP760 [301] consists of two parts, toughened epoxy as base and modified amine as curing agent enclosed in a dual syringe plastic cartridge. The maximum overlap shear strength is 30.4 MPa when the system is cured at 65±3°C for 120 min ensuring high strength structural bonding between the two adjacent surfaces.

4.1.2.13 PTFE Virgin-FE1000 Rod

A PTFE Virgin-FE1000 rod [302] was used as a mandrel for the manufacturing of composite pipes. The rod was supplied by Theplasticshop.co.uk®. Due to its low friction coefficient, varying between 0.05-0.07, PTFE Virgin-FE1000 rod is ideal for extrusion purposes. The working temperatures of this material vary between -200°C to 260°C providing coefficient of linear thermal expansion of $15 \cdot 10^{-5} °C^{-1}$ from 25°C to 100°C.

4.1.2.14 Shrink Tite tape

A polyester tape supplied by East Coast Fiberglass Supplies with the commercial name Shrink Tite tape [303] was wound on top of the composite pipe. This polyester tape has the ability to shrink and apply pressure when heated. The compression forces applied provide compaction and consolidation between layers as well as elimination of air bubbles and voids while giving a smooth resin rich finish to the part. The tape is covered with PTFE release coating on one side to ensure easy removal from the part. The temperature at which shrinking starts is 65°C, whilst the operating temperature goes up to 180°C. The Shrink Tite tape can provide 20% shrinking.

4.2 Manufacturing processes

This section describes the manufacturing processes that were followed for the production of composite laminates and pipes. The first part is dedicated to the manufacturing of flat composite laminates used for preparing testing coupons. Two sets of different types of laminates were manufactured. The first set consisted of the manufacturing of SE84LV carbon fibre prepreg laminates, which were produced for the execution of the experimental campaign that involved the acquisition of mechanical and damage properties for the development of the

constitutive model. The second set consisted of the manufacturing of RP507 carbon fibre prepreg laminates for the preliminary study of a defect modelling strategy for the development of the LBB concept. The second part of this section is dedicated to the manufacturing process followed for the production of composite pipes. The material that was used was SE84LV carbon fibre prepreg following a manual type of towpreg filament winding technique.

4.2.1 Processing of flat laminates

The process steps that were followed for the manufacturing of composite laminates consisted of lay-up of the composite plies at the desired fibre orientations based on the requirements of the tests. Subsequently, the curing process followed was based on the manufacturer's datasheet, depending on the material used. The last step involved the preparation of the test specimens.

4.2.1.1 Ply lay-up

Initially, the prepreg roll was removed from the freezer and was kept at ambient temperature until its defrosting. The prepreg roll was cut into sheets of dimensions 300x300mm using a guillotine. The number of sheets cut were defined based on the requirements of the tests for the specimen thickness. The roll was then bagged and returned in the freezer for its protection from premature curing at ambient temperature and a log was kept about the remaining life of the roll. The sheets were then laid up at the required orientations. For out-of-plane delamination specimens a non-stick PTFE sheet was embedded at the mid-plane of the lay-up covering certain area corresponding to a pre-crack. The stack was debulked every 4 plies to achieve high levels of consolidation and to remove voids and air bubbles. The alluminium tool was cleaned and coated with Chemlease® PMR-90 EZ release agent in a fume cabinet. Subsequently, VACsealY-40 tacky tape was attached at the periphery of the metallic mould and a sheet of peel ply was placed in the centre. The composite laminate was then removed from the debulking bed and was positioned on top of a Bleeder Lease® B peel ply sheet. The sequence of materials that were positioned on top of the composite laminate was one additional sheet of peel ply, an A4000 perforated release film and an

Airweave® N-4 breather. The consumable materials were cut in such dimensions so that they would overhang from the prepreg stack. Vacuum fittings were used in order to achieve a complete vacuum line extraction configuration. A base plate was placed on top of the breather, as part of vacuum through bag connectors, at a location that would not cause indentation on the prepreg stack. The assembly was completed by placing a sheet of Ipplon® WN1500 vacuum bag on top of the stack, which was sealed through the tacky tape that was applied on the periphery of the release coated mould. The vacuum bag was then pierced at the location where the thread of the base plate was in order to insert and thread the top piece of the vacuum valve. A quick disconnect part was threaded on the top part of the valve and was connected to a pump through a vacuum hose. The assembly of the lay-up and the consumables that were used is presented in Figure 4.2.

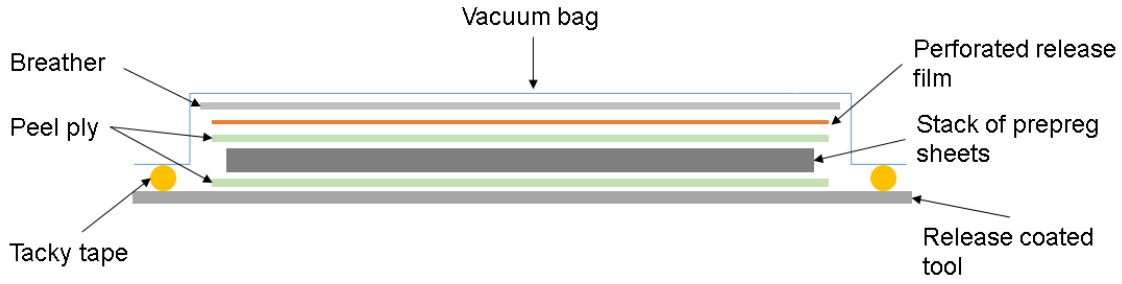

Figure 4.2 Lay-up configuration

4.2.1.2 Curing

The curing process followed was the same for the laminates manufactured using SE84LV for the extensive experimental campaign dedicated to the development of the constitutive model and laminates produced using RP507 for the preliminary investigation of a defect modelling strategy for the development of the LBB concept. The lay-up assembly was placed in the oven, whilst being connected through a hose to a pump to ensure vacuum conditions throughout the curing process. Based on the manufacturer datasheets, the cure cycle consisted of three steps, which involved heating up, curing at a consistent temperature and cooling down. The system was heated up from 23°C to 120°C at a rate of 2°C/min. Once 120°C was reached, the system remained at that temperature for one hour (1 h). Subsequently, the cooling down occurred at a controllable rate of 2°C/min until

approximately 55°C was reached. The nominal glass transition temperature of SE84LV reached following this profile is 115°C, whilst for RP507 it is 120°C. Figure 4.3 presents the configuration of composite laminate with the consumables inside the oven at the end of the curing cycle.

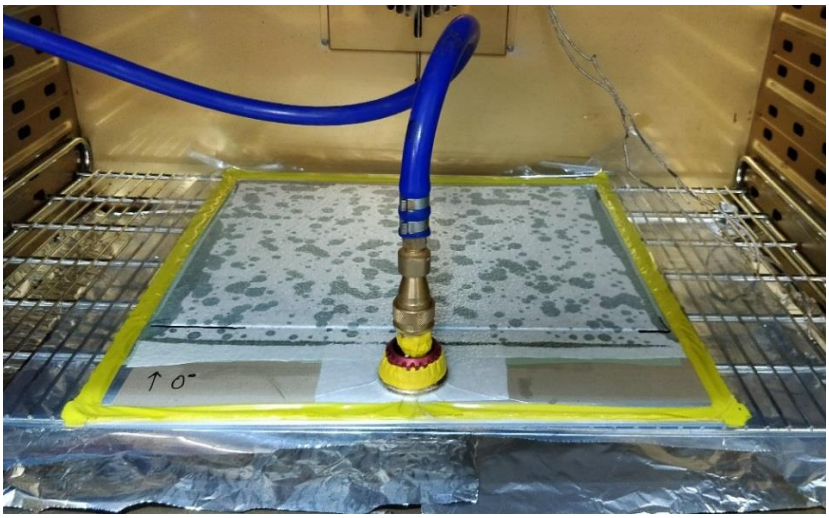

Figure 4.3 Cured laminate in the oven under vacuum

4.2.1.3 Preparation of specimens for testing

After curing the composite laminate was cleared from consumables utilised for its manufacturing. In the case of specimens for in-plane testing the next step was preparation for tabbing. More specifically, the laminate sides and edges were cleaned from any excess resin using a diamond saw and sand paper. Glass fibre tabs had been previously cut and their surface had been treated using grit blasting. The selected abrasive was 120 grit alumina. In this way the surface of the tabs had a relatively abrasive finish to achieve successful adhesion. The surfaces of both the composite laminate and the tabs were cleaned from dust that would contaminate the bond. Araldite 2014-1 adhesive was applied on the surfaces that had to be bonded through an EPX applicator system adhesive gun and a nozzle that was attached on the bottle of the adhesive in order to allow mixing of the two parts. The mixture was applied on the composite laminate and the tabs and a spatula was used to spread it. The two parts were joined together and excess adhesive was removed with the use of a spatula. Initially the top and bottom edge of one side of the composite laminate were prepared. The

configuration was placed on a release coated tool, sealed with a vacuum bag and cured in the over according to the datasheet of the Araldite 2014-1 at 60°C for 20 min. The use of a vacuum bag enabled the creation of an inclination of approximately 45° from the tab to the specimen surface, providing a smooth transition of the force distribution. The same process was followed for the tabbing of the other side of the composite laminate. Laminates prepared for the out-of-plane specimens did not require bonding of tabs.

Laminates prepared with tabs for in-plane testing as well as laminates for out-of-plane testing were then cut to suitable dimensions using a diamond blade saw. The use of diamond blade ensures the minimisation of microcracks and cutting marks, due to the abrasive nature of CFRP composites and the hardness of the diamond.

Aluminium blocks were bonded onto Mode I specimens at the edge of the specimens where the PTFE was, on both sides (Figure 4.4). Lastly, all specimens that were used for out-of-plane Mode I and Mode II testing were coated on both side surfaces with white spray, ahead of the PTFE insert, for visual detection of delamination and were later marked. For Mode I specimens a scale was drawn ahead of the insert every 1mm. For Mode II specimens, marks were drawn on the sprayed sides at locations that indicated the position of the support rollers on which the samples were mounted during the testing as described in Chapter 4.3.3.2.

Figure 4.4 Mode I DCB specimen

4.2.1.4 Strain gauging of composite specimens

Biaxial and 45° rosette type strain gauges acquired from Techni Measure Ltd were utilised for strain recording during testing. The biaxial strain gauges were aligned to the longitudinal and transverse direction of the 0°, +45° and ±45° tensile and 0° compression coupons. The rosette type strain gauges comprised three strain gauges aligned to the longitudinal, transverse and a 45° angle direction between the longitudinal and transverse direction. The 45° rosette type strain gauges were used on ±35°, ±55° and ±67.5° specimens. The position of the strain gauges was at the middle of the gauge length at one side of the specimen. Back-to-back strain gauges were attached on the faces of compression specimens in order to examine bending and buckling phenomena. Figure 4.5 illustrates the position of biaxial and 45° rosette type strain gauges.

The attachment of strain gauges on the specimens faces involved preparation of the finish of the composite surface. The preparation was carried out using scotch-brite abrasive pads supplied from 3M. Cyanoacrylate adhesive was used for the attachment of the strain gauge on the desired position. The wires of the strain gauge were slightly lifted and tags were bonded on the composite specimen underneath the wires. A soldering iron was utilised to solder the strain gauge wires onto the tags. The cyanoacrylate adhesive and tags were supplied from Techni Measure Ltd.

(a) (b)

Figure 4.5 Position of (a) biaxial and (b) 45° rosette type strain gauges

4.2.2 Processing of tubular vessels

The manufacturing of tubular vessels involved lay-up of composite plies onto a mandrel at the desired fibre orientation followed by curing. The composite pipe surfaces were prepared for end cap attachment on both pipe ends of each cylinder.

4.2.2.1 Lay-up

The SE84LV prepreg was utilised for the manufacturing of composite pipes. Sheets of prepreg were cut in a parallelogram shape, based on the required dimensions of spiral wound pipes. The parallelogram is presented in Figure 4.6 and its dimensions are calculated as follows:

$$d_{tot}=d+2B \quad (4.1)$$

Here, α is the wrapping angle of the prepreg (complementary to the winding angle which is 55°), C represents the circumference of the pipe, W is the width of the

tow-preg and B is the base of the designed triangle. The distance d is calculated based on the area of the cylinder and the parallelogram, where L the length of the finished wrapped pipe. The total length of the tow-preg is designated as d_{tot}. These values change, since the diameter is increasing after the placement of each layer.

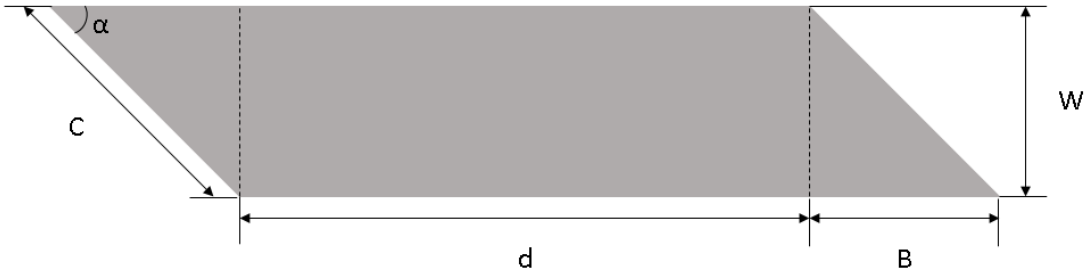

Figure 4.6 Spiral wound pipe dimensions

A PTFE Virgin-FE1000 Rod was cleaned and used as mandrel, on which the prepreg strips were wound. Bench top pipe rollers were also used to facilitate winding of the tow-pregs as the pipe was spinning. The manufacturing process and the set-up of the mandrel and the bench top pipe rollers are presented in Figure 4.7 and Figure 4.8 respectively.

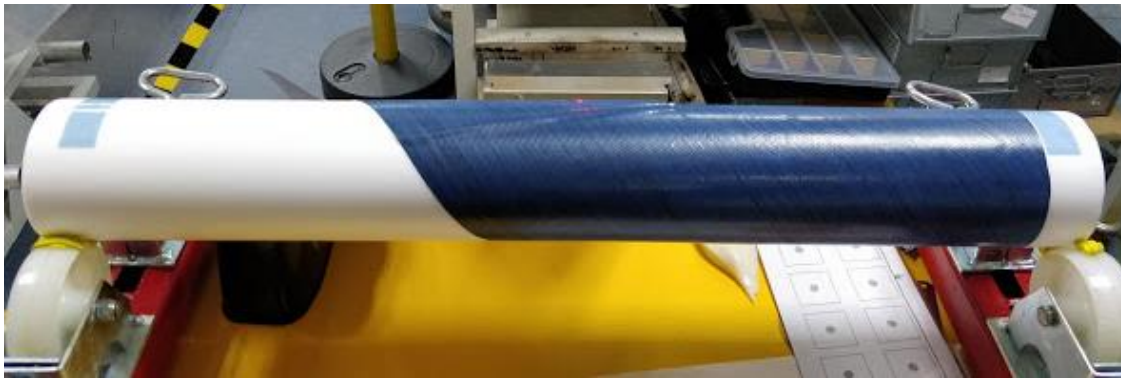

Figure 4.7 Moment from the manufacturing process

All the pipes that were manufactured comprised 8 layers at $[\pm 55°]_{2s}$ stacking sequence. The orientation of the fibres was defined with respect to the longitudinal axis of the tube. After the completion of pipe winding with fibre tow-pregs, two layers of Shrink Tite tape were wrapped around the pipe. The width of the tape was 32mm and the overlap that was used was approximately 22mm.

The wide overlap that was selected led to a finer finish of the surface and ensured that the wall thickness would remain approximately constant along the length of the pipe. This allowed later the optimal performance of Non Destructive Testing, preventing the scattering of the transmitted ultrasound on the pipe, leading to minimisation of the distortion of the shape of the received signal.

Figure 4.8 Set-up of composite pipe and bench top pipe rollers

4.2.2.2 Curing

The pipe wrapped with shrink tape was placed in a Binder M240 oven [304] as illustrated in Figure 4.9. The use of supports at the edges of the mandrel allowed the pipe to be raised and not to touch the base of the oven. The curing involved heating up at a rate of 2°C/min from 23°C to 120°C. The pipe remained at 120°C for one hour and was cooled down with a rate of 2°C/min from 120°C to 60°C. The removal of the pipe from the oven allowed the system to cool down to ambient temperature.

Figure 4.9 Pipe wrapped with shrink tape for curing in the oven

4.2.2.3 Preparation of tubular vessels for testing

The composite pipe, after its curing, was placed on the bench top pipe rollers for the removal of the shrink tape. The next step involved the extrusion of the pipe from the mandrel, which was easily performed due to the non-stick PTFE rod surface. The pipe ends were cut using a diamond saw to the desired length of 600 mm. The composite pipe after its initial preparation is presented in Figure 4.10. A Dremel Platinum Edition 4000 Multitool was used to treat the surfaces where the end caps would be attached. This was carried out using a sanding wheel in order to enable strong adhesion between the composite pipe and the metallic end caps. Each treated area was 150 mm long allowing 300 mm of uncovered area of the pipe. Figure 4.11 shows the areas of the composite pipe that have been treated.

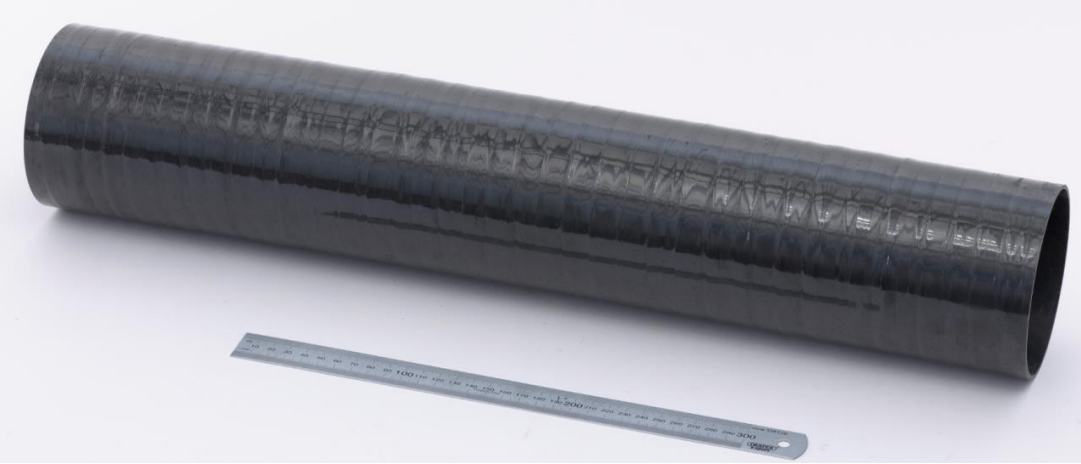

Figure 4.10 Manufactured composite pipe

Figure 4.11 Treated areas of pipe for bonding

4.2.2.4 End caps

Closed-end caps were attached to the two ends of composite pipes to allow internal pressurisation. The end caps were made of steel and were manufactured based on the requirements of the hydrostatic burst test [305]. More specifically, they were manufactured and positioned in such way so that they would allow displacement in both hoop and axial directions enabling the pipe to resemble a CPV. The dimensions of the end caps follow the standard requirement for pipes with external diameter less than 150 mm that the uncovered distance between the end caps is the least 300 mm long. The drawings and a photo of the end caps are presented in Figure 4.12 and Figure 4.13 respectively. Two sets of end caps

were manufactured. One set had domed ends whilst the other was kept at its cylindrical form. This difference on the two sets of end caps is only aesthetic and has no influence on the performance of the pressurised vessel. Four holes of 5 mm diameter were drilled on the end caps at a distance of 25 mm from the end cap base. An angle notation at 0°, 90°, 180° and 270° was drawn for the indication of the hole locations. Four additional holes were also drilled at a distance of 75 mm from the end cap base at 45°, 135°, 225° and 315° angle with respect to the initial angle notation. The existence of holes facilitated the bonding process of the end caps on the composite pipe.

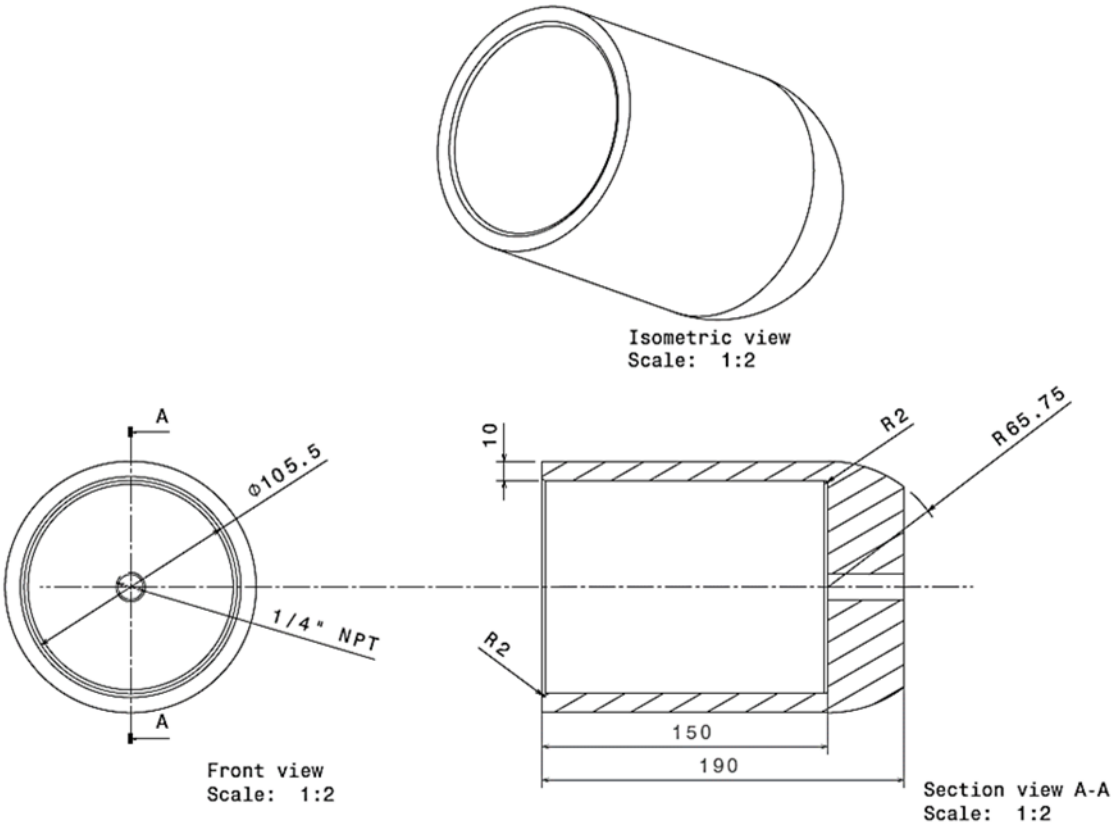

Figure 4.12 End cap drawings (dimensions in mm)

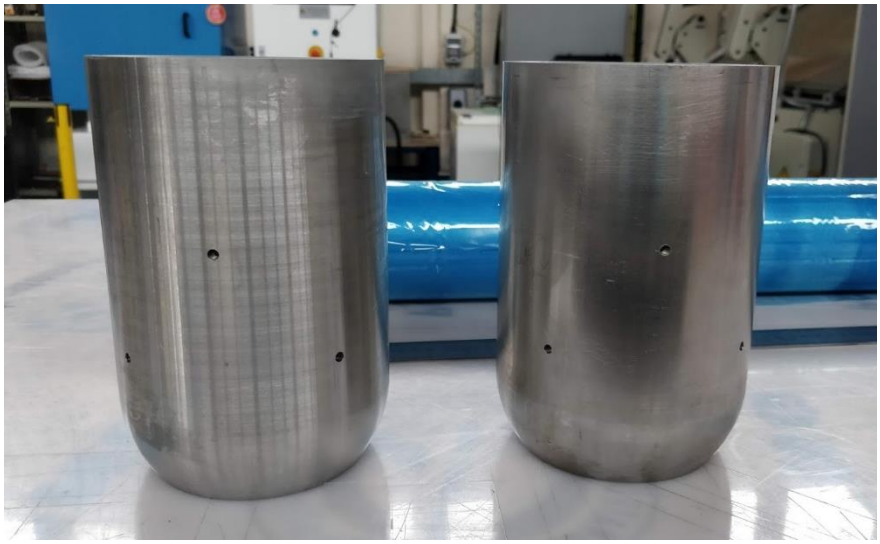

Figure 4.13 Steel end caps

The attachment of the end caps to the composite pipe involved the application of 3M Scotch-Weld™ DP760 adhesive on both end caps and the pipe. The end caps had been heated up to 50°C in order to improve the curing heat up rate of the large thermal mass of the thick steel end caps. One composite pipe end was inserted in the end cap and subsequently the other end followed. Additional adhesive was injected to the bond line through the holes drilled on the end caps until all the air had been removed from the bonded area. The end-closed pipe was then placed in a Caltherm oven in a vertical position and was cured based on the manufacturer's datasheet at 65°C for two hours (2h). The positioning of the pipe in the oven for its curing is illustrated in Figure 4.14.

Figure 4.14 Adhesive bonding of end caps on pipe through curing

4.2.2.5 Strain gauging of tubular vessels

Strain gauges were attached on the tubular vessels at suitable locations prior to hydrostatic burst testing. The strain gauges used were 3 mm rectangular rosette gauges supplied by Techni Measure Ltd. Figure 4.15 presents the locations of the strain gauges for intact composite pipes. The strain gauges were placed in the centre of the pipe/gauge length, in the middle of the distance between the centre of the pipe /gauge length and the end cap edge and diametrically opposed from the gauge located in the middle of the pipe/gauge length. A numbering system from 1-9 was utilised to designate the extracted strains and their correspondence to the respective locations and angles.

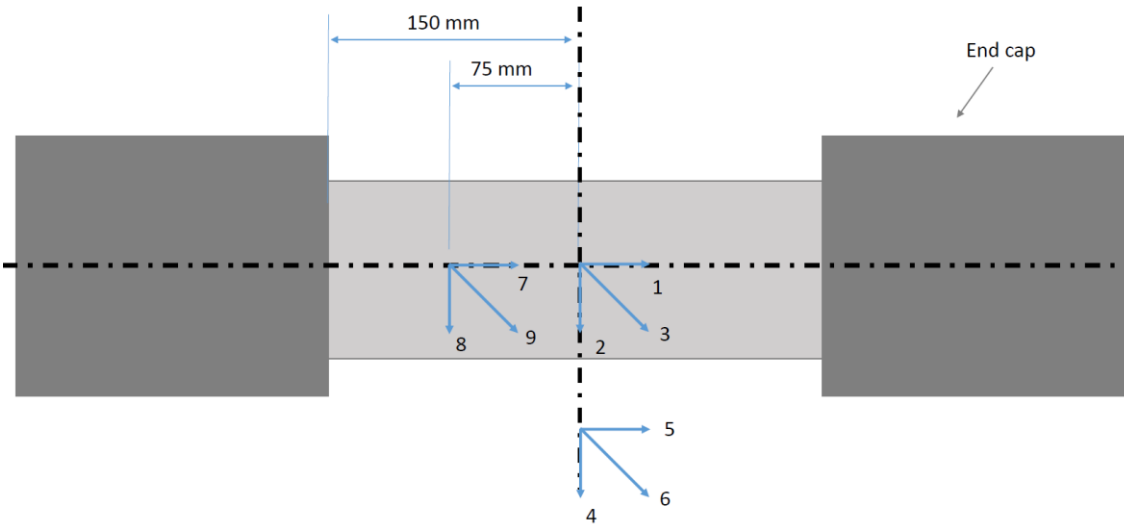

Figure 4.15 Strain gauge locations for intact pipe

4.3 Test protocols

An extensive experimental campaign was carried out on SE84LV for the extraction of material properties and damage parameters for the implementation of the continuum damage model presented in Chapter 3. The experimental study involved in-plane and out-of-plane testing. The in-plane tests consisted of tensile and compressive tests performed on $[0°]_8$ specimens, as well as cyclic in-plane shear tests performed on $[\pm45°]_{2s}$, $[+45°]_8$ and $[\pm67.5°]_{2s}$ specimens. Out-of-plane tests were carried out for the estimation of the interlaminar fracture toughness for Mode I and Mode II. In the case of Mode I $[0°]_{10}$ specimens were manufactured and tested, whilst in the case of Mode II testing $[0°]_{12}$ fibre orientation specimens were used. Five specimens were tested for each test case according to the requirements of the respective standards. Performance of Non Destructive Testing (NDT) before and after the destructive test investigation enabled the qualitative examination of the composite laminates and investigation of their failure behaviour. The experimental campaign was completed with hydrostatic tests on composite pipes. Two composite pipes without liner and $[\pm55°]_{2s}$ layup were tested for the assessment of their failure behaviour and maximum operational pressure. One of the pipes was used as control test and

did not incorporate artificial defects. One pipe included cut fibre artificial defects for the validation of the LBB concept.

A preliminary investigation on the defect modelling strategy for the development of the LBB concept was performed on the RP507 material. The experiments comprised tensile testing of coupons with and without fibre cut defects for $[0°]_{16}$ and $[\pm35°]_{4s}$ layups. All tests were repeated on five specimens. The experimental investigation for flat and cylindrical structures is summarised in Table 4.3.

Table 4.3 Description of experimental investigation

Material type	Structural type	Structural characteristic	Test	Stacking sequence	Number of specimens
SE84LV	Flat	Intact	Tensile	[0°]8	5
SE84LV	Flat	Intact	Cyclic tensile	[±45°]2s , [+45°]8, [±67.5°]2s	5
SE84LV	Flat	Intact	Compression	[0°]8	5
SE84LV	Flat	Intact	Mode I	[0°]10	5
SE84LV	Flat	Intact	Mode II	[0°]12	5
SE84LV	Cylinder	Intact	Hydro-static	[±55°]2s	1
SE84LV	Cylinder	Fibre cuts	Hydro-static	[±55°]2s	1
RP507	Flat	Intact	Tensile	[0°]16, [±35°]4s	5
RP507	Flat	Fibre cuts	Tensile	[0°]16, [±35°]4s	5

4.3.1 Non Destructive Testing

NDT provided the opportunity to assess the structure before or after testing by examination of the location, shape and size of defects that might be present. In the current research work, the non-destructive evaluation that was carried out consisted of C-Scan and x-ray computed tomography (XCT).

4.3.1.1 C-Scan

C-Scan was carried out on composite laminates (Figure 4.16) and pipes for the inspection of the quality of the structure before testing. Flat composite panels were submerged into a Motion Link immersion tank. The tank was filled with water and was used as the medium to facilitate sound transmission. A Panametrics probe of 12.7 mm diameter was submerged into the water and positioned at the edge of the laminate at an angle of 0° and a distance of approximately 40 mm. The ultrasound frequency used was 3.5 MHz. The probe was moving and scanning along one side of the panel with an increment step of 0.8 mm. The ultrasonic acquisition software used was Ultravision 3.6R2. A Bacus RT 6 immersion tank was used for composite pipes. The pipe was submerged into the water and was positioned on a base that enabled rotation. The probe was positioned at a 0° angle and distance of 68 mm from the pipe. The frequency was set at 10 MHz to acquire higher sensitivity in order to detect defects of dimensions less than 1 mm. The scanning angular length was set at 360° and the inspection length to 310 mm, which was the area between the end caps and part of the covered area. The probe increment step was 2 mm. The ultrasonic acquisition software used was Multi2000.

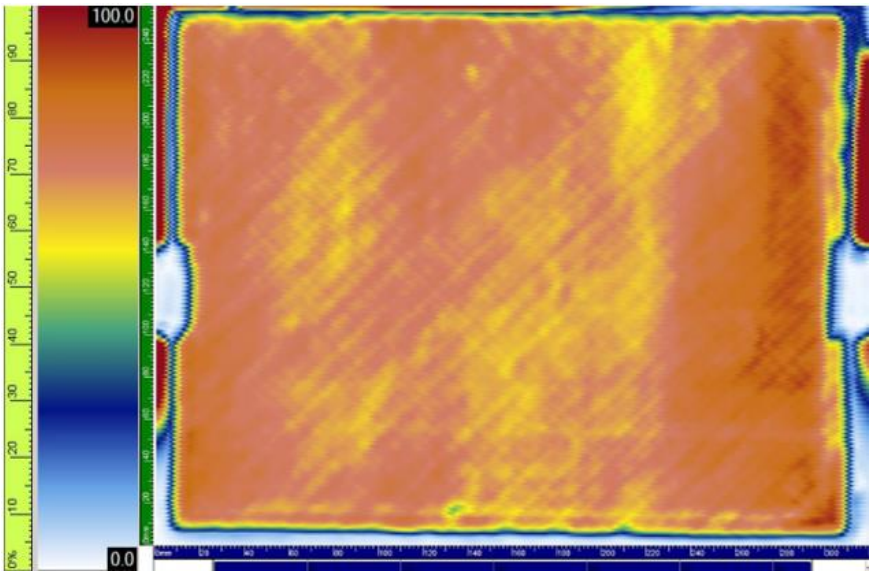

Figure 4.16 C-scan image of composite angle ply laminate

4.3.1.2 X-ray computed tomography

The investigation of failure mechanisms and imperfections in the interior of the composite structure was performed through XCT. A ZEISS Xradia 520 Versa 3D X-ray microscope was used for the examination of flat specimens. The specimen was attached on a stage between the x-ray source at a distance of 53 mm and the detector assembly at a distance of 92 mm. An electron accelerating voltage of 30 kV was used as well as a beam current of 66 μA. The generated power was 1.98 kW. This enabled the reconstruction of volumes to be carried out with resolution of 25 μm pixel size. The optical magnification, which refers to the ratio between the size of the sample in the image and its actual size, was set to 0.4. The image process and analysis was performed using the Avizo software package. To examine part of the composite pipe a Nikon X-Tek-225 X-ray microscope was utilised. The specimen was positioned on a stage with distance of 92 mm from the x-ray source and 1053 mm from the detector assembly. The voltage and beam current used was 100 kV and 150 μA, respectively, generating power of 15 kW. The magnification was set at 12.5 providing resolution of 16 μm pixel size. The image process was carried out using the myVGL software package.

4.3.2 In-plane tests

4.3.2.1 Tensile test

Tensile testing was carried out for the determination of the mechanical properties of the materials under study. The tensile test method was based on ASTM D3039 [306] which covers various cases of fibre orientation and symmetry. Tensile tests performed on the SE84LV carbon fibre prepreg were carried out for the identification of material properties for the development of a constitutive model that was used for the validation of the LBB concept. For tensile tests at 0° fibre orientation the identified material properties included the Young's modulus of elasticity, Poisson's ratio, initial and ultimate stress-strain and ultimate damage. The maximum stress-strain values, the Poison's ratio and Young's modulus were estimated for RP507 tensile specimens as a preliminary study of a defect

modelling strategy for the development of the LBB concept. The specimen dimensions for tensile tests are summarised in Table 4.4 and are based on the standard recommendations as well as on the test requirements.

Table 4.4 Recommended specimen geometry

Test	Fibre orientation (°)	Length (mm)	Width (mm)	Internal diameter (mm)	Thickness (mm)	Tab length (mm)	Tab thickness (mm)	Initial delamination length (mm)
Tensile	$[0°]_{16}$, $[0°]_{8}$	250	15	-	2.4	50	1.5	-
In-plane shear	$[\pm35°]_{4s}$, $[\pm45°]_{2s}$, $[+45°]_{8}$, $[\pm67.5°]_{2s}$	250	25	-	2.4	50	1.5	-
Compression	$[0°]_{8}$	140	13	-	2.4	63.5	1.5	-
Mode I	$[0°]_{10}$	≥125	25	-	3	-	-	50
Mode II	$[0°]_{12}$	160	25	-	3.5	-	-	≥45
Hydro-static burst	$[\pm55°]_{2s}$	300	-	105.68	2.4	-	-	-

According to the standard, the material properties were obtained by the preparation and testing of five identical specimens for each test. An 8802 Instron servo hydraulic test machine was used for the tensile testing. A load cell of 250 kN was utilised for 0° fibre orientation specimens. The speed of the test was 2 mm/min. The strain gauges were connected to a data acquisition system. During the testing, time, displacement, force and strain were recorded until ultimate failure of the sample. Any samples that failed prematurely due to incorrect gripping and alignment of the sample with respect to the loading direction or excessive gripping force were rejected from the calculations of the material properties. The stress-strain data recorded during testing were transformed with

respect to the two-dimensional principal material axes (1, 2) for the calculation of material properties in the fibre direction. The transformation equations are the following:

$$\begin{bmatrix}\sigma_{11}\\ \sigma_{22}\\ \tau_{12}\end{bmatrix}=[T]\begin{bmatrix}\sigma_x\\ \sigma_y\\ \tau_{xy}\end{bmatrix} \text{ and } \begin{bmatrix}\varepsilon_{11}\\ \varepsilon_{22}\\ \varepsilon_{12}\end{bmatrix}=[T]\begin{bmatrix}\varepsilon_x\\ \varepsilon_y\\ \varepsilon_{xy}\end{bmatrix}$$

where

$$[T]=\begin{bmatrix}c^2 & s^2 & 2cs\\ s^2 & c^2 & -2cs\\ -cs & cs & c^2-s^2\end{bmatrix} \tag{4.2}$$

and

$$c=\cos\theta,\ s=\sin\theta$$

Here, σ_x corresponds to the longitudinal stress of the global coordinate system and ε_x and ε_y represent the longitudinal and transverse strains in the global frame respectively. Parameter θ represents the angle between the global x-axis with respect to the direction of the fibre in the principal material direction, 1-axis. In the case of [0°] specimens, the global and principal axes coincide. For this case, Equation (4.2) becomes:

$$\begin{bmatrix}\sigma_{11}\\ \sigma_{22}\\ \sigma_{12}\end{bmatrix}=\begin{bmatrix}\sigma_x\\ 0\\ 0\end{bmatrix} \text{ and } \begin{bmatrix}\varepsilon_{11}\\ \varepsilon_{22}\\ 2\varepsilon_{12}\end{bmatrix}=\begin{bmatrix}\varepsilon_x\\ \varepsilon_y\\ 0\end{bmatrix} \tag{4.3}$$

The tensile modulus E_{11} in the fibre direction [306] was obtained from the stress-strain test data. Two strain points were utilised at 0.001 and 0.003 absolute strain as well as the tensile stresses corresponding to this strain range. The tensile Young's modulus was calculated as follows:

$$E_{11}^{0t}=\frac{\sigma''_{11}-\sigma'_{11}}{\varepsilon''_{11}-\varepsilon'_{11}} \tag{4.4}$$

Here, ε'_{11} and ε''_{11} are the strains at 0.001 and 0.003 absolute strain respectively and σ'_{11} and σ''_{11} are the stresses corresponding to them. The Poisson's ratio v_{12}^0 was identified based on the strains in the longitudinal and transverse direction with respect to the fibre orientation. The longitudinal strain range is determined

at 0.001 and 0.003 absolute strain and their corresponding transverse strain values are identified through plotting. The value of v_{12}^{0} was estimated as follows:

$$v_{12}^{0} = \frac{\varepsilon_{22}^{''} - \varepsilon_{22}^{'}}{\varepsilon_{11}^{''} - \varepsilon_{11}^{'}} \tag{4.5}$$

4.3.2.2 In-plane shear tests

In-plane shear tests were performed on $[\pm 45°]_{2s}$, $[+45°]_{8}$ and $[\pm 67.5°]_{2s}$ SE84LV specimens to develop the constitutive model. The in-plane shear tests of the balanced and symmetric ±45° specimens were carried out following ASTM D3518 [307] taking into account certain restrictions on dimensions and stacking sequence. The shear tests of $[+45°]_{8}$ and $[\pm 67.5°]_{2s}$ SE84LV specimens were performed in correspondence to ASTM D3039 [306]. The failure stresses and strains for $[\pm 45°]_{2s}$, $[+45°]_{8}$ and $[\pm 67.5°]_{2s}$ specimens were identified through quasi-static tests for the identification of the maximum deformation/strain for each loading cycle. Cyclic in-plane shear tests were carried out for the acquisition and incorporation of material properties in the constitutive model. The in-plane shear modulus of elasticity, initial and critical shear damage, shear damage fracture limit, initial yield stress and inelastic hardening coefficients were obtained from cyclic in-plane shear tests at ±45°. Cyclic in-plane shear tests of +45° fibre orientations were used to obtain the shear, transverse elastic modulus and coupling factor between transverse and shear inelastic strains. Cyclic in-plane shear tests at ±67.5° fibre orientation led to the acquisition of the initial and critical transverse damage, brittle transverse damage limit and coupling factor between transverse and shear damage. The preliminary study on $[\pm 35°]_{4s}$ RP507 specimens was carried out based on ASTM D3039 [306] for the investigation of a defect modelling strategy for the LBB concept development. The maximum stress and strain values were acquired from the testing. Five samples were prepared and tested for each in-plane shear case. Their dimensions, which are summarised in Table 4.4, are based on the standard recommendations and the test requirements. The quasi-static testing of in-plane shear samples took place on an 8802 Instron servo hydraulic test machine using a load cell of 250 kN with a head cross displacement of 2 mm/min. A 100kN load cell was used for cyclic

tensile tests of ±45°, +45° and ±67.5° laminates at a loading rate of 1mm/min. Cyclic tests comprised five load/unload cycles with increasing load levels. Time, force and displacement data were recorded throughout the tests and the strain of the samples was documented through strain gauges. In cases where premature failure of samples was observed due to invalid incorporation of loading during the cyclic tests, the test results were excluded from the calculations of the material properties. The stress-strain data along the principal material axes for ±45° and ±67.5° specimens were calculated from classical laminate theory of symmetric laminates taking into account the axial force equilibrium between two layers with opposite signs, θ and −θ. A parameter B is defined with respect to the lamina elastic properties and the fibre orientation θ. The transformed stress and strain results are calculated as follows:

$$\begin{bmatrix}\sigma_{11}\\ \sigma_{22}\\ \tau_{12}\end{bmatrix}=\begin{bmatrix}B\\ 1-B\\ -\frac{1}{2cs}\left[\left(B\left(1-2c^2\right)+c^2\right)\right]\end{bmatrix}\sigma_x$$

where (4.6)

$$B=\frac{c^2\left(2c^2-1\right)+4c^2s^2\frac{G_{12}}{E_{22}}\left(\frac{E_{22}}{E_{11}}v_{12}+1\right)}{4c^2s^2\frac{G_{12}}{E_{22}}\left(\frac{E_{22}}{E_{11}}+2\frac{E_{22}}{E_{11}}v_{12}+1\right)+(2c^2-1)(c^2-s^2)}$$

Here, the modulus in the longitudinal direction was determined based on Equation (4.4) following the ASTM 3039 [306]. The moduli in the shear and transverse directions were obtained from the slope between the strain range of 0.01 and 0.05 based on ASTM 3518 [307]. In the case where $E_{11}^0 \gg E_{22}^0$, coefficient B is calculated as follows:

$$B_a=\frac{c^2\left(2c^2-1\right)+4c^2s^2\frac{G_{12}}{E_{22}}}{4c^2s^2\frac{G_{12}}{E_{22}}+(2c^2-1)(c^2-s^2)} \quad (4.7)$$

Based on Equations (4.6)-(4.7), the stress and strain data of ±45° specimens in the principal material coordinates are calculated. The stress and strain response is:

$$\begin{bmatrix}\sigma_{11}\\ \sigma_{22}\\ \tau_{12}\end{bmatrix}=\begin{bmatrix}\sigma_x\\ 0\\ \frac{\sigma_x}{2}\end{bmatrix} \text{ and } \begin{bmatrix}\varepsilon_{11}\\ \varepsilon_{22}\\ \varepsilon_{12}\end{bmatrix}=\begin{bmatrix}0\\ 0\\ \frac{\varepsilon_x-\varepsilon_y}{2}\end{bmatrix} \tag{4.8}$$

In the case of off-axis +45° specimens, the calculation of the stress and strain results in the principal material directions followed from classical laminate theory for symmetric laminates. Having no bending phenomena due to symmetry of the laminate, the in-plane stresses can be expressed as follows:

$$[\bar{\sigma}]=\frac{1}{2H}[A]\left[\varepsilon^0\right] \tag{4.9}$$

where

$$[A]=\sum_{k=1}^{N}\left[\bar{Q}\right]^k(z_k-z_{k-1})$$

Here, $[\bar{\sigma}]$ is the laminate average stress, 2H is the total laminate thickness and matrix [A] is the summation of all the stiffness matrices $\left[\bar{Q}\right]^k$ over N layers of the laminate. Exponent k corresponds to each layer within the laminate and $\left[\varepsilon^0\right]$ are the mid-plane strains associated with the laminate. Utilising Equations (4.7), (3.1) and (4.2) relations for the off-axis +45° specimens can be obtained as follows:

$$\begin{bmatrix}\sigma_{11}\\ \sigma_{22}\\ \tau_{12}\end{bmatrix}=\begin{bmatrix}0\\ \frac{\sigma_x}{4}\\ \frac{\sigma_x}{2}\end{bmatrix} \text{ and } \begin{bmatrix}\varepsilon_{11}\\ \varepsilon_{22}\\ \varepsilon_{12}\end{bmatrix}=\begin{bmatrix}\frac{\varepsilon_x+\varepsilon_y}{2}\\ \frac{\varepsilon_x+\varepsilon_y}{2}\\ \frac{\varepsilon_x-\varepsilon_y}{2}\end{bmatrix} \tag{4.10}$$

4.3.2.3 Compression test

Compression tests were carried out following ASTM D6641 [308]. This test was performed on SE84LV compressive specimens. The material properties identified

through compressive testing were the ultimate compressive stress and strain, compressive modulus of elasticity, ultimate compressive damage factor and non-linearity corrective factor. The recommended specimen dimensions for compression tests are summarised in Table 4.4.

In total, five specimens of 0° fibre orientation were prepared for this type of test for the acquisition of material properties. The tests were performed on an 8801 Instron servo hydraulic test machine with a load cell of 100 kN. The crosshead displacement for compression tests was set to 1 mm/min. The samples were gripped on the jigs according to ASTM D6641. The strain gauges from both the sides of the gauge length were connected to a data acquisition system.

The validity of the compression test was examined through the calculation of the bending percent from the back-to-back strain gauges attached on each specimen for the examination of bending phenomena. A maximum of 10% of bending is required in order to establish the validity of the test and to confirm that there is no systematic error with the quality of the specimens or the testing procedure. The bending percent is calculated as follows:

$$B=\frac{\varepsilon_1-\varepsilon_2}{\varepsilon_1+\varepsilon_2} \tag{4.11}$$

Here, ε_1 and ε_2 are the recorded strains from strain gauges 1 and 2 respectively. The recorded stress and strain results in the global coordinate system coincide with the principal material axes due to alignment of the loading direction to the orientation of the fibres. The stress and strain response of the compression specimens is expressed through Equation (4.3). The calculation of the compressive modulus E_{11}^{0c} is carried out through Equation (4.4) for the strain range of 0.01 and 0.03 absolute strain based on ASTM 6641 [308]. The strains for this strain range are calculated as an average from the back-to-back strain gauges.

4.3.3 Out-of-plane tests

4.3.3.1 Mode I Double Cantilever Beam (DCB)

The measurement of the ability of a material to resist fracture was carried out through the Mode I fracture toughness test based on ASTM D5528 [299]. This test provides information about the susceptibility of the composite material to delamination through the calculation of the strain energy release rate G_I. Table 4.4 presents the recommended dimensions for the Mode I specimens.

Five specimens were prepared for testing and their dimensions were initially recorded. The experimental setup consists of a 5567A Instron servo hydraulic test machine with a load cell of 5 kN, a switch used to record the points on the load-displacement curve when the crack would propagate. A magnifying glass was also used to follow the crack propagation and a video camera was recording the tests to ensure that all the delamination increments were captured. The crosshead displacement was 1 mm/min. The specimens were gripped in the jig using pins inserted in the holes of the metallic blocks. The delamination initiated at the insert tip and the crack propagation points were documented. The specimen was unloaded at a constant rate of 1 mm/min the instant the delamination crack was at the first 3-5 mm beyond the insert tip. The position of the tip of crack on both sides was observed. Load and crack opening displacement values were recorded every 1 mm for the first 5 mm beyond the insert tip and every 5 mm for 40 mm of delamination propagation. The specimen was unloaded with 2 mm/min and the position of the tip of crack on both sides was observed and recorded. The critical strain energy release rate G_{IC} in Mode I testing is calculated as follows [28]:

$$G_{IC} = \frac{3P\delta}{2b(\alpha + |\Delta|)} \frac{F}{N} \tag{4.12}$$

Here, P corresponds to load, δ is the load point displacement, b is the width of the specimen, α represents the delamination length and Δ is a correction factor accounting for potential rotation of the DCB arms at the onset of delamination. The calculation of Δ is based on the plot of the cube root of compliance against

the delamination length. Factor Δ is the extrapolation of the linear fit of the plotted points identified as the x-intercept. If the value of Δ from the curve is positive, factor Δ equals to zero. The compliance is calculated as the fraction of displacement over force. Parameters F and N are a large displacement and a load block correction factor respectively. These parameters are calculated as follows:

$$F=1-\frac{3}{10}\left(\frac{\delta}{\alpha}\right)^{2}-\frac{2}{3}\left(\frac{\delta l_1}{\alpha^2}\right) \tag{4.13}$$

$$N=1-\left(\frac{l_2}{\alpha}\right)^{3}-\frac{9}{8}\left[1-\left(\frac{l_2}{\alpha}\right)^{2}\right]\frac{\delta l_1}{\alpha^2}-\frac{9}{35}\left(\frac{\delta}{\alpha}\right)^{2} \tag{4.14}$$

Here, l_1 represents the distance from the centre of the loading pin to the mid-plane of the specimen, whilst l_2 signifies the distance from the centre of the load pin to the edge of the loading block.

4.3.3.2 Mode II End Notched Flexure (ENF)

The ENF test for Mode II interlaminar fracture toughness G_{II} was used under Mode II shear loading based on ASTM D7905 [309]. Five identical specimens were prepared with 0° fibre orientation. The ENF Mode II test was performed on a 5567A Instron servo hydraulic test machine with a load cell of 5 kN. The ENF test fixture consisted of jigs dedicated to three point bending. The diameter of the support rollers was 8 mm whilst the diameter of the loading roller was 10 mm. The crosshead displacement was set to 1 mm/min. The test procedure that was followed involved the utilisation of the same specimens for non-precracked (NPC) and pre-cracked (PC) tests. For the NPC compliance calibration (CC) tests, the specimen had initially been prepared with CC marks introduced at a distance of 20, 30 and 40 mm from the insert tip towards the insert side. Initially, the specimen was positioned in such way so that the support roller would be at the CC mark of 20 mm away from the insert tip. The specimen was then loaded at 0.5 mm/min until the peak CC force that corresponded to 20 mm distance away from the insert tip and subsequently unloaded with the same loading rate. Each peak CC force was calculated based on Classical Beam Theory (CBT) and was different for each

CC mark [309]. The specimen was repositioned so that the support roller was placed at the 40 mm CC mark and was loaded at 0.5 mm/min until the respective peak CC force. The NPC fracture test took place by positioning the specimen so that the support roller was at the 30 mm CC mark. The sample was loaded at 0.5 mm/min until the delamination was visually advanced or up to the instance the force was dropped on the force-displacement plot. The specimen was unloaded anew with a loading rate of 0.5 mm/min. The performance of the PC test, initially involved the determination of the crack length (α_{calc}) from the central CC mark at 30 mm, based on calculations of the unloading line of the NPC tests. This enabled the determination of the PC crack tip mark and subsequently the PC CC markings at 20, 30, 40 mm distance from the PC crack tip mark on the specimen. The next steps involved the same loading process that was followed for the NPC CC by placing the specimen on the test fixture so that the support roller would be positioned on the 20, 40 and 30 mm PC CC mark. The test was concluded by reduction of the force on the load-displacement curve or by visually observed delamination propagation. Throughout the test the load-displacement data were recorded continuously.

The critical strain energy release rate G_{IIC}in Mode II testing is calculated as follows [39]:

$$G_{IIC} = \frac{3mP_{max}^2\alpha_{PC}^2}{2B} \tag{4.15}$$

Here, P_{max} is the maximum force occurred during the fracture tests, α_{PC} is the crack length of 30 mm used during the fracture tests, B is the specimen width and m denotes the compliance calibration coefficient. Factor m was calculated as the slope of the linear curve of compliance values against the crack length α to the power of three. Similarly to Mode I, the compliance is calculated as the ratio of displacement over force.

4.3.4 Hydrostatic burst test

Hydrostatic burst testing following the American Standard Test Method (ASTM) 1599 [305] for resistance to short-time hydraulic pressure of plastic pipe, tubing and fittings and the British Standards 12245 [41] for transportable gas cylinders-

fully wrapped composite cylinders and 17339 [40] for transportable gas cylinders-fully wrapped composite cylinders and tubes for hydrogen use was carried out on composite pipes without and with artificial defects. One composite pipe without defects was tested for the calculation of the maximum burst pressure the system could withstand, as well as for the determination and examination of the failure mechanisms that took place throughout the pressurisation. This control test also was used for the verification of the constitutive model for composite pipes and the development of a methodology for the establishment of the LBB concept. Based on this methodology one composite pipe with fibre cut artificial defects was also tested. The pressurisation data acquired were used for the validation of the LBB concept and the examination of the failure mechanisms that accompanied the introduced defects leading to the operational failure of the pipe. The dimensions of the control pipes are presented in Table 4.4.

All tests were performed in a pressure pit for safety purposes. An inlet hose was screwed on one side of the end cap and an outlet on the other end. The pressurised cylinder was secured with belts for safety reasons, without restricting its movement axially or at the hoop direction, resembling in this way the behaviour of a CPV loaded under hoop to axial stress ratio of 2:1. The strain gauges that were attached on the pipe were connected to a data collection acquisition and were calibrated. A pump was used for the performance of the test with a loading rate of 67 bar/min after the occupation of the whole volume of the pipe with the test fluid. The pressure applied on the composite pipe was manually introduced through the pressure pump by adjusting the flow rate as needed based on the indication on the pump pressure gauge. The pressurising medium was water which was dyed pink to allow visual leak detection. Time, pressure and strain data were recorded throughout the tests and videos were produced through a camera system. The hoop and axial stresses were calculated as follows:

$$\sigma_H = \frac{PD}{2t} \tag{4.16}$$

$$\sigma_A = \frac{PD}{4t} \tag{4.17}$$

Here, σ_H and σ_A are the hoop and axial stresses respectively. P represents the pressure, D is the inner diameter of the pipe and t is the thickness.

The experimental setup of the pump, data acquisition system from strain gauges and computer is presented in Figure 4.17. The pressure pit, where the pressure vessel was tested, is shown in Figure 4.18.

Figure 4.17 Experimental setup for pressure testing

Figure 4.18 Pressure pit for pressure testing

5 Constitutive model development and verification

This chapter describes the development and verification of the constitutive model that enabled the simulation and establishment of the LBB concept to be carried out. The constitutive model development was based on a series of in-plane and out-of-plane characterisation tests for the SE84LV carbon prepreg. Material properties and damage parameters were acquired from these tests and were estimated based on fitting of analytical models to the experimental response. The constitutive model was verified through simulation and comparison of the experimental and simulation results. This chapter comprises three sections. The first section is dedicated to the characterisation tests that were carried out based on the requirements of the material model used for FEA. The second part addresses the identification of the model parameters through conventional calculations and fitting. The final section is devoted to the verification of the constitutive model.

5.1 Characterisation test results

This section is dedicated to the characterisation test results that were acquired from in-plane and out-of-plane tests for the identification of material model properties required for the development of the constitutive model. A set of minimum of five specimens was utilised for each test case. The in-plane experiments included quasi-static loading in the fibre direction under tension and compression of specimens with fibre orientations at 0° as well as cyclic loading of specimens with ±45°, +45° and ±67.5° layups. Properties for the initiation and propagation of delamination were acquired from Mode I and Mode II experiments on specimens with 0° fibre orientation.

5.1.1 In-plane tests

Five tensile specimens at $[0°]_8$ were tested under quasi-static loading for the acquisition of Young's modulus, the Poisson's ratio, initial and ultimate failure strains as described in 4.3.2.1. Figure 5.1 depicts the stress-strain results. The failure stresses of the specimens occurred at 1800-1900 MPa showing good reproducibility and that the failure was brittle. The stress-strain curves at the lower

region of the graphs are governed by the elastic modulus and present similar slope. An average stress-strain curve for the tensile specimens at $[0°]_8$ is illustrated in Figure 5.2. The average value of strength was at 1840 MPa corresponding to a strain value of 1.42%, which is in close agreement with results from the literature [310]. The Young's modulus value was 125 GPa and it was calculated based on the slope of the stress-strain graph for the lower region of the stress-strain curve at 0.001 and 0.003 absolute strain based on Equation (4.4). The average and standard deviation values for the strength, strain and modulus are summarised in Table 5.1.

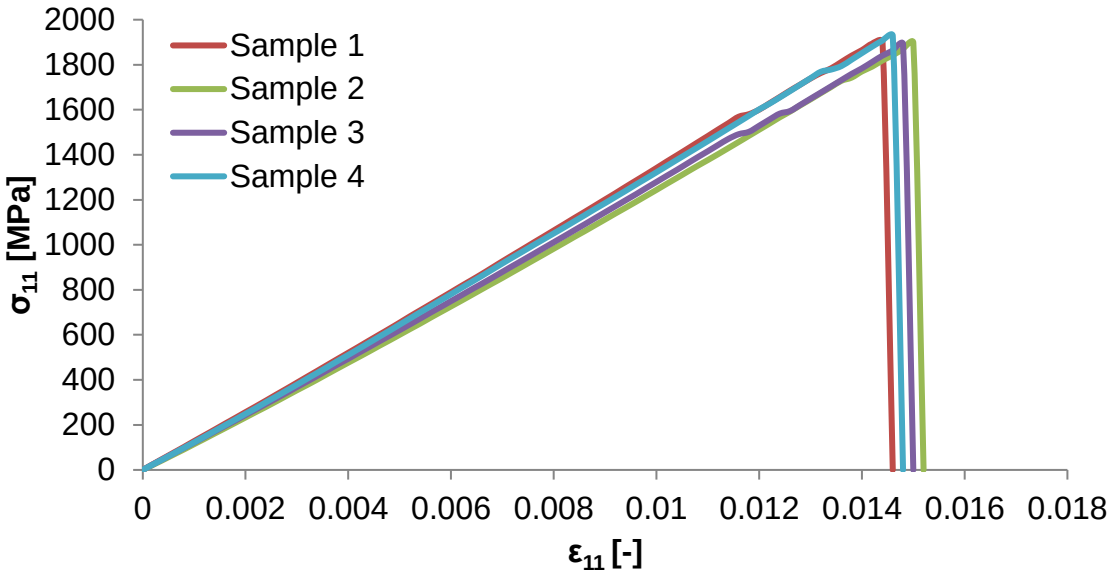

Figure 5.1 Stress-strain curves for tensile tests of $[0°]_8$ specimens

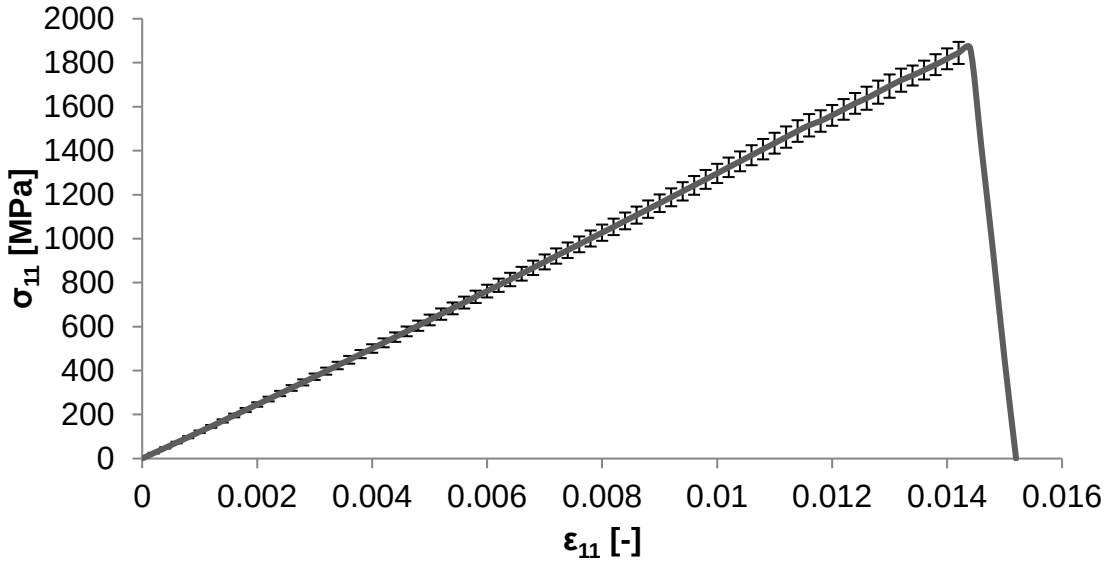

Figure 5.2 Average stress-strain curve for tensile tests of $[0°]_8$ specimens

Table 5.1 Average strength, strain and modulus values for tensile tests of $[0°]_8$ specimens

Property	Value	Average	Standard deviation
Strength	MPa	1840	50.2
Strain	-	0.0142	0.001
Tensile Modulus	GPa	125	4.5
Poisson's ratio	-	0.33	0.001

A set of five specimens of $[\pm45°]_{2s}$ fibre orientation was tested (Figure 5.10) under cyclic tensile loading for the acquisition of the shear moduli of each cycle, the damage evolution functions, the initial inelastic stress and hardening coefficients. The tests comprised of at least five load/unload cycles with increasing load levels as described in 4.3.2.2. Figure 5.3 illustrates the stress-strain curves of the five specimens tested under cyclic loading. The samples showed relatively good reproducibility taking into account the difficulties of the manual alteration of the direction of the loading the moment the required strain of each cycle was reached in combination with the achievement of successively higher loads during loading and zero loads during unloading. All samples exhibit nonlinear behaviour accompanied by hysteresis due to permanent inelastic deformation upon unloading, which is common for this type of testing [227, 311]. The damage

evolution is calculated based on the shear modulus degradation after each successively higher load level. The average value of the undamaged elastic shear modulus was 4.82 GPa with a standard deviation of 0.08 GPa.

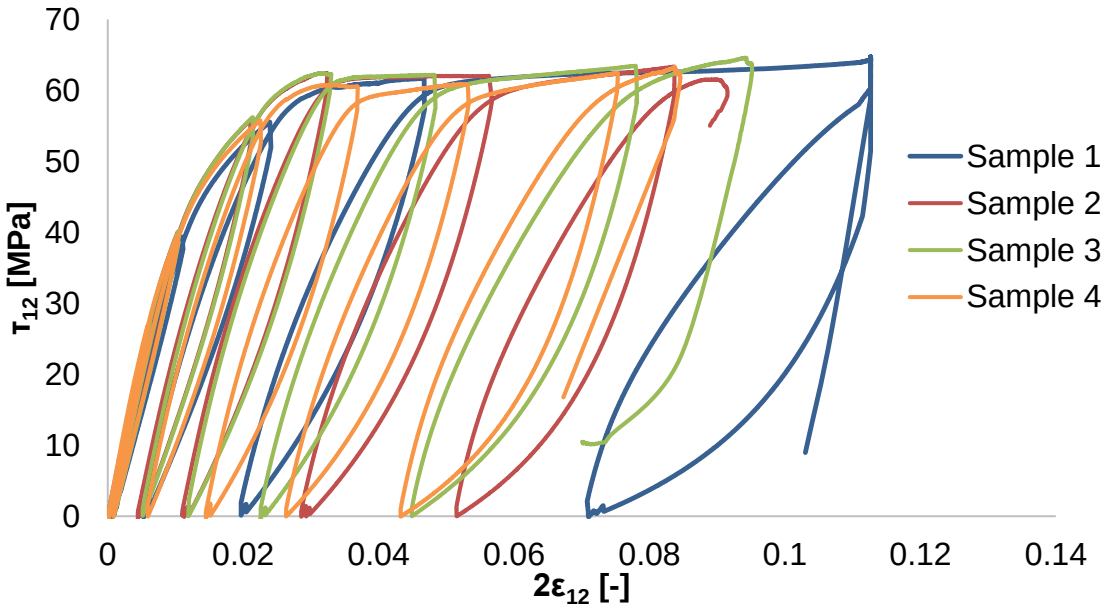

Figure 5.3 Shear stress-strain curves for cyclic loading of $[\pm 45°]_{2s}$ specimens

Cyclic tensile testing was performed on five $[+45°]_8$ fibre orientation specimens (Figure 5.10) comprising of five cycles with increasing loading levels as described in 4.3.2.2. The values of shear, transverse elastic modulus and coupling factor between transverse and shear inelastic strains were obtained. The cyclic shear and transverse stress-strain curves are illustrated in Figure 5.4 and Figure 5.5 respectively indicating good reproducibility. The average undamaged shear modulus of elasticity calculated from the first loading cycle was 4.77 GPa with a standard deviation of 0.12 GPa and the average transverse modulus was 8.96 GPa with a standard deviation of 0.4 GPa. The shear moduli acquired from $[\pm 45°]_{2s}$ and $[+45°]_{2s}$ specimens were found to vary by 0.7%.

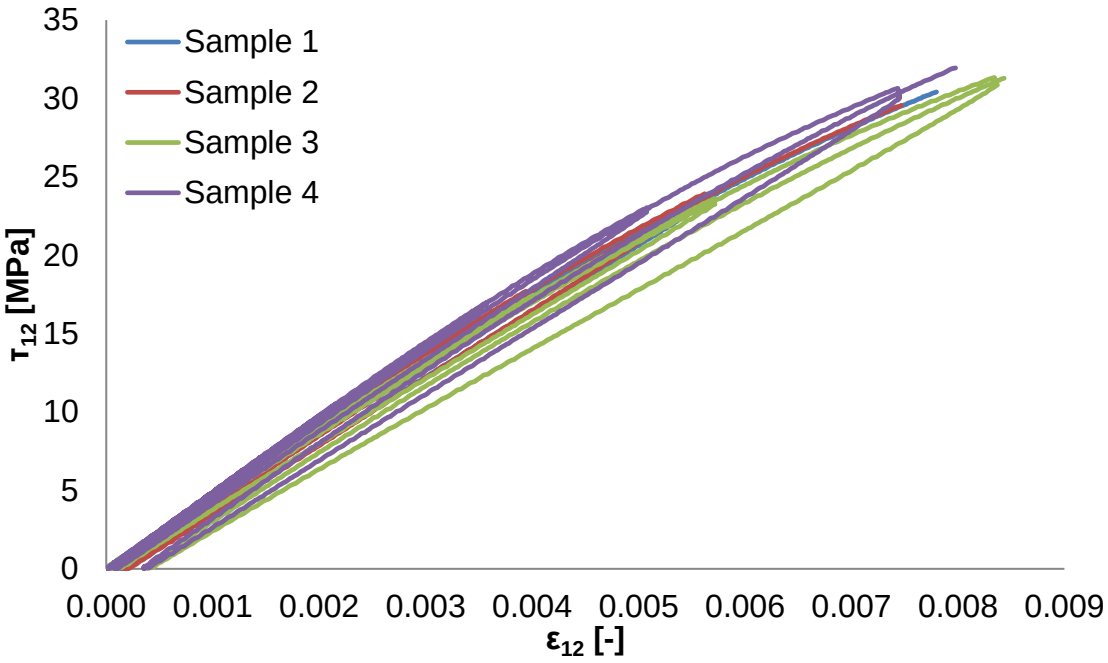

Figure 5.4 Shear stress-strain curves for cyclic loading of $[+45°]_8$ specimens

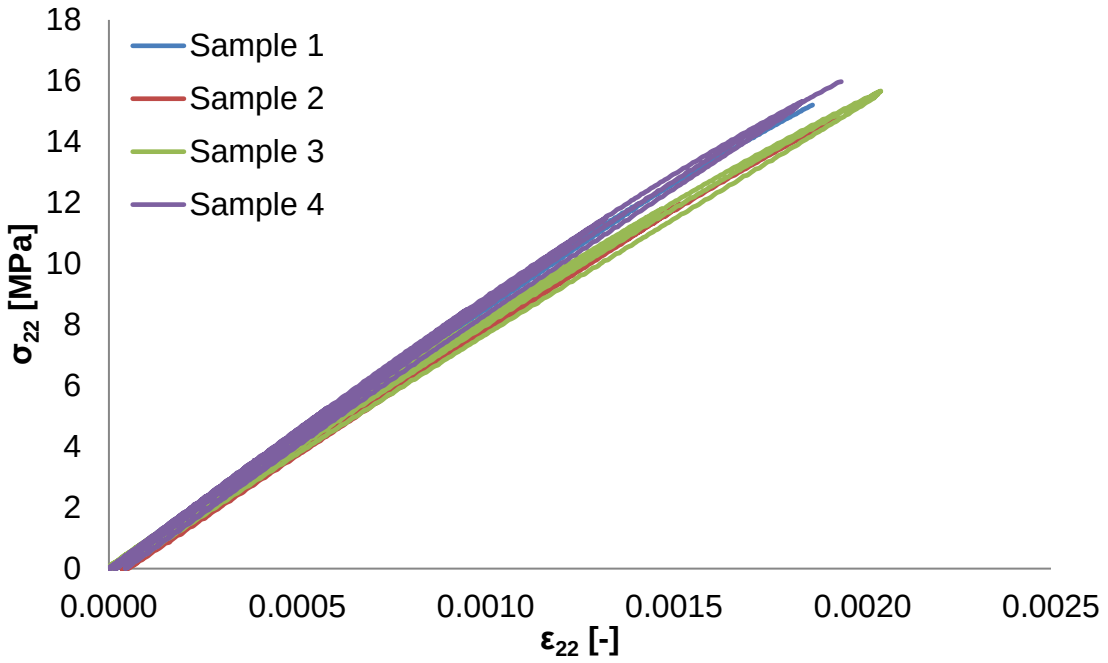

Figure 5.5 Transverse stress-strain curves for cyclic loading of $[+45°]_8$ specimens

Five specimens at $[\pm 67.5°]_{2s}$ fibre orientation were tested (Figure 5.10) under cyclic tensile loading in order to obtain the initial and critical transverse damage, brittle transverse damage limit and coupling factor between transverse and shear damage through classical laminate theory as described in 4.3.2.2. Similarly to $[+45°]_8$, during the $[\pm 67.5°]_{2s}$ cyclic test the interlaminar stresses associated to initiation of damage and failure are very low providing a biaxial state of loading in the principal coordinate system to study coupling phenomena. The shear and transverse stress and strain curves are presented in Figure 5.6 and Figure 5.7 respectively. The stress-strain curves for all samples show good repeatability. The average initial shear modulus is 4.78 GPa with a standard deviation of 0.08 GPa in good agreement with the results of $[\pm 45°]_{2s}$ and $[+45°]_8$ specimens. The average transverse modulus was 9.28 GPa with a standard deviation of 0.55 GPa which shows a variation by 2% compared to the cyclic tests on $[+45°]_8$ specimens.

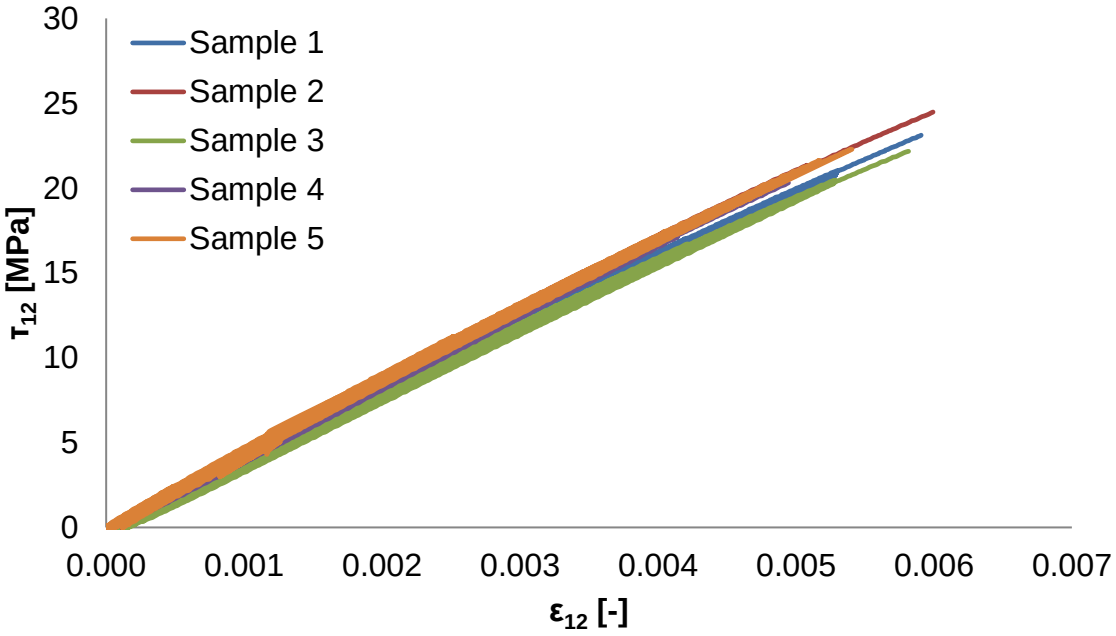

Figure 5.6 Shear stress-strain curves for cyclic loading of $[\pm 67.5°]_{2s}$ specimens

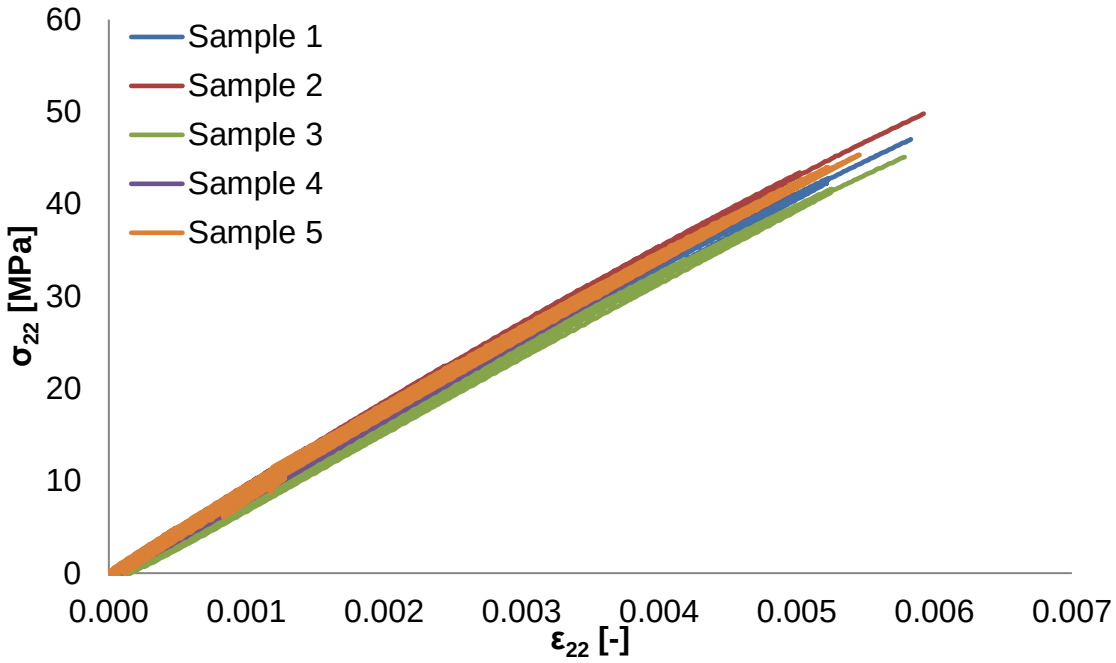

Figure 5.7 Transverse stress-strain curves for cyclic loading of $[\pm 67.5°]_{2s}$ specimens

The compressive modulus in the fibre direction was estimated through compression tests on five specimens with $[0°]_8$ fibre orientation (Figure 5.10). The stress-strain curves of the specimens are presented in Figure 5.8. The results show that all samples follow the same trend down to approximately -1% strain. The average maximum compressive strength was 1020 MPa and its corresponding strain was 0.01 as illustrated in Figure 5.9. The average compressive modulus deducted from the five sample curves was 112 GPa. The average and standard deviation values of strength, strain and modulus are summarised in Table 5.2.

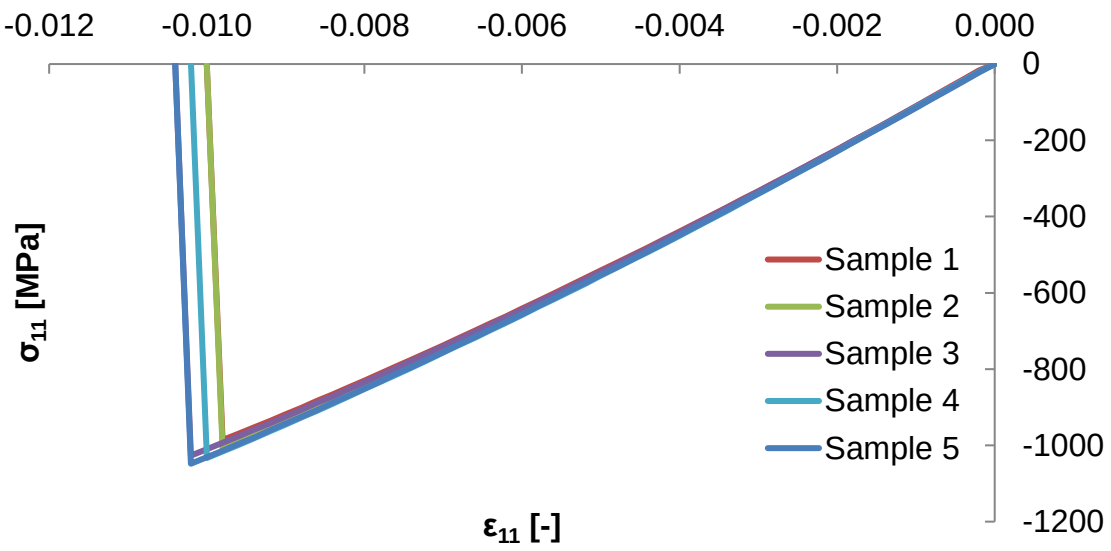

Figure 5.8 Stress-strain curves for compressive tests of $[0°]_8$ specimens

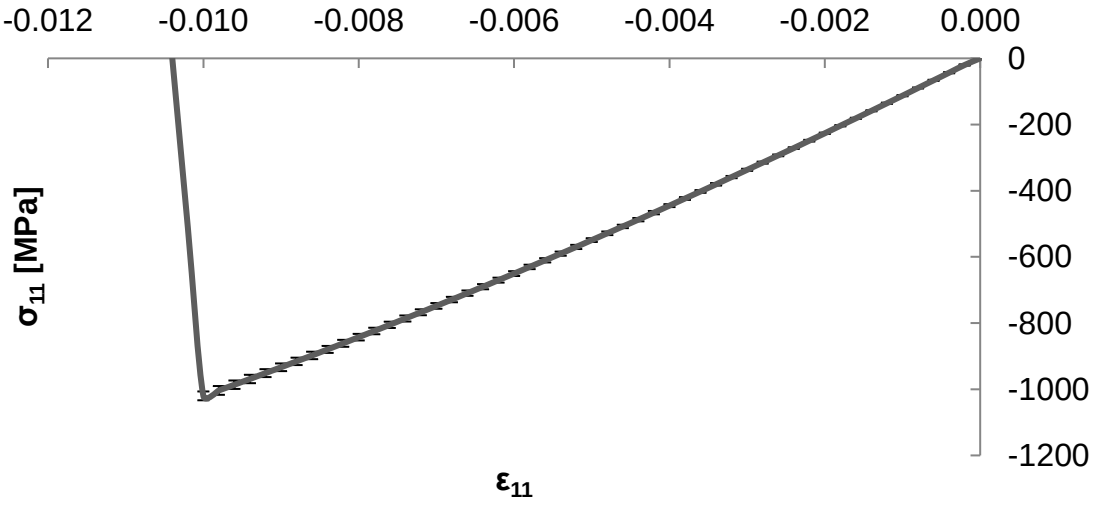

Figure 5.9 Average stress-strain curve for compressive tests of $[0°]_8$ specimens

Table 5.2 Average strength, strain and modulus values for compressive tests of $[0°]_{8s}$ specimens

Property	Value	Average	Standard deviation
Strength	MPa	1020	13.3
Strain	-	0.01	0.0015
Compressive Modulus	GPa	112	0.85

(a) (b) (c) (d)

Figure 5.10 Illustration of (a) $[0°]_8$ compression, (b) $[\pm45°]_{2s}$, (b) $[+45°]_8$ and (c) $[\pm67.5°]_{2s}$ specimens

5.1.2 Out-of-plane tests

The resistance of the material to delamination initiation and propagation is obtained through the curves of strain energy release rate against the crack length of DCB and ENF specimens. The resistance curves of six DCB specimens under Mode I testing are presented in Figure 5.11. A similar trend is followed and the results show good reproducibility. The delamination initiation values show some inconsistency with an average delamination initiation value of 127 J/m^2 and standard deviation of 27.15 J/m^2. The delamination propagation values show a plateau at an average fracture toughness value of 203.5 J/m^2 with a standard deviation of 24.46 J/m^2.

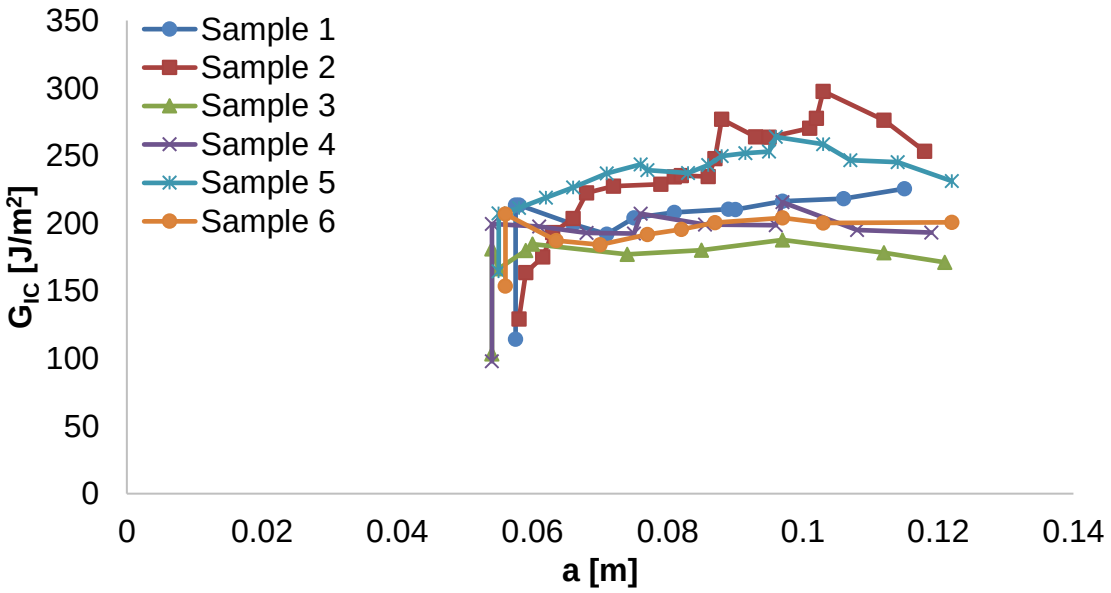

Figure 5.11 Mode I results of $[0°]_8$ DCB specimens

Mode II curves of force against displacement of seven non-precracked ENF specimens are presented in Figure 5.12. All samples show the same trend and good reproducibility with failure around 0.95 kN. The average non-precracked G_{IIC} for delamination initiation was calculated and has the value of 1509.5 J/m^2 with standard deviation of 88.46 J/m^2. Figure 5.13 illustrates the plots of force against displacement of seven precracked ENF specimens. The specimens are in agreement leading to a failure load of 0.83 kN. The average precracked value

of G_{IIC} for delamination propagation is 1116.6 J/m^2 with standard deviation of 43.34 J/m^2.

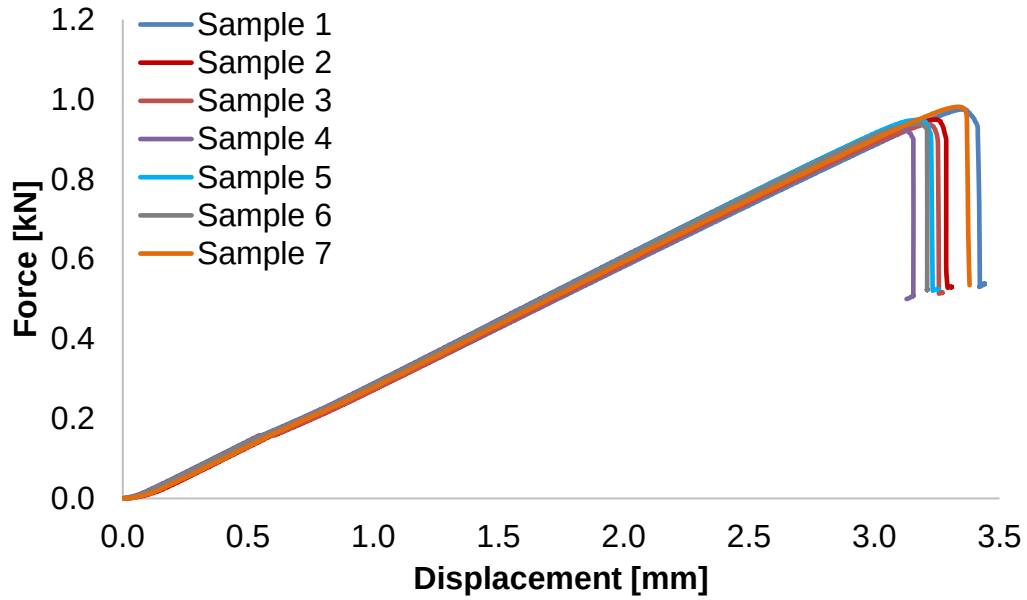

Figure 5.12 Mode II results for $[0°]_8$ non-precracked ENF specimens

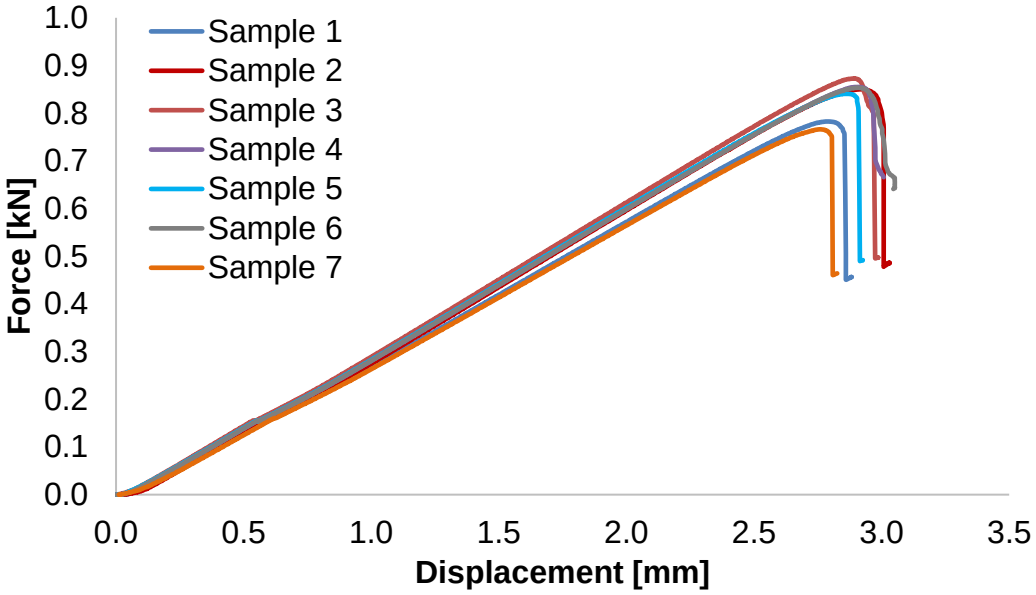

Figure 5.13 Mode II results for $[0°]_8$ precracked ENF specimens

5.2 Model parameter identification

This section is dedicated to the identification of material properties, damage factors and thermodynamic parameters for the different cases of in-plane and out-of-plane tests. The first part is dedicated to the calculation of the Pam-Crash^{TM} parameters which followed a conventional procedure recommended by the relevant literature for the material model [275] based on the experimental results. The second part involves the identification of the material model parameters through fitting based on error minimisation utilising a gradient based solver [312, 313].

5.2.1 Conventional model parameter identification method

5.2.1.1 In-plane properties

5.2.1.1.1 Material model properties in the fibre direction

Elastic properties and damage parameters in the fibre direction of the composite material were obtained through tensile and compression tests of $[0]_8$ specimens. The undamaged elastic tensile modulus in the fibre direction E_1^{0t} and the Poisson's ratio were identified following the methodology presented in 4.3.2.1, whilst the calculation of the compressive modulus E_1^{0c} was described in 4.3.2.3. Subscript t is used for the representation of the tensile case and c for compression. The initial and ultimate strain values were identified by observation of the stress-strain curves acquired through testing. Figure 5.14 depicts the experimental stress-strain curve for tensile and compression loading at 0° fibre orientation as well as the points of 0.001 and 0.003 strain at which the tensile and compressive moduli were calculated. The initial strain threshold values ε_i^{ft} and ε_i^{fc} correspond to the maximum stress value on the stress-strain curve whilst the ultimate threshold strains ε_u^{ft} and ε_u^{fc} are extracted from the region that corresponds to complete failure of the specimen at the strain. The points of ultimate threshold strain according to Figure 5.14 are 0.0152 for the tensile case and 0.0104 for the compression case. At these points the ultimate damage factors d_u^{ft} and d_u^{fc} become equal to 1 as they reach their ultimate value. For the tensile case a linear stress-strain relation exists until the initial failure strain. However, in

the compression case a linear region exists at the beginning of the loading, and the behaviour becomes non-linear as the material approaches the initial failure strain. The non-linearity is associated with fibre microbuckling and misalignment that take place during compression. The non-linear region is described through the non-linear compressive modulus, which is calculated as the tangent line of an arbitrary point of the non-linear region and a corrective parameter. This parameter is defined by solving Equation (3.16) as follows:

$$\gamma = \frac{E_1^{0c} - E_1^{\gamma}}{E_1^{\gamma} E_1^{0c} |\varepsilon_{11}|} \tag{5.1}$$

Here, E_1^{γ} is the non-linear compressive modulus and γ is the corrective parameter. The material model properties extracted from tensile and compression loading in the fibre direction are summarised in Table 5.4.

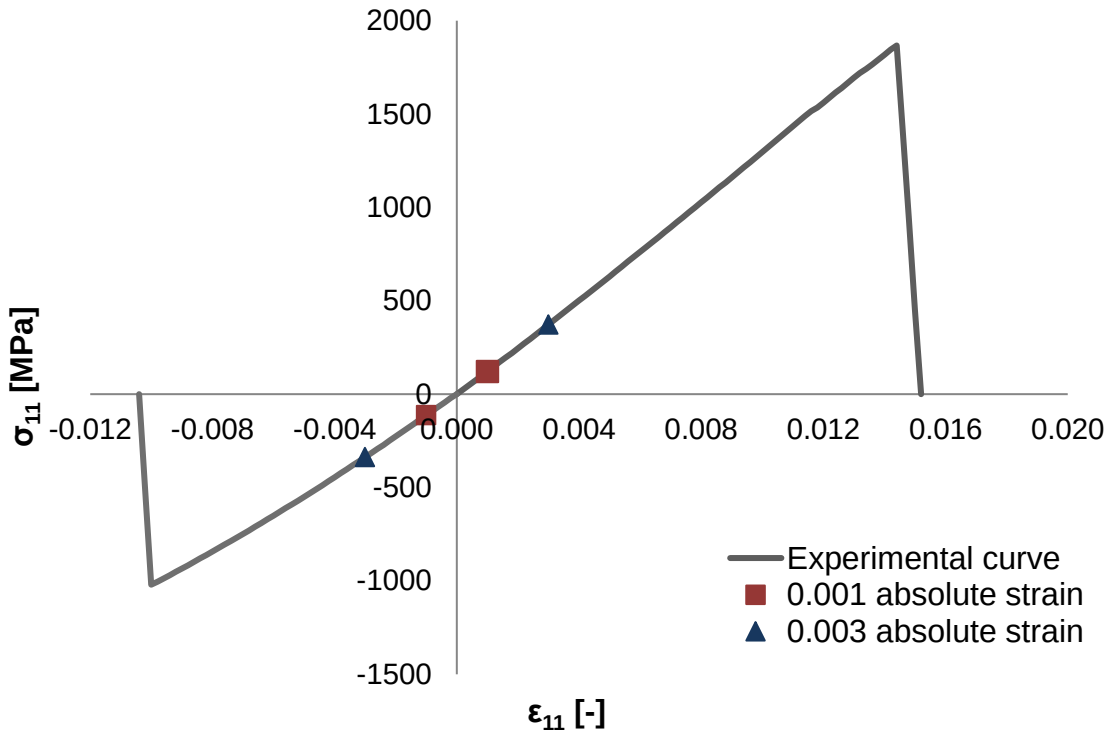

Figure 5.14 Experimental stress-strain curve from tensile and compression testing of 0° specimens

5.2.1.1.2 Cyclic tensile test on $[\pm 45°]_{2s}$

Shear damage phenomena were studied through cyclic tensile tests at $[\pm 45°]_{2s}$. Properties associated with shear damage are the shear moduli of each cycle, damage evolution functions, initial inelastic stress and hardening coefficients. Each test consisted of at least five load-unload cycles out of which the shear moduli were extracted. The experimental stress-strain curve of a sample is presented in Figure 5.15. The undamaged shear modulus was obtained from the initial cycle using the experimental points corresponding to strain values of 0.001 and 0.005.

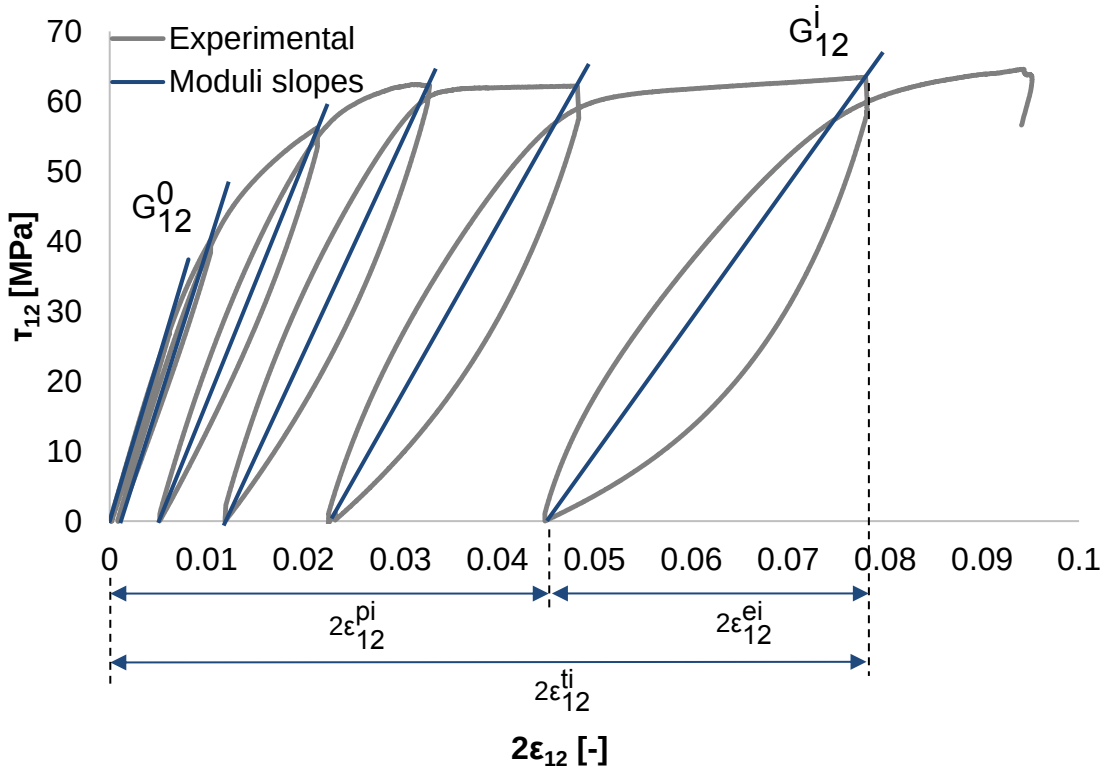

Figure 5.15 Experimental stress-strain curve for cyclic tensile test of $[\pm 45°]_{2s}$ specimens

The shear modulus of each subsequent cycle is calculated from the slope of the line between the minimum point of the unloading part of a cycle and the maximum point of the loading part of its subsequent cycle. The shear damage occurring at each cycle is calculated as follows:

$$d_{12}^{i}=1-\frac{G_{12}^{i}}{G_{12}^{0}} \tag{5.2}$$

As observed in Figure 5.15 the undamaged shear modulus (G_{12}^{i}) decreases in subsequent cycles due to the increase of shear damage (d_{12}^{i}) and the initiation of inelastic phenomena. The shear moduli and damage values extracted from each cycle are summarised in Table 5.3.

Table 5.3 Shear moduli, strain and damage at each cycle

Cycle	G_{12}^{i} [GPa]	$2\varepsilon_{12}$ [-]	d_{12}^{i} [-]
0	4.92	0.004	0
1	4.67	0.006	0.049
2	4.23	0.009	0.140
3	3.37	0.017	0.315
4	2.70	0.022	0.451
5	2.29	0.027	0.535
6	1.96	0.032	0.602

The damage development due to shear loading at each cycle is associated with thermodynamic forces and therefore the stored energy of a damaged layer. This leads to the calculation of the shear damage evolution function for each cycle as follows:

$$Y_{12}^{i}(t)=\sqrt{\frac{1}{2}G_{12}^{0}(2\varepsilon_{12}^{i})^{2}} \tag{5.3}$$

Utilising Equation (5.3), the damage evolution values for each cycle were calculated and plotted against the damage corresponding to each cycle. Figure 5.16 shows the curve obtained. As illustrated, the curve is optimally described by a linear relation, which is expressed by the following equation:

$$Y_{12}(t)=Y_{12}^{c}d_{12}^{i}+Y_{12}^{0} \tag{5.4}$$

Here, Y_{12}^{c} is the critical shear damage determined by the slope of the linear equation and Y_{12}^{0} is the initial shear damage calculated based on the intercept of the linear function. The shear damage fracture limit Y_{12}^{U} is given by the maximum value the shear damage evolution function takes throughout the loading utilising Equation (5.4) defined as follows:

$$Y_{12}^{U}=\max(Y_{12}^{i}) \tag{5.5}$$

The shear damage limit values of the five cyclic tensile specimens at $[\pm 45°]_{2s}$ were calculated and an average value was obtained. The values of the initial shear modulus, the initial, critical and ultimate shear damage limit are summarised in Table 5.4.

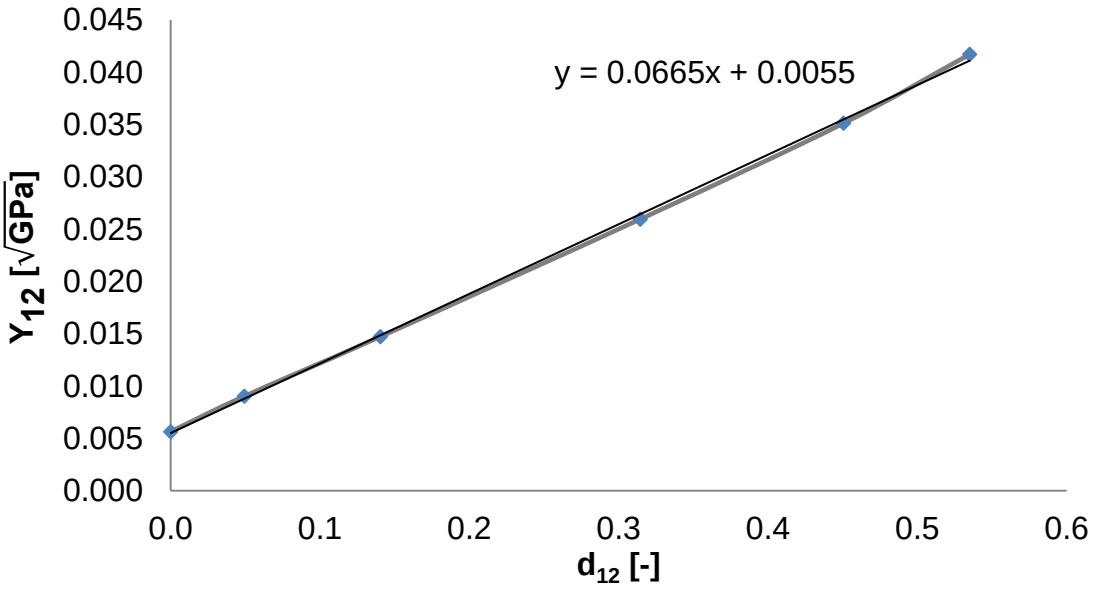

Figure 5.16 Shear damage evolution

Inelastic damage phenomena that occur during the test are expressed through an inelasticity law due to shear damage. The relationship is defined as follows:

$$R_i=\frac{\tau_{12}^{i}}{1-d_{12}^{i}}-R_0 \tag{5.6}$$

Here, R_0 is the initial inelastic stress calculated at the onset of inelasticity on the stress-strain curve for approximately 0.005 absolute strain. Results obtained from

the strain hardening function are plotted against the accumulated effective inelastic strain accounting for the inelastic strains from the commencement of the loading up to present. The curve is illustrated in Figure 5.17.

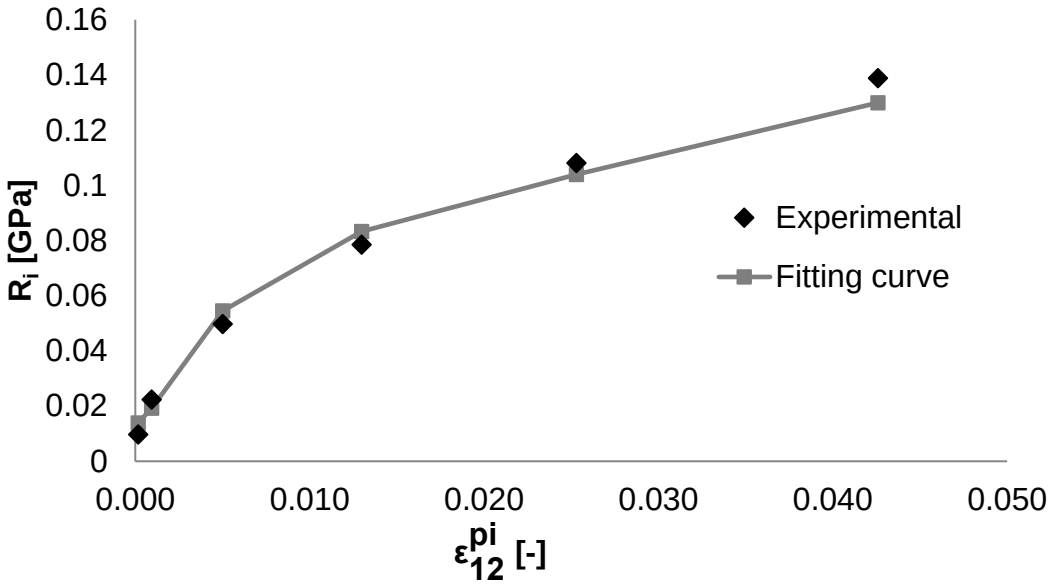

Figure 5.17 Strain hardening curve

The strain hardening curve can be represented by a power law as a function of the accumulated effective inelastic strains. The law is as follows:

$$R_i=\beta(\varepsilon_{12}^{pi})^m \tag{5.7}$$

Here, β and m are the hardening coefficients. The values of the hardening coefficients are identified based on fitting of the experimental results performed using the gradient based Microsoft Excel Solver [314, 315]. The accumulated inelastic strains are calculated based on the area underneath the curve of damage evolution against the inelastic strain. This area consists of the summation of the individual areas for each loading cycle. Figure 5.18 illustrates this graphically. The accumulated inelastic strain is expressed as follows:

$$\varepsilon_{12}^{pi}=\int_{\varepsilon_{12}^{p(i-1)}}^{\varepsilon_{12}^{pi}} 2(1-d_{12}^{i})\, d\varepsilon_{12}^{pi} = \sum_{i=1}^{i} 2\varepsilon_{12}^{pi} \tag{5.8}$$

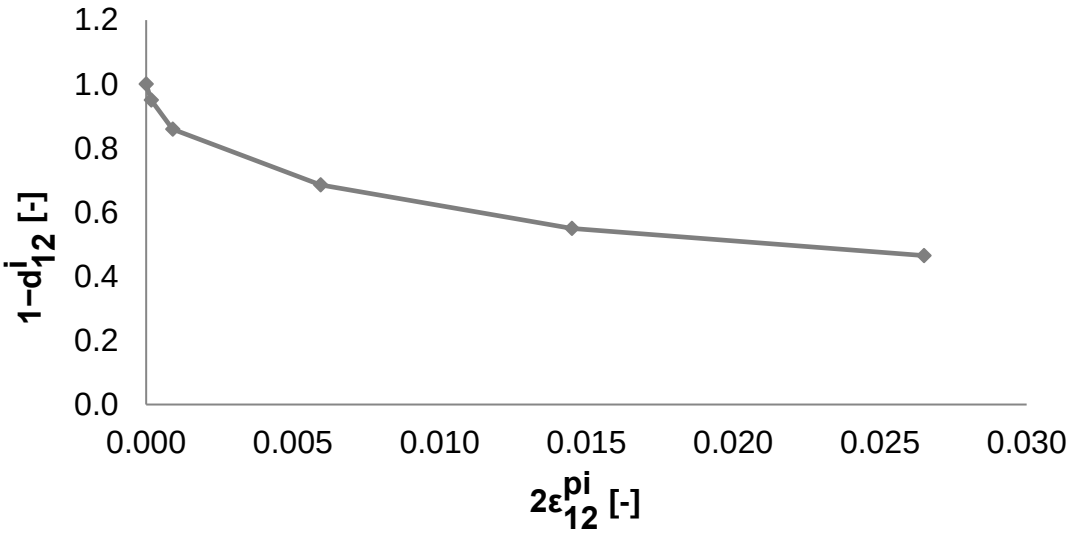

Figure 5.18 Curve of damage evolution with respect to inelastic strain

5.2.1.1.3 Cyclic tensile test on $[+45°]_8$

The transverse elastic modulus as well as a coupling factor between shear and transverse inelastic strains were calculated through tensile tests of $[+45°]_8$ specimens. The stress and strain experimental results were transformed into the material coordinate system as follows:

$$\begin{bmatrix}\sigma_{11}\\ \sigma_{22}\\ \tau_{12}\end{bmatrix}=\begin{bmatrix}0\\ \frac{\sigma_L}{4}\\ \frac{\sigma_L}{2}\end{bmatrix} \text{ and } \begin{bmatrix}\varepsilon_{11}\\ \varepsilon_{22}\\ 2\varepsilon_{12}\end{bmatrix}=\begin{bmatrix}0\\ \frac{\varepsilon_L+\varepsilon_T}{2}\\ \varepsilon_L-\varepsilon_T\end{bmatrix} \tag{5.9}$$

The cyclic loading comprised at least five load-unload cycles with increasing loading levels. The undamaged transverse modulus was obtained from the slope of the initial cycle. The determination of the coupling factor between shear and inelastic strains requires the calculation of transverse and shear damage factors. The transverse damage factor is calculated from the stiffness reduction of each cycle. Based on this, the transverse damage factor can be calculated as follows:

$$d^i_{22}=1-\frac{E^i_{22}}{E^0_{22}} \tag{5.10}$$

Here, E_{22}^{0} is the transverse elastic modulus. The shear damage factor is calculated based on the shear response of the $[+45°]_8$ specimens through Equation (5.2). A coupling factor is defined to account for shear and transverse strains and damage. The coupling factor was identified as follows:

$$A^{i}=\frac{\left(\varepsilon_{22}^{pi}-\varepsilon_{22}^{p(i-1)}\right)\left(1-d_{22}^{i}\right)^{2}}{\left(2\varepsilon_{12}^{pi}-2\varepsilon_{12}^{p(i-1)}\right)\left(1-d_{12}^{i}\right)^{2}} \tag{5.11}$$

Here, A is the coupling factor between shear and transverse inelastic strains. An average value of the coupling factor A from all cycles was identified. The values of the undamaged transverse modulus as well as the average coupling factor between transverse and shear inelastic strains are summarised in Table 5.4.

5.2.1.1.4 Cyclic tensile test on $[\pm 67.5°]_{2s}$

Material model parameters associated with transverse damage evolution and coupling between shear and transverse damage were determined through cyclic tensile tests of $[\pm 67.5°]_{2s}$ specimens. The stress and strain results obtained through experimental investigation were transformed from the global to the material coordinate system based on Equations (4.6)-(4.8). The values of coefficients B and B_a were determined and compared. It was found that using Equation (4.6) the value of B was 0.19072 whilst in the case of Equation (4.7) the value was 0.19041 leading to a difference of 0.2%.

The shear and transverse elastic strains were identified at each loading cycle which led to the calculation of the thermodynamic variables as follows:

$$Z_{12}^{i}=\frac{1}{2}G_{12}^{0}(2\varepsilon_{12}^{i})^{2} \tag{5.12}$$

$$Z_{22}^{i}=\frac{1}{2}E_{22}^{0}\left(v_{12}^{0}\varepsilon_{11}^{i}+\varepsilon_{22}^{i}\right)^{2} \tag{5.13}$$

The calculation of the shear damage evolution was identified through Equations (5.3)-(5.4). The shear damage evolution function can also be determined through the coupling of shear and transverse thermodynamic variables as follows:

$$Y_{12}(t)=\sqrt{Z_{12}(\tau)+bZ_{22}(\tau)} \tag{5.14}$$

Here, b is a coupling factor between the shear and transverse thermodynamic forces. Combining Equations (5.3) and (5.14) and solving for the coupling factor yields:

$$b_i=\frac{\left(Y_{12}^{c}d_{12}^{i}+Y_{12}^{0}\right)^{2}-Z_{12}^{i}}{Z_{22}^{i}} \tag{5.15}$$

The transverse damage evolution function at each loading cycle was calculated as the square root of Equation (5.13). The relation is formed as follows:

$$Y_{22}^{i}(t)=\sqrt{\frac{1}{2}E_{22}^{0}\left(v_{12}^{0}\varepsilon_{11}^{i}+\varepsilon_{22}^{i}\right)^{2}} \tag{5.16}$$

The results of Equation (5.16) for each cycle were plotted against the corresponding transverse damage parameters utilising Equation (5.10). The curve is illustrated in Figure 5.19. The demonstrated curve is described by a linear function as follows:

$$Y_{22}(t)=Y_{22}^{c}d_{22}^{i}+Y_{22}^{0} \tag{5.17}$$

Here, Y_{22}^{c} is the critical transverse damage limit calculated from the slope of the linear curve and Y_{22}^{0} is the initial transverse damage limit which correspond to the intercept of the curve. The brittle transverse damage limit for the fibre-matrix interface Y_{22}^{U} is determined as the maximum value obtained through Equation (5.17):

$$Y_{22}^{U}=\max(Y_{22}^{i}) \tag{5.18}$$

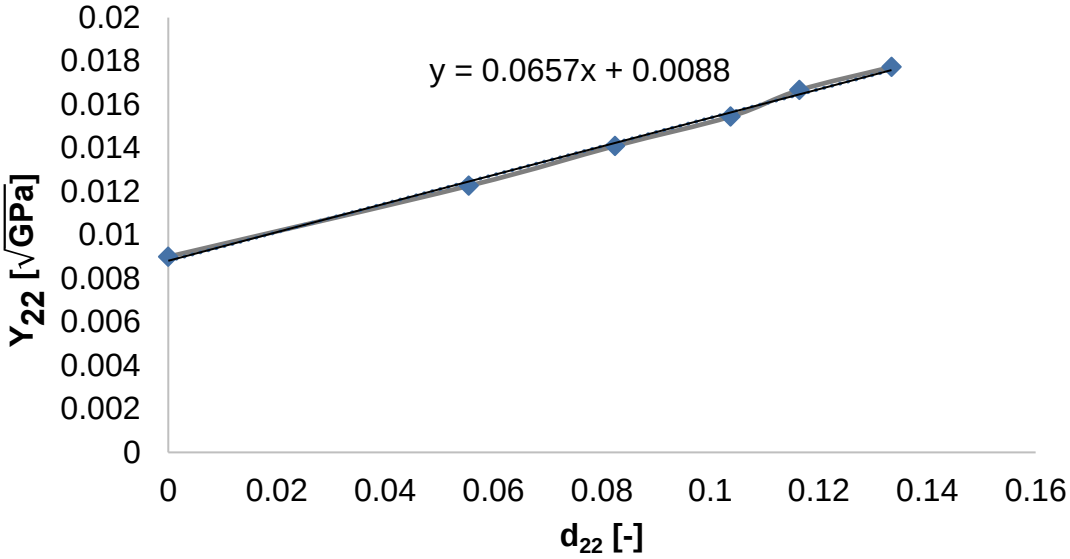

Figure 5.19 Shear damage evolution

Table 5.4 Material model properties identified through conventional calculations

Property	Unit	Standard method values
E_{11}^{0t}	GPa	125
v_{12}^{0}	-	0.33
ε_{i}^{ft}	-	0.0142
ε_{u}^{ft}	-	0.0152
d_{u}^{ft}	-	1
E_{11}^{0c}	GPa	112
γ	-	0.07
ε_{i}^{fc}	-	0.01
ε_{u}^{fc}	-	0.0104
d_{u}^{fc}	-	1
G_{12}^{0}	GPa	4.92
Y_{12}^{0}	$\sqrt{GPa}$	0.005
Y_{12}^{c}	$\sqrt{GPa}$	0.07
Y_{12}^{U}	$\sqrt{GPa}$	0.085
R_0	GPa	0.027
β	-	0.63
m	-	0.48
E_{22}^{0}	GPa	8.96
Y_{22}^{0}	$\sqrt{GPa}$	0.009
Y_{22}^{c}	$\sqrt{GPa}$	0.069
Y_{22}^{U}	$\sqrt{GPa}$	0.075
b	-	2.6
A	-	0.19

5.2.1.2 Out-of-plane properties

Out-of-plane properties associated with the fracture toughness of the material were identified through Mode I and Mode II testing on [0°] specimens. The properties comprised the critical strain energy release rates for Mode I and Mode II, the stresses required for the initiation and propagation of delamination, as well as the normal and shear moduli. The calculation of the strain energy release rates followed the methodology described in section 4.3.3.1 for Mode I and 4.3.3.2 for Mode II. The results were presented in section 0. Based on the methodology detailed in section 3.3.3, the delamination initiation stresses for Mode I and Mode II were calculated from the area of the triangle that corresponds to the initiation G_i^0 of the delamination as illustrated in Figure 3.6. The propagation delamination stress values were assumed to be 10% of the initiation values. Exact identification of the out-of-plane stresses involves some uncertainty due to the collection of data based on observation. However, any inaccuracy included in the stress values is of secondary importance as the model is primarily driven by the energy absorbed at the crack interface in order the crack to grow [230].The normal and shear moduli as described in 3.3.3 were calculated from the slope of the elastic region of the stress versus strain curve for Mode I and Mode II. Another material model parameter identified was the thickness of the model tied interface designated as h_{cont}. This thickness is the distance between the upper and lower arm of the DCB model between the slave nodes and the master segment. The out-of-plane material properties are summarised in Table 5.5.

Table 5.5 Mode I and II model material properties

Property	Unit	Value
G_{IC}	J/mm2	2.035E-4
σ_{Ist}	GPa	5.263E-3
σ_{Ipr}	GPa	5.263E-4
E_0	GPa	3.9
G_{IIC}	J/mm2	1.51E-3
σ_{IIst}	GPa	2.05E-2
σ_{IIpr}	GPa	2.05E-3
G_0	GPa	2.67
h_{cont}	mm	1.5

5.2.2 Material model parameter identification method for in-plane properties through fitting

The material model properties identified in this section were calculated through fitting of analytical models to the experimental response. This method was based on the utilisation of the Microsoft Excel Solver for the optimisation of the analytical solution by minimising the error between the analytical and experimental response through fitting. The error minimisation function is the sum of squared error (SSE) [312, 313] and is calculated as follows:

$$ESS = \sum_{i=1}^{n} (x_i - \hat{x}_i)^2 \tag{5.19}$$

Here, x_i is the observations from the experimental data and $\hat{x}_i$ is the projected analytical results. The Solver uses the Generalised Reduced Gradient Nonlinear Optimisation solving method which is applicable for smooth nonlinear minimisation problems [314, 315]. In the case of cyclic loading, the computation requires the definition of multiple parameters. This was carried out by the implementation of the in-plane material model in Visual Basic for Applications (VBA) for Microsoft Excel. The implementation is detailed in Appendix A.

Fitting for the tensile response in the fibre direction was performed with respect to the tensile modulus and was based on the acquisition of the minimum error between these values. The Solver results led to an average error of 2.2%, which corresponds to an average of 10.24 MPa per data point. Figure 5.20 illustrates the stress-strain data from the experimental investigation and the analytical solution indicating that the two curves are in close agreement. The values of damage model parameters identified through fitting were utilised for the development of the shell element model to study fibre damage under tensile loading.

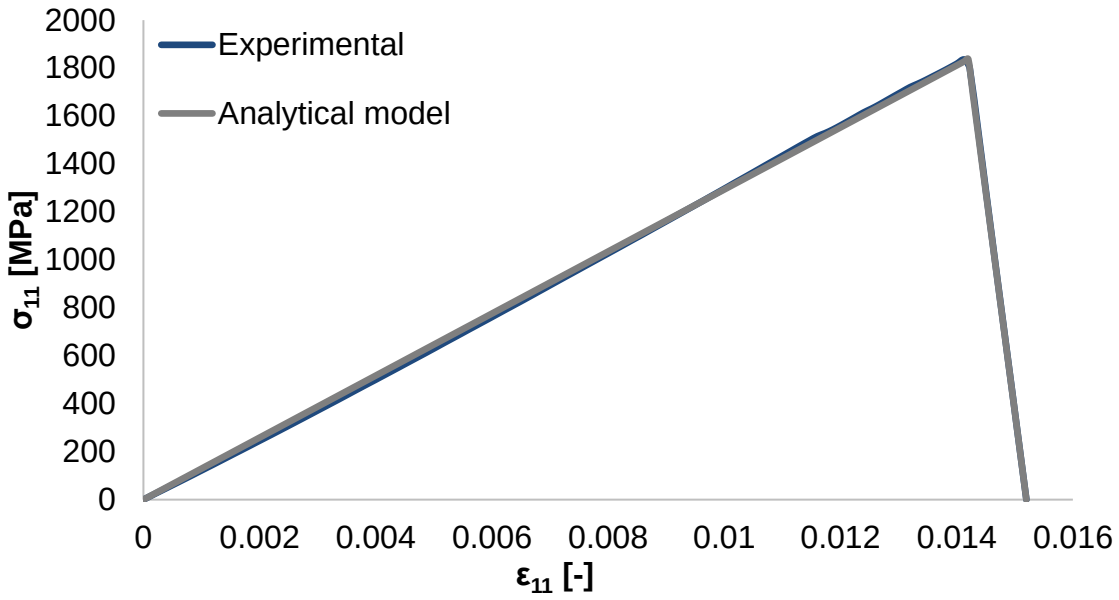

Figure 5.20 Experimental and analytical model results of $[0°]_8$ tensile specimens

The identification of fibre damage parameters under compression loading was carried out following a similar procedure as for tensile loading. The stress-strain results acquired from experimental investigation were compared with the results obtained through the analytical solution. The fitting was performed with respect to the compressive modulus and the corrective parameter γ. The average error was found to be 1.76% corresponding to an average difference of 6.9 MPa per data point. Figure 5.21 illustrates the stress-strain curves of the experiment and the analytical model which are in close agreement.

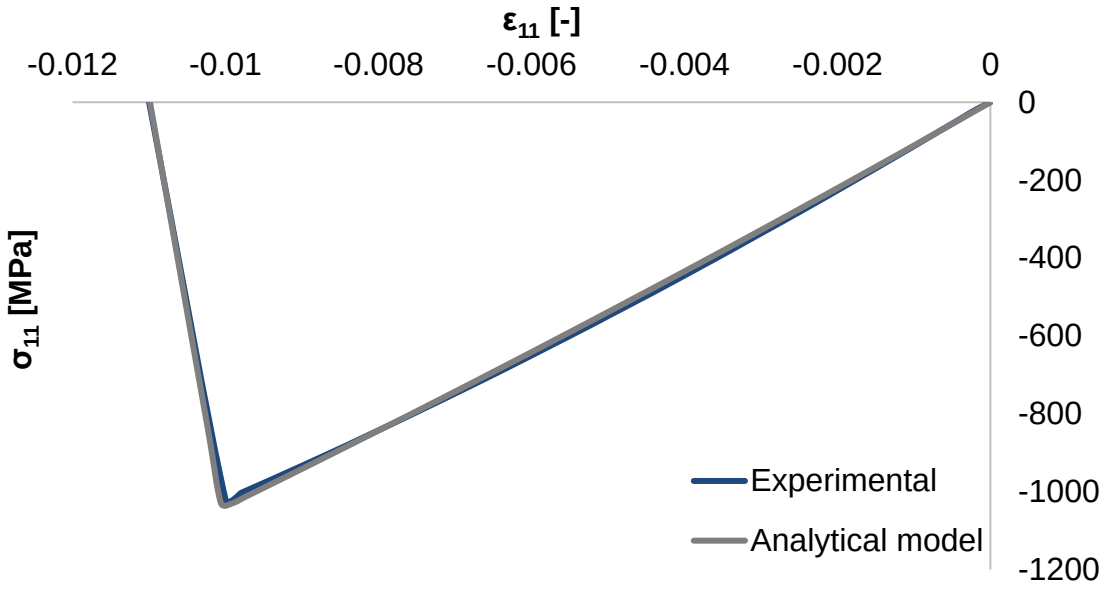

Figure 5.21 Experimental and analytical model stress-strain results for $[0°]_8$ compression specimens

The identification of the damage model parameters acquired from cyclic loading was carried out through the implementation of the damage material equations on VBA and the use of the Solver in order to minimise the error between the comparison of the experimental and analytical solution. In the case of $[\pm 45°]_{2s}$ case the shear stress versus strain results acquired from experimental and analytical investigation are presented in Figure 5.22. The average difference was calculated to be 4.53 MPa per data point.

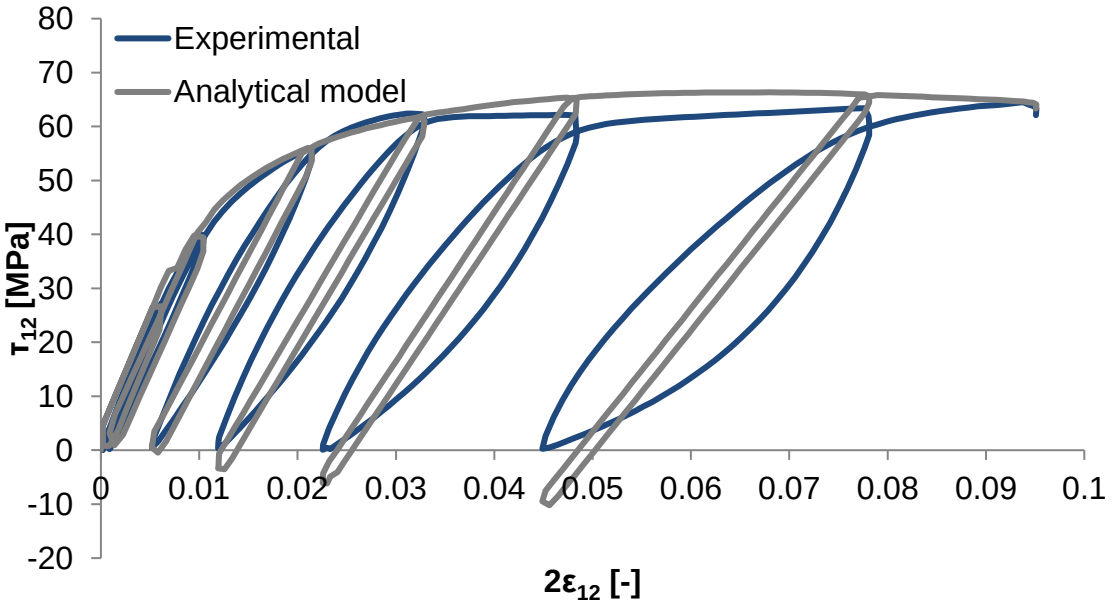

Figure 5.22 Experimental and analytical model stress-strain results for $[\pm 45°]_{2s}$ cyclic tensile specimens

In the case of $[+45°]_8$ specimens, the stress-strain results from the experiments were plotted against the analytical solutions for shear and transverse response which were identified utilising VBA coding and the Solver. Figure 5.23 for shear and transverse response against the analytical model illustrate that the curves are in agreement. The identified average error was 0.73 MPa per data point for the shear and 0.34 MPa per data point for the transverse response. The results from $[\pm 67.5°]_{2s}$ specimens were analysed in a similar manner. Figure 5.24 shows the experimental against the results from the analytical investigation. In the case of shear response the average error per data point was 0.59 MPa whilst for transverse was 1.09 MPa. Table 5.6 summarises the values of the in-plane material model properties utilised for the development of the constitutive model.

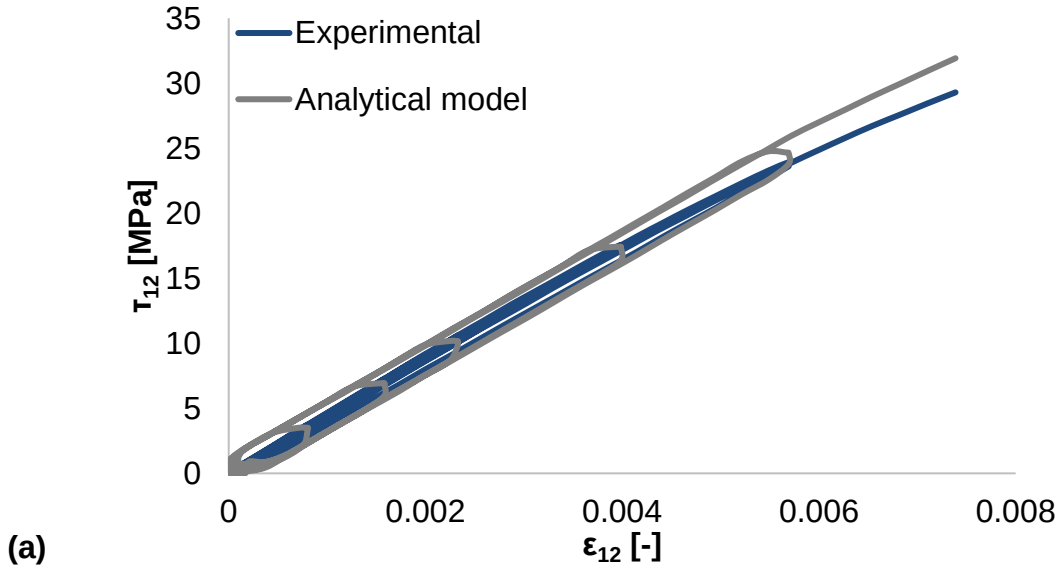

(a)

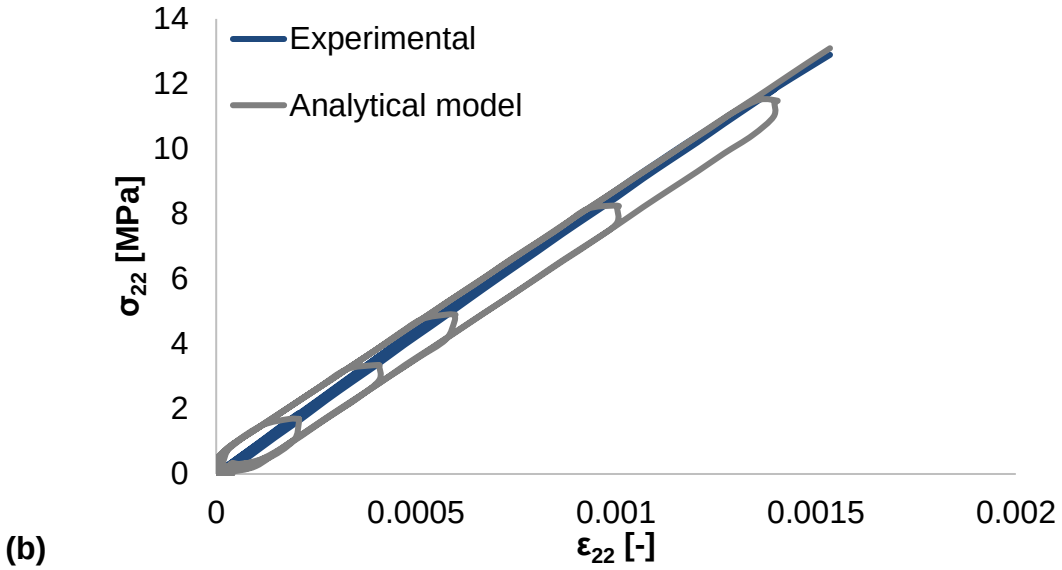

(b)

Figure 5.23 Shear (a) and transverse (b) experimental and model stress-strain results against time for $[+45°]_8$ cyclic tensile specimens

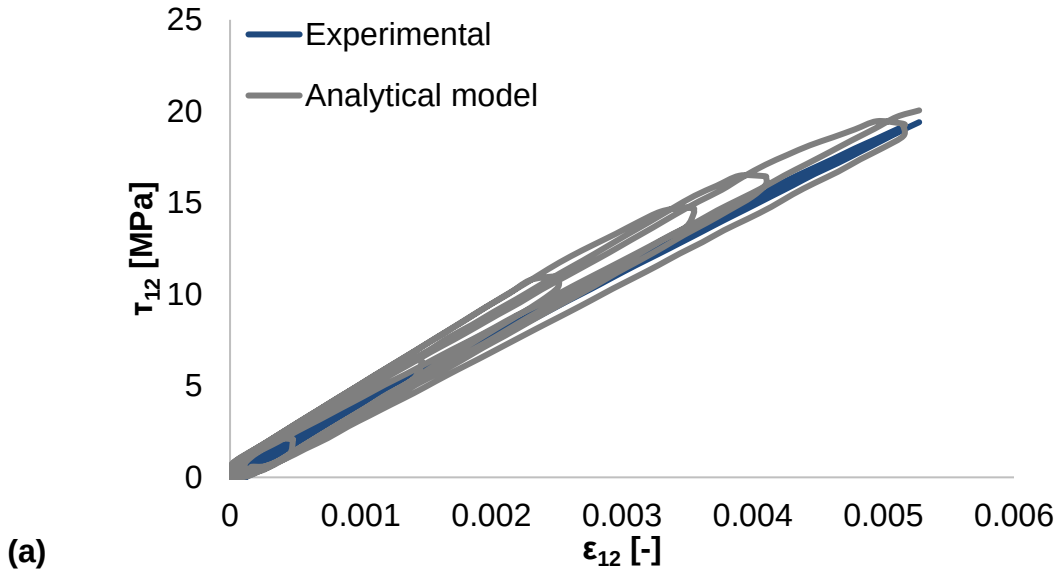

(a)

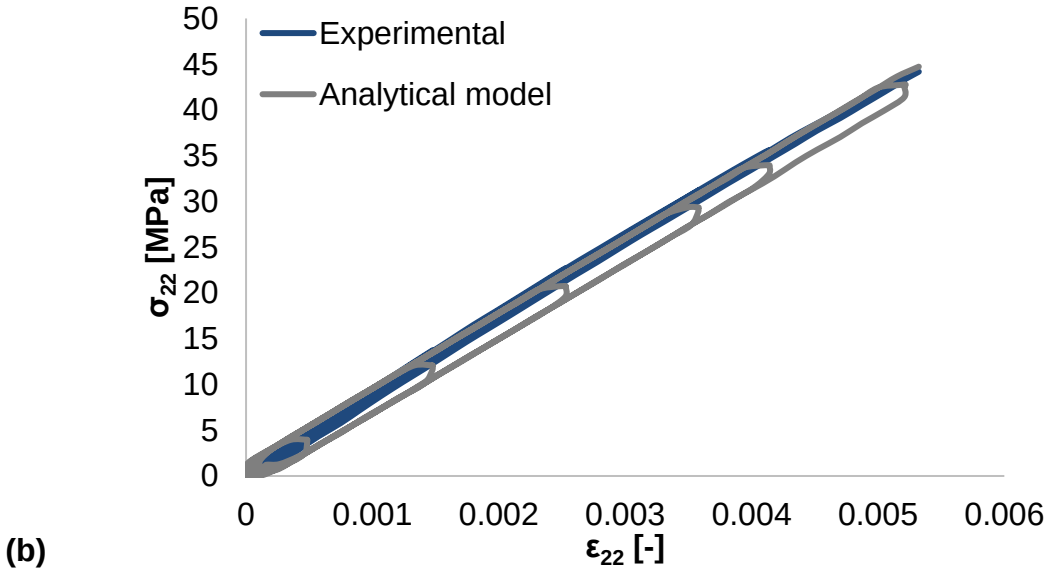

(b)

Figure 5.24 Shear (a) and transverse (b) experimental and model stress-strain results against time for $[\pm 67.5°]_{2s}$ cyclic tensile specimens

Table 5.6 Material model parameters for the development of constitutive model

Property	Unit	Material model properties
E_{11}^{0t}	GPa	129.36
v_{12}^{0}	-	0.33
ε_{i}^{ft}	-	0.0142
ε_{u}^{ft}	-	0.0152
d_{u}^{ft}	-	1
E_{11}^{0c}	GPa	117.9
γ	-	0.128
ε_{i}^{fc}	-	0.01
ε_{u}^{fc}	-	0.0104
d_{u}^{fc}	-	1
G_{12}^{0}	GPa	4.37
Y_{12}^{0}	$\sqrt{GPa}$	0.009
Y_{12}^{c}	$\sqrt{GPa}$	0.07
Y_{12}^{U}	$\sqrt{GPa}$	0.08
R_0	GPa	0.035
β	-	0.92
m	-	0.62
E_{22}^{0}	GPa	8.2
Y_{22}^{0}	$\sqrt{GPa}$	0.0088
Y_{22}^{c}	$\sqrt{GPa}$	0.0657
Y_{22}^{U}	$\sqrt{GPa}$	0.075
b	-	2.6
A	-	0.19

5.3 Constitutive model verification

This section addresses the details of the verification of the constitutive model for the loading cases that were used for the extraction of damage material model parameters. The in-plane tests of tensile loading at 0°, cyclic tensile at ±45°, +45°, ±67.5°, compression at 0° and out-of-plane Mode I test at 0° were simulated using FE according to the respective experiments in order to verify that the identified damage model parameters calculated based on the fitting can reproduce the experimental failure response. The simulation results of in-plane and out-of-plane cases were compared against experimental results and the average error per data point was calculated.

5.3.1 In-plane damage model verification

The experimental cases of tensile loading at 0°, cycle tensile at ±45°, +45°, ±67.5° and compression at 0° were simulated in order to compare and repeat their failure response using suitable material properties. The in-plane material damage parameters utilised for all the simulated cases were acquired through fitting and are summarised in Table 5.6. All models comprised one shell element through the thickness and eight layers with thickness of 0.3 mm. The assigned boundary conditions represented the in-plane testing conditions. The movement of all nodes on the z-axis was constrained as well as their rotation on x, y and z axes with respect to the global frame. Movement on x-axis was also constrained for the nodes of the fixed end. The nodes of one side of the shell element were set with restrained movement on y-axis allowing contraction due to the Poisson's effect. The nodes of the free end of each model were assigned with a displacement versus time loading condition curve that was based on the displacement results acquired from the experimental investigation.

The $[0°]_8$ tensile model comprised one shell element with size of 150x15 mm. The shell consisted of 250 elements with mesh size of 3 mm and 306 nodes. In the case of the compression model the shell element dimensions were 140x13 mm^2 and its mesh size was set at 2.6 mm. The number of elements and nodes comprising the model were 270 and 330 respectively. The fibre orientation for both the tensile and compression models was set at 0° with respect to the

orthotropic axis. The dimensions of the shell cyclic tensile models of $[\pm 45°]_{2s}$, $[+45°]_8$ and $[\pm 67.5°]_{2s}$ specimens were 150x15 mm^2. The mesh size was set to 5 mm, which led to 150 elements and 186 nodes. The fibre orientation was set according to the respective specimen case.

Figure 5.25 illustrates the results for tensile loading. The two curves are in agreement. The model maximum failure stress is indicated at 1800 MPa and the ultimate strain at 0.0152. The data point error between the experimental and modelling response was calculated at 11.2 MPa.

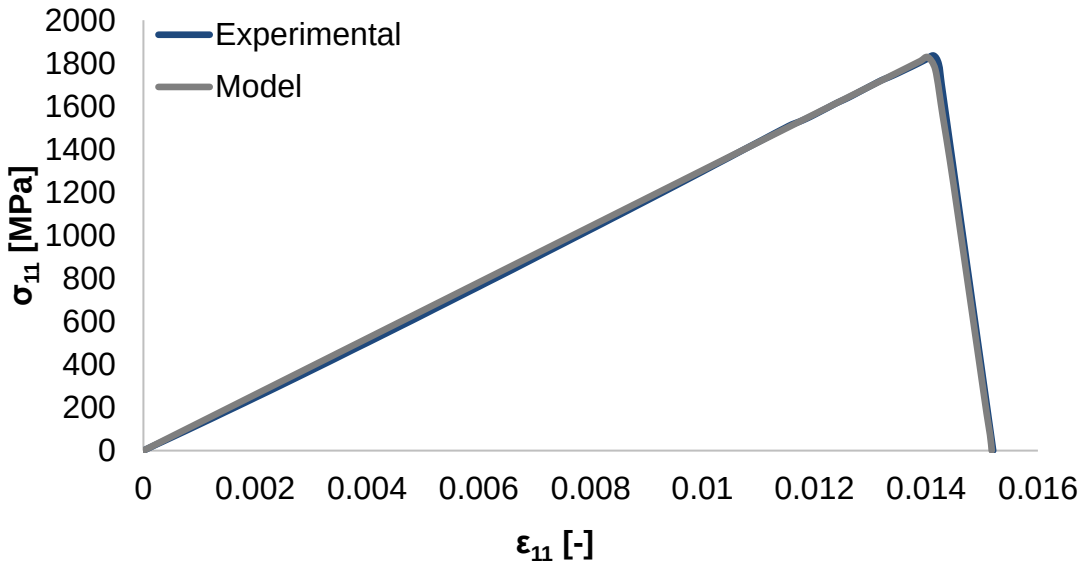

Figure 5.25 Experimental and simulation results of $[0°]_8$ tensile model

The stress-strain results from the experimental and modelling investigation for compression loading are presented in Figure 5.26. The curves are in good agreement as the experimental response is reproduced from the model. The maximum stress reaches 1026 MPa whilst the ultimate strain observed at 0.011 absolute strain. The average data point error is 4.35 MPa.

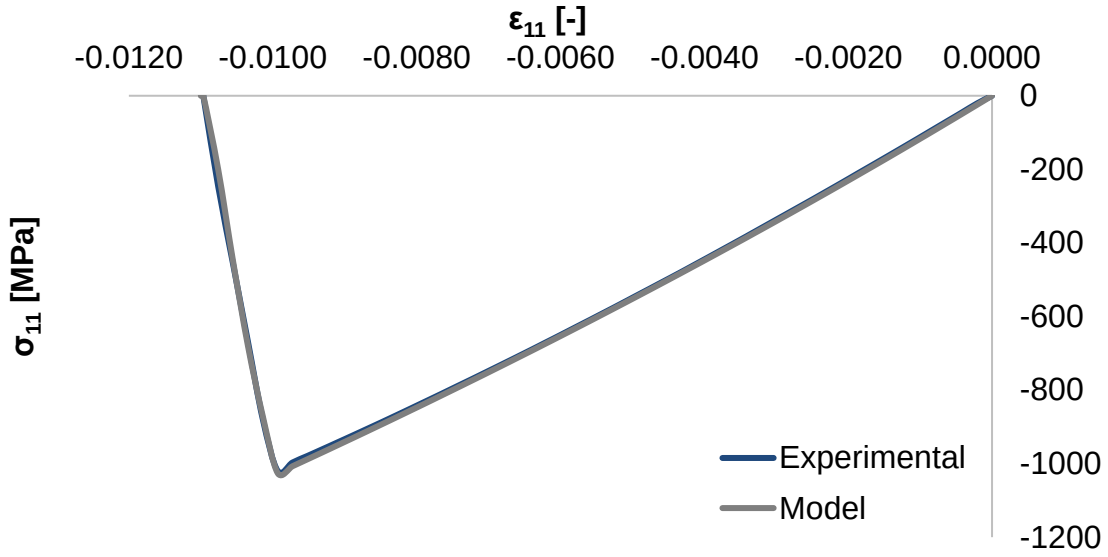

Figure 5.26 Experimental and simulation results of $[0°]_8$ compression model

Figure 5.27 illustrates the comparison between the experimental results and the results of the model for the case of $[\pm 45°]_{2s}$ specimens. The two curves show similar response, although as expected the model curve does not include the hysteresis. The model curve shows that it repeats the cyclic loading quite close to the experimental behaviour. The average error per data point was calculated at 5.26 MPa.

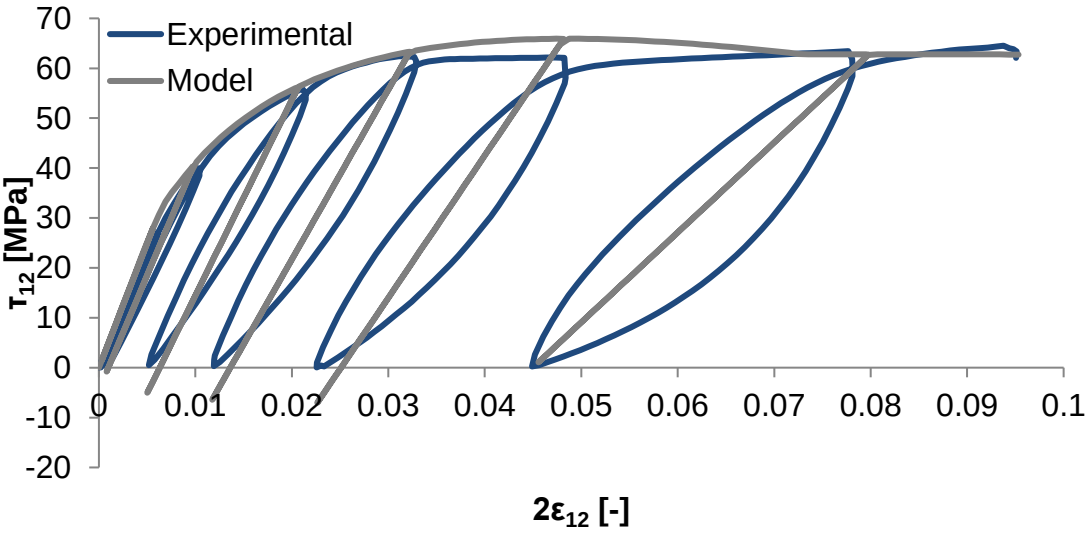

Figure 5.27 Experimental and simulation results of cyclic tensile damage model at $[\pm 45°]_{2s}$

The stress-strain comparison of experimental against simulation results for $[+45°]_8$ specimens is illustrated in Figure 5.28. The shear response is represented in Figure 5.28a. The plotted model curve shows good fitting to the experimental results. The average error per data point was 2.63 MPa. Figure 5.28b represents the transverse response of the model and experimental curves. The two plots show to have small differences up to 0.001 absolute strain. The curves diverge after that that point until the end of loading. The average error per data point was found to be 0.19 MPa.

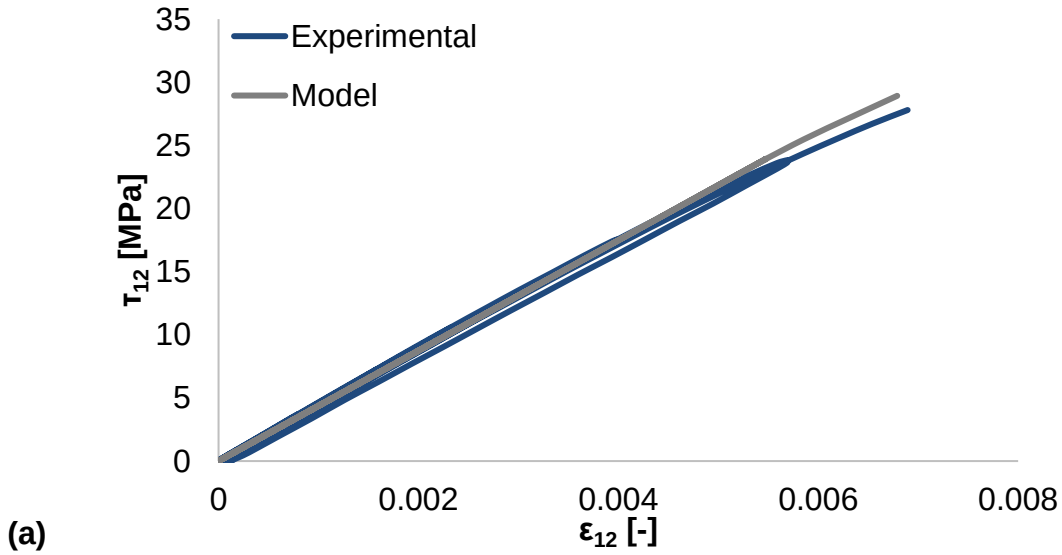

(a)

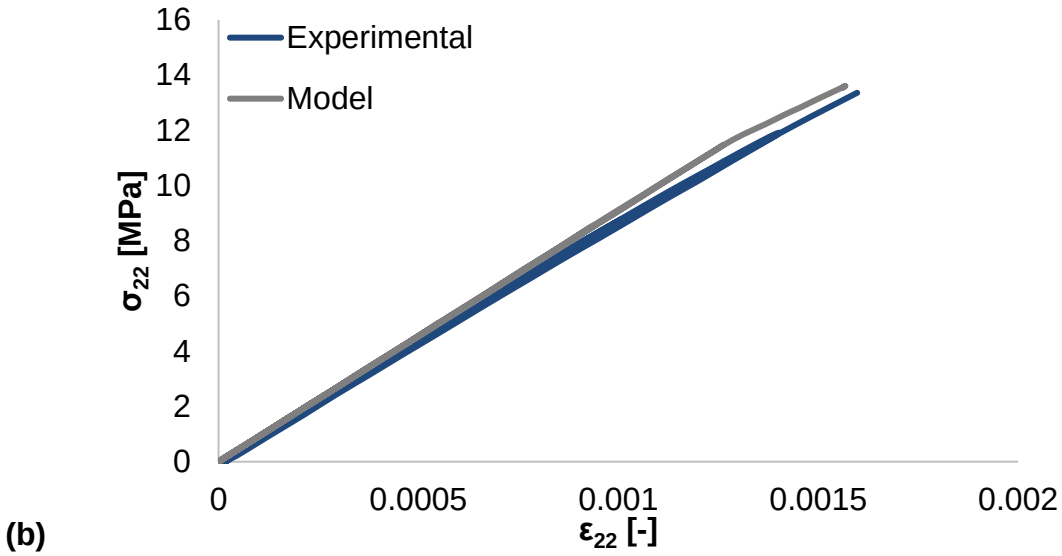

(b)

Figure 5.28 Experimental and simulation results of cyclic tensile damage model at $[+45°]_8$

The simulation results for the cyclic tensile model at $[\pm 67.5°]_{2s}$ were plotted against the results acquired through experimental investigation. The comparison curves are illustrated in Figure 5.29. The shear (Figure 5.29a) and transverse (Figure 5.29b) stress versus strain results show good agreement for the examined cases. The fitting between the experimental and simulation results verifies that the experimental results are reproduced by the model. The average error per data point for shear was calculated at 0.97 MPa, whilst for the transverse response is 0.85 MPa.

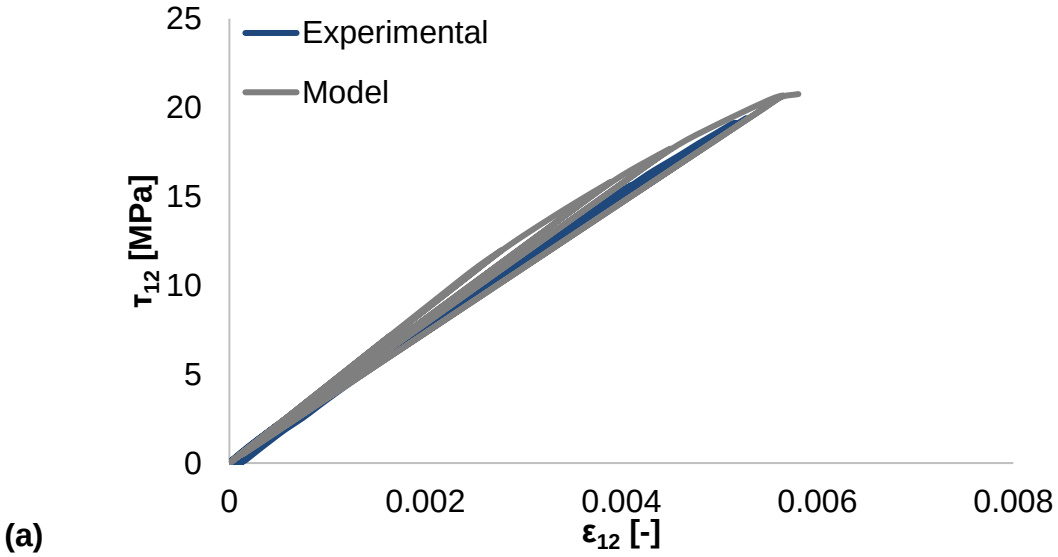

(a)

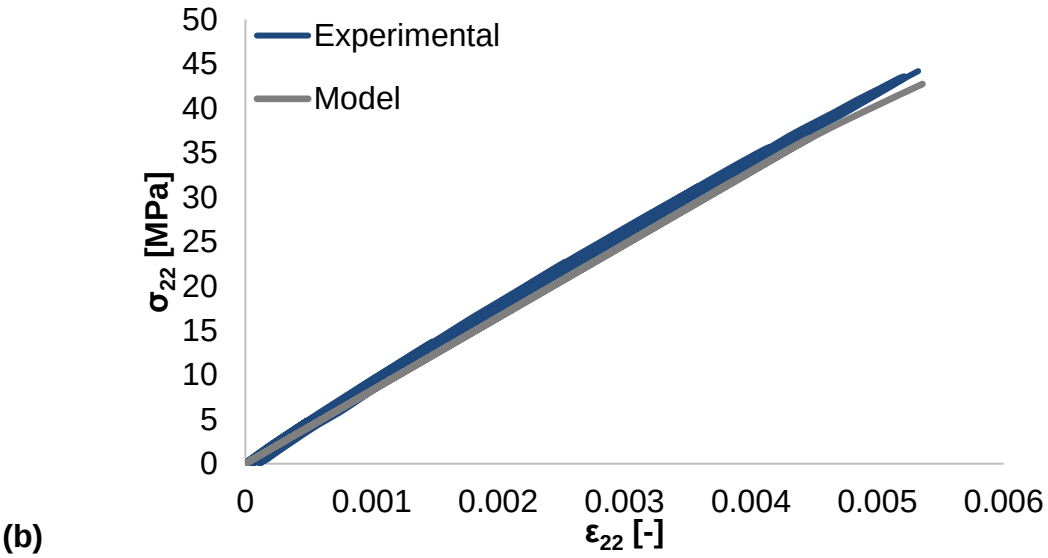

(b)

Figure 5.29 Experimental and simulation results of cyclic tensile damage model at $[\pm 67.5°]_{2s}$

5.3.2 Out-of-plane damage model verification

In order to verify the out-of-plane damage model, a $[0°]_{10}$ DCB model identical to the test sample was simulated. The DCB model consisted of two shell arms. The element mesh size of the cohesive zone should be smaller than the cohesive zone length for the accurate representation of the delamination behaviour and the load-displacement conditions of the test [316, 317]. The cohesive zone length (l_{ch}) was calculated as follows:

$$l_{ch}=0.5\ \min(l_{ch,\ I}, l_{ch,\ II}, l_{slender,\ I}, l_{slender,\ II}) \tag{5.20}$$

where

$$l_{ch,\ I}=E_I^{'}\frac{G_{IC}}{(\sigma_{I,\ max})^2} \tag{5.21}$$

$$l_{ch,\ II}=E_{II}^{'}\frac{G_{IIC}}{(\sigma_{II,\ max})^2} \tag{5.22}$$

$$l_{slender,\ I}=\left(E_I^{'}\frac{G_{IC}}{(\sigma_{I,\ max})^2}\right)^{1/4} h^{3/4} \tag{5.23}$$

$$l_{slender,\ II}=\sqrt{\left(E_{II,\ slender}^{'}\frac{G_{IIC}}{(\sigma_{II,\ max})^2}\right)h} \tag{5.24}$$

$$\frac{1}{E_I^{'}}=\sqrt{\frac{b_{11}b_{33}}{2}}\sqrt{\left(\frac{b_{33}}{b_{11}}\right)^{1/2}+\frac{2b_{31}+b_{55}}{2b_{11}}} \tag{5.25}$$

$$\frac{1}{E_{II}^{'}}=\sqrt{\frac{b_{11}}{2}}\sqrt{(b_{11}b_{33})^{1/2}+b_{31}\frac{b_{55}}{2}} \tag{5.26}$$

$$E_{II,\ slender}^{'}=\frac{E_{11}}{1-\nu_{13}\nu_{31}} \tag{5.27}$$

$$\begin{array}{lll} b_{11}=1/E_{11} & b_{12}=-\nu_{12}/E_{11} & b_{66}=1/G_{12} \\ b_{22}=1/E_{22} & b_{23}=-\nu_{23}/E_{22} & b_{55}=1/G_{31} \\ b_{33}=1/E_{33} & b_{31}=-\nu_{31}/E_{31} & b_{44}=1/G_{23} \end{array} \tag{5.28}$$

Parameter h represents the laminate half thickness, b_{ij} are the Voigt elastic constants in the material directions and $E_I^{'}, E_{II}^{'}$ are the equivalent elastic moduli for Mode I and Mode II respectively. The calculations indicate that the cohesive zone length is approximately 2 mm which leads to the selection of a mesh size of

1 mm. Each arm shell comprised eight thousand (8000) elements. The dimensions of each shell were 160x25 mm^2 and the distance between them was set at half the thickness of the experimental DCB specimen (1.5 mm). Each DCB shell arm included a stacking sequence of five layers, 3 mm thick with 0° fibre orientation in order to create a laminate of two arms consisting of ten layers in total. All layers were assigned the in-plane material properties of Table 5.6. The interface between the two arms was assigned the material properties summarised in Table 5.5. The two sublaminates were tied selecting slave nodes from the lower DCB arm without the initial 50 mm of the arm which represent the pre-crack as presented in Figure 5.30. The master segment included the entire upper DCB arm. Boundary conditions were applied on two rows of elements at the fixed end of both arms constraining movement and rotation on all axes. A loading curve based on the Mode I testing conditions was assigned on the edge nodes of the free end on both arms. The direction of the loading was different on each arm in order to allow separation similarly to the experiment.

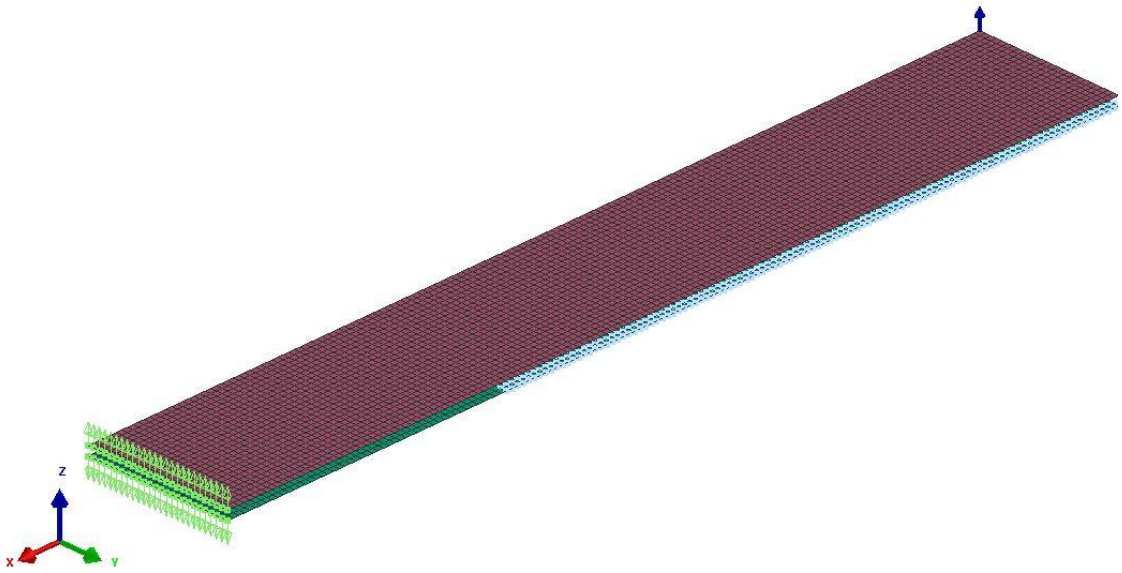

Figure 5.30 DCB model at $[0°]_{10}$

Figure 5.31 illustrates the comparison data. The results of crack growth during Mode I acquired from the model are in good agreement with the experimental results. The simulation curve shows that certain amount of noise is present, which is the result of the loading conditions with respect to the delamination properties.

The average error per data point between experimental and simulation results was calculated at 0.0023 kN.

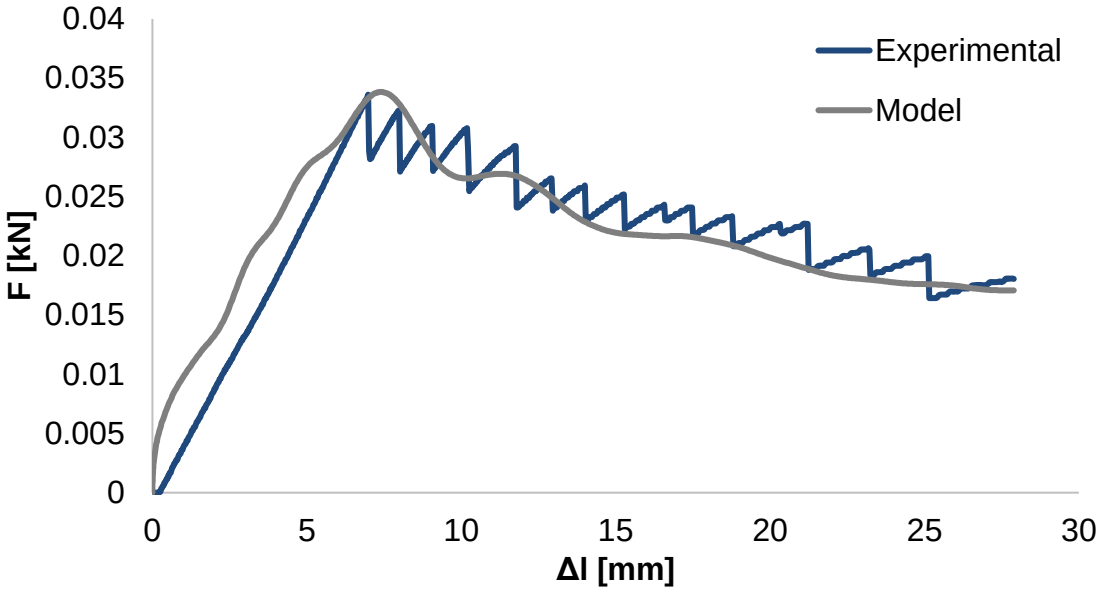

Figure 5.31 Experimental and simulation results of delamination model at $[0°]_{10}$

6 Introduction of defects for development of leak-before-break

This chapter is dedicated to the incorporation of defects for the development of the LBB concept. The motivation leading to the selection of the defect types, as well as the methodology for defect introduction are described. The methodology is based on the results of an initial experimental investigation on the RP507 UD carbon prepreg. This investigation sets the ground for a simulation study for the identification of the most suitable design pattern of defect types and the degree of damage associated with it, which under certain loading conditions can trigger failure mechanisms that lead to controllable and predictable failure of the structure.

6.1 Motivation for defect type selection

Carbon fibre reinforced composites can suffer from brittle and abrupt failure without previous warning. The development of the LBB concept is based on the modification of the material properties of the composite locally through the introduction of weak areas in order to produce a fail-safe structure which achieves a gradual, controllable and predictable way of failure. These weak points can act as stress concentration points under certain loading conditions and based on the way they are positioned, they can facilitate the manipulation and control of the failure of the structure. This is enabled by the adjustment of the local design and architecture of the constituents of the materials. In the case of CPVs undergoing internal pressurisation, the LBB concept relies on the generation of leakage which as described in Chapter 2 occurs mainly due to matrix dominated failure mechanisms, which, in these structures, is occasionally accompanied by intralaminar failure [74, 318]. Therefore, the investigation of introduction of defects that initiate these failure mechanisms is of main interest in this work.

Randomly oriented fibre discontinuities affect the load bearing capability of reinforcement leading to deterioration of the structural integrity of the composite [170, 319, 320]. Highly aligned fibre discontinuities can provide material properties that can be comparable to those of UD composite materials; while

affecting the local state of stress and strain of the structure in comparison to the intact composite. The arrangement of fibre cuts in a well-designed, pre-arranged manner can lead to controlled deterioration of reinforcement strength and predictable structural failure. The dominant failure mechanisms that have been reported for composite materials with introduced slits under tensile loading are inter-tow debonding and splitting as well as matrix cracks and delamination [178, 321, 322]. These are consistent with the failure mechanisms that can initiate LBB behaviour on a CPV. In this work, fibre cut defects on UD carbon fibre prepreg are utilised in order to achieve a gradual, pseudo-ductile structural failure providing warning before ultimate failure.

In addition to the controlled deterioration of the composite mechanical properties through the introduction of fibre cut defects, matrix dominated defects are also investigated. The incorporation of matrix defects, such as resin rich areas, voids, inclusions, and interfacial weakness points can trigger the development of matrix and interface dominated failure mechanisms [16, 323–325]. Particularly, the implementation of poor bonding between neighbouring layers can lead to the development of delamination under certain loading conditions, which in the case of CPVs facilitates the creation of leakage.

6.2 Methodology for defect introduction

6.2.1 Fibre cut defects

6.2.1.1 Manufacturing process

Two UD laminates of $[0°]_{16}$ and $[\pm35°]_{4s}$ lay-up were manufactured using RP507 carbon prepreg. Both laminates accommodated seven tensile specimens in prearranged locations for easier implementation of the fibre cut defects. These were introduced perpendicularly to the fibres during the lay-up. The process took place using a scalpel to cut the fibres and a ruler on which tape was attached at specific intervals and length to indicate the exact positions for the cuts on the prepreg plies. For exploratory purposes, the length of each cut was equal to 20% of the cross section across the width of each tensile coupon, which corresponds to 3 mm and 5 mm for 0° and ±35° specimens, respectively. The composite

laminate consisted of 16 layers. The fibre cut defects were positioned on 15 consequent layers at a lateral distance of 5 mm forming an “S” shape pattern at the cross section along the sample length, whilst the outer layer did not contain defects as illustrated in Figure 6.1. The curing and specimen preparation for testing were the same as the procedure described in section 4.2.1, whilst the tensile testing was carried out according to the process detailed in sections 4.3.2.1-4.3.2.2.

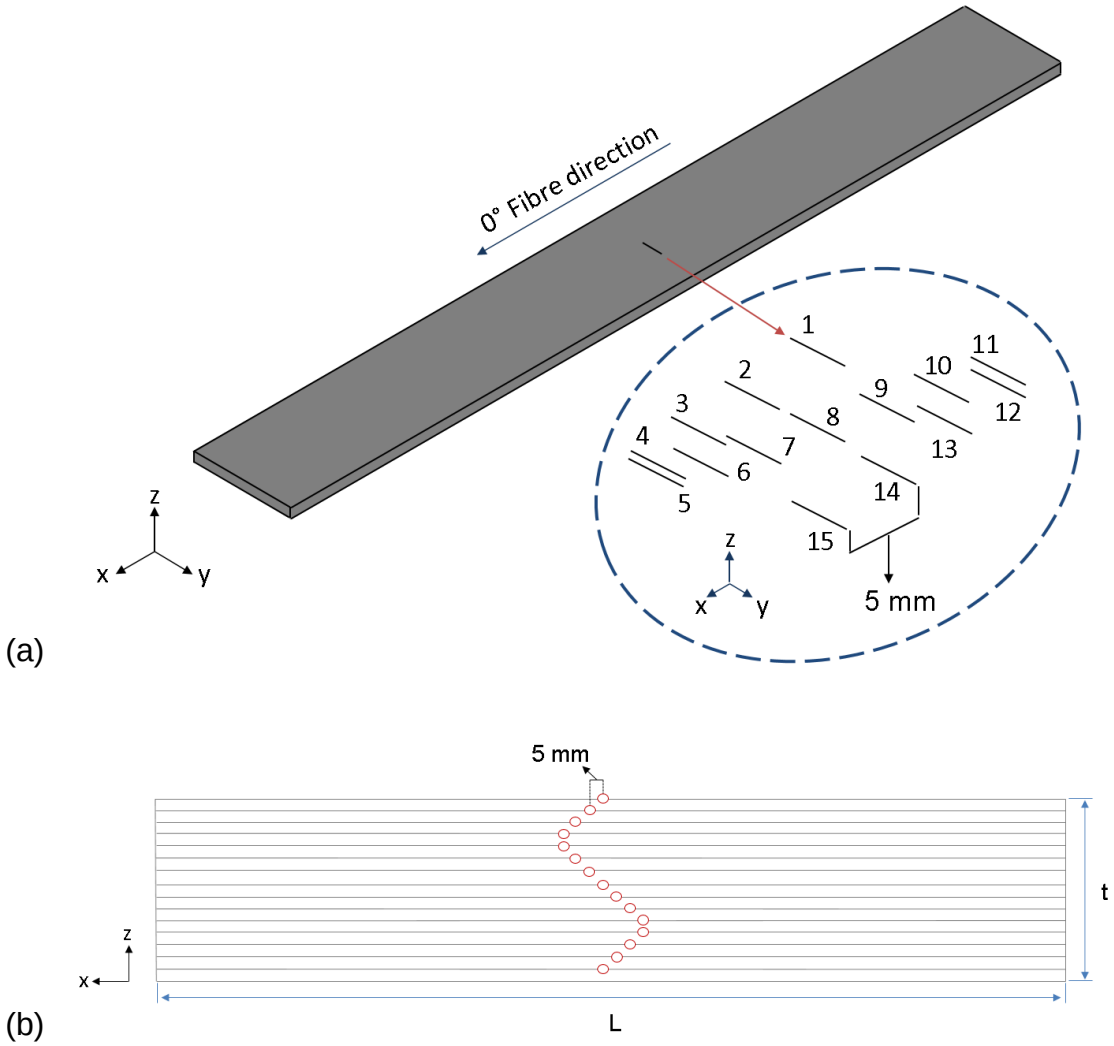

Figure 6.1 Schematic representation of S crack path on (a) consequent layers (3D view), (b) longitudinal cross section of specimen (xz coordinates)

6.2.1.2 Simulation investigation

Simulation investigations were carried out to reproduce the mechanical testing conditions. Four models were simulated; two intact models with $[0°]_{16}$ and $[\pm 35°]_{4s}$

lay-ups and their respective with fibre cut defects, introduced as indicated in section 6.2.1.1. The models corresponding to the intact/defective $[0°]_{16}$ and $[\pm35°]_{4s}$ specimens consist of 16 shells through the thickness with dimensions of 250x15x2.4 mm^3 and 250x25x2.4 mm^3 respectively. Each layer was identified with a certain fibre orientation based on the lay-up sequence of the respective model. For the intact specimen with a $[0°]_{16}$ lay-up, the model comprises 4896 nodes and 4000 elements with mesh size of 3x3 mm^2, whilst the intact specimen with $[\pm35°]_{4s}$ lay-up consists of 2976 nodes and 2400 elements with dimensions of 5x5 mm^2. The fibre cut defect models with $[0°]_{16}$ and $[\pm35°]_{4s}$ lay-ups were prepared using finer shell elements to account for the defective areas. In the $[0°]_{16}$ case, the model consists of a total of 12864 nodes and 9600 elements with mesh of 3x3 and 3x0.5 mm^2 in the intact and fibre cut defects areas following the requirements of the fibre cut pattern. Figure 6.2 illustrates the $[0°]_{16}$ fibre cut defective model. Each layer of the defective model with $[\pm35°]_{4s}$ lay-up consists of 10620 nodes and 8160 elements with mesh of 5x5 and 5x0.5 mm^2.

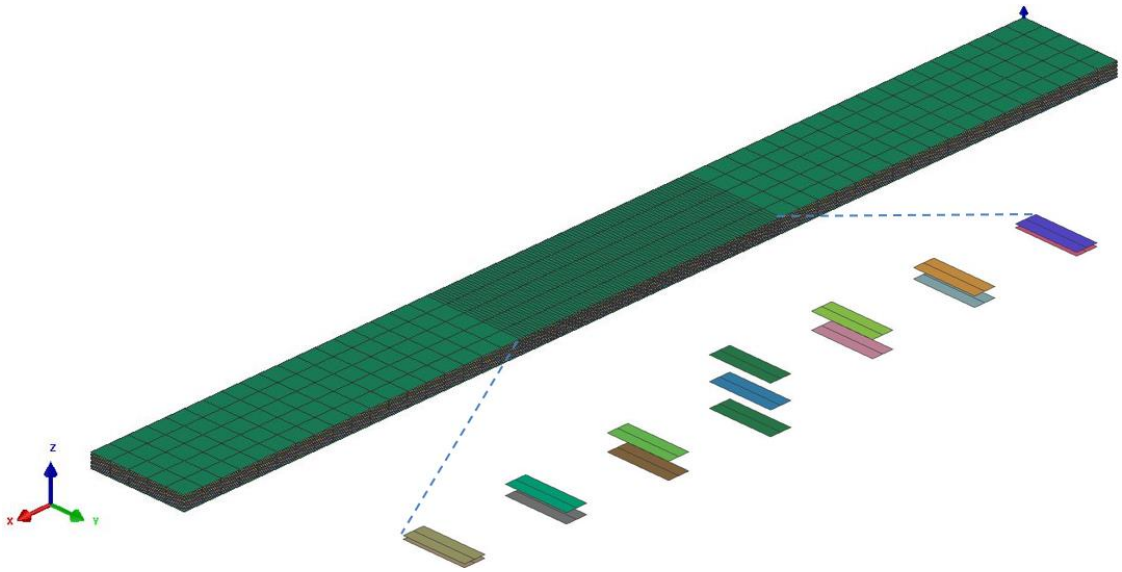

Figure 6.2 Simulated fibre cut defects in 0° specimen

The 0° tensile material properties assigned to intact elements were extracted through mechanical testing, whereas the shear and transverse material properties required for the simulation of the $[\pm35°]_{4s}$ tensile specimen were based on literature for similar materials [224, 277] due to the limited experimental

campaign carried out for the specific material. Table 6.1 summarises the in-plane material properties utilised.

The material properties in the direction of the fibre assigned to the fibre cut defective areas were identified through an analytical expression for the development of a controlled failure methodology. The fibre volume fraction in the region of the cuts is expressed as:

$$V_f^{'}=V_f-V_c \tag{6.1}$$

where, $V_f^{'}$ is the fibre volume fraction of the defective composite, V_f the original fibre volume fraction of the intact material and V_c is the fibre cut volume fraction. Following an isostrain assumption for loading in the fibre direction, the stress can be expressed as:

$$\sigma^{'}=\sigma_f V_f^{'} + \sigma_c V_c + \sigma_m V_m \tag{6.2}$$

Where, σ_f, σ_m and σ_c represent the fibre, matrix and fibre cut stress respectively and V_m is the volume fraction of the matrix.

The material model described in section 3.3.2.4 expresses fibre damage through the definition of an initial threshold (ε_i^{ft}) and an ultimate (ε_u^{ft}) damage strain. Assuming that the stress carried by cut fibres and the matrix is negligible, the initial and ultimate strains for the region with cuts become:

$$\varepsilon_i^{'}=\varepsilon_i^{ft}\frac{V_f-V_c}{V_f} \tag{6.3}$$

$$\varepsilon_u^{'}=\varepsilon_u^{ft}\frac{V_f-V_c}{V_f} \tag{6.4}$$

The initial and ultimate strain of the defective composite region from this analysis for the case of 20% cut fraction are given in Table 6.1. The mid-plane interface for the investigation purposes corresponds to the real interlaminar properties summarised in Table 5.5. The remaining fourteen interfaces of the individual layers of the models are tied perfectly. The interlaminar properties corresponding to a perfectly tied interface are summarised in Table 6.2 and were identified based on the real interface properties. To ensure that no interlaminar failure is present, the moduli are multiplied by a factor of 10 and the strength and strain energy release rate values are increased by a factor of 1000. The interlaminar thickness h_{cont} is set to 0.15 mm since each shell is located at the midplane of

each layer. In-plane boundary conditions are assigned to the nodes of the four models in accordance to section 5.3. The loading conditions applied to the models follow the response of the respective experiment.

Table 6.1 Material model parameters extracted from experiments, literature [224, 277] and fibre cut methodology

Property	Unit	Material model properties
E_{11}^{0t}	GPa	136
ν_{12}^{0}	-	0.34
ε_{i}^{ft}	-	0.0138
ε_{u}^{ft}	-	0.014
$\varepsilon_{i}^{'}$	-	0.011
$\varepsilon_{u}^{'}$	-	0.0112
d_{u}^{ft}	-	1
G_{12}^{0}	GPa	5.8
Y_{12}^{0}	$\sqrt{GPa}$	0.0047
Y_{12}^{c}	$\sqrt{GPa}$	0.088
Y_{12}^{U}	$\sqrt{GPa}$	0.045
R_0	GPa	0.024
β	-	2.36
m	-	0.64
E_{22}^{0}	GPa	10.8
Y_{22}^{0}	$\sqrt{GPa}$	0.0076
Y_{22}^{c}	$\sqrt{GPa}$	0.12
Y_{22}^{U}	$\sqrt{GPa}$	0.02
b	-	2.6
A	-	0.33

Table 6.2 Perfect interlaminar properties

Property	Unit	Value
G_{IC}	J/mm2	0.2035
σ_{Ist}	GPa	5.263
σ_{Ipr}	GPa	0.5263
E_0	GPa	39
G_{IIC}	J/mm2	1.51
σ_{IIst}	GPa	20.5
σ_{IIpr}	GPa	2.05
G_0	GPa	26.7
h_{cont}	mm	0.15

6.2.1.3 Model validation

6.2.1.3.1 Validation of 0° model

Simulation and experimental results were extracted and compared to validate the methodology developed for the introduction of fibre cut defects in the structure as well as the chosen material properties. The comparison between experimental and simulation force against displacement results for the $[0°]_{16}$ intact and defective specimens is presented in Figure 6.3 and Table 6.3. Figure 6.3 shows that the simulated intact and defective cases are in good agreement with the respective experiments. The average difference per data point between the experimental and modelling results for the intact composite is 2.8 kN, whilst for the results of the composite with the fibre cut defects the average difference was 4.4 kN. The non-linearity of the experimental plots is attributed to the strain gauge. Comparison between intact and fibre cut results show that the maximum force drop is 24.7% for the case of the model in comparison to the experimental results which led to a drop of 20.1%. Overall, the experimental response of the

$[0°]_{16}$ intact specimens and with fibre cuts was reproduced and confirmed the methodology for fibre cut introduction in the structure.

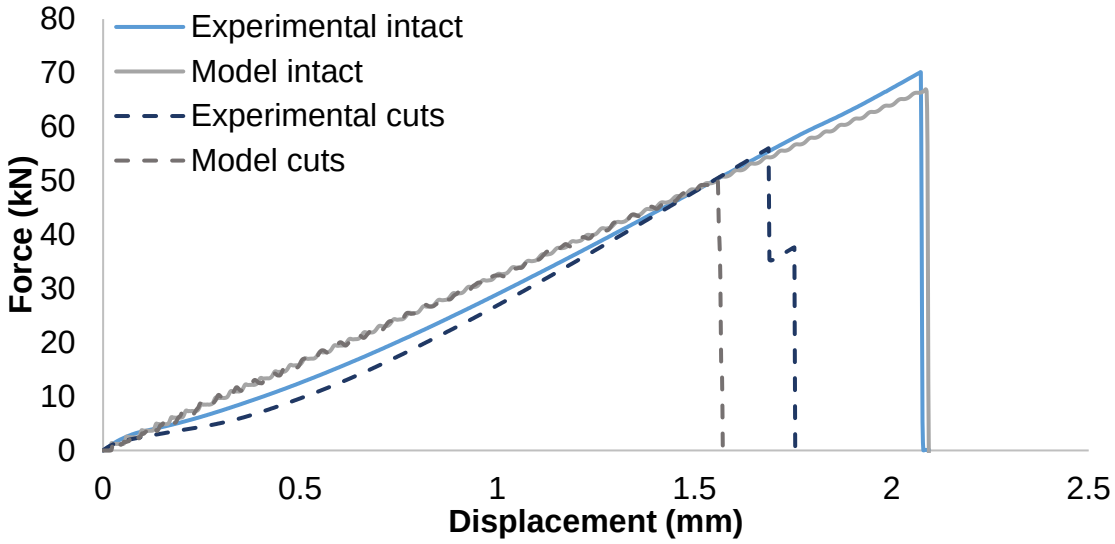

Figure 6.3 Average force-displacement of $[0°]_{16}$ intact specimens and with fibre cuts

Table 6.3 Maximum force-displacement results of $[0°]_{16}$ intact specimens and with fibre cuts

0°	Intact		Fibre cuts		Force drop (%)
	Displacement (mm)	Force (kN)	Displacement (mm)	Force (kN)	
Model	2.1	67.0	1.6	50.4	24.7
Experimental	2.1	70.2	1.7	56.0	20.1

An investigation on the failure mechanisms developing during loading was carried out. The model and damage evolution results are presented in Figure 6.4. Fibre damage initiates at the defective areas. The increase of loading leads to damage initiation at areas around defects at which the failure mechanisms of fibre and matrix damage are dominant. Their combination with matrix transverse and delamination leads to ultimate failure of the specimen.

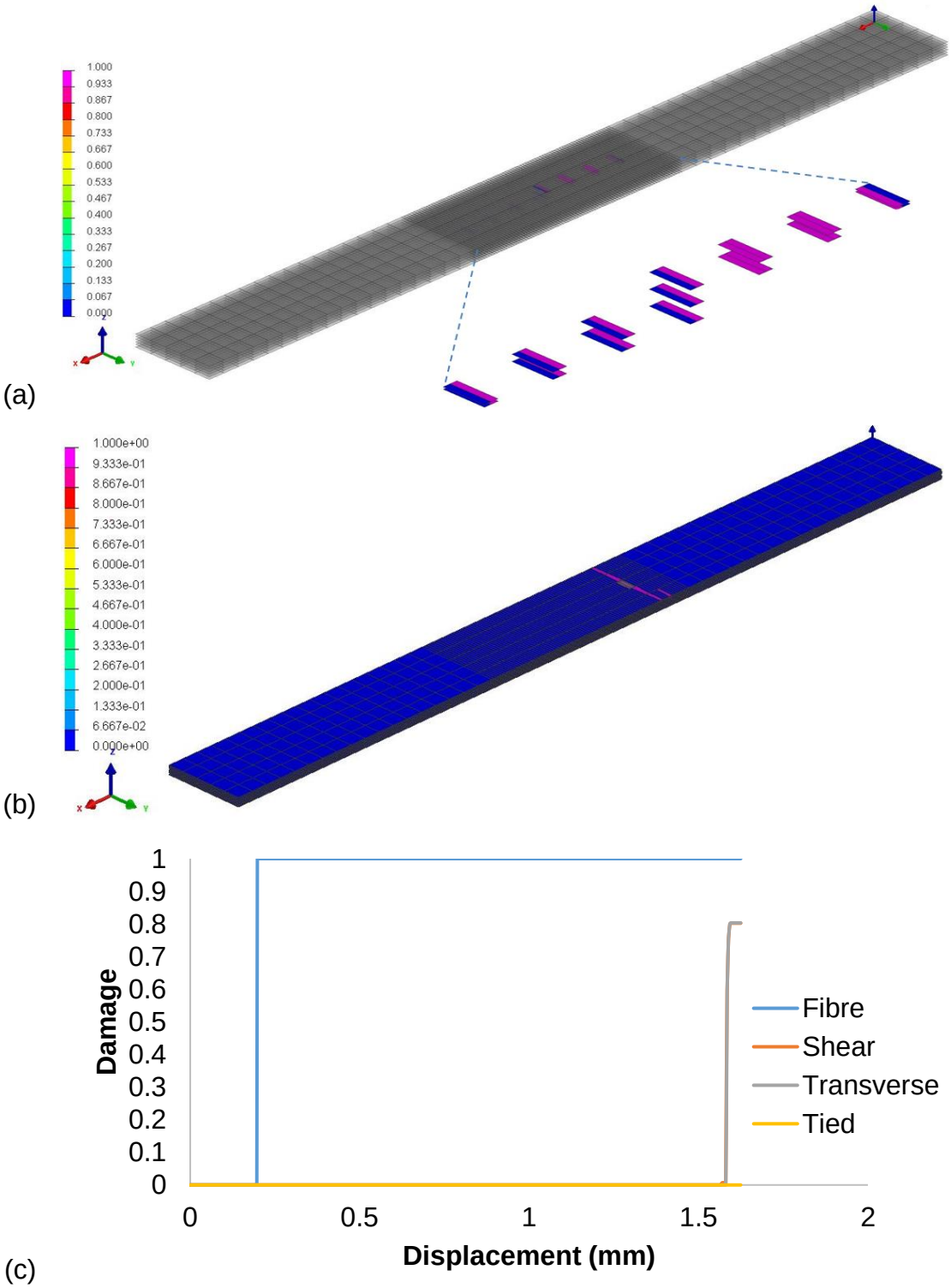

Figure 6.4 (a) Fibre damage developing on defects at 6.9 kN, (b) fibre damage around defects at the 12th layer at 50.5 kN and (c) damage evolution on defective shell at 12th layer of $[0°]_{16}$ specimens with fibre cuts. The colour maps represent fibre damage factors.

XCT scanning of a tested specimen with defects was performed and correlated to the damage mechanisms observed through simulation. The results, as illustrated in Figure 6.5 indicate that failure occurred around the embedded fibre cuts. An “S” shaped failure pattern is evident proving that the embedded fibre cut damage dominated the rupture of the specimen. Due to the separation and lack of certain layers it is safe to assume that matrix damage did also contribute towards failure. These observations prove the validity of the simulated model.

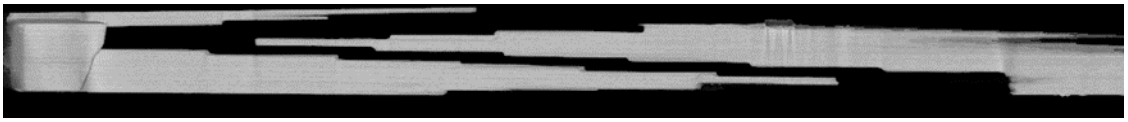

Figure 6.5 Representation of “S” shape defects from XCT results on $[0°]_{16}$ specimen with fibre cuts

6.2.1.3.2 Validation of ±35° model

Comparison between the simulation against experimental response of the $[\pm35°]_{4s}$ intact and defective cases was carried out. The results of force against displacement are presented in Figure 6.6 and Table 6.4.

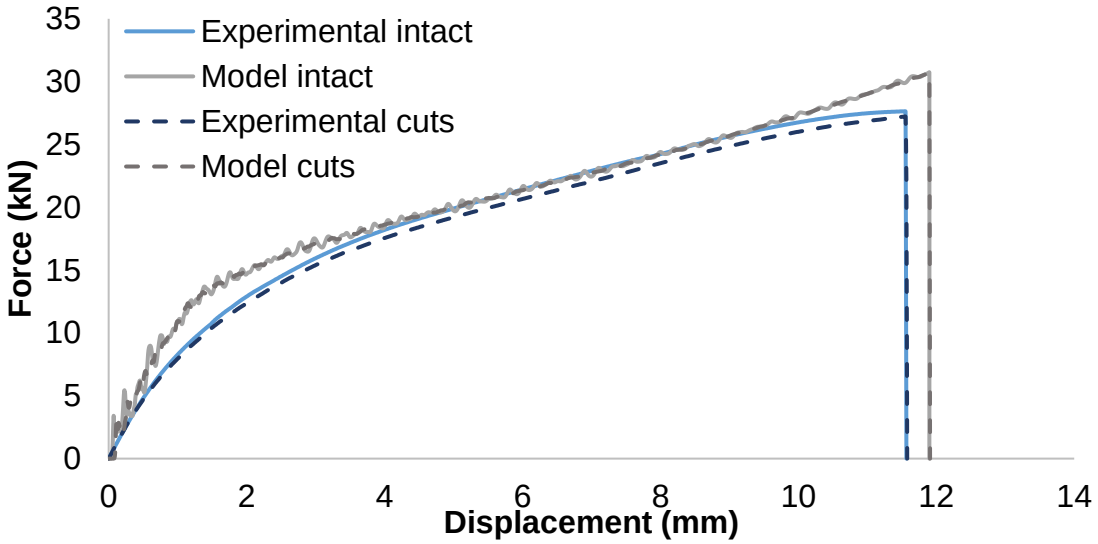

Figure 6.6 Average force-displacement of $[\pm35°]_{4s}$ intact specimens and with fibre cuts

Table 6.4 Maximum force-displacement results of $[\pm 35°]_{4s}$ intact specimens and with fibre cuts

±35°	Intact		Fibre cuts		Force drop (%)
	Displacement (mm)	Force (kN)	Displacement (mm)	Force (kN)	
Model	11.9	30.7	11.9	30.7	0.2
Experimental	11.5	27.6	11.5	27.2	1.5

Based on the results in Figure 6.6 the experimental and modelling response are in good agreement. The average force difference per data point between the experimental and modelling results for the intact case is 0.8 kN in comparison to the fibre cut defective cases where the average difference is 1.4 kN. The introduction of the fibre cut defects on ±35° tensile specimens did not affect the force-displacement results as observed experimentally and proved through simulation. In fact, the drop of maximum force of intact specimens compared to the fibre cut defective specimens based on the experimental results is 1.5%, whilst through simulation the drop was found to be 0.2%. The results indicate that the presence of fibre cut defects in the structural design can lead to minimal alteration of the off axis mechanical response of the system. The design of the surrounding area of the defects has a significant role on the development of failure mechanisms from the defective areas that can contribute to the ultimate failure of the structure. Factors that can affect the way the fibre cut defects act are, apart from the type of the fibres and the matrix, the fibre and load orientation, the orientation of the cut with respect to the fibre orientation and the fibre cut design pattern, which involves the size of the defects and the intervals between them.

The failure mechanisms and damage evolution were investigated based on the simulation results. Matrix shear damage starts at the defective fibre cut areas, which is accompanied by shear damage in the middle around the defects and the edges of the specimen. The development of transverse, fibre damage and delamination occurs at a later stage during loading. The failure mechanisms, as well as the damage development at the defects and the surrounding areas are illustrated in Figure 6.7.

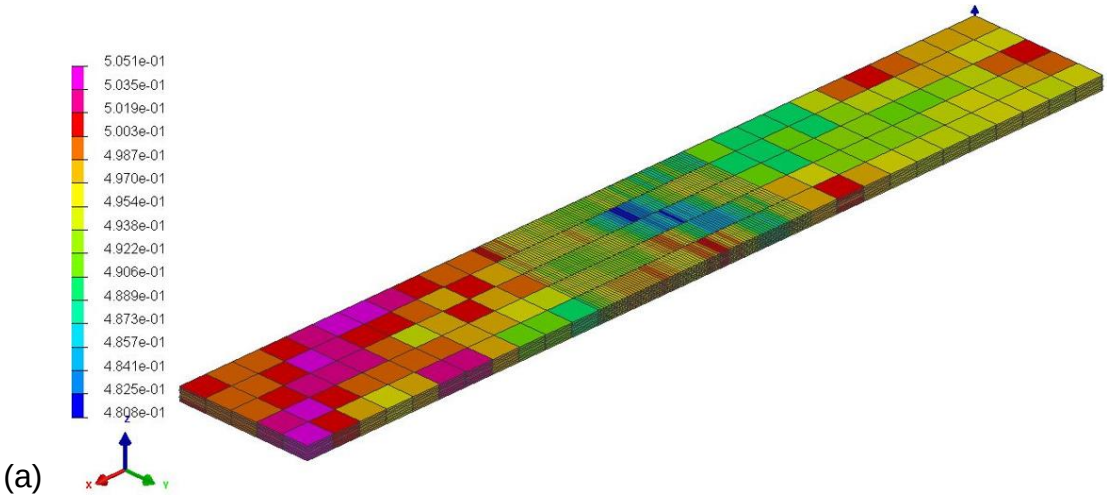

(a)

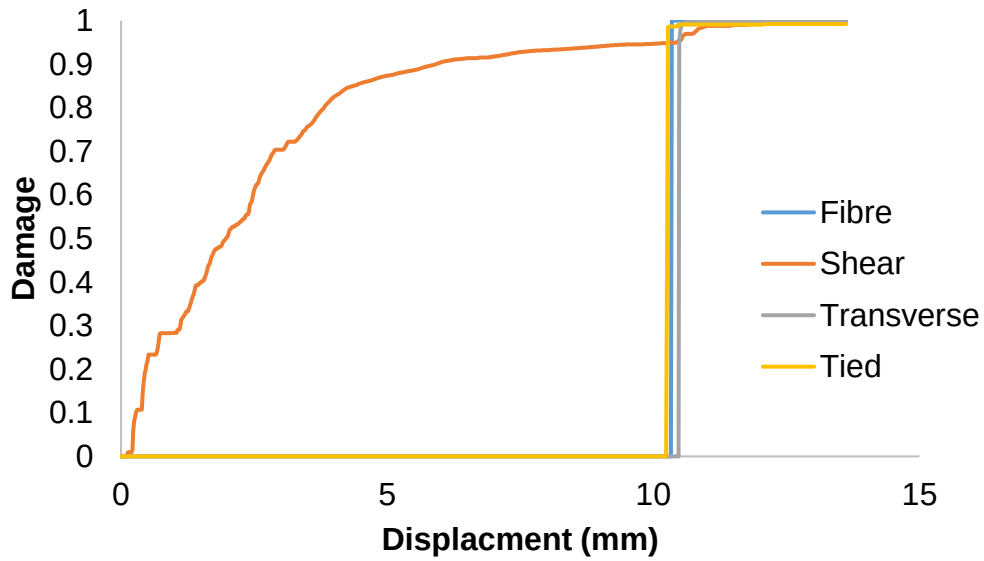

(b)

Figure 6.7(a) Matrix shear damage developing on specimen at 12.7 kN and (b) damage evolution on defects at the 14th layer of $[\pm 35°]_{16}$ specimens with fibre cuts. The colour map represents matrix shear damage factor.

The results of XCT scanning on a ruptured defective specimen are presented in Figure 6.8. As illustrated, the “S” type of defects does not dominate the failure of the specimen. Rupture occurs at the location of fibre cuts at the lower layer of the specimen, but this does not follow the fibre cut path. It is unsure if the failure initiated at this point. Ultimately, failure took place as fibre, matrix damage as well as delamination, which is in agreement with the simulation results.

Figure 6.8 XCT results on $[\pm 35°]_{16}$ specimen with fibre cuts

6.2.2 Interlaminar weak bond areas

6.2.2.1 Manufacturing process

Weak interface defects were established by embedding pieces of Teflon film in the structure. This type of defect was examined experimentally in combination with fibre cut defects on $[\pm 35°]_{4s}$ tensile specimens. The manufacturing process of the fibre cut and Teflon defective laminate followed the procedure reported in section 6.2.1. During the lay-up of each lamina, a Teflon strip was placed on top of the fibre cut defect occupying the same length of 5 mm as the fibre cuts, whilst their width was 1 mm. Figure 6.9 illustrates the C-scan of the $[\pm 35°]_{4s}$ laminate in which cut and interfacial defects were introduced. The blue areas in the middle of the laminate indicate the location of the defects corresponding to each tensile specimen. The different colouring indicates the existence of poor interface between the layers, which is caused by the Teflon. The tensile testing, which is reported in section 4.3.2.2, followed the experimental procedure.

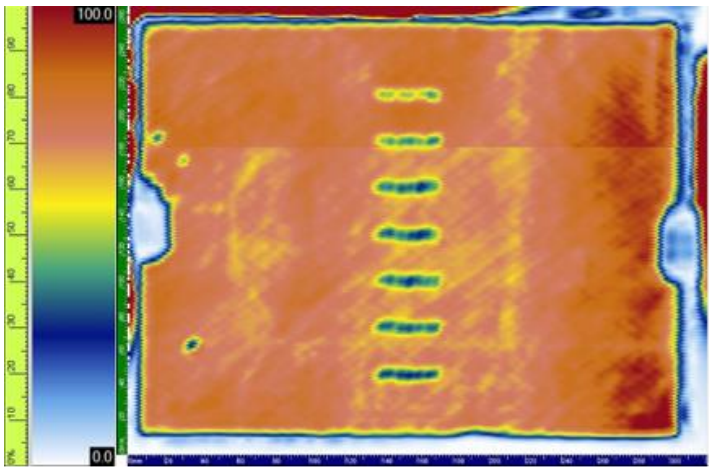

Figure 6.9 C-scan result of $[\pm 35°]_{4s}$ interlaminar weak bond areas

6.2.2.2 Simulation investigation

The $[\pm 35°]_{4s}$ tensile model developed in section 6.2.1.2 was utilised for the introduction of delamination defects. The model was updated with weak interlaminar properties between the areas assigned to fibre cut defects and their neighbouring elements. The rest of the elements and their slave nodes correspond to perfect or real interface properties as described in section 6.2.2.1. The methodology applied for the identification of the properties of the weak interface was based on the deterioration of the properties of the intact/strong interface in order to acquire a weak interlaminar bond. The weak interlaminar properties are presented in Table 6.5. Based on an exploratory investigation, the normal and shear moduli were decreased by a factor of 0.1, whilst the strength and strain energy release rate values were decreased by a factor of 0.001. The contact thickness was considered to remain constant. The boundary and loading conditions applied on the model remained the same as for the investigation of intact and fibre cut defective specimens.

Table 6.5 Weak interlaminar properties

Property	Unit	Value
G_{IC}	J/mm2	2.035E-7
σ_{Ist}	GPa	5.263E-6
σ_{Ipr}	GPa	5.263E-7
E_0	GPa	0.39
G_{IIC}	J/mm2	1.51E-6
σ_{IIst}	GPa	2.05E-5
σ_{IIpr}	GPa	2.05E-6
G_0	GPa	0.267
h_{cont}	mm	0.15

6.2.2.3 Model validation

The force against displacement experimental and simulation results for the $[\pm 35°]_{4s}$ specimens involving cut and interfacial defects are presented in Figure 6.10 and Table 6.6. The results of Figure 6.10 indicate that the modelling response of the defective specimen is not in close agreement with the experimental results with a calculated average difference per data point of 2.45 kN. The force versus displacement plot of the model of the specimen with cut and interfacial defects shows a force plateau at approximately 22 kN. This is not the case for the experimental response of the specimen of which the force reaches a maximum of 31 kN approximately, before its abrupt drop. Based on Table 6.6, the experimental results show a force reduction of 16.9% between intact and cut and Teflon defective specimens, whilst the simulation results show a minimal drop of 0.13%. Recalling the results of section 6.2.1.3.2, the existence of fibre cut defects as the only type of defect on the $[\pm 35°]_{4s}$ specimen led to minimal force drop of 0.16% and 1.5% based on simulation and experimental investigation respectively. Therefore, the observed force reduction between intact and defective experimental results highlight the importance of the Teflon introduction for the reduction of the force response. The deviation between the experimental and simulation results of the cut and interfacial defective case is considered to occur due to the fact that delamination damage is not coupled to other modes of damage, including shear, in the model.

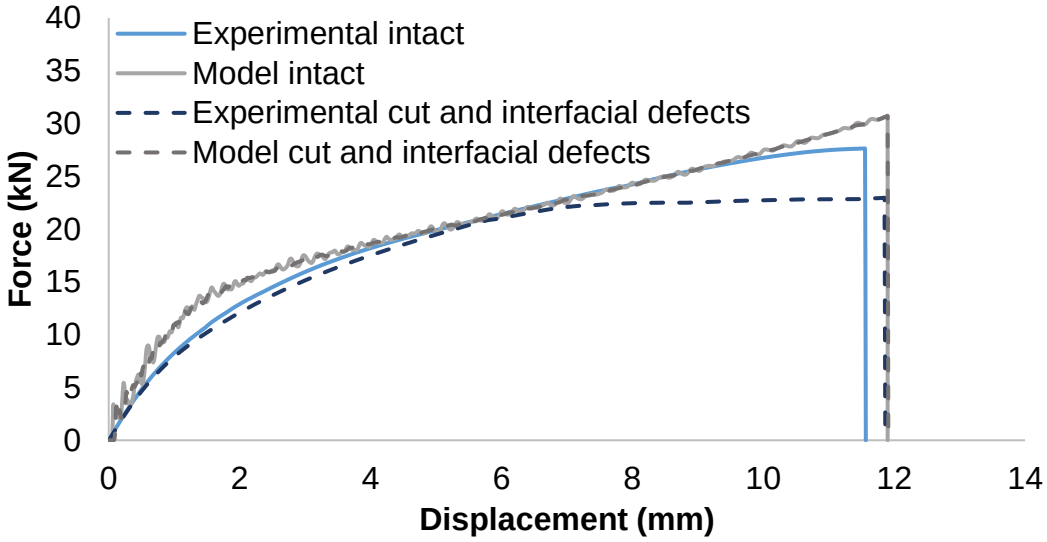

Figure 6.10 Average force-displacement of $[\pm 35°]_{4s}$ intact and with cut and interfacial defects specimens

Table 6.6 Maximum force-displacement results of $[\pm 35°]_{4s}$ intact and with cut and interfacial defects specimens

±35°	Intact		Interfacial defects		Force drop (%)
	Displacement (mm)	Force (kN)	Displacement (mm)	Force (kN)	
Model	11.9	30.7	11.9	30.7	0.1
Experimental	11.5	27.6	11.8	23.0	16.9

The failure mechanisms taking place as well as the damage development during loading are presented in Figure 6.11. The simulation results indicate behaviour similar to the ±35° model with fibre cut defects presented in 6.2.1.3.2. However, the interfacial damage introduced leads to delamination initiation alongside matrix shear damage. The areas surrounding the defects develop shear damage; however, delamination as well as fibre and transverse damage take place at a later stage leading to ultimate failure.

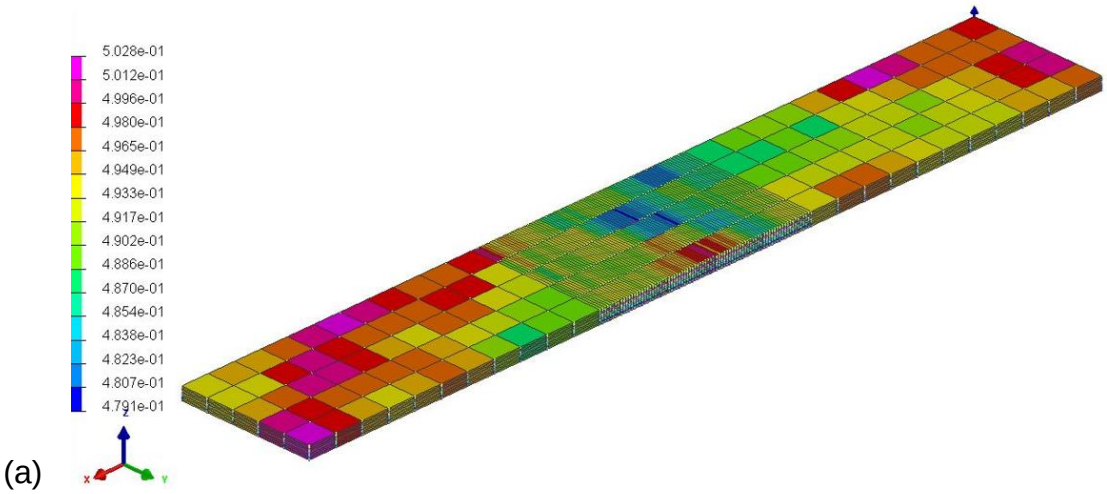

(a)

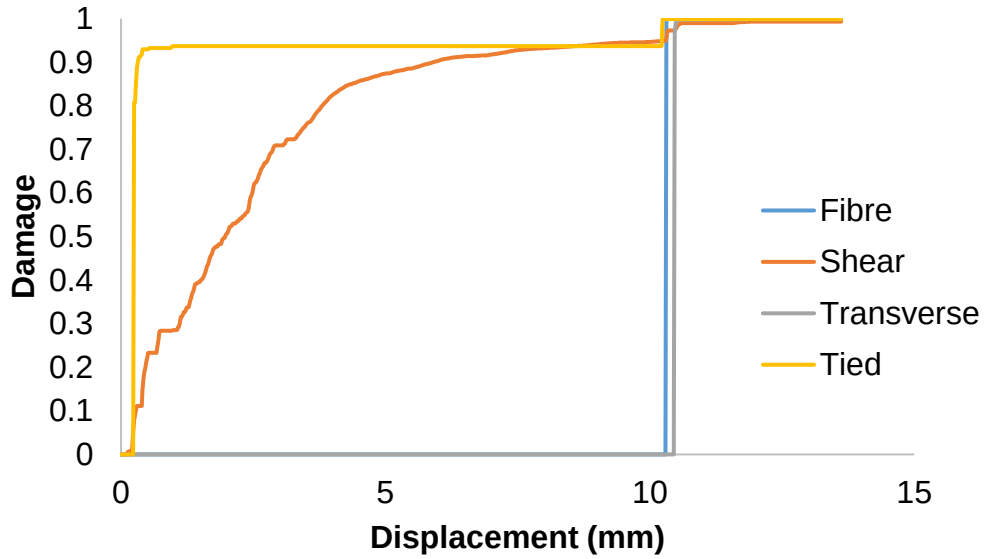

(b)

Figure 6.11(a) Matrix shear damage developing on specimen at 14.7 kN and (b) damage evolution on defects at the 14th layer of $[\pm 35°]_{16}$ specimens with fibre cuts and Teflon. The colour map represents matrix shear damage factor.

7 Simulation and design of leak-before-break response

This chapter focuses on the simulation of the leak-before-break concept on CPVs that aims to establish a controllable and predictable way of failure preventing catastrophic events. This involves the simulation of intact pipes and pipes with weak regions for the investigation and selection of most suitable defect types and design patterns that result in the desirable LBB behaviour.

7.1 Leak-before-break methodology

The LBB concept is based on the development of a detectable leakage on CPVs and pipes that will act as warning prior to their catastrophic failure. The success of the concept hinges on an adequate delay between the incident of leakage and the final rupture, which can provide sufficient time for reaction in an evacuation event or repair/replacement of the pressurised system. In this work, the focus is set on the establishment of two leakages/ruptures in the composite tubular vessel and the development of a design approach that results in significant separation of their occurrence. The first leakage represents the feature of failure detection. It occurs due to the existence of defects deteriorating the structural integrity of the vessel locally and its development is accompanied by pressure relief. The manifestation of the second leakage is associated with additional deterioration of the intact structure and its inability to further withstand the pressurised fluid. The second leakage represents the catastrophic rupture or burst of the structure. The leak development and propagation in the cylindrical model is based on an assumption of a minimum threshold damage percentage of 50%. This required the acquisition of 50% damage or more from all the shells through the thickness at a certain location to signify the occurrence of leakage. The first two leakage appearances were investigated for all cases for the shell elements of each layer of the cylindrical model. The cases in which adequate delay between the occurrence of the first and second fracture occurred are considered relevant for the development of the LBB concept.

The methodology followed for the development of the LBB concept involved intact tubular vessel simulation for the identification of maximum burst pressure providing control information. Two models of the intact pipe were simulated; one

comprising one shell and one with two shells through the thickness. This provided information on the durability of the interface by direct comparison of the one and two shell model and set the ground for investigations on its effect when defects are introduced in the two cylindrical sub- laminas, as well as between them. The interface of the mid-plane was tied by implementing the real out-of-plane data that were presented in Table 5.5 with an updated contact thickness of 1.2 mm corresponding to half of the composite cylinder thickness of 2.4 mm. In this way, the outer layer of the inner shell theoretically coincides with the inner layer of the outer shell. Interfaces that do not belong to the mid-plane were treated as perfect, based on the methodology described in section 6.2.1.2. The comparison indicated that the two shells model lost accuracy by 4.5% compared to the one shell model, which is due to the interface separation. Acknowledging the small inaccuracy introduced, the two shells model was utilised for the investigation of the LBB concept through the development of an effective defect design pattern.

Areas of investigation for the development of the cylindrical model were also the loading rate, as well as the boundary and loading conditions. The loading rate was examined in order to reduce the computational time without incorporating inertia effects. It was found that inertia effects of approximately 6% were incorporated by introducing a loading rate of $4\ 10^6$ bar/min, which was considered a good compromise for the simulation studies. In CPVs subjected to internal pressurisation, stresses and strains act in both the axial and hoop direction in a ratio of 2:1. In this work, the composite pressure vessel is represented through a cylinder in which end caps are attached on both ends. In order for the two shell cylindrical model to account for the behaviour of a CPV, boundary conditions were applied on the edge nodes of the two cylindrical shells by restraining movement in the y and z axes, as well as rotation around the x axis. Internal pressure was applied only on the inner face of the shell at the interior and not on both cylindrical shells of the model. The pressure load was also translated into force applied on the edge nodes of the two cylindrical shells, which was distributed to the surrounding nodes of the edges in the case finer mesh was required. The application of internal pressure on the inner face of the cylindrical shell at the interior of the model, as well as its translation into force to account for

the end caps, was verified by comparison of the simulation results to the one shell model and through analysis.

The simulation studies for the development of the LBB behaviour involved the investigation of two types of defects, as described in Chapter 6, as well as of the amount of damage they introduce and the incorporation of additional design features. The investigation was based on the following:

- Fibre cut damage;
- Reinforcing patch thickness;
- Interfacial defects;
- Combination of types of defects.

A series of fibre cut damage levels was investigated. This involved the introduction of fibre cut damage of 0, 12.5, 25, 37.5, 50, 62.5, 75, 87.5 and 99% at a pre-specified location in the structure (section 7.2.2, 8.1) following the methodology developed in Chapter 6. According to this, the only deteriorated mechanical properties due to the introduction of fibre cut defects are the initial and ultimate damage strains in the fibre direction. The calculated properties with respect to the fibre cut damage are presented in Table 7.1. These were assigned to the pre-specified location to account for the deteriorated properties of the defective area.

The addition of a patch in the structural design aimed to provide distinctive separation between the first and second leakage for the development of the LBB concept. The study was carried out for the incorporation of three patches with thickness comprising 2, 4 and 8 layers with lay-up of $[\pm 55°]$, $[\pm 55°]_s$ and $[\pm 55°]_{2s}$, respectively. The material properties assigned to the patch for all three cases were the same as for the tubular vessel (Table 5.5-Table 5.6). The addition of the patch in the composite cylindrical structure was performed considering perfect interfacial properties, in order for the focus to be on its effect as a feature to separate the two leak incidents. Further optimisation of the design of defects was carried out through exploration of its shape, which varies between rectangular and circular. The use of circular shape defective area aims towards the

acquisition of highly accurate results through the reduction of the stress concentration introduced by the corners of the rectangular shape.

Table 7.1 Strain values for fibre cut percentages

Fibre cuts (%)	ε_i (-)	ε_u (-)
0	0.0142	0.0152
12.5	0.0124	0.0133
25	0.0107	0.0114
37.5	0.0089	0.0095
50	0.0071	0.0076
62.5	0.0053	0.0057
75	0.0036	0.0038
87.5	0.0018	0.0019
99	0.0001	0.0002

Investigation of interlaminar weak bond areas, as well as of the combination of different types of defects and patterns is also of prime interest. The simulation of interfacial defects provides information on the interfacial damage distribution to the surrounding material in the structure thus contributing to the ultimate failure of the cylindrical structure. Additionally, information on the interaction between fibre and interfacial damage evolution can be extracted.

7.2 Implementation of simulation of CVPs incorporating LBB designs

The types of defects studied were fibre cuts and artificial interfacial defects between adjacent layers and a combination of those. Square and cylindrical shape weak regions were examined. An investigation on the addition of a design feature was also carried out. The most suitable design pattern was selected for the development of the LBB concept on a composite pipe subjected to internal pressurisation.

7.2.1 Intact cylindrical model simulation

The simulation of the CPV involved the design of a composite cylinder. The cylinder contains two shells through the thickness. The diameter of the inner shell is 104.5 mm, whilst the outer shell diameter is 106.9 mm. The contact thickness between the two cylindrical shells is 1.2 mm. The mesh size of the two shells is 4x4 mm^2 providing 12300 elements and 12464 nodes for both shells in total. Each of the two shells contains four layers with thickness of 0.3 mm each. The lay-up sequence of the inner shell is [+55°/-55°/+55°/-55°], whereas the outer shell stack is [-55°/+55°/-55°/+55°]. The material properties assigned to the shells were the in-plane intact properties of the constitutive model summarised in Table 5.6. The two shells are tied as presented in Figure 7.1(a) through implementation of the interfacial properties of Table 5.5 with contact thickness of 1.2 mm. End cap boundary conditions were applied on the edge nodes of both shells, as described in section 7.1, restraining movement in the y and z axes as well as rotation around the x axis. A pressure rate of 4 10^6 bar/min was applied on the inner face of the internal shell and a load rate of 21400 kN/min on each of the 82 nodes of both cylindrical shells of the edges to account for the end caps as illustrated in Figure 7.1(b). The simulation was carried out until the ultimate failure of the tubular vessel.

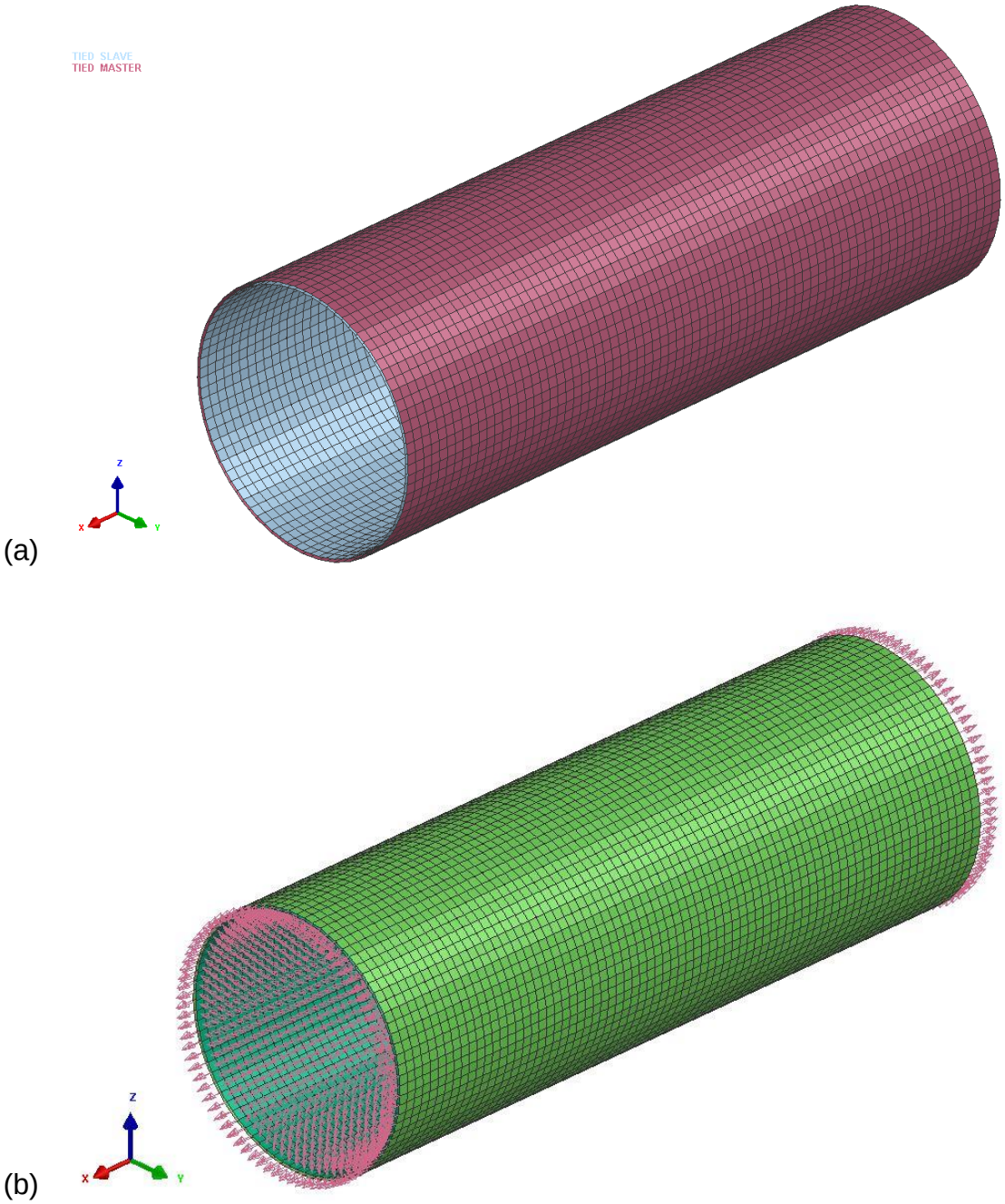

Figure 7.1 Composite cylindrical model with representation of (a) tied interface and (b) pressure and force application

The results indicate that damage takes place at the edges of the cylindrical model. If this damage is neglected in order to identify the failure occurring in the middle of the pipe, this takes place at pressure of 509 bar. The failure mechanisms acting towards the rupture of the system consist of delamination and

matrix shear damage. Figure 7.2 shows the cylindrical model under pressure and the locations of rupture with light blue colour. The damage evolution at a layer in the middle of the pipe with respect to pressure is also illustrated.

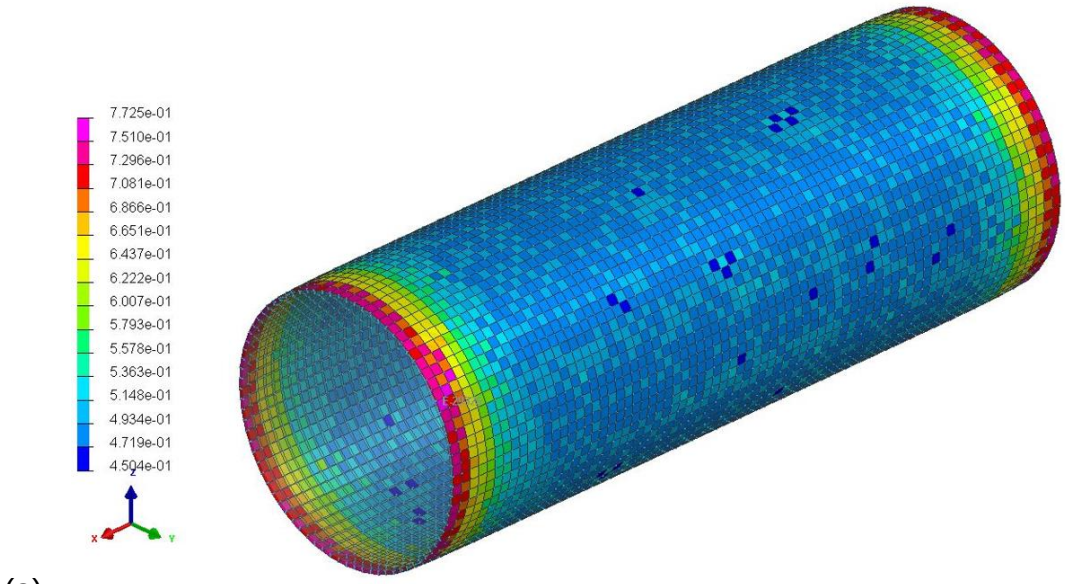

(a)

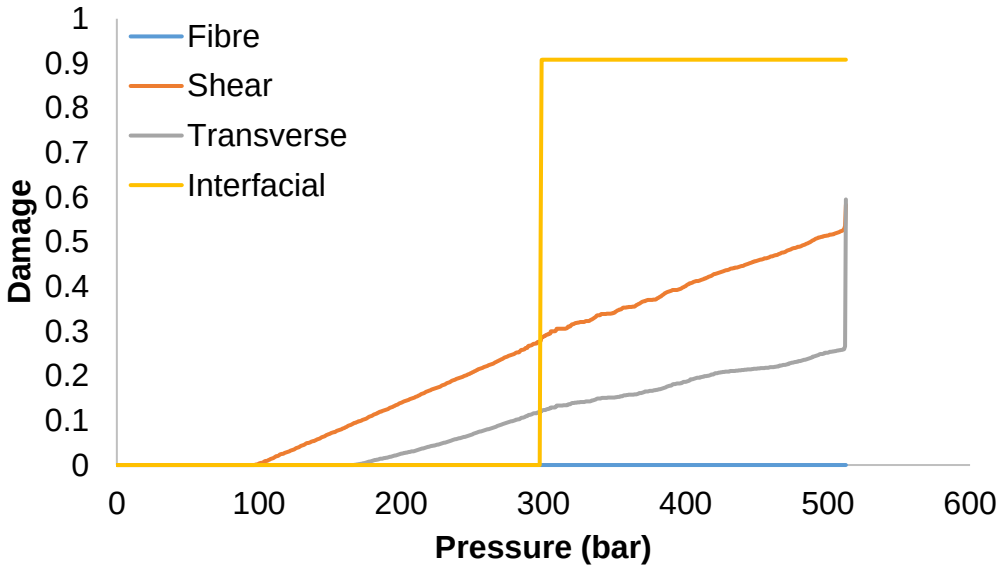

(b)

Figure 7.2 Composite cylindrical model (a) failure response under internal pressurisation at 509 bar and (b) damage development at shell from the middle of the pipe. Colour map represents the matrix shear damage factor.

7.2.2 Description of models for LBB concept

The development of the LBB concept was based on the simulation of pipes with weak regions. Various cases of types of defects and design patterns are examined in this section taking into account geometry and shape effects.

7.2.2.1 Fibre cuts

The composite cylindrical model presented in section 7.2.1 was utilised for the implementation of defects. For efficiency in computational time, the element mesh size applied to the two shells was refined to 8x8 mm^2 and 2x8 mm^2 for the elements of the edges leading to the formation of 3198 elements and 3280 nodes. A square area of 8x8 mm^2 was selected in the middle of both composite cylindrical shells to accommodate defects. The elements of this area and their coinciding elements in the hoop and longitudinal direction were split into smaller 4x4, 8x4 and 2x4 mm^2 elements to increase the accuracy of the results as illustrated in Figure 7.3. This led to the creation of a total of four more nodes at the edges of the two cylindrical shells and a total of 3526 nodes and 3440 elements. The two cylindrical shells with the exception of the defective shells incorporated the in-plane intact properties of the constitutive model summarised in Table 5.6. The material properties designated for the defective area were those defined in Table 7.1. The two cylindrical shells including the defective shells were tied using the out-of-plane properties of Table 5.5 with contact thickness of 1.2 mm. The surface of the inner cylindrical shell consisting of both defective and non-defective elements was subjected to internal pressure at a rate of 4 10^6 bar/min. The force applied to the edge nodes of the two cylindrical shells to account for the end caps was redistributed to include the nodes created due to the refinement of the mesh to accommodate the elements of the defective area. The force corresponding to the equally distributed 2x8 mm^2 nodes is 42800 kN/min. The nodes at the edges of the refined mesh 2x4 mm^2 correspond to force of 32100 kN/min, whilst the three intermediate nodes to 21400 kN/min.

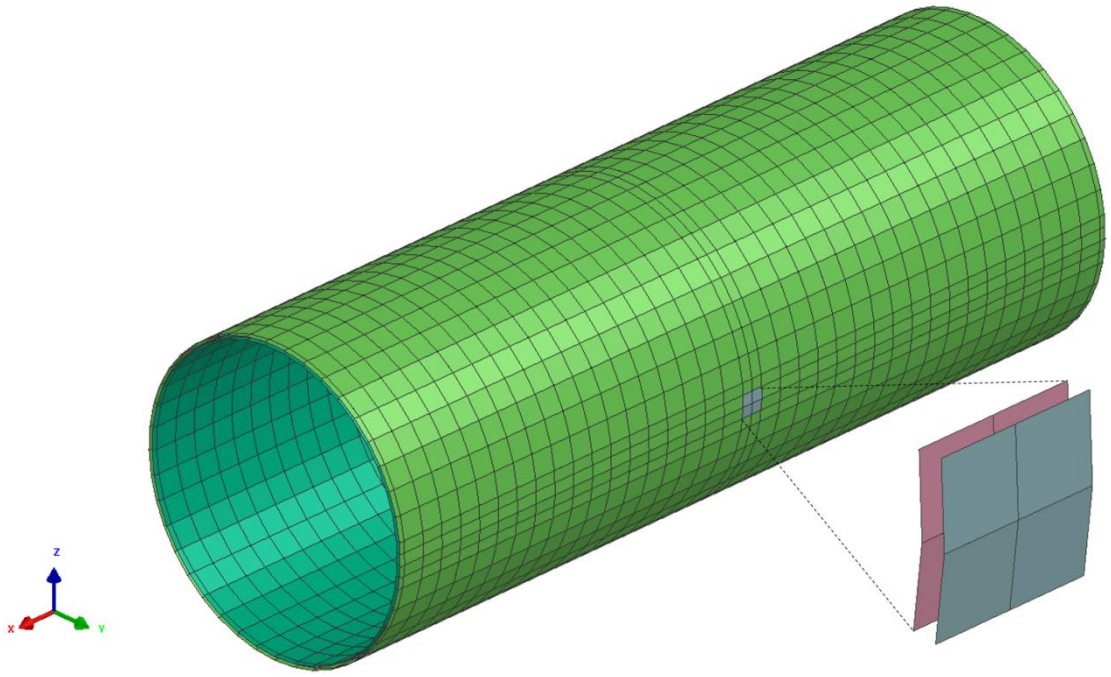

Figure 7.3 Tied two-shell meshed composite cylindrical model with square shape fibre cut defective area

7.2.2.2 Fibre cuts and patch

An additional design feature was considered in the model presented in section 7.2.2.1 as a solution to enhance the separation and delay of occurrence of the second leakage with respect to the first leakage. This involves the incorporation of a patch surrounding but not covering the defective area, as illustrated in Figure 7.4. The composite patch was created as an external curved shell at a distance of 1.2 mm from the outer cylindrical shell of the composite pipe. The size of the patch was set to six times the size of the defective area in order to provide sufficient enhancement of the structural integrity of the intact area surrounding the defects. The dimensions of the patch were 48x48 mm^2 with a hollow centre of 8x8 mm^2 leaving the defective area uncovered. The patch consisted of 80 nodes and 60 elements at a size defined based on the outer and inner cylindrical shell elements as well as by the size of the patch. In total, the model comprised 3778 nodes and 3672 elements. The patch shell elements were tied to the respective external cylindrical shell nodes using the perfect interfacial properties reported in Table 6.2 in order to ensure that the bond between the adjacent layers of that area was ideal. The thickness of the patch was investigated considering

the addition of two, four and eight layers of SE84LV carbon prepreg material with lay-up of [±55°], $[\pm 55°]_s$ and $[\pm 55°]_{2s}$, respectively. The material properties assigned to the three patch types were the same as for the intact pipe, presented in Table 5.5 and Table 5.6.

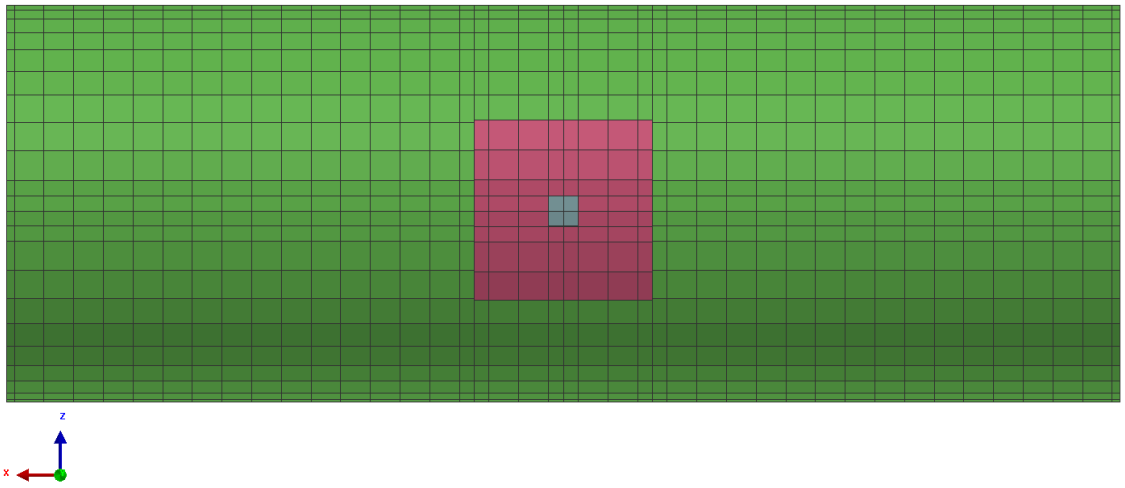

Figure 7.4 Square shape fibre cut defective area with patch

The square defective area was updated to a circular shape in order to reduce stress concentration at corner points. The circular defective area has a diameter of 8 mm in accordance to the 8x8 mm^2 square defective area. The circular shape defective area consists of 192 quadratic elements and 217 nodes for each of the inner and outer cylindrical shell. The mesh of the pipe around the circular defective area was restructured. The mesh consists of five rings which achieve the circular shape of the defective area as illustrated in Figure 7.5. The shape of the rings gradually takes the shape of squares in order to meet the square mesh shape of the rest of the cylinder.

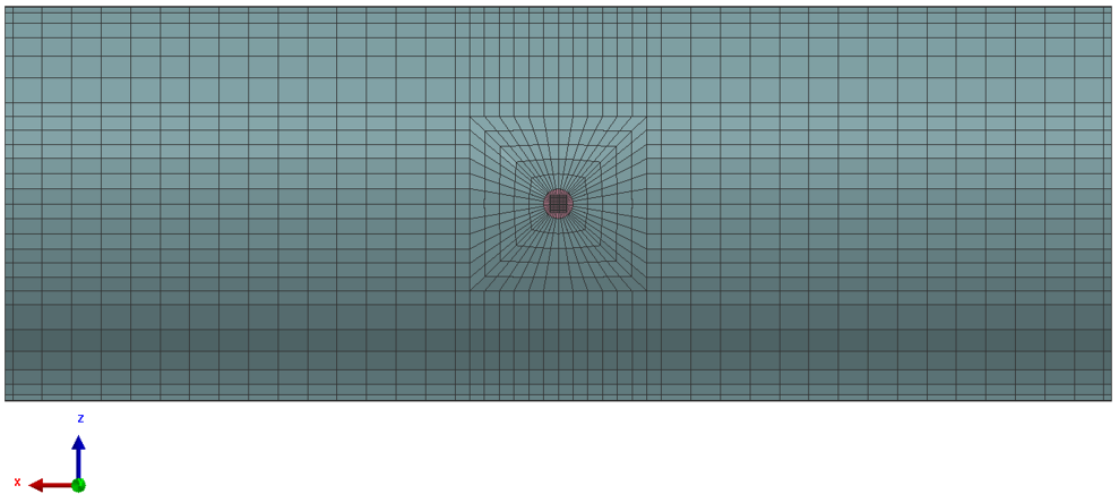

Figure 7.5 Design of circular shape fibre cut defective area

The design and mesh of the patch were also updated in order to be in agreement with the circular defective area and the refined mesh of its surrounding area. The design of the patch for the circular shape defects remains a square of 48x48 mm^2, as presented in Figure 7.6. In total the model consists of 5232 elements and 5376 nodes.

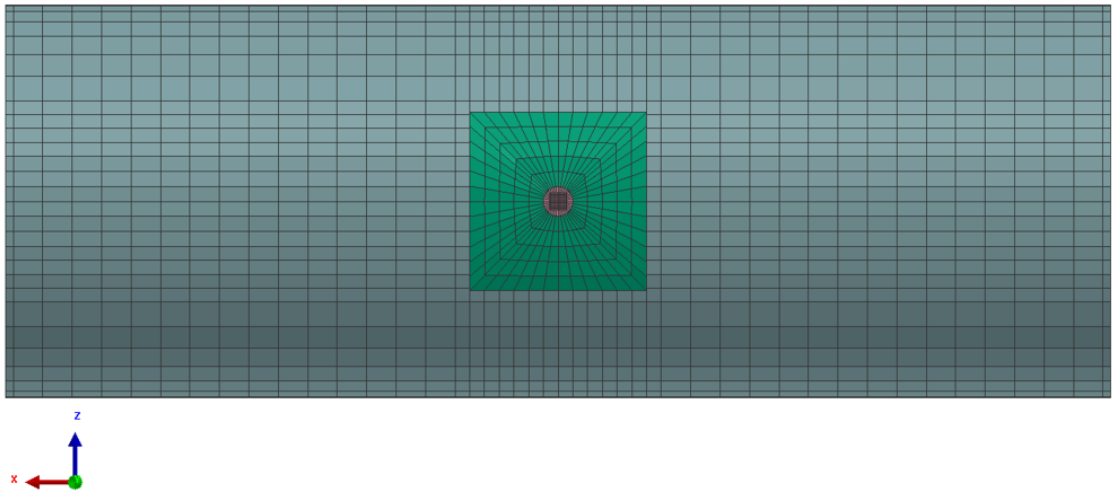

Figure 7.6 Design of four layer patch of circular shape fibre cut defective area

7.2.2.3 Interfacial defects

The cylindrical model of section 7.2.2.1 was utilised for the introduction of areas with interfacial defects for the development of LBB behaviour. The intact in-plane properties of Table 5.6 were applied to all shell elements of the two cylindrical

shells. A square area of 8x8 mm^2 consisting of four shells with mesh size of 4x4 mm and located in the middle of the two cylindrical shells was selected, as illustrated in Figure 7.7.

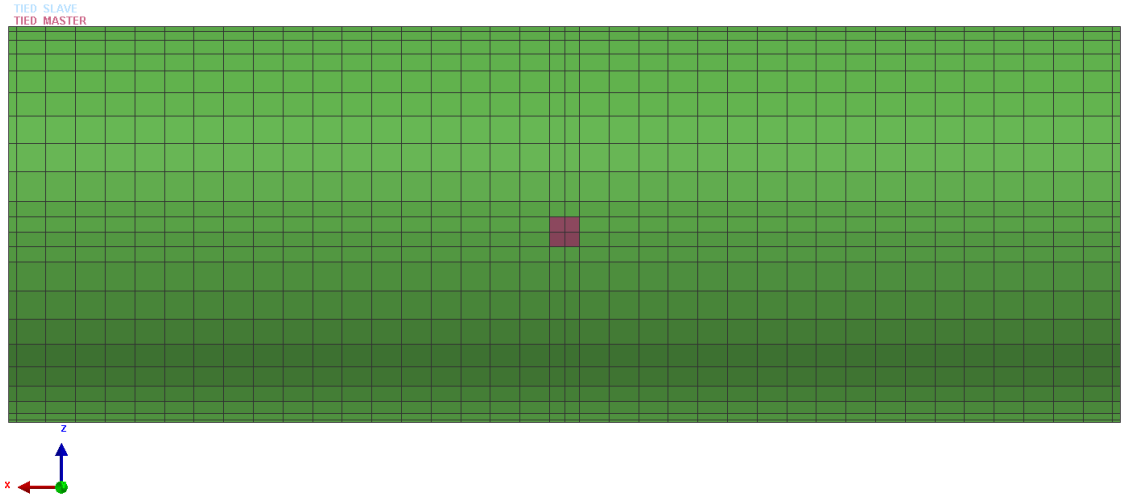

Figure 7.7 Delamination defective area

The deteriorated interfacial properties of Table 6.5 were assigned to the interface of the slave nodes of the four elements belonging to the inner cylindrical shell and the adjacent master elements of the outer cylindrical shell. The rest of the interface between the nodes of the inner cylindrical shell and the master elements of the outer cylindrical shell was defined utilising the real interlaminar properties, which are summarised in Table 5.5 with contact thickness of 1.2 mm.

7.2.2.4 Fibre cuts and delamination

7.2.2.4.1 Neighbouring fibre cut defects connected through interfacial defects

The combination of fibre cut and delamination defects as a mechanism to initiate leakage in the cylindrical model under pressurisation was investigated based on the model described in section 7.2.2.1. The mesh in the middle of the cylindrical shells was refined for accuracy of the results leading to a total of 3698 nodes and 3612 elements. A square area of four 4x4 mm^2 elements was selected from either side of the middle of each cylindrical shell to accommodate the fibre cut defects. As illustrated in Figure 7.8, the fibre cut defective elements of the internal cylindrical shell are represented with red colour and the fibre cut defective elements of the external cylindrical shell with grey. The dark green coloured area

corresponds to the intact elements of the inner cylinder and the intact elements of the external are shown in light green.

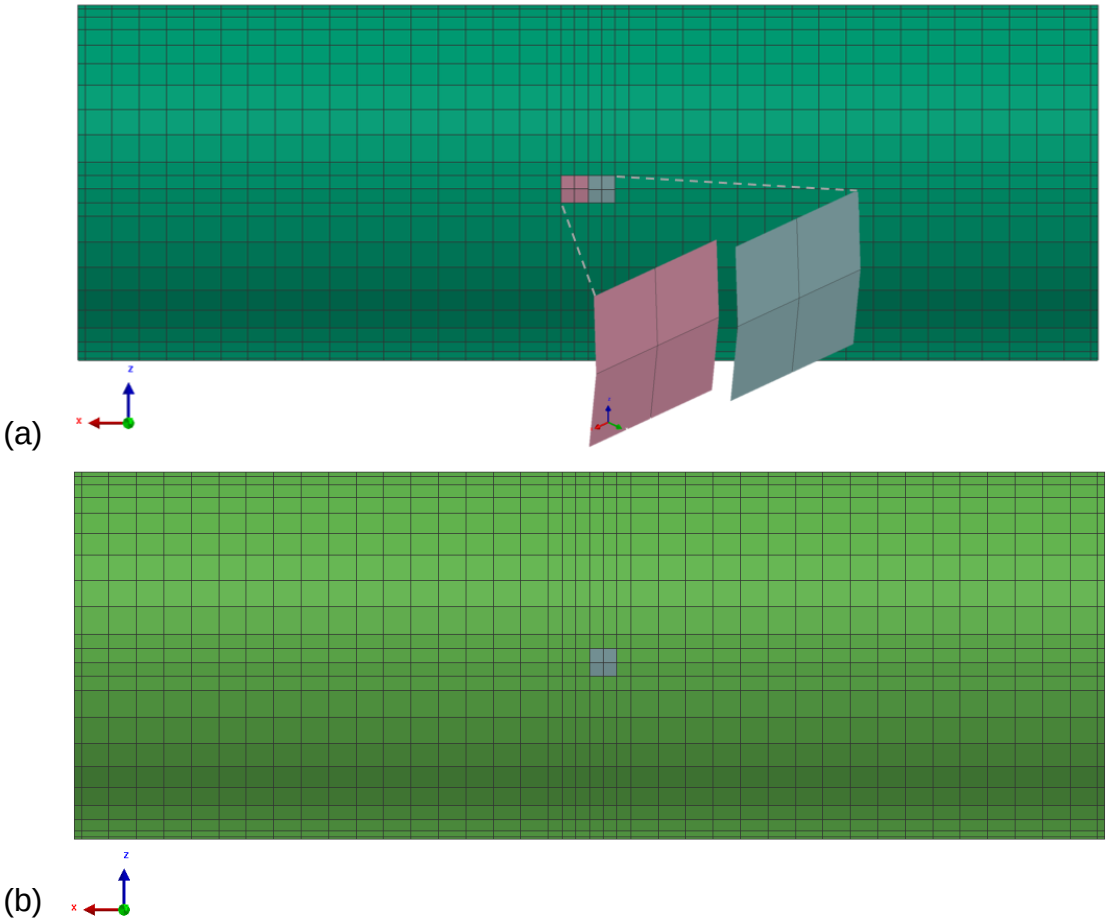

Figure 7.8 Fibre cut defective shells in red and grey colour for the internal and external cylinder respectively, (a) without and (b) with external cylindrical shell

The weak interface properties of Table 6.5 were assigned to four central elements of the inner cylindrical shell and their adjacent elements of the external cylinder. The slave nodes of the weak interface belong to two defective and two intact shells on each side from the middle of the inner cylindrical shell, whilst the master segment consists of their adjacent shell elements of the external cylindrical shell from which two are intact and two defective. This leads to an arrangement of internal intact shells weakly connected to external defective shells, as well as internal defective shells weakly connected to external intact shells. The interface between the rest of the cylindrical shells was assigned the real interface properties of Table 5.5, with contact thickness of 1.2 mm. A representation of the weak and real interfaces is illustrated in Figure 7.9.

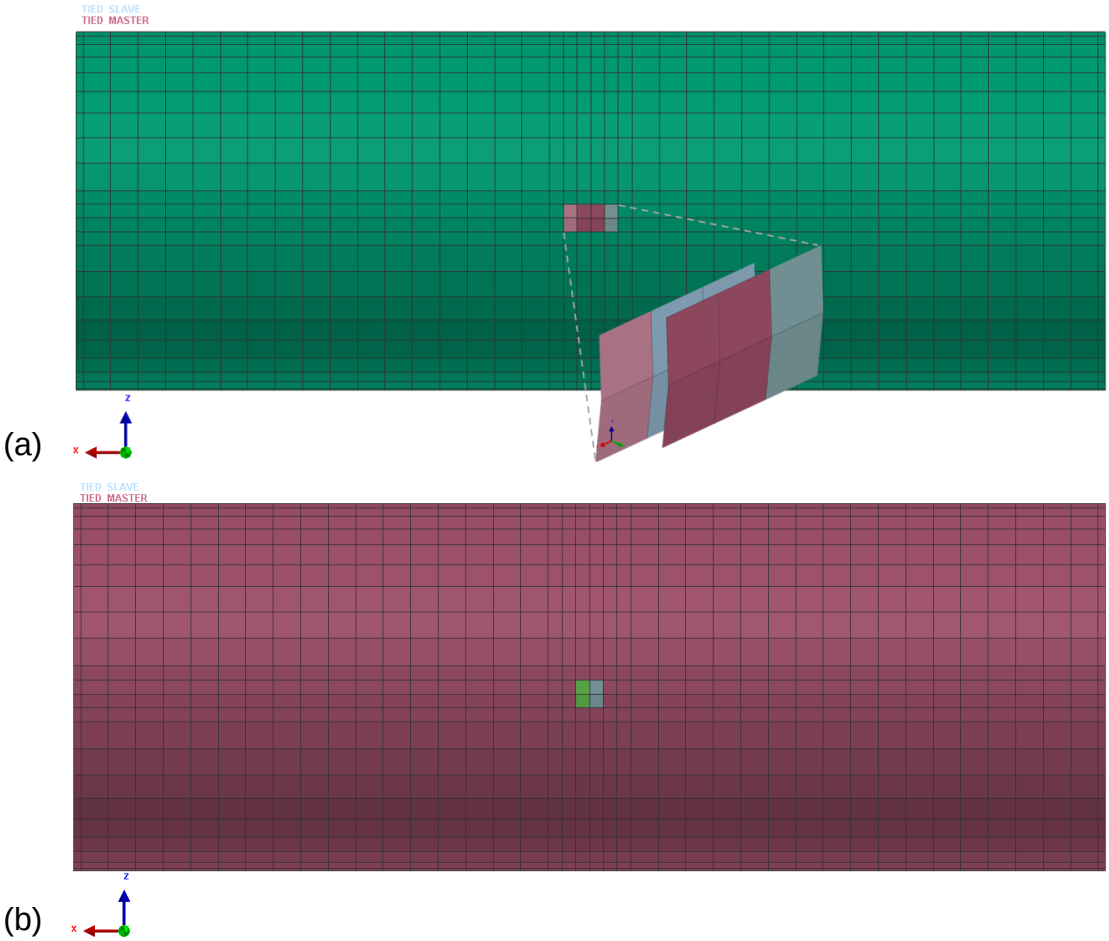

Figure 7.9 Representation of (a) weak tied interface between grey/blue inner and dark red external shells and (b) real interface assigned to the rest of shells

7.2.2.4.2 Consecutive fibre cut defects connected through interfacial defects

The cylindrical model of section 7.2.2.4.1 was updated in order to examine the failure behaviour in the case adjacent fibre cut defective shells are connected through a weak interface. The inner and external fibre cut defective shells located in the middle of the cylindrical shell were extended to include two more shells 4x4 mm^2 each. The representation of the fibre cut defective elements is illustrated in Figure 7.10.

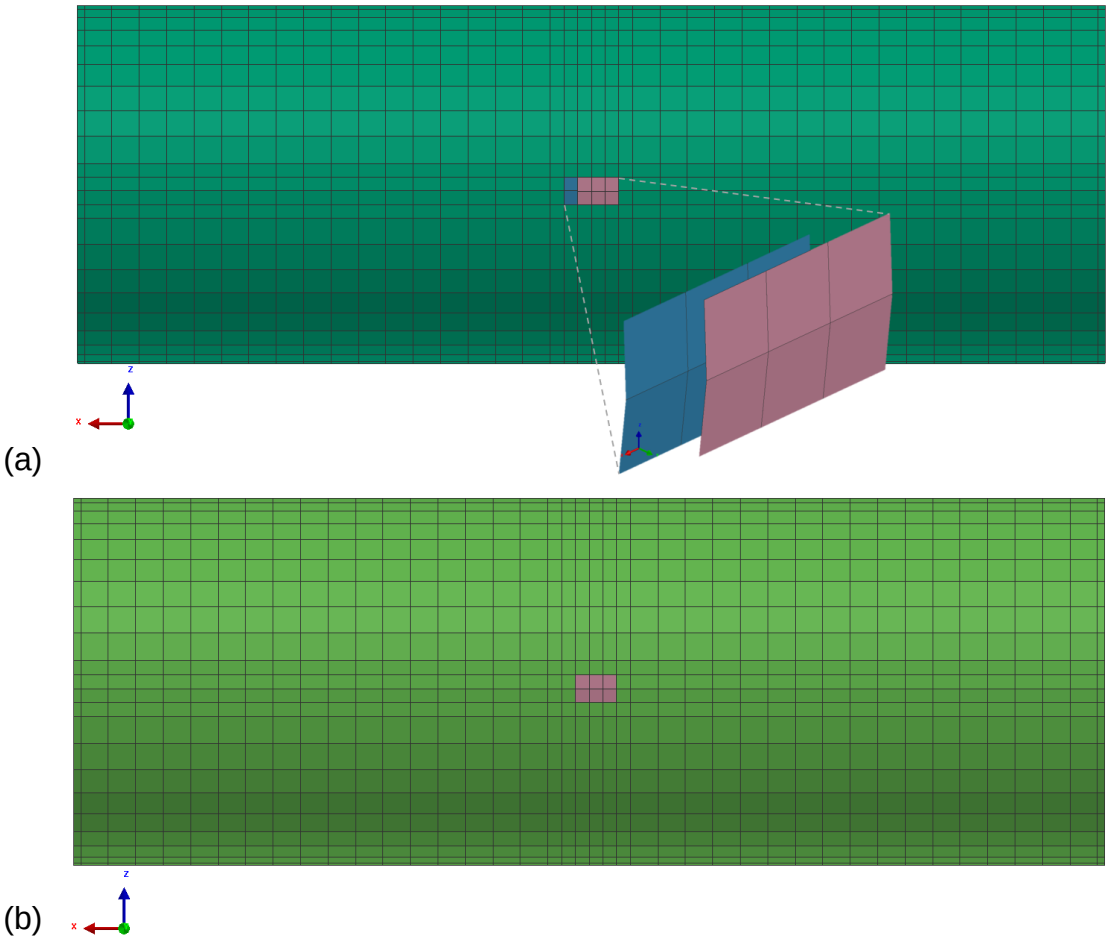

Figure 7.10 Fibre cut defective shells in blue and red colour for the internal and external cylinder respectively, (a) without and (b) with external cylindrical shell

The deteriorated interlaminar properties reported in Table 6.5 were assigned to the four overlapping fibre cut defective shells of Figure 7.10(a), which are located in the middle of the cylindrical structure. The interface between the rest of the inner and outer elements of the two cylindrical shells including intact and four defective elements, two in the inner and two in the outer cylinder was defined utilising intact interface properties as summarised in Table 5.5 with contact thickness of 1.2 mm. Overall, the model consisted of 3612 elements and 3698 nodes.

7.3 Simulation results for CVPs incorporating LBB designs

This section is dedicated to the simulation results of the investigated concepts described in section 7.2.2. The pressure results with respect to fibre cut damage

and interfacial defects are identified. The damage evolution, as well as the failure mechanisms leading to the first leakage and final rupture are presented.

7.3.1 CPV with square defective fibre area

The simulation results from the model with fibre cuts introduced in a square region of section 7.2.2.1 were extracted and analysed for the evaluation of the LBB concept. The shell elements of each layer of the two cylindrical shells were examined in order to identify the instant and value of leak pressure. The results are summarised in Figure 7.11, which illustrates the level of pressure as a function of fibre cut damage of the two first leakages/ruptures that appear during loading.

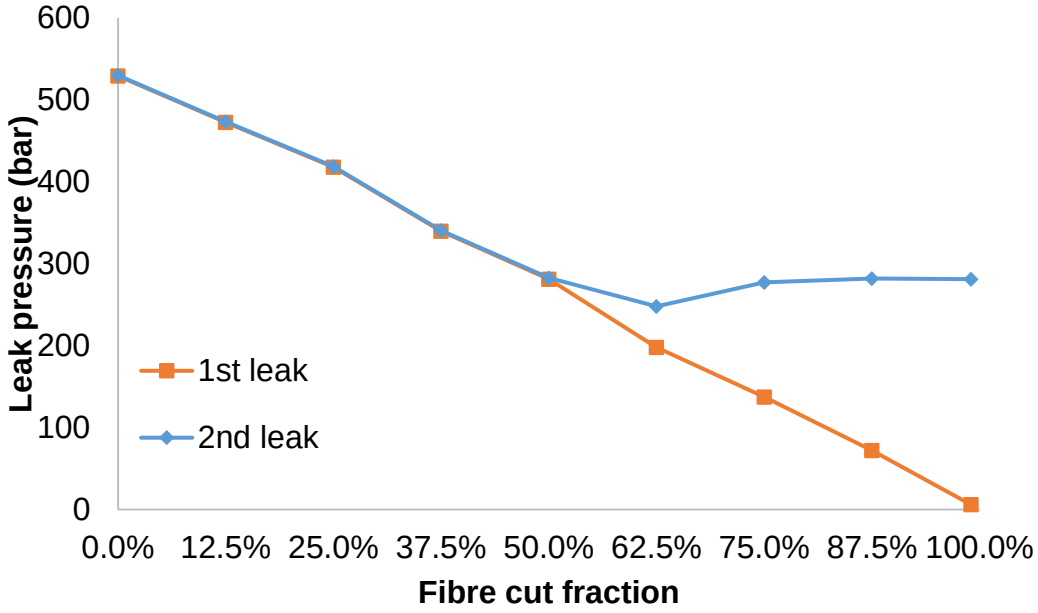

Figure 7.11 Level of pressure for CPV with square shape fibre cut defective area with respect to fibre cut damage

In the 0% fibre cut case, leakage occurs in the centre of the pipe away from the defective area, whereas in all the other cases damage first starts at the defective shells. The results illustrated in Figure 7.11 show that for fibre cut damage up to 50% the first and second leakage occur at very close instants or at the same level of pressure. As the percentage of fibre cut damage increases, the first leakage occurs in lower pressure values whilst the second leakage shows a plateau of pressure between fibre cut damage of 50-99% averaging at 274 bar. This is an

indication that the LBB concept can be achieved for fibre cut damage higher than 50%, with the most successful case at 75 and 87.5%, which lead to complete separation and adequate delay between the two leak pressures. Similar to the 75 and 87.5% behaviour is observed for fibre cut damage of 99%. However, the first leakage occurs very early during the loading and at a low pressure value which is not appropriate for the operation of a CPV. The simulation results indicate that for fibre cut damage from 0 to 75% the failure mechanisms are combination of fibre, matrix and interface damage. For 87.5 and 99% fibre cut damage, the first failure occurs in the defective location due to fibre damage, whilst the second failure occurs mostly as a result of shear and interfacial damage. The first leakage and the damage evolution at the defective area of the pipe with fibre cut damage of 87.5% are presented in Figure 7.12. The results indicate that fibre damage is the dominant failure mechanism for the occurrence of the first leakage, whilst matrix shear, transverse and interfacial damage is present without governing the failure. Figure 7.13 represents the second leakage results at the intact area surrounding the defects. Interfacial damage occurs at an early stage, but rupture occurs mainly due to shear damage, whilst transverse and fibre damage also develop.

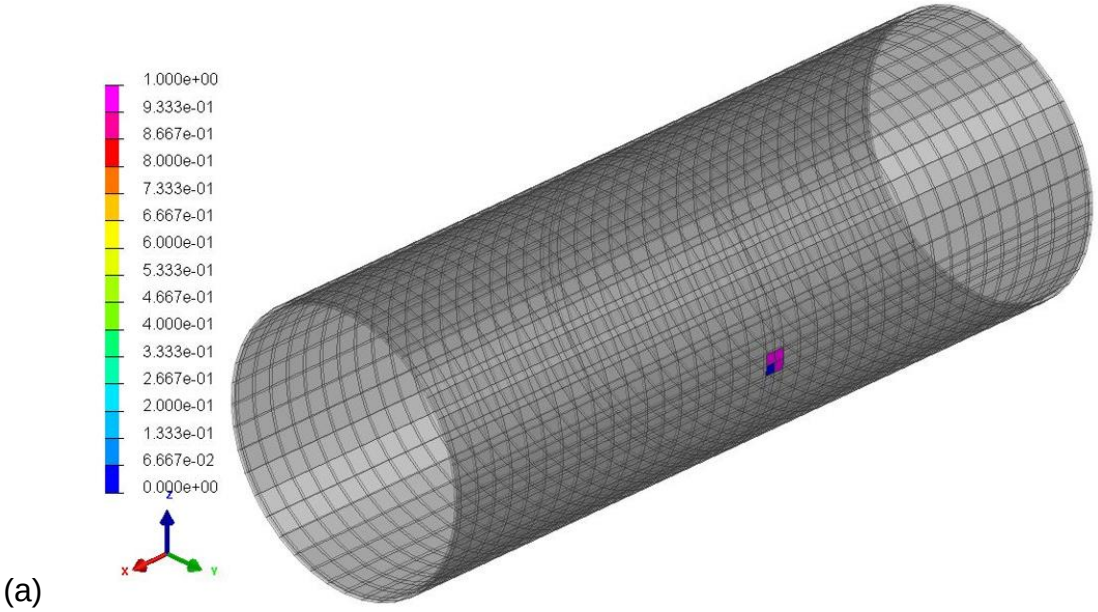

(a)

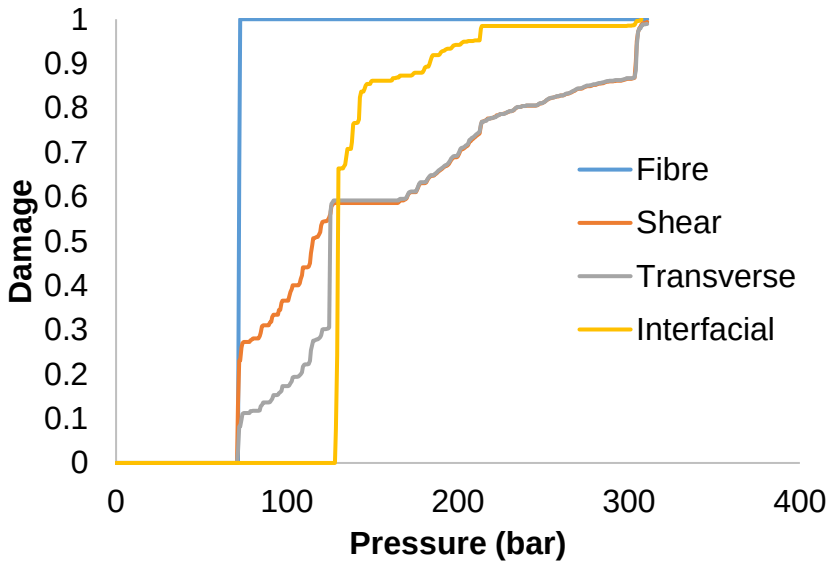

(b)

Figure 7.12 First leakage for CPV with square shape fibre cut defective area due to (a) fibre damage at 72 bar and (b) damage evolution at the top right defective shell for the case of square fibre cut defects of 87.5% fibre cut damage. Colour map represents the fibre damage factor.

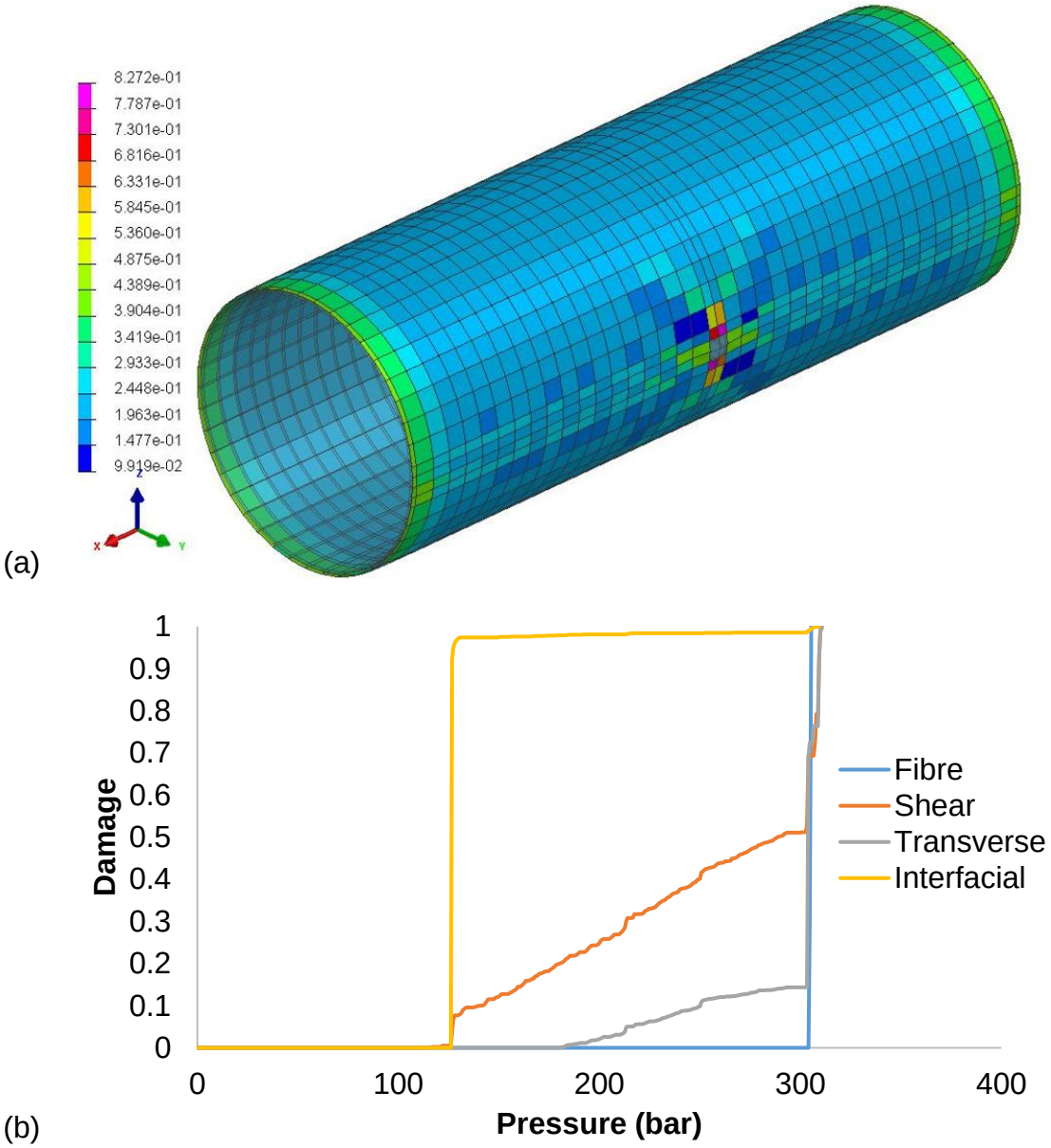

Figure 7.13 Second leakage for CPV with square shape fibre cut defective area due to (a) matrix shear damage at 282 bar and (b) damage evolution at the top right intact shell above the defective area for the case of square fibre cut defects of 87.5% fibre cut damage. Colour map represents the matrix shear damage factor.

7.3.2 CPV with square defective fibre area and two layer reinforcing patch

The simulation results of the model with square shape fibre cut defective area and a two layer patch are reported in this section. The level of pressure as a

function of the fibre cut damage of the two first leakages are presented in Figure 7.14. The results show that the increase of the fibre cut damage forces the first leakage to occur at lower pressure values at the defective elements. The second leakage remains approximately constant for the fibre cut damage cases between 37.5 to 99% creating a pressure plateau of 324 bar. For fibre cut damage lower than 75%, the first and second failures occur as combination of fibre, matrix and interface damage. In the cases of 75, 87.5 and 99% the dominant failure mechanism during the first leakage is fibre damage; however, a combination of all failure mechanisms acts for the second leakage.

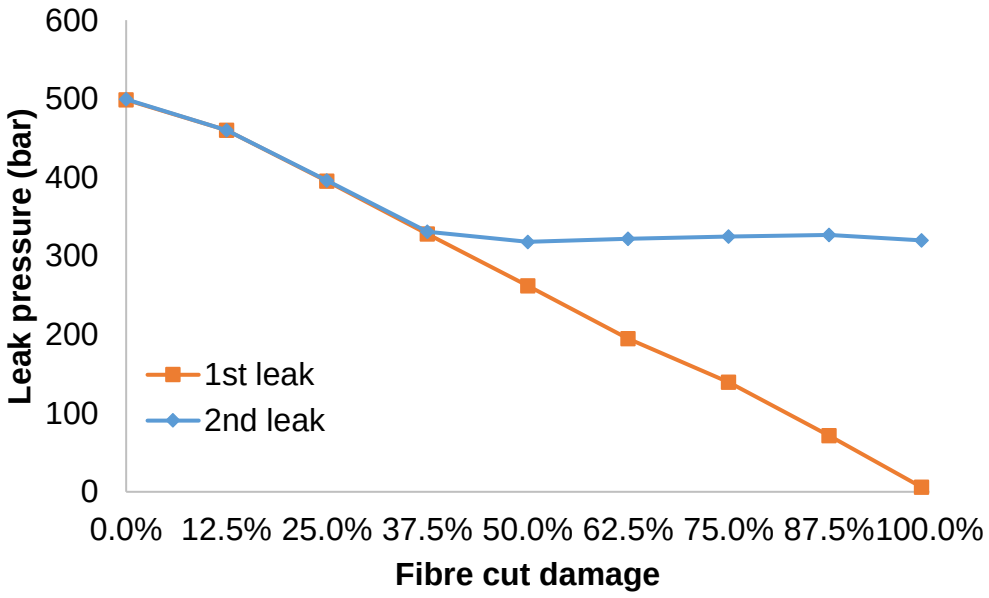

Figure 7.14 Level of pressure for CPV with square shape fibre cut defective area and two layer patch with respect to fibre cut damage

Figure 7.15 illustrates the fibre failure mechanism taking place at the defective area during the first leakage for fibre cut damage of 87.5%. The dominant failure mechanism is fibre damage, whilst matrix shear and transverse damage, as well as delamination are present. Figure 7.16 illustrates the failure mechanisms leading to the second leakage in the model with 87.5% fibre cut damage. The rupture takes place on the intact elements of the pipe and the patch due to combination of matrix shear, transverse and fibre damage with the first dominating mostly.

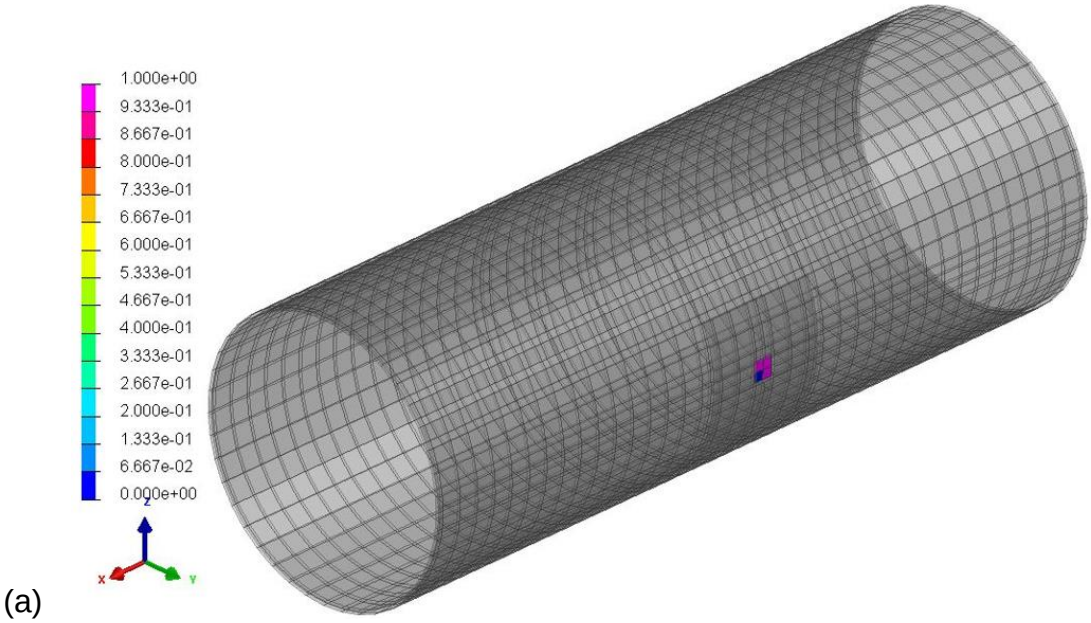

(a)

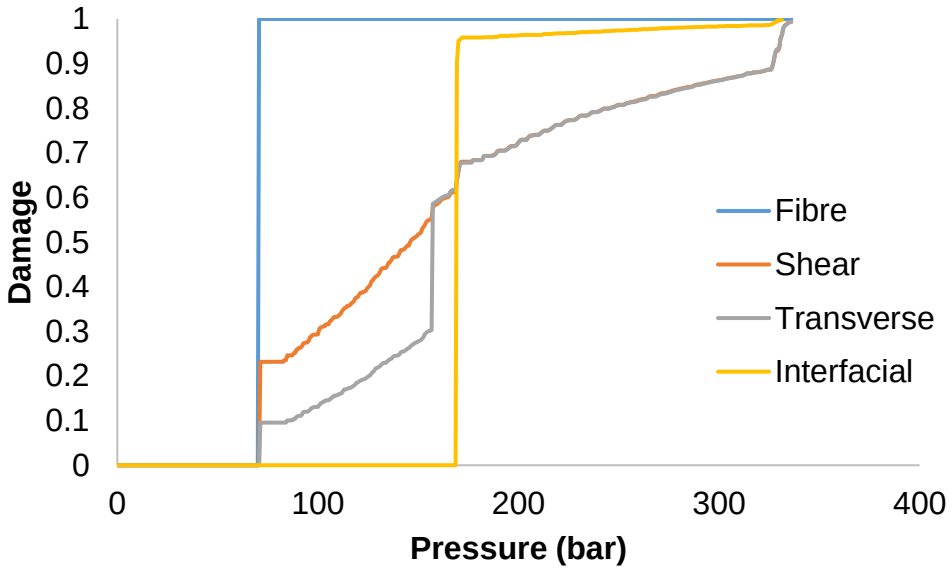

(b)

Figure 7.15 First leakage for CPV with square shape fibre cut defective area and two layer patch due to (a) fibre damage at 71.3 bar and (b) damage evolution at the top right defective shell for the case of square fibre cut defects of 87.5% fibre cut damage and two layer patch. Colour map represents the fibre damage factor.

(a)

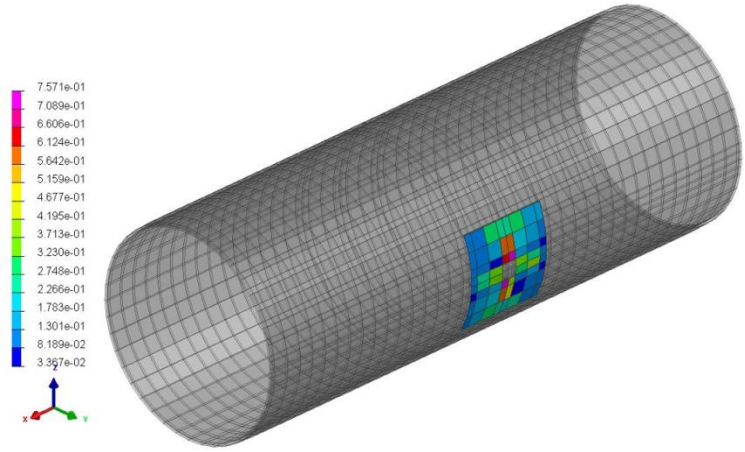

(b)

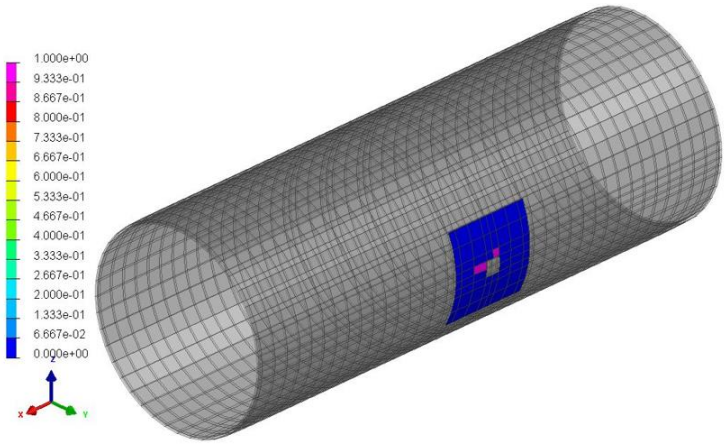

(c)

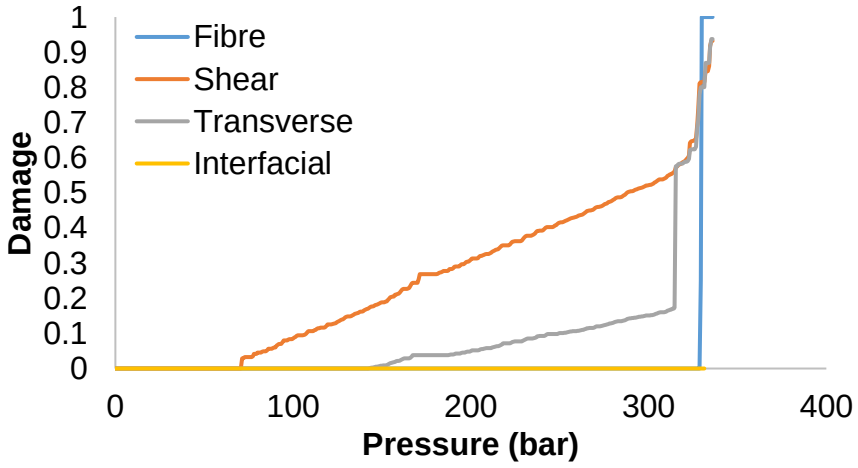

Figure 7.16 Second leakage CPV with square shape fibre cut defective area and two layer patch due to (a) shear and (b) fibre damage at 326.7 bar and (c) damage evolution at the top right intact shell of the patch above the defective area for the case of square fibre cut defects of 87.5% fibre cut damage and two layer patch. Colour maps represent the shear and fibre damage factors respectively.

The comparison of the results of the cylindrical models without a square shape reinforcing patch with the models with a two layer patch shows that the addition of the two layer patch increases the delay between the occurrence of the first and second leak thus enhancing the development of a valid LBB concept. The addition of the two layer patch, leads to earlier separation of the first from the second leak pressure, from 50% to 37.5%. The comparison also shows that the values of the first leak pressures are slightly decreased for the model with patch by an average difference of 11 bar; however, the second leakage takes place at higher pressure values. The increase of the plateau pressure values by adding the two layer patch is 18%.

7.3.3 CPV with square defective fibre area and four layer reinforcing patch

Figure 7.17 summarises the results of the level of pressure as a function of fibre cut damage the instant of appearance of the first two leakages for the case of square shape fibre cut defective area with a four layer patch. Separation between the first and second leak pressures takes place for fibre cut damage higher than 25%. A pressure plateau of 382 bar occurs for the second leakages of the fibre cut damage cases from 37.5 to 99%. The failure mechanisms taking place involve fibre, matrix damage and delamination, similarly to the two layer patch. Figure 7.18 indicates that the first leakage occurrence is caused due to fibre damage, however from the plot in Figure 7.18(b), matrix shear and transverse damage as well as delamination also develop. Figure 7.19 corresponds to the second leakage which takes place on the intact shells of the pipe adjacent to the defective area and passes through the patch. Rupture occurs due to combination of the failure mechanisms of fibre, matrix shear and transverse damage. The comparison of the results of the two layer patch and of the four layer patch indicates that the separation of the first from the second leakage occurs slightly earlier for the four layer patch case. The comparison of the first leakages of both cases for the respective fibre cut damage indicates that they occur at very similar pressures with an average difference per data point of 5.9 bar. The second leak pressure values show that the use of the four layer patch enhances the development of the LBB behaviour as the second leak pressures increase by

18%. Comparing the four layer patch to the model with no patch, the second leak pressure values increase by 39% improving the development of the LBB behaviour.

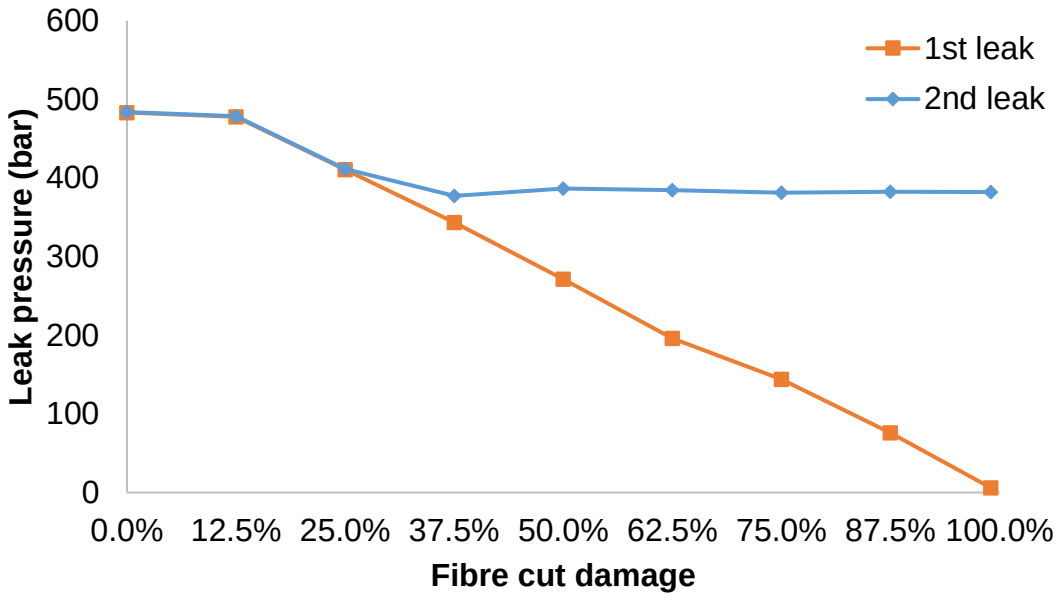

Figure 7.17 Level of pressure of CPV with square shape fibre cut defective area with four layer patch with respect to fibre cut damage

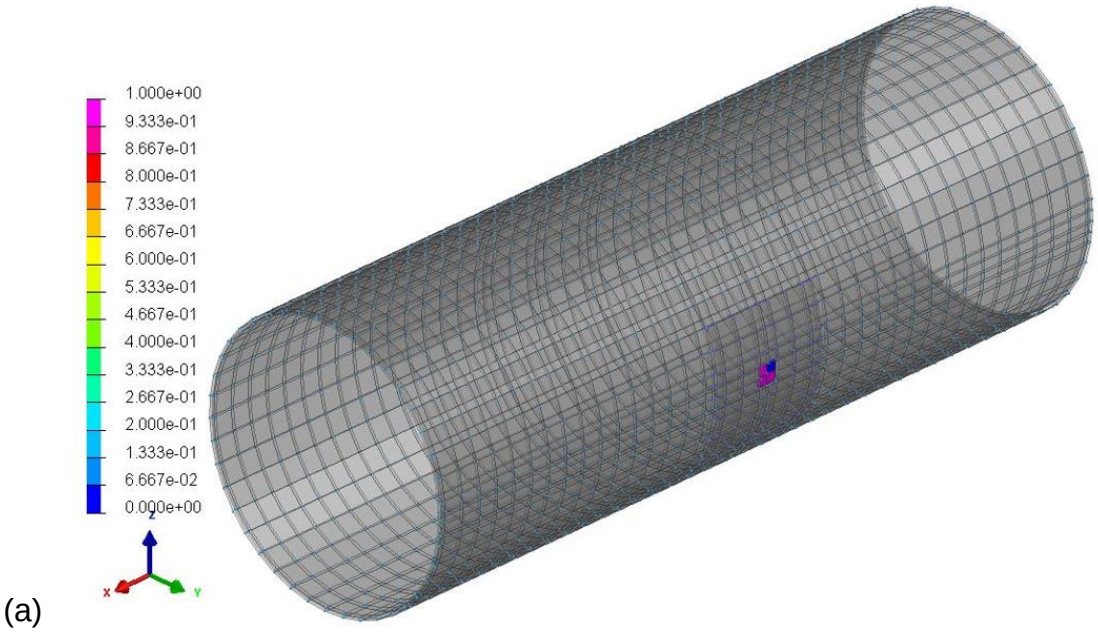

(a)

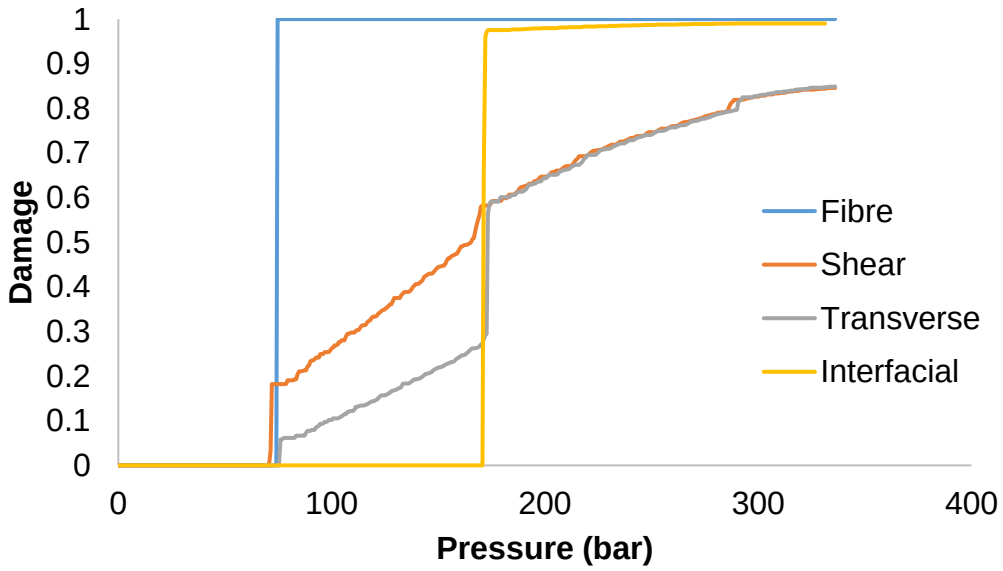

(b)

Figure 7.18 First leakage for CPV with square shape fibre cut defective area with four layer patch due to (a) fibre damage at 76 bar and (b) damage evolution at bottom left defective shell for the case of fibre cut defects of 87.5% fibre cut damage and four layer patch. Colour map represents the fibre damage factor.

(a)

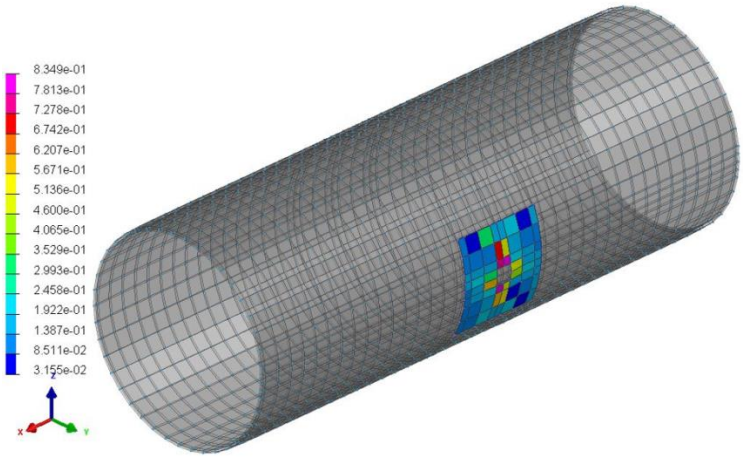

(b)

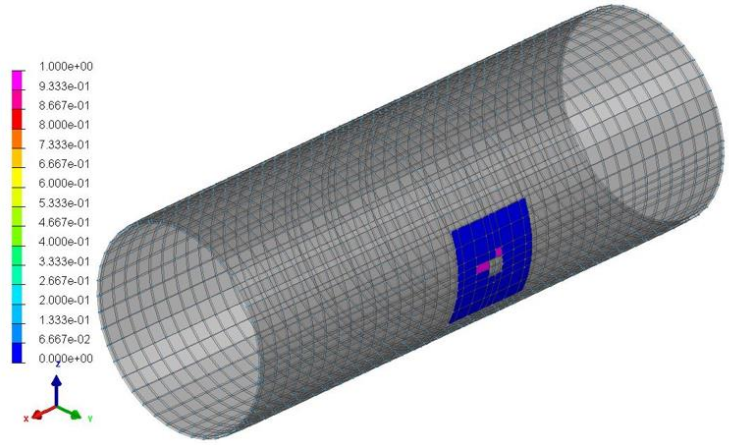

(c)

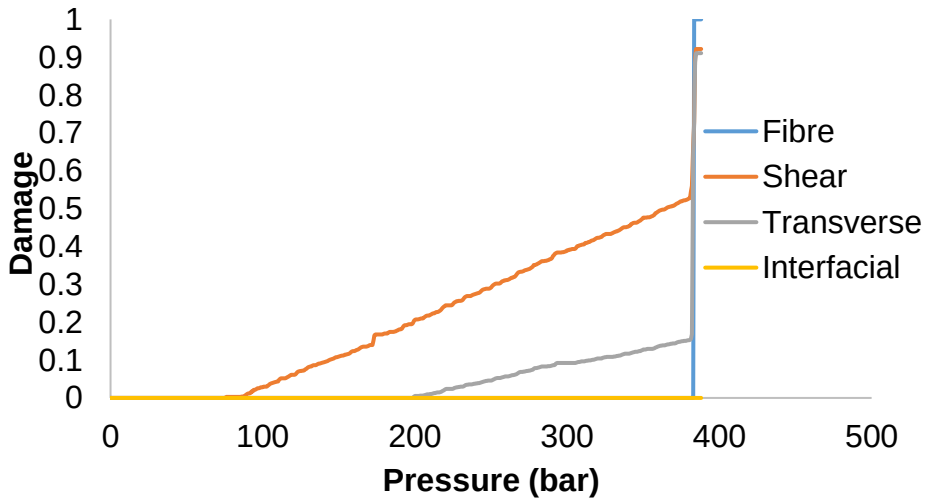

Figure 7.19 Second leakage for CPV with square shape fibre cut defective area with four layer patch due to (a) shear and (b) fibre damage at 382.7 bar and (c) damage evolution at the top right intact shell above the defective area for the case of fibre cut defects of 87.5% fibre cut damage and four layer patch. Colour maps represent the matrix shear and fibre damage factors respectively.

7.3.4 CPV with square defective fibre area and eight layer reinforcing patch

The simulation results for the square shape fibre cut defective area with an eight layer patch are illustrated in Figure 7.20, which presents the level of pressure as a function of fibre cut damage of the two first leak occurrences. The results indicate similarities with the results of the four layer patch with respect to the separation of the first from the second leak pressure and the types of failure mechanisms leading to their occurrence as illustrated in Figure 7.21 and Figure 7.22. However, the second leakage occurs at the intact pipe area, which is not covered by patch primarily due to combination of fibre, matrix shear and transverse damage. The patch area undergoes rupture immediately after. As indicated in Figure 7.22(c), matrix shear damage starts occurring at 378 bar, but leakage does not initiate until a pressure of 408.7 bar at which damage threshold of more than 50% is evident on all the plies of both shells through the thickness. Comparison of the first leak pressure results between four and eight layer patch shows an average difference of 11.3 bar. For these cases, a small pressure plateau is evident for low fibre cut damage as shown in Figure 7.17 and Figure 7.20. This is explained by the addition of the patch of more layers, which balances the effect of the defects thus providing a level of robustness to the structure. Comparison of the plateau of second leak pressures for the eight layer patch against two and four layer patch indicated an increase by 26 and 6% respectively. Comparing the results between the eight layer patch and no patch, the LBB behaviour is enhanced by 48%.

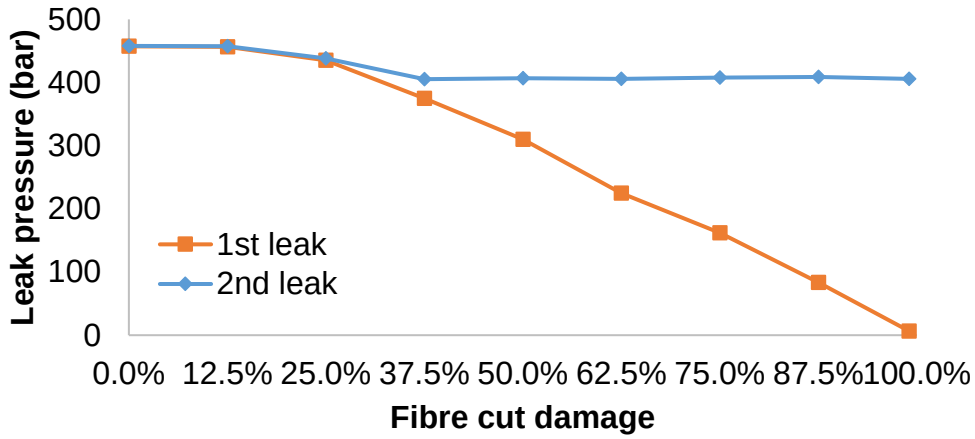

Figure 7.20 Level of pressure for CPV with square shape fibre cut defective area with eight layer patch with respect to fibre cut damage

(a)

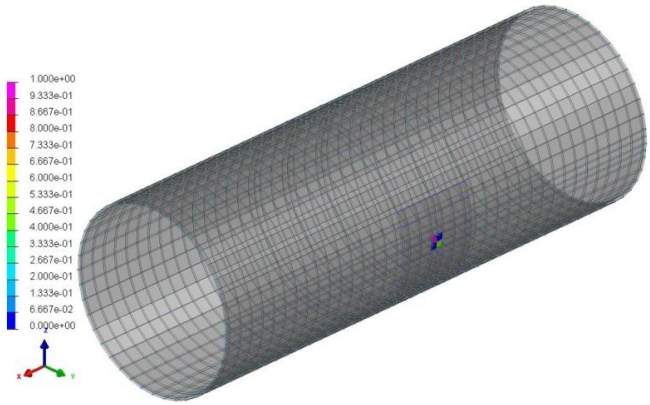

(b)

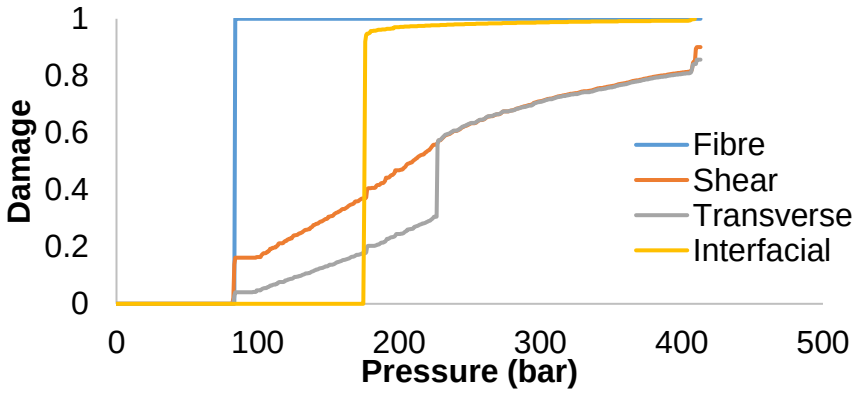

Figure 7.21 First leakage for CPV with square shape fibre cut defective area with eight layer patch due to (a) fibre damage at 83.3 bar and (b) damage evolution at the top left defective shell for the case of fibre cut defects of 87.5% fibre cut damage and eight layer patch. Colour map represents the fibre damage factor.

(a)

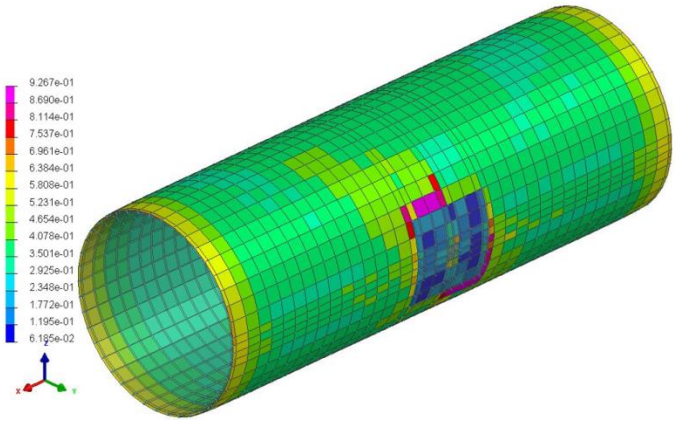

(b)

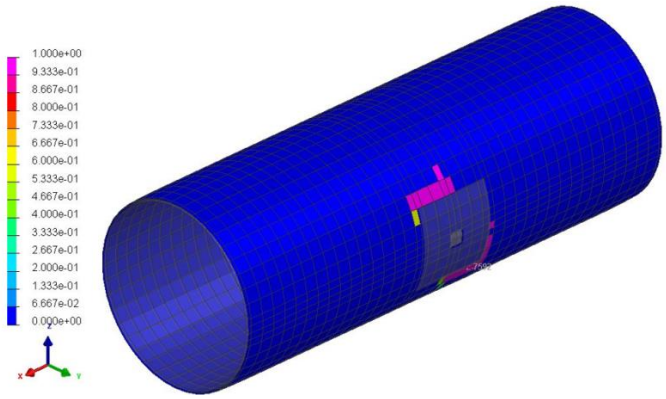

(c)

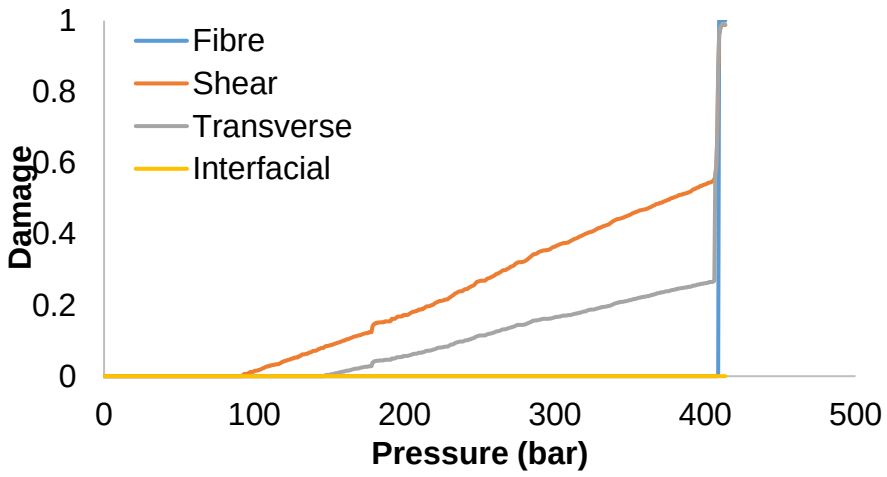

Figure 7.22 Second leakage for CPV with square shape fibre cut defective area with eight layer patch due to (a) shear and (b) fibre damage at 408.7 bar and (c) damage evolution at the top left intact shell in the middle of the pipe that is not covered by patch for the case of fibre cut defects of 87.5% fibre cut damage and eight layer patch. Colour maps represent the matrix shear and fibre damage factors respectively.

7.3.5 Influence of reinforcing patch thickness in the response of CPVs with square defective fibre area

The investigation of the addition of patch at the area surrounding the defects indicates that LBB behaviour is enhanced in comparison to no use of patch. As the patch thickness increases the first leak pressures remain approximately the same for the respective fibre cut damage cases, whilst the plateau of the second leak pressures increase, as illustrated in Figure 7.23. This provides an increased delay with respect to the first leakage causing an LBB response. The patches of four and eight layer thickness show satisfactory performance. The pressure response as a function the fibre cut damage are close in these two cases providing an increase of 6% with doubling the layers of patch for four to eight. Due to the similarity of the pressure response between these two suitable types of patch for the development of the LBB concept, the four layer thickness patch case, which provides an overall enhancement of 39% compared to no use of patch, was selected for further investigation.

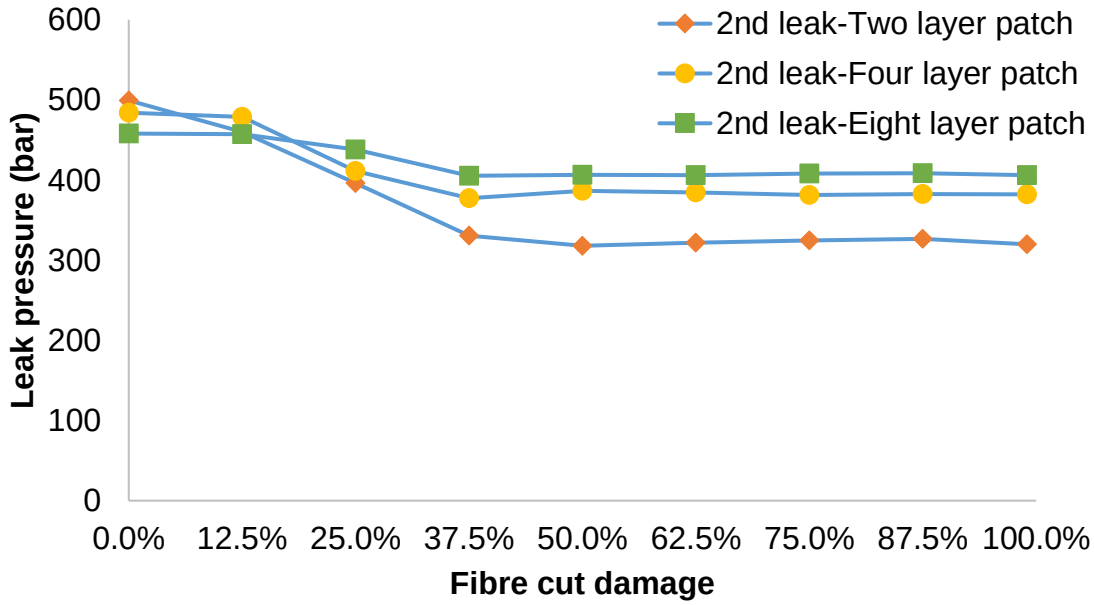

Figure 7.23 Level of second leak pressures with respect to fibre cut damage for CPSs with square shape fibre cut defective area with two, four and eight layer patch

7.3.6 CPV with circular defective fibre area and four layer reinforcing patch

The simulation results of the cylindrical model with circular shape defective area and four layer patch described in section 7.2.2.2 are reported in Figure 7.24. Separation between the first and second leakage occurs for fibre cut damage greater than 12.5%. The second leak pressures indicate a pressure plateau between 12.5 to 99% fibre cut damage at an average of 353.3 bar. As illustrated in Figure 7.25, in the case of fibre cut damage of 87.5%, the failure mechanisms leading to first failure is a combination of fibre, matrix shear and transverse as well as interfacial damage. The defective area of the external shell is isolated and the shell elements of a certain layer within the eight layer thickness undergoing fibre, shear and transverse rupture are presented. In the case of the second leak for fibre cut damage of 87.5%, which is depicted in Figure 7.26, the failure mechanisms acting upon the rupture of the system are interfacial, matrix shear and transverse damage. As indicated from the damage evolution of a shell located at the patch of Figure 7.26(c), damage occurs at 307.3 bar. However, leakage does not take place until a damage threshold of more than 50% is achieved through all the layers of all the shells through the thickness.

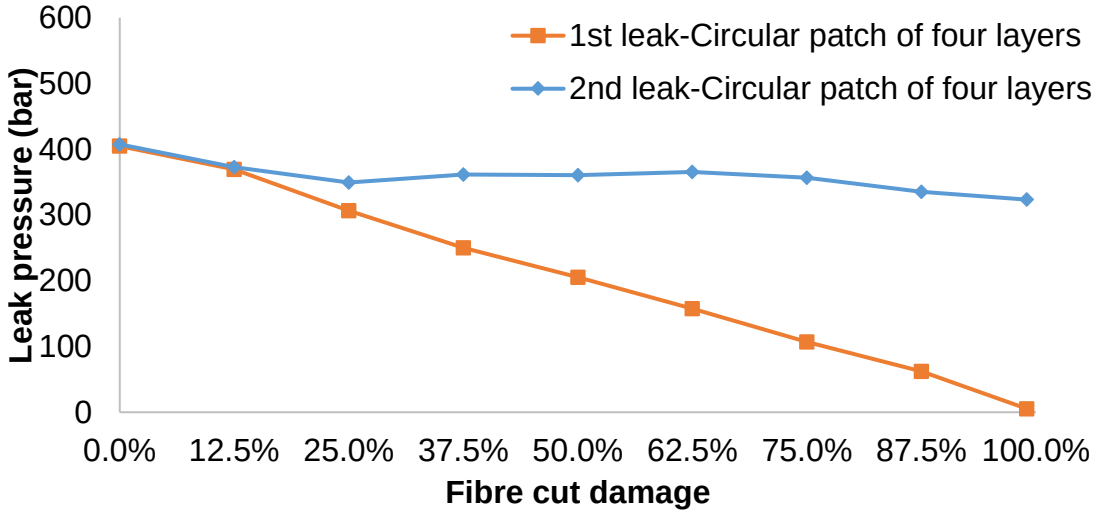

Figure 7.24 Level of pressure for CPV with circular shaped fibre cut defective area with four layer patch with respect to fibre cut damage

(a)

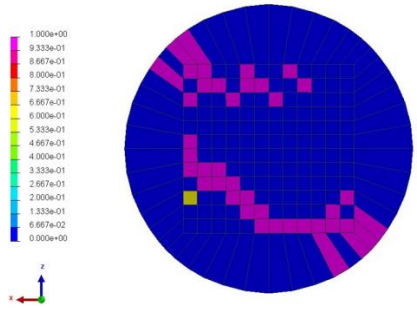

(b)

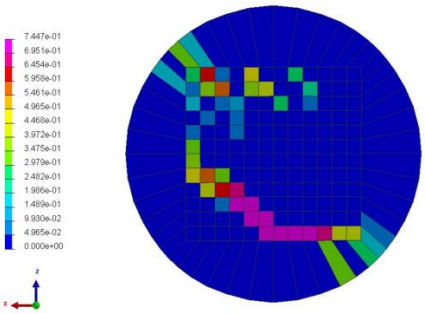

(c)

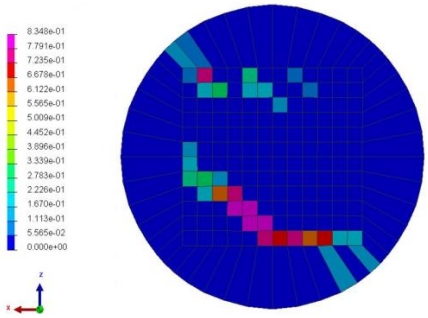

(d)

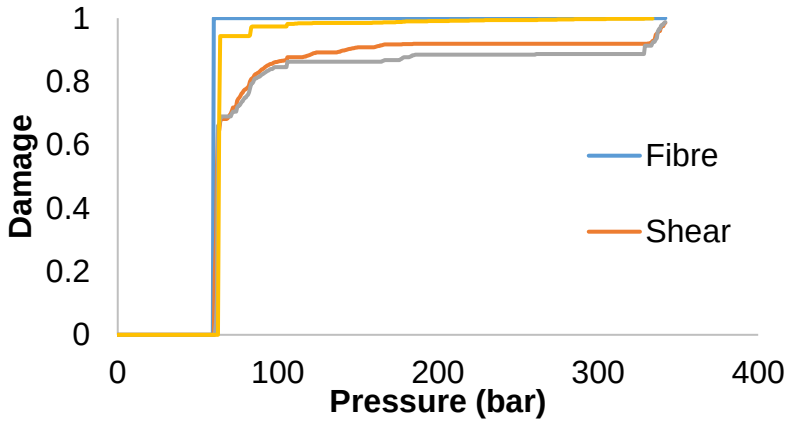

Figure 7.25 First leakage of CPV with circular shaped fibre cut defective area with four layer patch due to (a) fibre, (b) shear, (c) transverse damage at 62 bar and (d) damage evolution at a defective shell at the bottom right side of the defective area for the case of circular fibre cut defects of 87.5% fibre cut damage and four layer patch. Colour maps represent the fibre, shear and transverse damage factors respectively.

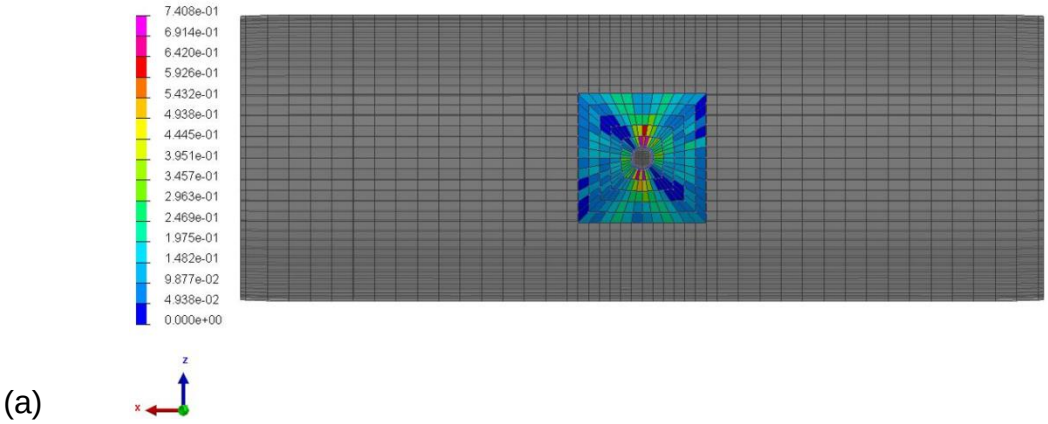

(a)

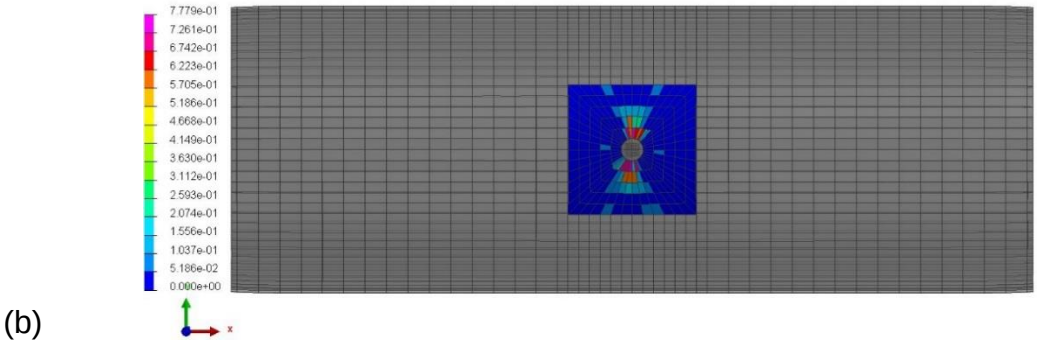

(b)

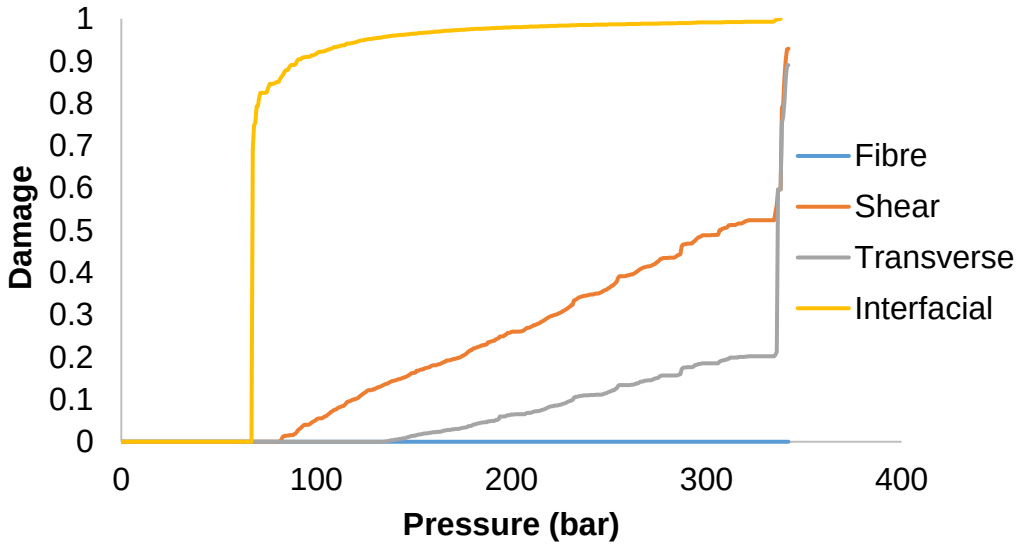

(c)

Figure 7.26 Second leakage CPV with circular shaped fibre cut defective area with four layer patch due to (a) shear, (b) transverse damage at 335.3 bar and (c) damage evolution at an intact shell of the patch above the defective area for the case of circular fibre cut defects of 87.5% fibre cut damage and four layer patch. Colour maps represent the matrix shear and transverse damage factors respectively.

7.3.7 Influence of defective fibre area shape in the response of CPVs

A comparison of the results between circular and square shape fibre cut defective area with a four layer patch is illustrated in Figure 7.27. Separation of the first and second leak pressures occurs sooner for the circular shape. The first leak pressure for the respective fibre cut damage is lower for the circular shape defective case indicating an average difference of about 60 bar. This can be attributed to the increased accuracy of the results of the circular shape defective area due to the very fine mesh compared to the respective of the square shape defective area. In the case of the occurrence of the second leakage, the difference of the pressure plateau is 8%. The pressure for both cases stabilises and is in good agreement for fibre cut damage higher than 25%; in particular for the damage level at which the first and second leakages separate. This indicates that the second leak is relatively independent of the shape of the defective area as the fibre cut damage increases. The differences introduced due to different shape of defective areas and their effect to the occurrence of the first and second leakage is small for the fibre cut damage cases of 62.5 to 99%.

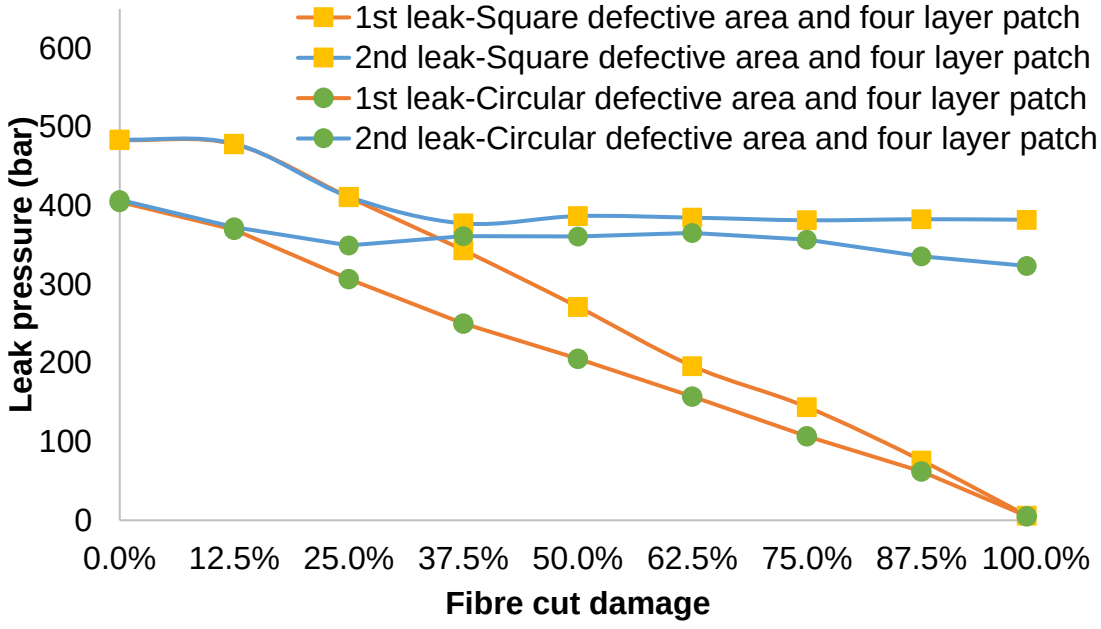

Figure 7.27 Comparison of first and second leak incidents for CPVs with square and circular defective area and a four layer patch.

7.3.8 CPV with delamination defects

The results of the cylindrical model of section 7.2.2.3 with embedded interfacial defects are summarised in Table 7.2. The results indicate that no separation takes place between the first and the second leak pressure. Based on the results presented in Figure 7.28, the weak tied interface undergoes failure at an early stage. Figure 7.28(b) indicates that the edges of the pipe are under high damage, which occurs earlier compared to the rupture due to the embedded delamination defect. If this is not taken into account and the focus is set on the way the interfacial defect acts upon internal pressurisation, shell element rupture that leads to the first leakage is developed as combination of interlaminar and matrix shear damage, whilst fibre and transverse damage follow immediately after. The second leak incident is presented in Figure 7.29 and occurs under the development of the same mechanisms leading to the first leakage. The colour maps indicate the individual damage factors of the failure mechanisms that ultimately lead to rupture.

Table 7.2 Simulation results for 1st and 2nd leakage of CPV with delamination defective area

1st leakage	**2nd leakage**
Leak Pressure (bar)	**Leak Pressure (bar)**
524.7	525.4

.

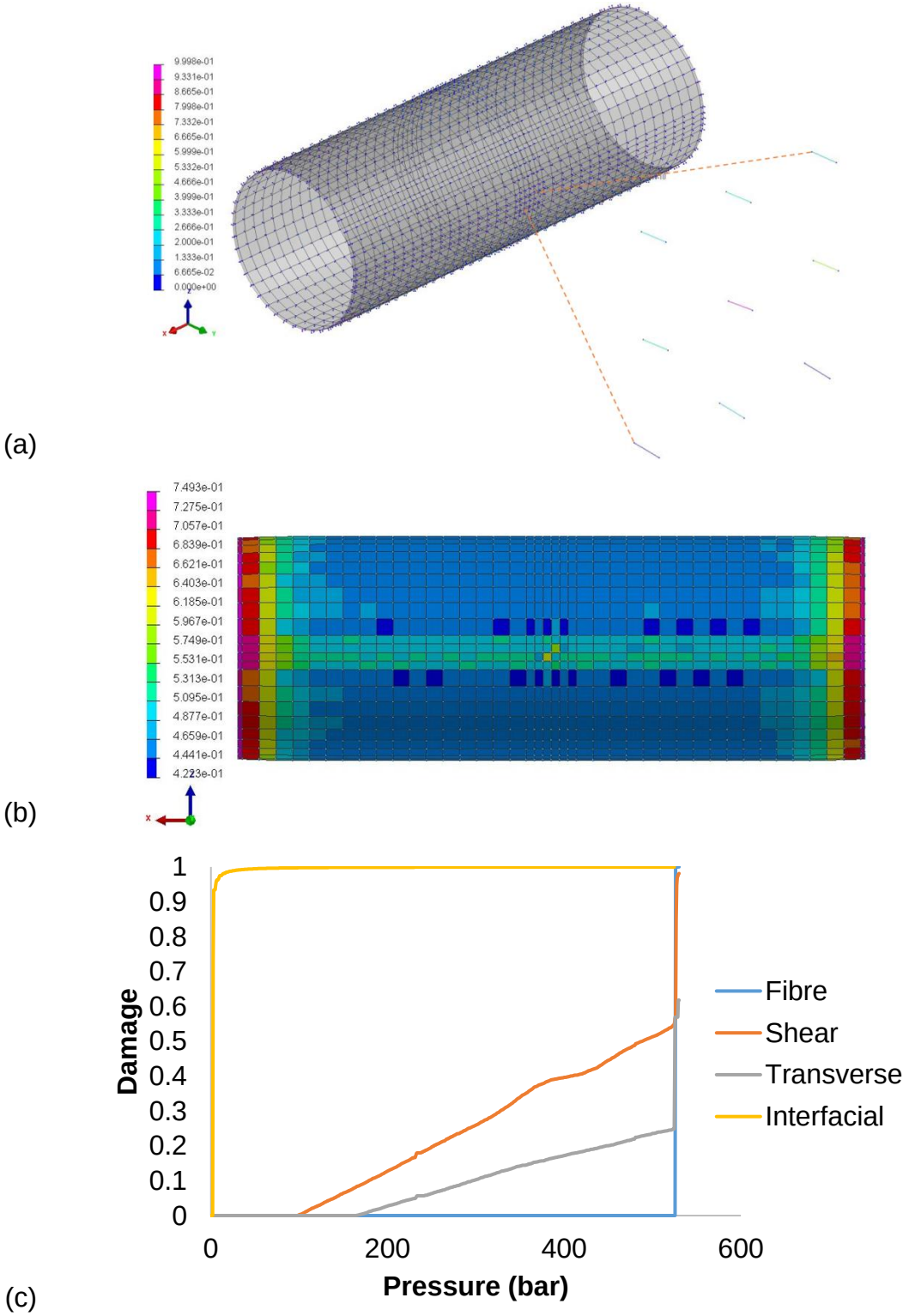

Figure 7.28 First leakage for CPV with delamination defects due to (a) interlaminar damage at 2.7 bar at the weak tied interfaces, (b) shear damage at 524.7 bar and (c) damage evolution at the top right defective shell. Colour maps represent the interlaminar and matrix shear damage factors respectively.

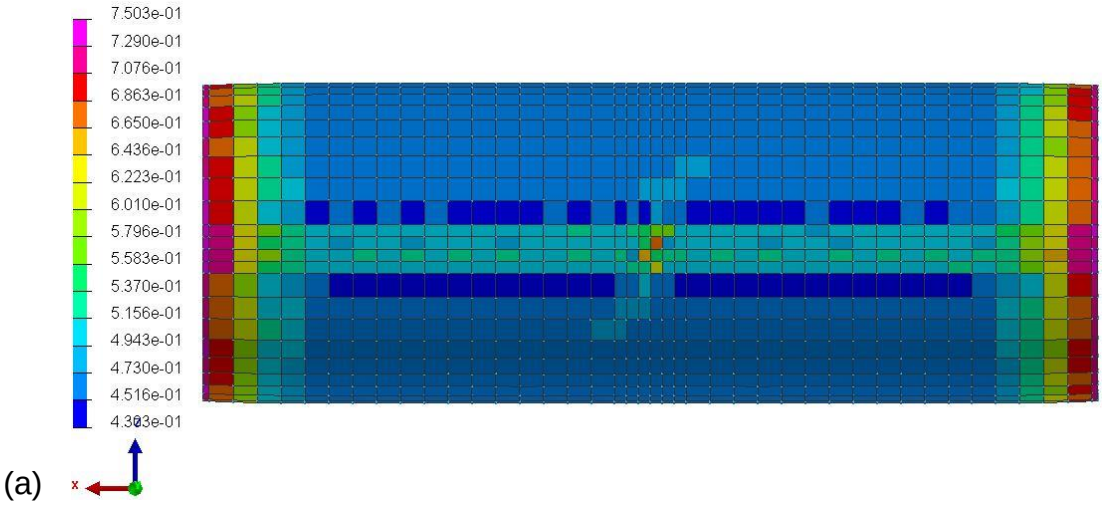

(a)

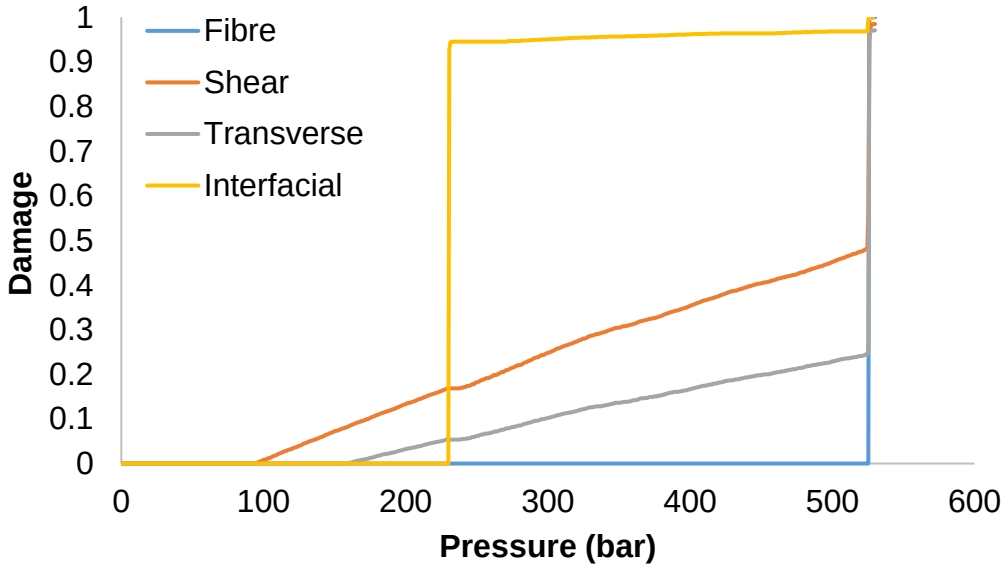

(b)

Figure 7.29 Second leak for CPV with delamination defects due to (a) shear damage at 525.4 bar and (b) damage evolution at the bottom right shell with real tied properties underneath the location with delamination defects. Colour map represents the matrix shear damage factor.

7.3.9 CPV with delamination and fibre cut defects

The simulation results for neighbouring fibre cut defects connected through interfacial defects, which is described in section 7.2.2.4.1 are presented in Table 7.3. For fibre cut damage of 50% the first leakage occurs at the area of the fibre cuts where weak interface exists. The second leakage takes place immediately

after at the fibre cut elements tied with the real interface properties to intact shells. For fibre cut damage of 62.5% and 99% the first leakage occurs at the weak interface between intact internal shells and outer defective shells, whilst the second leakage involves internal defective shells weakly tied to outer intact shells. This can be explained by the fact that as the pressure increases the outer cylindrical shell experiences higher degree of tension and failure occurs earlier compared to the layup arrangement with defective shells in the inner cylindrical shell. The failure mechanisms acting during the first and second leakages for all fibre cut damages are a combination of fibre, matrix shear and transverse damage as well as delamination. Figure 7.30 and Figure 7.31 illustrate the first leak pressure for the 99% fibre cut damage case. In the fourth layer failure occurs due to fibre damage as illustrated in Figure 7.30, whilst the fifth layer fails due to development of matrix shear and transverse damage, as shown in Figure 7.31. The behaviour is similar for the second leakage, which also occurs as a combination of failure mechanisms. Overall, the separation between the first and the second leak pressures is insignificant as the difference between the first and second leak pressures is minimal. This indicates that LBB behaviour cannot be achieved utilising this design of defect pattern.

Table 7.3 Simulation results for 1st and 2nd leakage of CPV with delamination and fibre cut defects

Fibre cut damage	1st leakage	2nd leakage
	Leak Pressure (bar)	Leak Pressure (bar)
50%	277	278
62.5%	217	223
99%	218	223

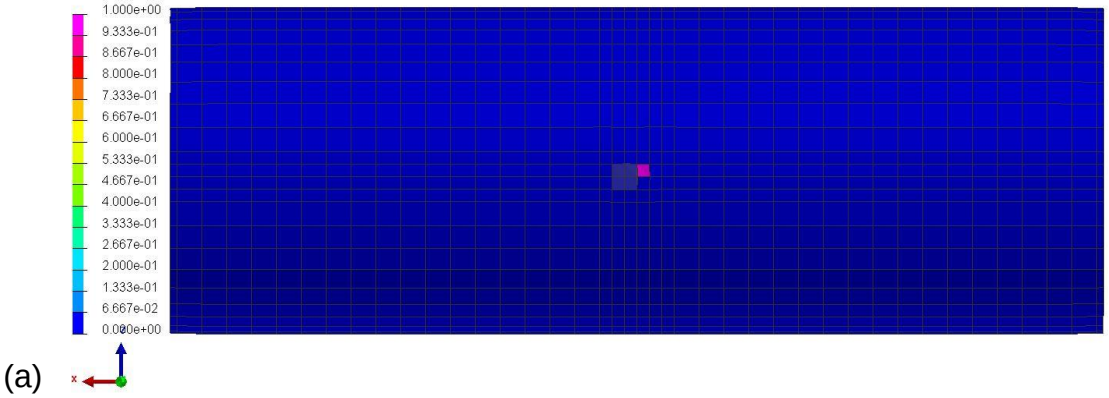

(a)

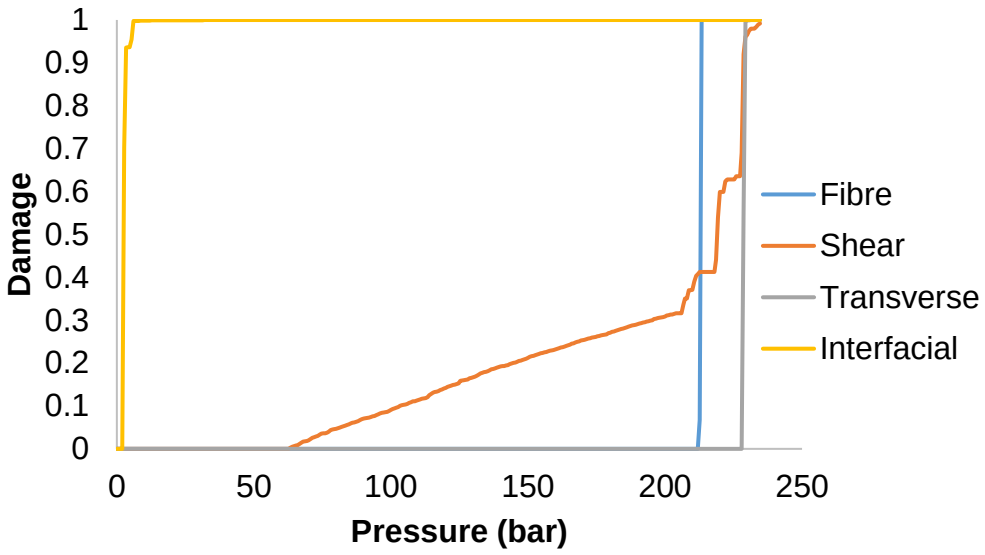

(b)

Figure 7.30 First leakage for CPV with delamination and fibre cut defects due to (a) fibre damage at 218 bar and (b) damage evolution at intact shell located at the inner pipe shell tied to an external defective for the case of square fibre cut defects of 99% fibre cut damage. Colour map represents the fibre damage factor.

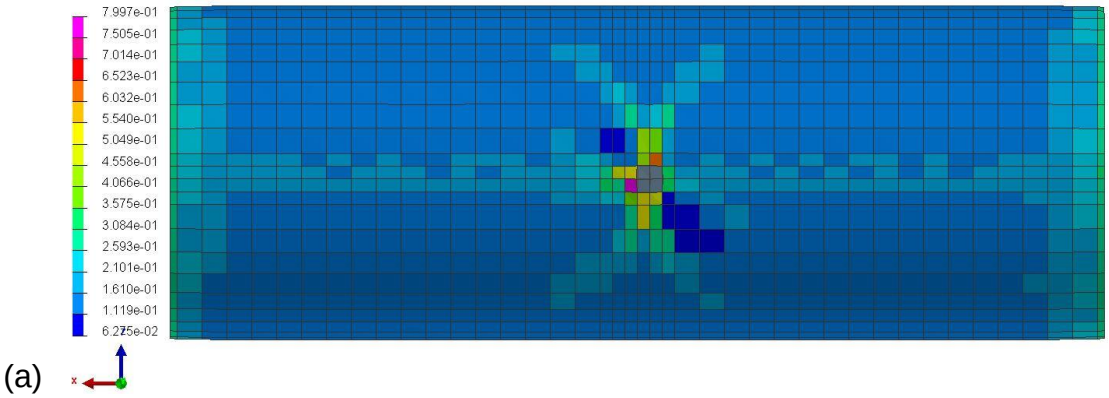

(a)

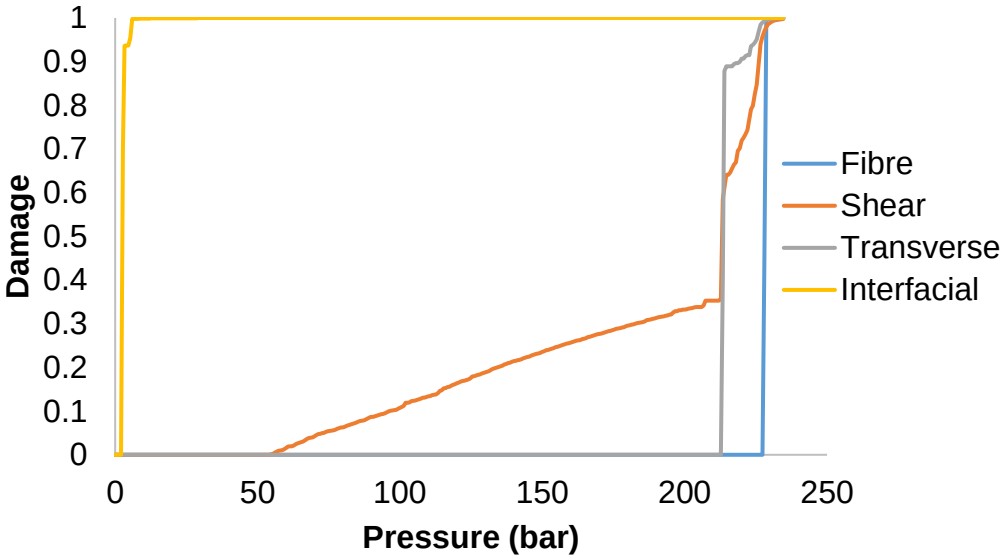

(b)

Figure 7.31 First leakage for CPV with delamination and fibre cut defects due to (a) matrix shear at 223 bar and (b) damage evolution at an intact shell located at the outer pipe shell tied to an internal defective for the case of square fibre cut defects of 99% fibre cut damage. Colour map represents the matrix shear damage factor.

7.3.10 CPV with delamination and consecutive fibre cut defects

The simulation results of the CPV with consecutive fibre cut defects tied utilising interfacial defects, which is described in section 7.2.2.4.2, are presented in Table 7.4. The results indicate distinctive separation between the first and second leak pressures being evident only for fibre cut damage of 99%. In all cases of fibre cut damage the first leakage is initiated at the defective areas where fibre cut shells of the internal and external cylindrical shells were tied weakly. For the cases of

50 and 62.5% fibre cut damage the second leakage occurs at locations with fibre cuts tied with real interface properties to intact shells of both internal and external cylindrical shells. The second leakage for fibre cut damage of 99% initiates from intact shells of the inner cylindrical shell tied using real interface properties to defective shells of the outer cylindrical shell. The occurrence of the two failures was accompanied by all failure mechanisms. The exception was the first leakage for the 99% fibre cut damage case in which fibre damage and delamination were the most dominant failure mechanisms, as illustrated in Figure 7.32. Figure 7.33 and Figure 7.34 show that the second leak failure occurs as a combination of all failure mechanisms acting all in one or on consecutive layers. In this investigation the LBB behaviour is achievable only for fibre cut damage of 99% even though the delay between the first and second leak pressures is not adequate.

Table 7.4 Simulation results for 1st and 2nd leakage of CPV with delamination and consecutive fibre cut defects

Fibre cut damage	1st leakage	2nd leakage
	Leak Pressure (bar)	Leak Pressure (bar)
50%	277.3	278
62.5%	197.3	199.3
99%	6	150.7

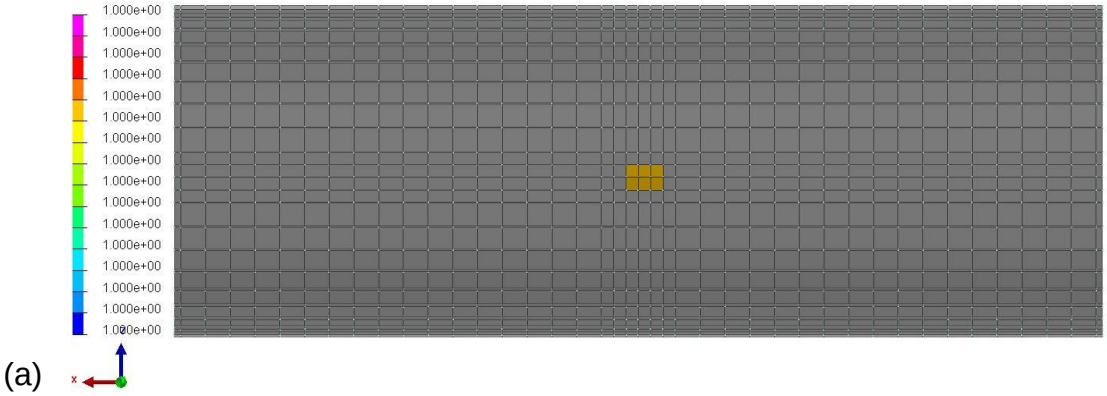

(a)

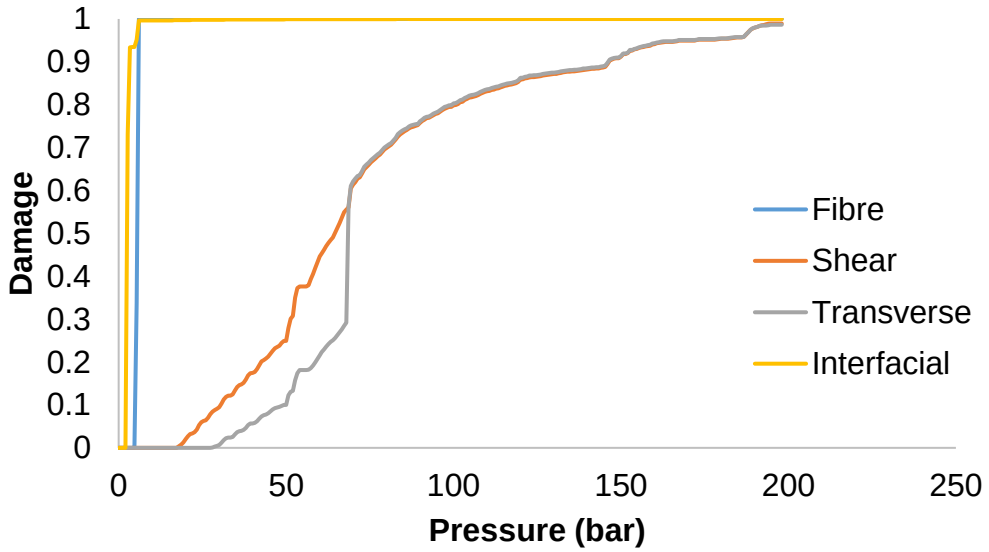

(b)

Figure 7.32 First leakage for CPV with delamination and consecutive fibre cut defects due to (a) fibre damage at 6 bar and (b) damage evolution at external defective shell tied weakly to internal defective shell. Colour map represents the fibre damage factor.

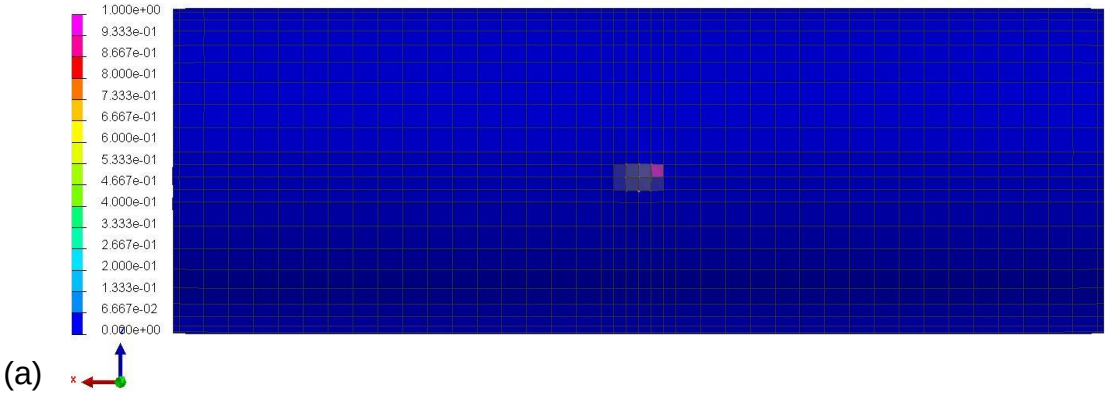

(a)

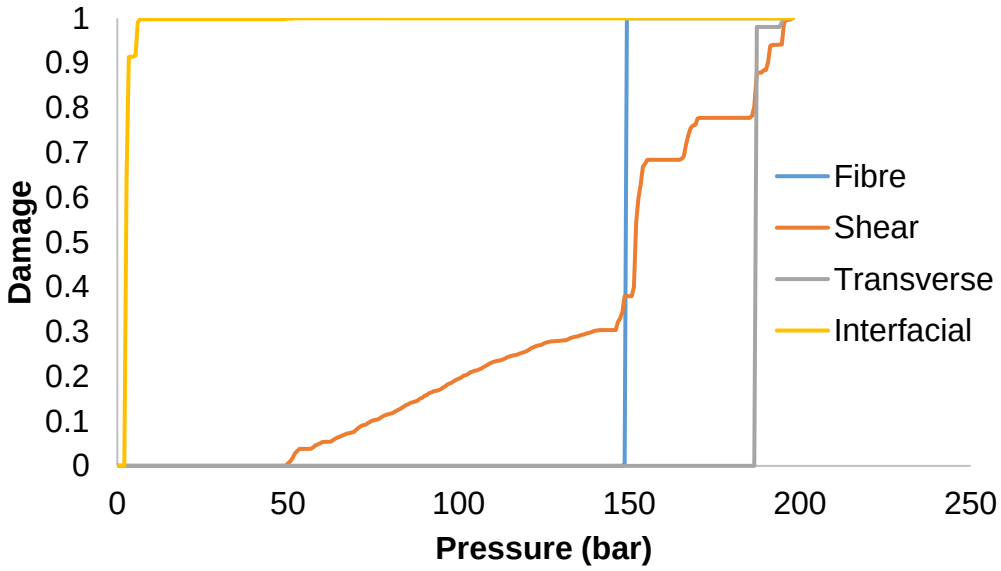

(b)

Figure 7.33 Second leakage for CPV with delamination and consecutive fibre cut defects due to (a) fibre damage 150.7 bar and (b) damage evolution at second layer of inner intact shell tied weakly to outer defective shell for consecutive fibre cut and delamination defect. Colour map represents the fibre damage factor.

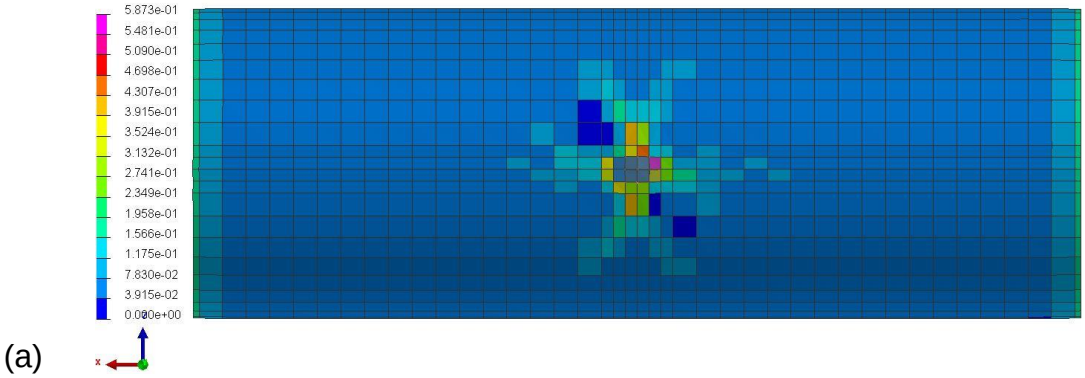

(a)

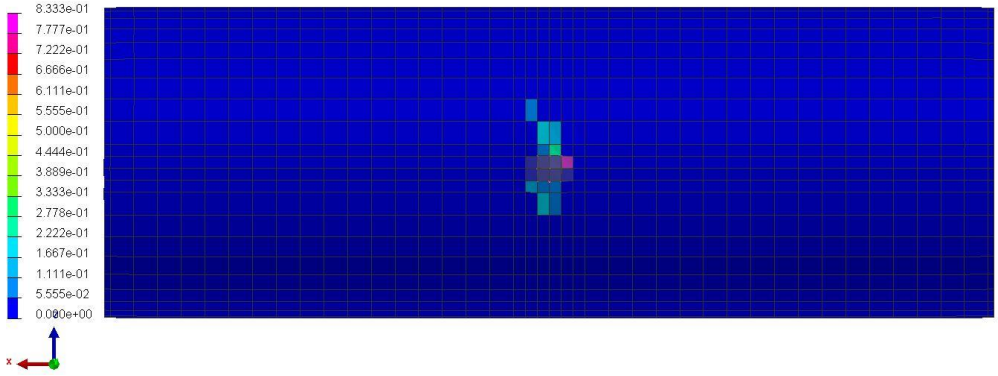

(b)

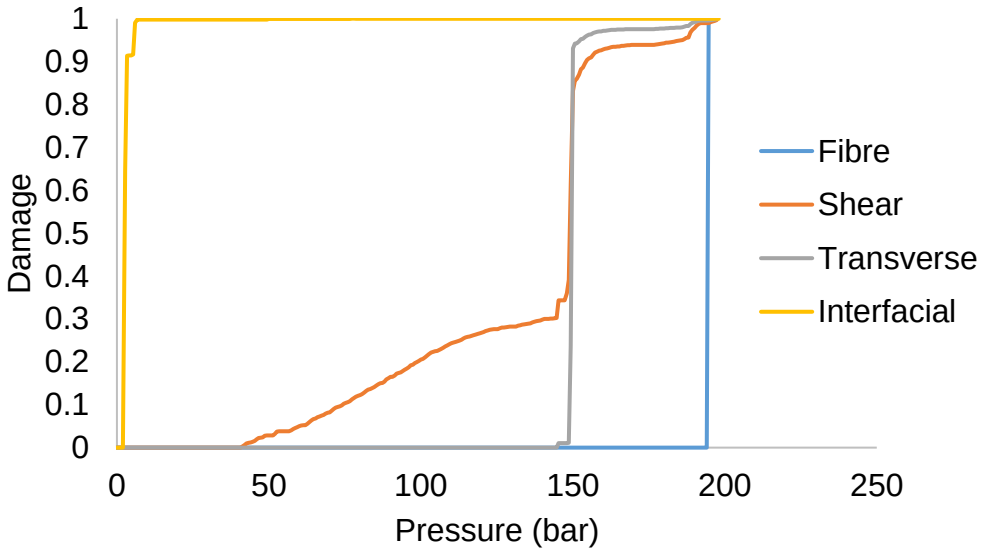

(c)

Figure 7.34 Second leakage for CPV with delamination and consecutive fibre cut defects due to (a) shear and (b) transverse damage at 150.7 bar and (b) damage evolution at third layer of inner intact shell tied weakly to outer defective shell for consecutive fibre cut and delamination defect. Colour maps represent the matrix shear and transverse damage factors respectively.

7.3.11 Design pattern for LBB development

The success of the LBB concept is based on the adequate delay that provides significant separation of the occurrence of the first compared to the second leakage incident. The fibre cut types of defects indicate that the LBB behaviour can be achieved for relatively high fibre cut damage providing separation between the first and second leak incidents. An investigation was carried out on an additional design feature, the patch, aiming to increase further the pressure difference of the first two leak occurrences. The selection of the best design of the patch was based on an examination of its thickness. The results indicated that the addition of four and eight layer patch provides effective performance for the development of the LBB concept. Due to only a slight increase of performance of the eight compared to the four layer patch, the focus was set onto the latter. Further optimisation was carried out through the reduction of the stress concentration points of the square defective shape through its alteration into a circular region. In this case, optimal performance is achieved for the fibre cut damage range of 75%-99% in terms of delay between the occurrence of the first and second leak incidents. Ultimately, the case of 87.5% fibre cut damage in a circular defective area was selected for the validation and proof of the concept as it provides the highest possible delay. Even though this fibre cut damage case does not fully deteriorate the primary function of the pressure vessel for the fluid storage under internal pressurisation, its application to real CPV cases leads to relatively low pressures at which the first leakage occurs. Interfacial defects, as well as the combination of the two types of defects under study, did not lead to scenarios more successful than the four layer patch for circular defective areas.

8 Assessment and validation of LBB concept

This chapter is dedicated to the assessment of the LBB concept performed through hydrostatic burst test of an intact tubular vessel as control test and a vessel manufactured utilising a pattern with defects as proposed in Chapter 7. The initiation of damage that led to leakage was identified on tubular vessels without and with introduced defects and is correlated to the damage initiation suggested by the respective models. The validation of the LBB concept is carried out through comparison of the experimental to the simulation damage and pressure results for tubular vessels.

8.1 Manufacturing of composite tubular vessel with effective defect pattern

A composite tubular vessel utilising the preferred defect design pattern, as described in Chapter 7, was manufactured for the validation of the LBB concept. This involves a circular defective fibre area with 87.5% fibre cut damage and a four layer reinforcing patch around the defective area. The defects were drafted on laminated paper that was used as indicator for the accurate positioning of fibre cuts. Two different patterns were drawn to account for the different fibre orientation of each layer. The 8 mm circular defective area was divided into chords perpendicular to the fibre orientation at a lateral distance of 1 mm. The chords were used for the positioning of the fibre cuts which correspond to 87.5% of the cross section of the length. The fibre cut lines at each cross section were placed at horizontal intervals of non-defective lines to the nearest of 0.5 mm distance. The circular fibre cut designs for a ±55° layup are presented in Figure 8.1.

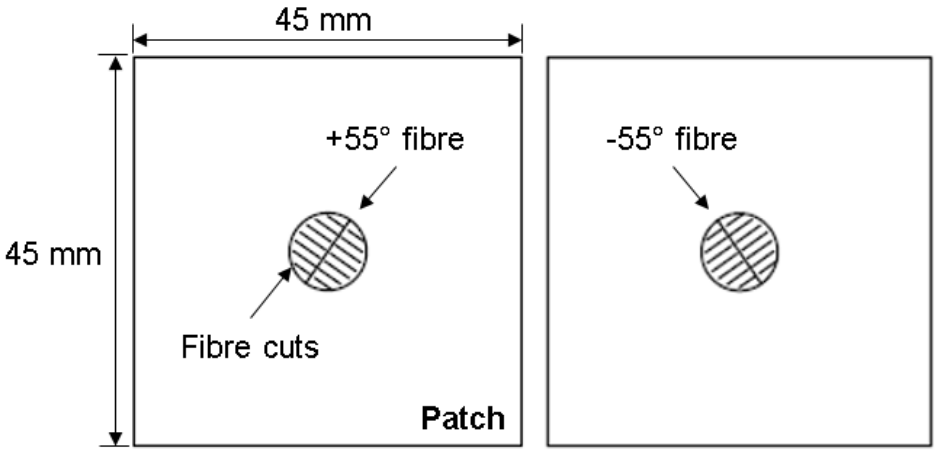

Figure 8.1 Design of circular fibre cut defective area for ±55° layup

The manufacturing process of the defective pipe was based on the respective manufacturing process of the intact pipe that was presented in section 4.2.2. The layup comprised 8 layers at $[\pm 55°]_{2s}$ stacking sequence. A laser setup was utilised to indicate the centre of the composite structure for the accurate positioning of the defects. The laser setup which is presented in Figure 8.2 consisted of a video camera with laser pointer and a metallic base.

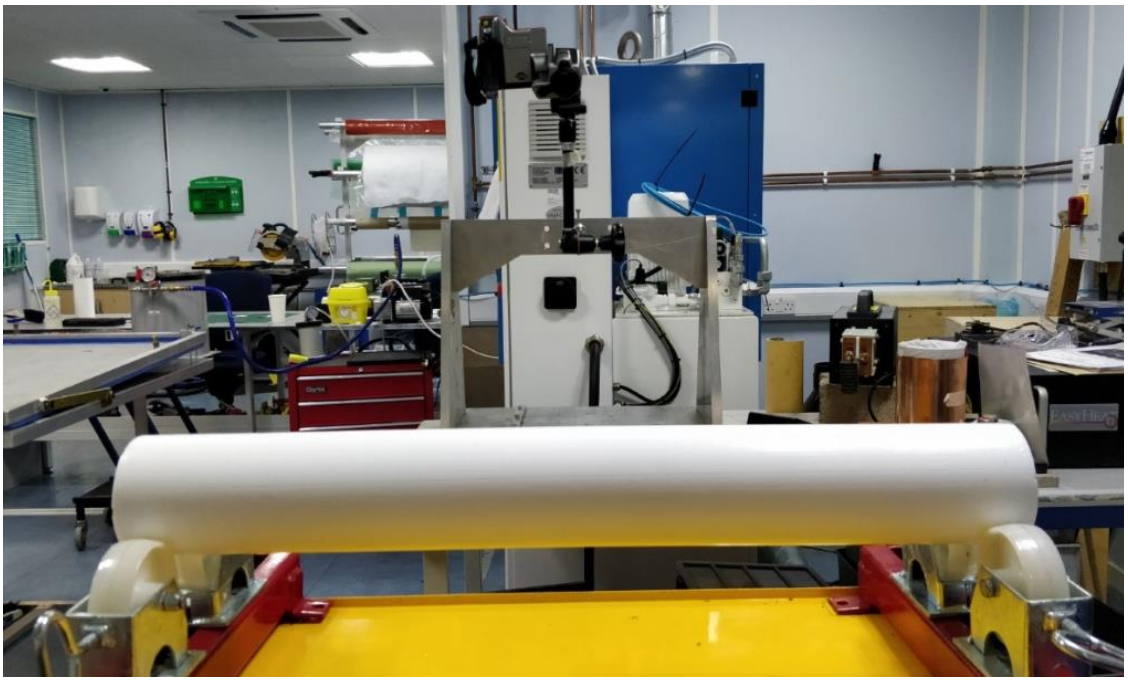

Figure 8.2 Laser setup consisting of camera with laser pointer and a metallic base

Each layer was wound around the PTFE Virgin-FE1000 Rod up to approximately the middle of the structure where the illuminated dot was. A small thin metallic sheet was utilised underneath the location of the layer where the defects were implemented in order to avoid the creation of slits on the mandrel or other layers of the stack. Utilising the laser setup as guidance, the centre of the laminated paper, where the defects of the corresponding to the fibre orientation design are, was positioned at the illuminated location as illustrated in Figure 8.3. A scalpel was used in order to introduce the defects cutting on the lines of the laminated paper which represent the fibre cut damage of 87.5%. Subsequently, the thin metallic sheet was removed and the remaining part of the layer was wound around the mandrel. All layers of the layup sequence were wound in the same way using the design on the laminated paper that corresponded to the respective fibre orientation. The patch that was attached around the defective area consisted of four layers 45x45 mm^2 at $[\pm 55°]_s$ stacking sequence and a circular hollow middle at a diameter of 8 mm.

(a)

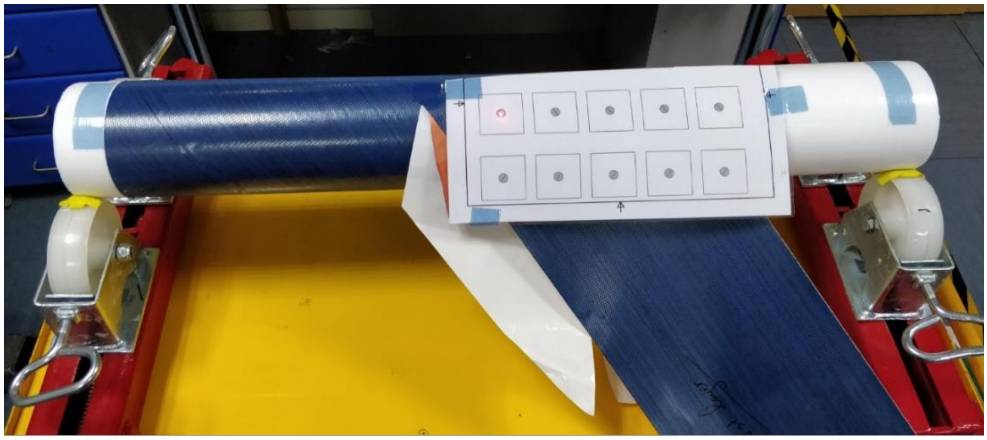

(b)

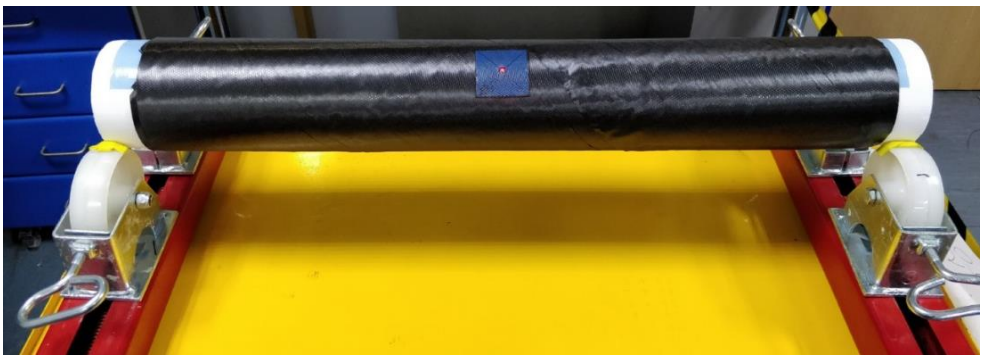

Figure 8.3 Manufacturing process of composite pipe: (a) introduction of defects and (b) attachment of patch.

The composite structure was then wrapped with two layers of Shrink Tite tape before its curing. The curing process of the pipe, as well as its preparation for testing and the attachment of the end caps was the same as the procedure described in section 4.2.2. The strain gauging took place using seven 3 mm rectangular rosette gauges supplied by Techni Measure Ltd. The locations of the strain gauges were one on the top of the defective area, one on the top left side of the patch, two strain gauges, each one positioned in the middle of the distance between the centre of the pipe/defective area and the two end cap edges, longitudinally aligned and three at the periphery of the pipe at 90° angular intervals from the strain gauge located in the middle of the pipe. The strain gauges of each rosette were numbered as illustrated in Figure 8.4 in order to facilitate the correlation of the extracted strain data to the exact locations and angles.

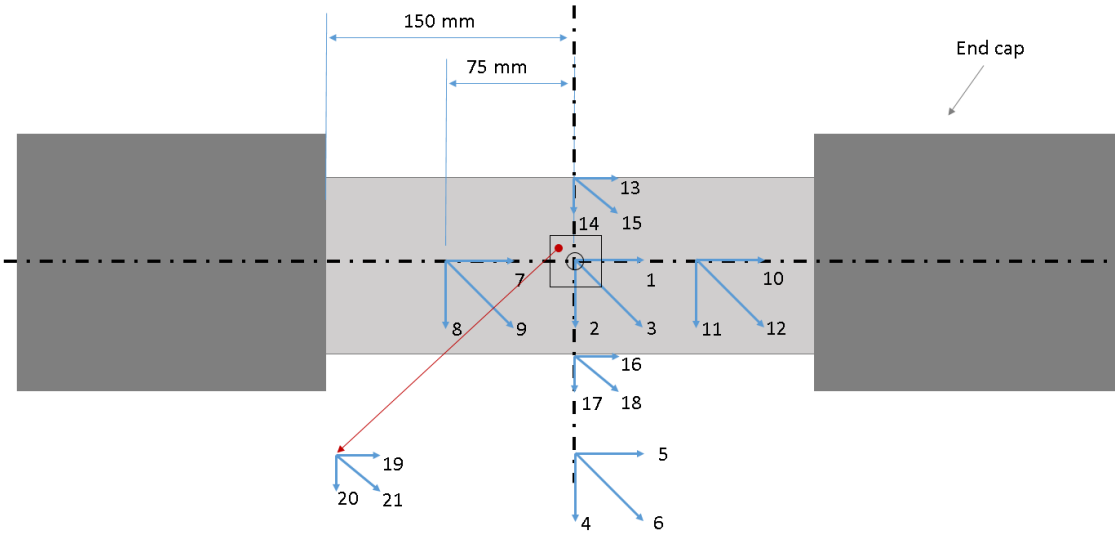

Figure 8.4 Strain gauge locations for pipe with fibre cut defects and a four layer patch

8.2 Damage assessment on control tubular vessel

One intact pipe with $[\pm 55°]_{2s}$ stacking sequence was tested under internal pressurisation as described in section 4.3.4. The testing of the intact pipe was utilised for the verification of the model and as the control for the assessment of the LBB development on a pipe with deliberately introduced defects. The experimental results presented in Figure 8.5 show the pump inlet pressure during

the experiment. The initial part of the curve, up to about 5 min, corresponds to filling. After this phase the pressure increases rapidly at a rate of about 67 bar/min after approximately 5.3 min of loading. At a pressure of 135 bar leakage occurs at the centre of the pipe which leads to drop of pressure in the vessel. The test was continued for the identification of the burst pressure of the pipe by increasing the flow rate in order to overcome the loss due to the leakage. Ultimate failure occurred at 137 bar due to slippage of one of the two end caps as a result of adhesive bond failure.

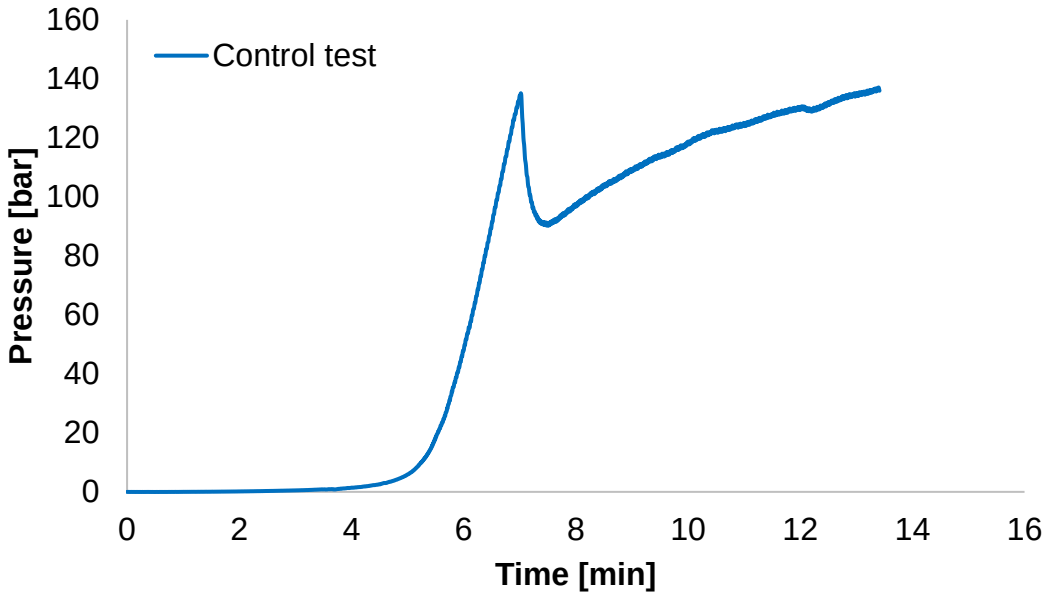

Figure 8.5 Pressure versus time results for intact pipe test

Figure 8.6 illustrates the measured strains as a function of internal pressure for the linear part of the curve presented in Figure 8.5. The locations of the strain gauges are presented in Figure 4.15. The results of Figure 8.6(a) for the hoop strains indicate that the strain gauge located at the centre of the pipe close to the location where the leakage occurs (strain gauge 2) has a different response compared to strain gauges positioned antidiametrically (strain gauge 4) or away from the area of leakage (strain gauge 8). The almost identical behaviour of the strain gauges located antidiametrically and away from the leakage area indicates that uniform stresses and strains were applied at the free pipe area. The presence of a potential manufacturing flaw or the gradual development of certain failure

mechanisms in the middle of the pipe close to the central strain gauge led to the occurrence of leakage, which is explained by the irregular strain response of the gauge compared to the rest of them. Figure 8.6(b) indicates that the axial strains with respect to pressure show similar responses at the three different locations, as per Figure 4.15, at which the strain gauges were attached. This is explained by the uniform loading state at the free pipe length similarly to the hoop case.

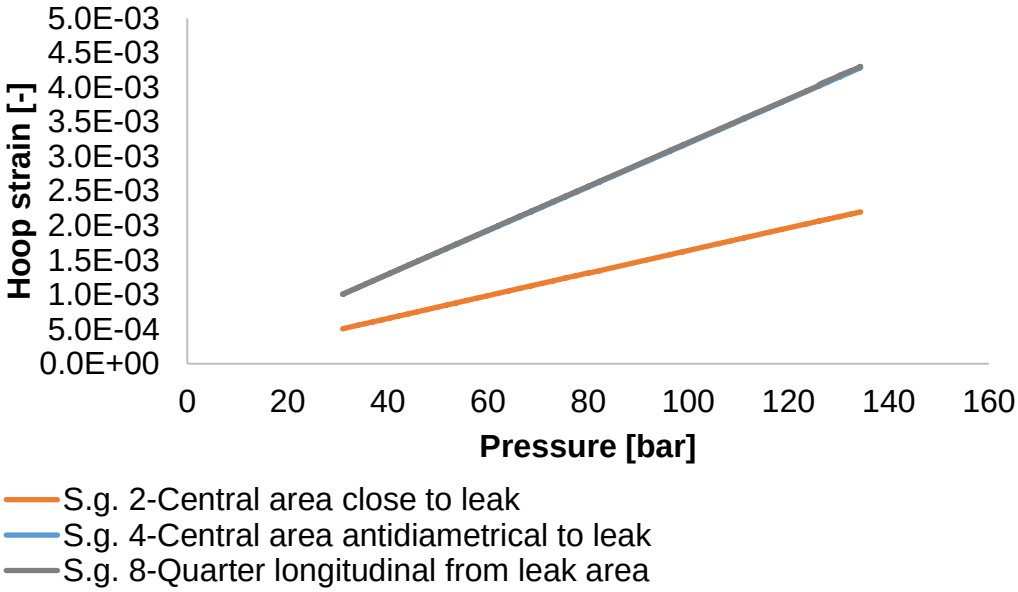

(a)

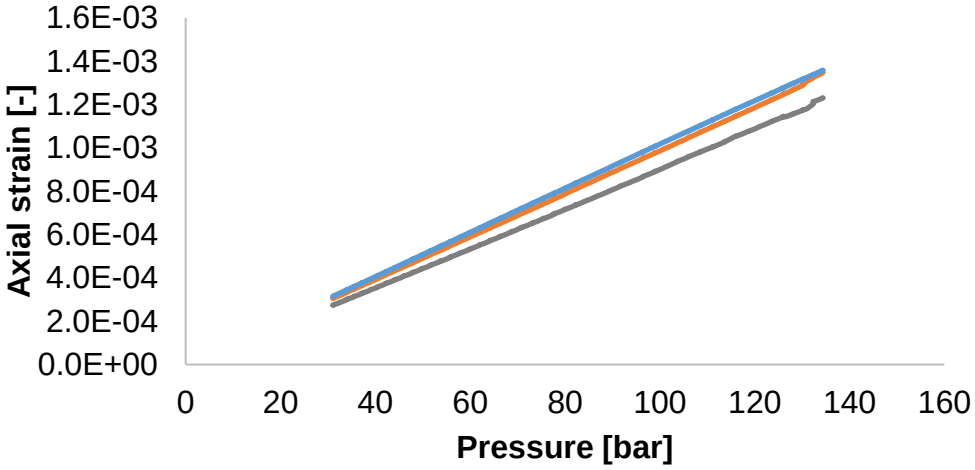

(b)

Figure 8.6 Plots of (a) hoop (S.g. 2, 4, 8) and (b) axial (S.g. 1, 5, 7) strains versus pressure results for intact pipe

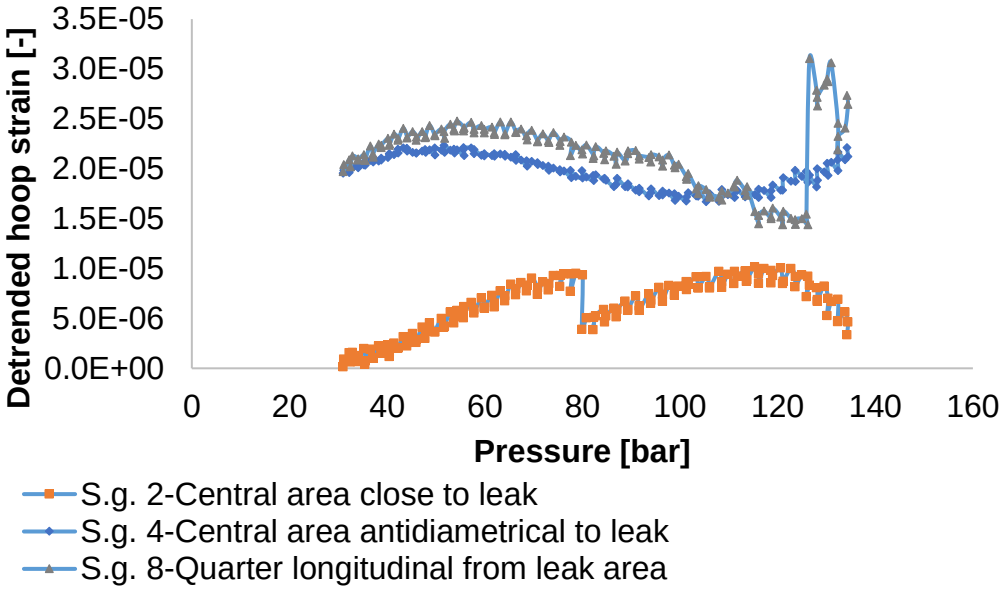

(a)

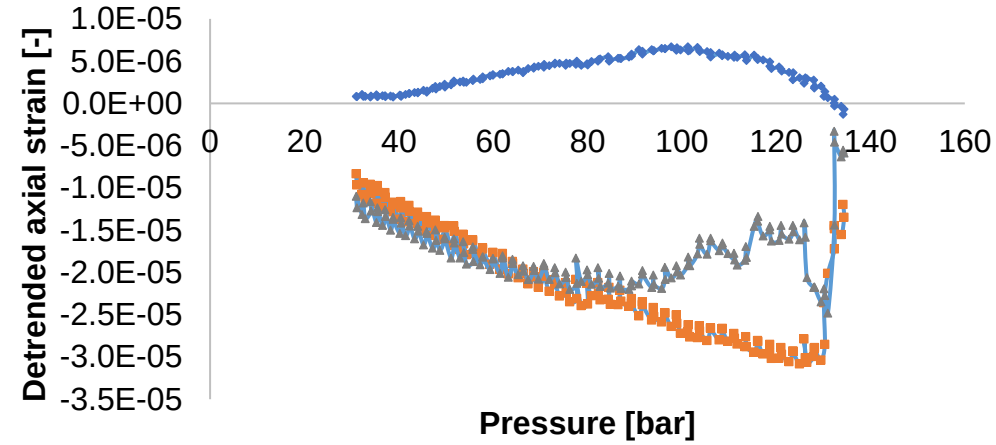

(b)

Figure 8.7 Detrended plots of (a) hoop (S.g. 2, 4, 8) and (b) axial (S.g. 1, 5, 7) strains versus pressure results for intact pipe

The strain versus pressure curves were detrended so that elastic effects do not dominate the results, whilst non-linearity due to damage and failure can be identified more easily. Figure 8.7 illustrates these results. Figure 8.7(a) shows damage initiation in the hoop strain close to the leak (strain gauge 2) at a pressure of 80 bar. The strain gauge diametrically opposite to the leak (strain gauge 4) did not indicate any damage. The results acquired from the strain gauge (strain gauge 8) located between the centre of the pipe and the edge of the free end,

longitudinally aligned to strain gauge close to the leakage (strain gauge 2) demonstrate the occurrence of damage at 126.5 bar. Figure 8.7(b), indicates damage shown in axial strain close to the leak (strain gauge 1) at approximately 130.3 bar. The strain gauge antidiametrically located to the leak (strain gauge 5) did not demonstrate damage initiation, whilst the gauge located between the centre of the pipe and the edge of the free end (strain gauge 8) indicates damage at 126.5 bar.

The pressurisation rate of the control pipe was extracted and utilised as input to the intact pipe model described in section 7.2.1. The pressurised pipe indicated failure at 564.6 bar. Analysis of the damage evolution during loading show that the dominant failure mechanisms leading to failure are matrix shear damage and delamination. Figure 8.8(a) illustrates the cylindrical model at the moment damage develops in the middle of the structure. The focus is on the examination of the failure pressure developing in the middle of the pipe as damage in the edges is governed by constraints in the model rather than real physical effects. Figure 8.8(b) shows the damage development at a layer in the middle of the pipe. As the pressure increases, additional damage takes place due to matrix shear, transverse and fibre damage as well as delamination as illustrated in Figure 8.9. The value of damage associated to the leakage of the experimental control pipe is approximately 6%, which is significantly low compared to the damage threshold of 50% utilised as indication of failure. The low damage factor signifies that other potential failure mechanisms drive the rupture due to manufacturing flaws.

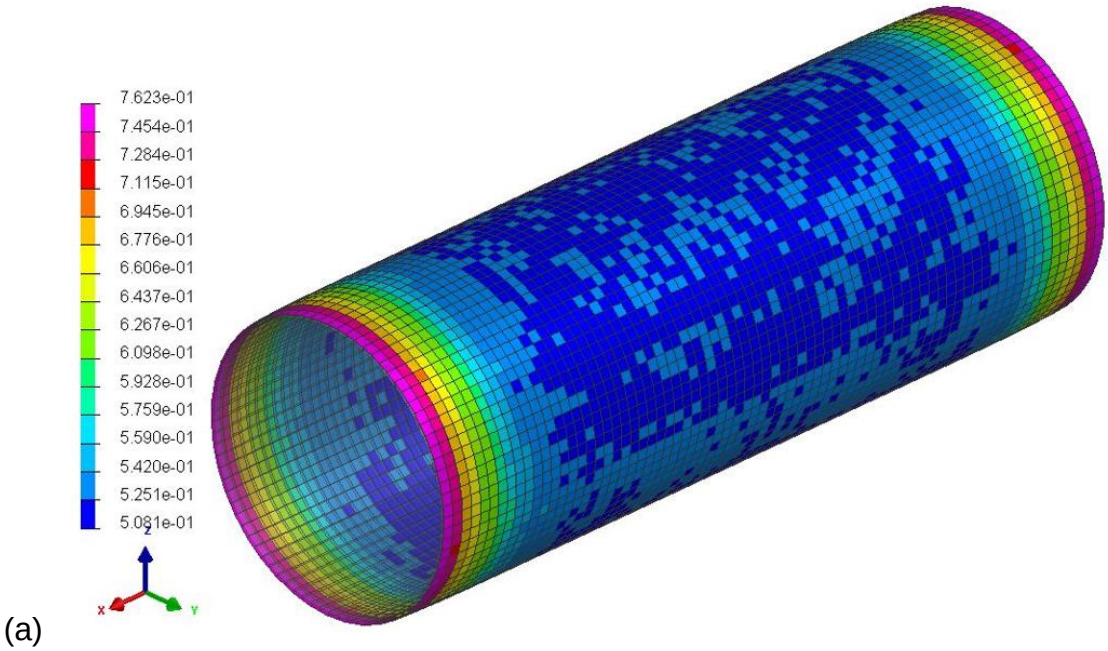

(a)

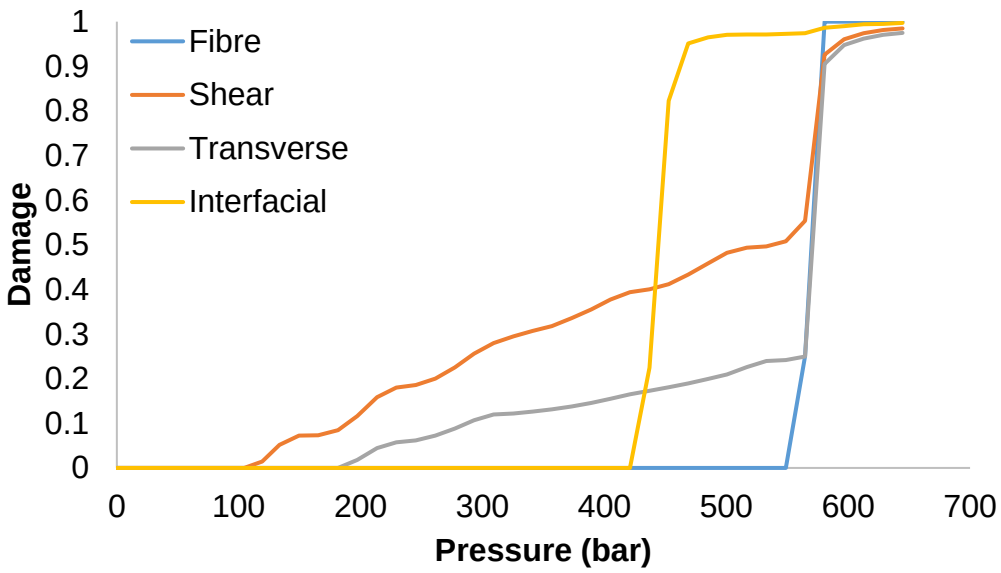

(b)

Figure 8.8 Composite cylindrical model (a) failure response under internal pressurisation at 564.6 bar and (b) damage development at shell in the middle of the pipe. Colour map represents the matrix shear damage factors.

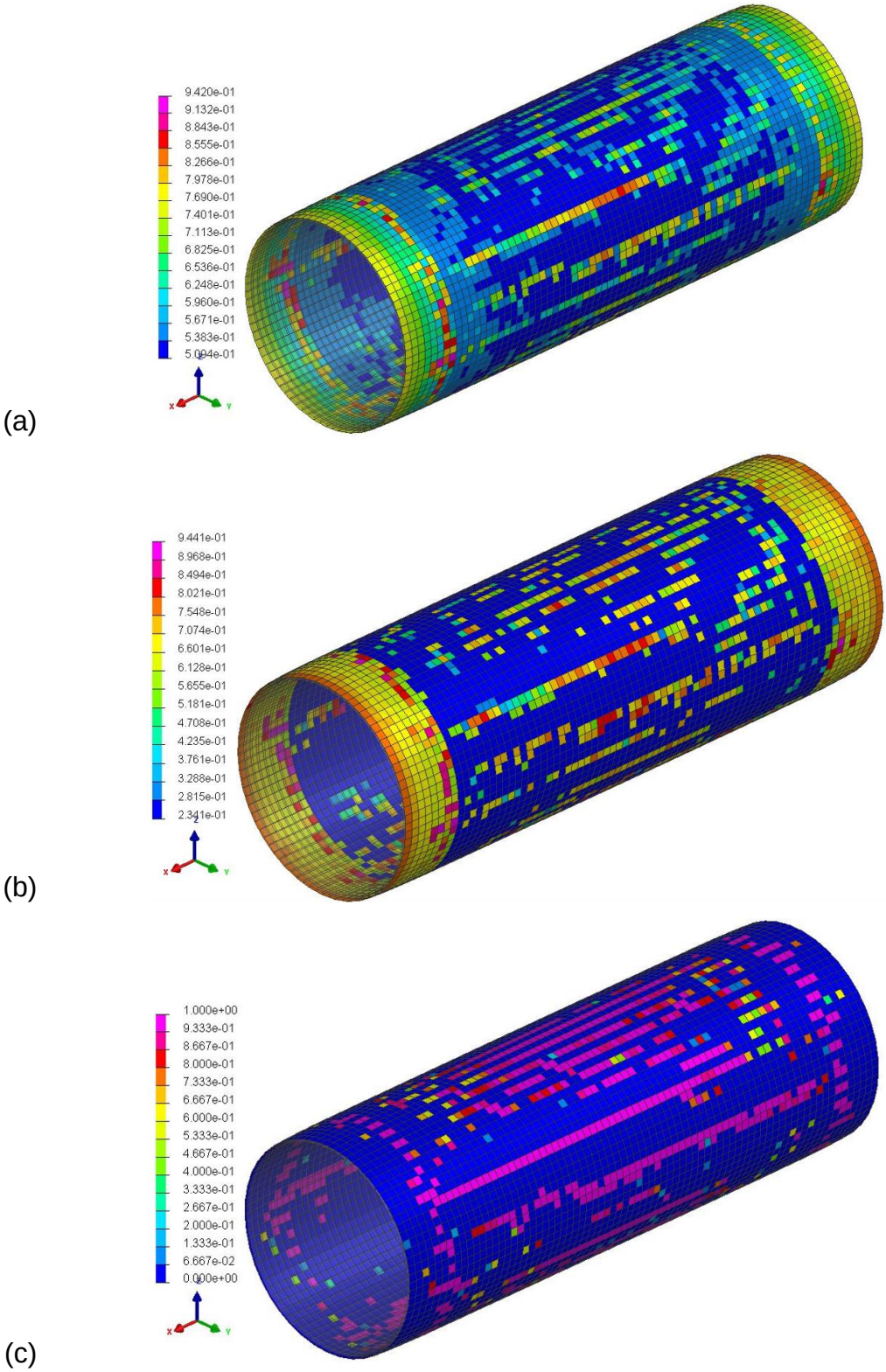

Figure 8.9 Development of (a) matrix shear, (b) transverse and (c) fibre failure mechanisms at 580.6 bar. Colour maps represent the matrix shear, transverse and fibre damage factors respectively.

8.3 Validation of LBB concept

The evolution of pressure over time in the test of the pipe described in section 8.1 is illustrated in Figure 8.10. Similarly to the intact pipe, the pressure was increased slowly until the entire volume of the pipe was filled with water. The pressure increased linearly at a rate of about 72 bar/min after 4.4 min of loading until the occurrence of leakage at approximately 150 bar. Based on the video the leakage did not occur at the defective area but from a point of the pipe close to the end cap. At the beginning of the leakage, the flow rate increased as indicated by the plateau of pressure until the ultimate functional damage of the pipe at approximately 178 bar due to excessive leakage.

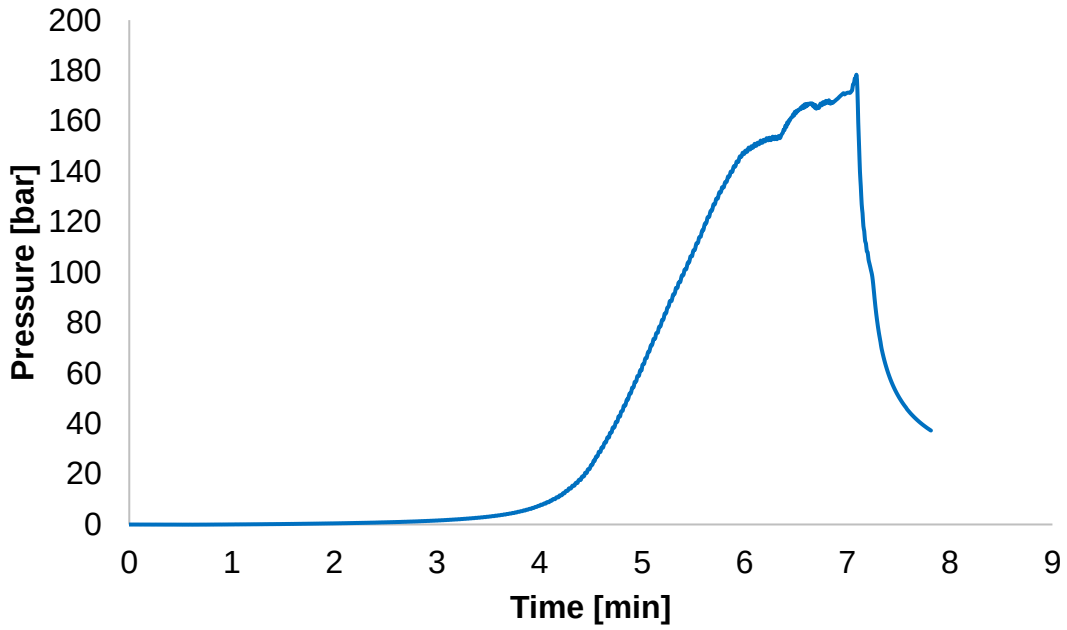

Figure 8.10 Pressure versus time results for defective pipe test

The hoop and axial strains as a function of pressure for the different strain gauges, located as illustrated in Figure 8.4, are depicted in Figure 8.11. The data correspond to the linear segment of the pressure versus time curve between 4.8 and 5.5 min of the loading, as only within this range non-linearities were observed. The strain gauges show almost identical responses apart from the strain gauge at the location of defects and of the patch which include certain irregularities. The strain gauge results from the defective area indicate slightly

higher strain response compared to the rest of the locations. The difference in strain response of the strain gauge located on the patch is due to the locally increased pipe thickness to 12 mm. The results of Figure 8.11(b) indicate that all strain gauges in the axial direction have similar response. A slightly different response is observed for the strain gauge of the patch due to the higher thickness location compared to the other locations. A non-linearity is also observed at 94 bar, which indicates damage occurrence, potentially attributed to manufacturing errors such as offset of the defect pattern through the thickness or inclusions.

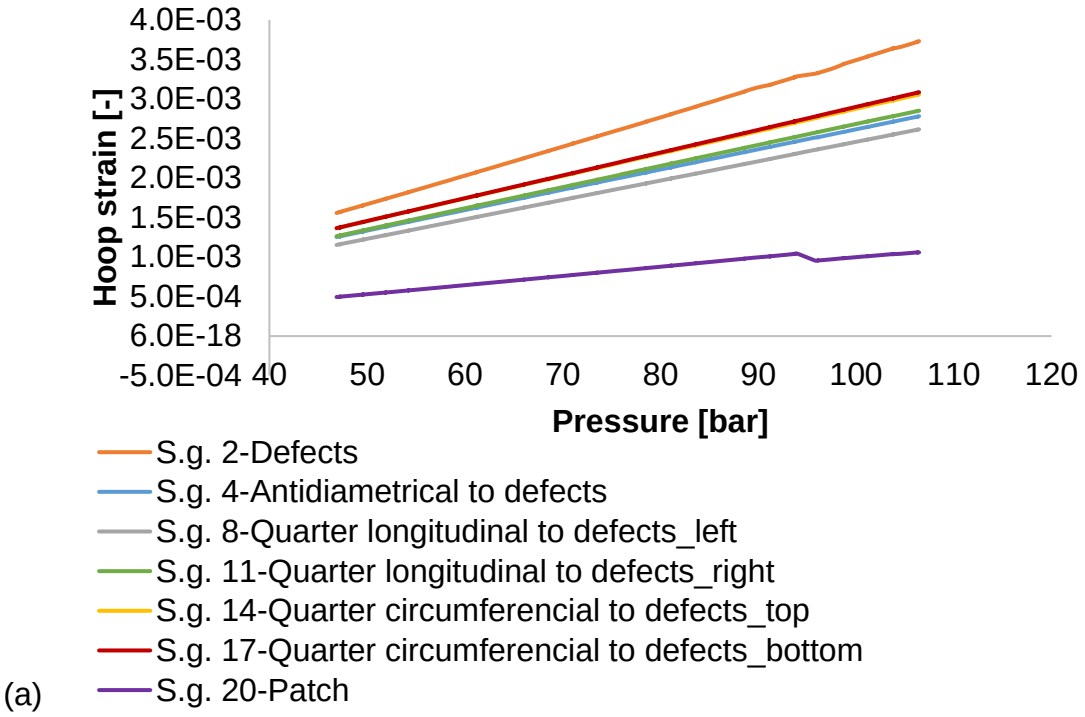

(a)

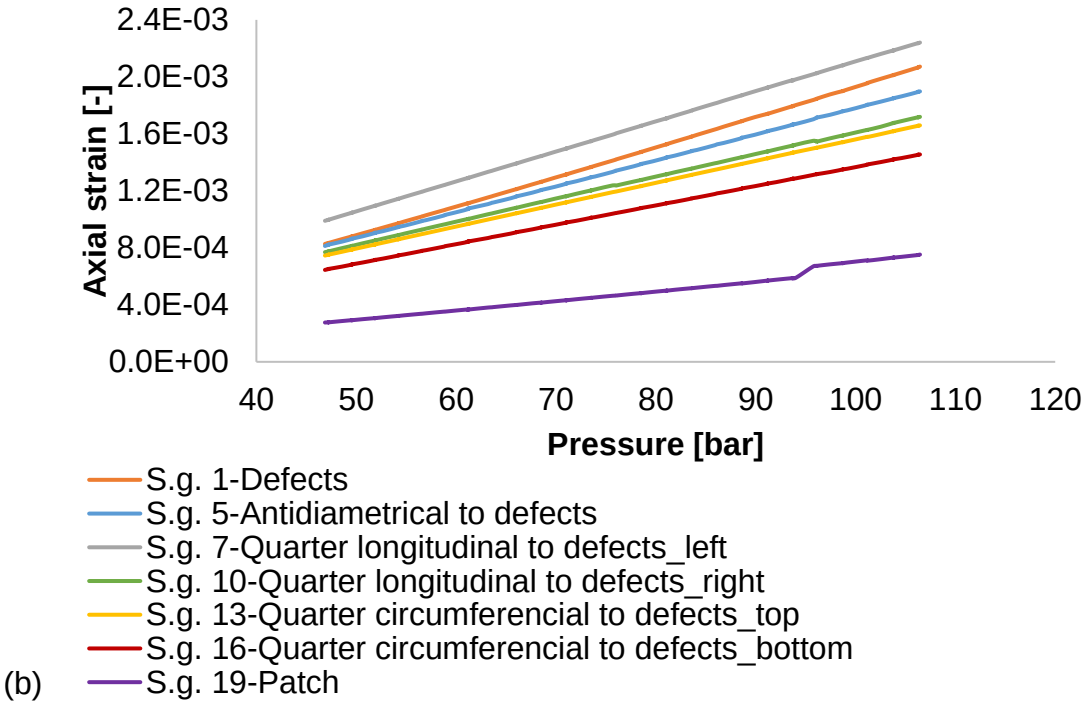

(b)

Figure 8.11 Plots of (a) hoop (S.g. 2, 4, 8, 11, 14, 17, 20) and (b) axial (S.g 1, 5, 7, 10, 13, 16, 19) strains versus pressure results for defective pipe

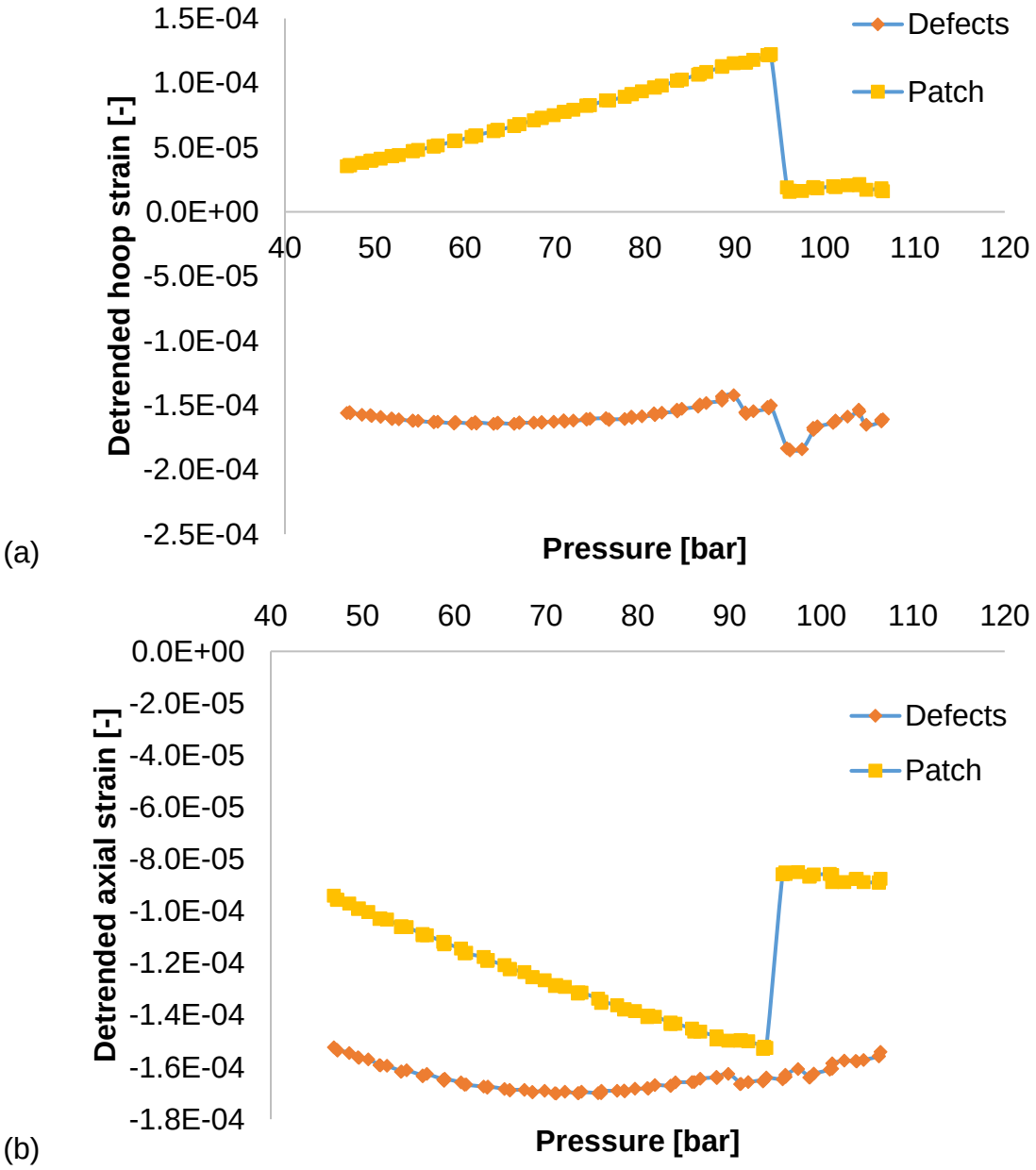

Figure 8.12 Detrended plots of (a) hoop and (b) axial strains versus pressure results for the location with defects (S.g. 2 hoop, S.g. 1 axial) and for the patch (S.g. 20 hoop, S.g. 19 axial)

The hoop and strain curves were detrended in order to uncover potential non-linearity. The results for the area with defects and of the patch are shown in Figure 8.12. The results indicate that damage initiation occurs in the area with defects at approximately 90 bar, whilst damage development lasts up to about 105 bar. Damage at the patch is manifested at about 97 bar.

The model described in section 7.3.6 with fibre cut damage of 87.5% was updated utilising the experimental loading history of the LBB pipe. The simulation results indicate that initiation of damage exceeding the threshold of 50% occurred at a pressure of 93 bar. This is in very close agreement with the experimental observations as they differ by 2%. Figure 8.13 illustrates the failure mechanisms leading to the first failure, as well as the damage evolution in the defect area. The first leakage occurs as a combination of fibre, matrix shear and transverse deformation as well as delamination with the first being the most dominant through the thickness in all layers of the two shells. The second leakage for damage threshold of 50% takes place at pressure of 385 bar, caused by combination of matrix shear, transverse damage and delamination. As illustrated in Figure 8.14 matrix shear damage starts occurring at 273.3 bar. However, it is not until 385 bar that the threshold damage of all layers of the two shells through the thickness reaches the value of 50% in order leakage to occur.

Correlating simulation and experimental results leads to the conclusion that the leakage generation from points different to the area with introduced defects might be the result of manufacturing flaws that led to relief of pressure from these locations. However, due to the fact that the leakage was expected to take place at 93 bar from the defective area, whilst this took place at 153 bar even though from a different location, indicates that the damage threshold of 50% does not necessarily correspond to leakage. The investigation on the damage occurrence with respect to pressure at the defective area between the simulation and experimental results leads to the assumption that the damage threshold corresponding to leakage should be equal or higher to the damage threshold of the defective location the moment leakage occurred on the tubular vessel from the point next to the end caps. The damage threshold at the defective area the instant leakage occurred on the tubular vessel during hydrostatic burst was calculated at 90%. Therefore, leakage can be assumed to occur for damage over 90%.

(a)

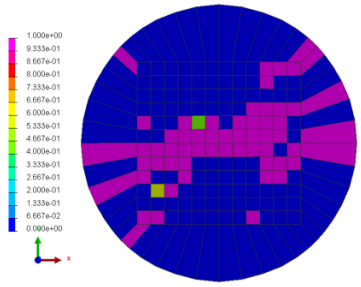

(b)

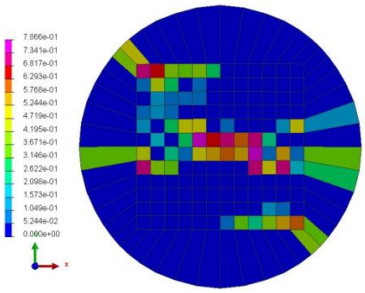

(c)

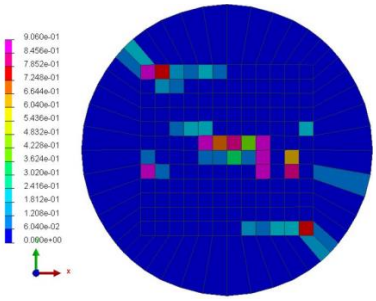

(d)

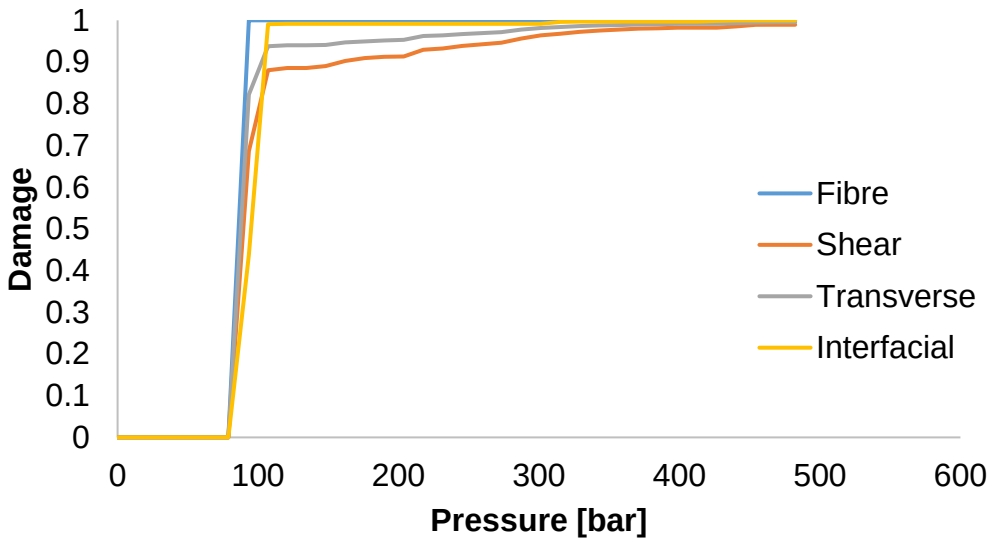

Figure 8.13 First leakage due to (a) fibre, (b) shear and (c) transverse damage at 93 bar and (d) damage evolution of layer of defective shell in the middle of the circular defective area. Colour maps represent fibre, matrix shear and transverse damage factors respectively.

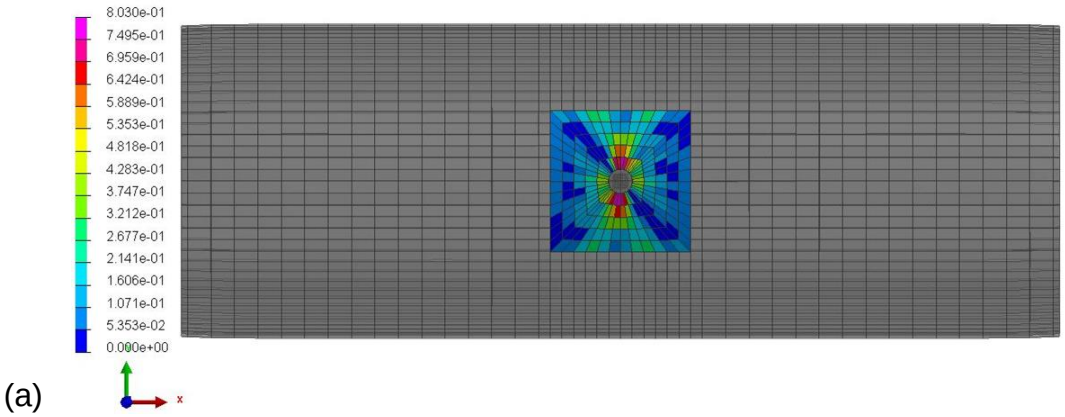

(a)

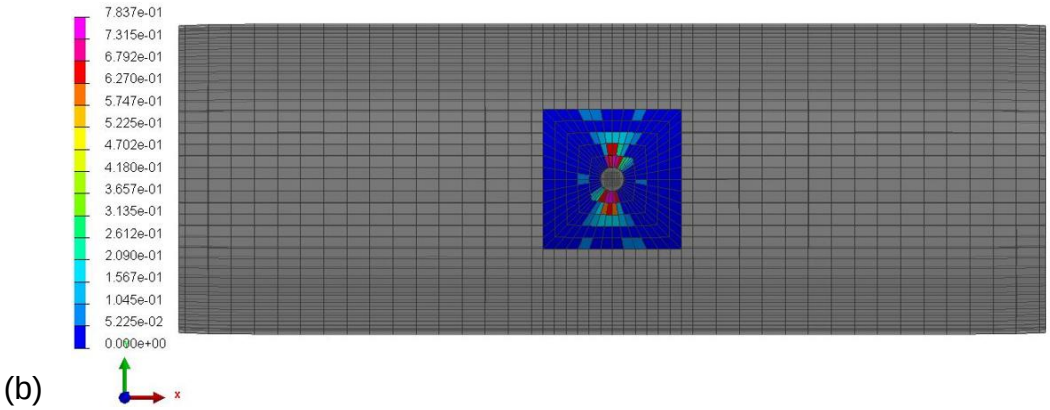

(b)

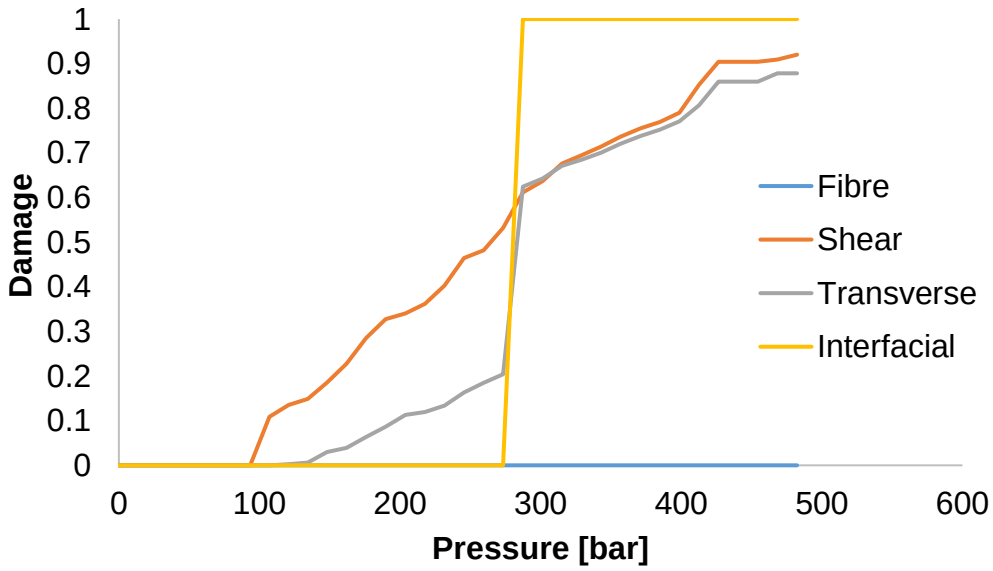

(c)

Figure 8.14 Second leakage due to (a) shear and (b) transverse damage at 385 bar and (c) damage evolution of layer of intact shell of the patch above the circular defective area. Colour maps represent matrix shear and transverse damage factors respectively.

A 25x25 mm^2 piece of pipe from the defective area was cut and examined through XCT to identify the failure mechanisms developing around the fibre cut defects. Figure 8.15 illustrates the results of the XCT focused on a fibre cut defect in order to verify the development of critical failure mechanisms around the defects under internal pressurisation. The 3D image of the extracted pipe piece is illustrated in Figure 8.15(a) in the centre of which the defective area can be observed. The red point/cross refers to the same characteristic of the structure in different views as presented in Figure 8.15(b)-(d). Figure 8.15(b) represents the defective area through the thickness at a depth of 2.48 mm from the curved surface of the piece. The total thickness of the pipe piece based on the reconstructed XCT images was 3.42 mm. The fibre cut defects are demonstrated as intralaminar defects and in some cases coalesce with defects of the same or neighbouring layers through the interface forming interlaminar cracks. Even though high resolution is not achieved through the XCT images, fibre damage and delamination areas associated with matrix damage can be observed, which is in agreement with the simulation results for the occurrence of the first leakage due to combination of these failure mechanisms. This indicates that the XCT image probably corresponds to an early stage of the development of the first leakage, where the damage mechanisms leading to its occurrence are at their commencement. Resin rich areas can also be observed around the slits. The resin flow taking place fills these locations leading to the creation of resin rich areas [163]. Similarly, the area directly above the defects is filled with resin as illustrated in Figure 8.15(c)-(d). This is the result of the difference in thickness due to the attachment of the four layer patch to the surrounding area of the defects. In this large resin rich area, air pockets and foreign material inclusions are evident. The matrix cracks created at that location are the result of the lower strength of the matrix compared to the composite material.

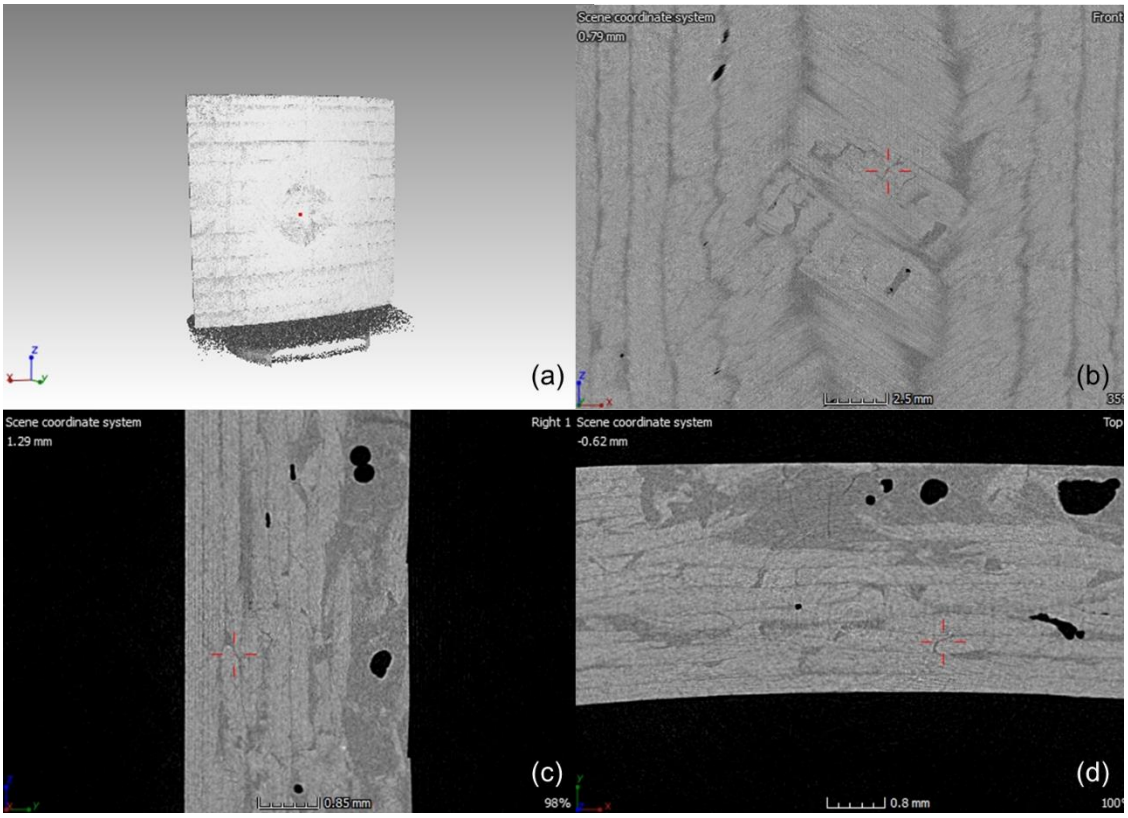

Figure 8.15 XCT of piece of pipe with fibre cut defects

9 Discussion

This chapter presents an overall discussion covering the main aspects of the work, including constitutive material model properties, as well as the overall development of the LBB concept comprising the simulation methodology and studies, experimental investigation and validation.

9.1 Constitutive model material properties

Damage material model properties were initially calculated through the conventional methodology utilising analytical model equations based on the experimental results. However, inaccuracies may be introduced due to human error in the selection of stress and strain values/ranges for the identification of the material properties. In this work, this was tackled through the fitting of analytical solutions to the experimental response utilising the error minimisation function of the sum of squared error. The analysis took place through the GRG nonlinear Microsoft Excel Solver making use of the Visual Basic for Applications (VBA) programming language. The GRG nonlinear solver is based on inverse analysis and its solution is very often highly dependent on local optimum values of initial conditions instead of a global optimum response. Therefore, vectors defined using the GRG solver might not represent a global optimum and hence global optimisation methods might need to be followed [326, 327].

9.2 Simulation of LBB

An investigation for defect introduction was carried out on CPVs for the development of LBB. This was carried out through the introduction of fibre cut defects and interlaminar weak areas, which control the initiation and propagation of damage in the structure, for the development of a safe-fail structure that can withstand damage and be progressively led to its failure [163, 188]. The methodology was initially developed and applied on flat specimens. The fibre cut methodology was validated through experimental and simulation investigation. The methodology for interlaminar weak bond areas was not validated due to deviation of simulation to experimental results. This is attributed to the absence of factors coupling the damage modes and in particular the delamination to matrix

shear and transverse damage. This can be resolved through the use of damage models that take into account the interaction between various damage mechanisms [256, 328, 329].

The developed defect introduction methodologies were investigated through simulation of CPVs consisting of two shells through the thickness and tied utilising information from out-of-plane tests. Further investigation can be carried out on defect introduction on each layer; however, deviation is expected to occur due to the introduction of the interface. Improvement of this is feasible by experimental investigation of similarly oriented plies as well as similarly angled plies with opposite signs in order to acquire out-of-plane results for both types of interface. Fibre cut defects embedded in two shells through the thickness showed that LBB can be achieved for high fibre cut damage, whilst the incorporation of interlaminar weak bond regions in combination with fibre cut defects showed LBB behaviour only for the highest fibre cut damage. This suggests that even though the LBB can be established, for real CPV applications leakage will occur in relatively small pressure values. In this research work, the introduction of defects was focused on one particular size in the case of square and circular defective areas. The investigation of a wider range of geometries of defects can lead to optimisation of the interaction between the size of the defective area and the pipe [149, 150]. The addition of a patch around the defective areas reinforced the surrounding intact material and enhanced gradual propagation of damage until the ultimate failure [144]. The present work focused on one size of patch. Examination of a range of sizes for the patch can lead to selection of an optimum so that damage does not occur around it on uncovered locations of the pipe.

An assumption of 50% damage threshold through the thickness for all layers of both shells was utilised to account for the occurrence of damage which leads to leakage. Alternative approaches can be utilised for the investigation of the fluid flow through the defective wall, providing information on the quantification of leakage. These approaches can include the utilisation of porous media to represent the defective areas in composite tubes or channels, which depending on their geometry [330], can lead to capillary flow or flow through porous media governed by Darcy’s law [331].

9.3 Experimental investigation of LBB

The manufacturing of composite pipes utilising hand lay-up of tow-preg sheets from prepreg rolls led to good quality composite pipes as examined through C-scan. However, during testing leakage occurred at a pressure which is associated to 6% damage based on the simulation results; a value significantly lower than the damage threshold of 50% used for the indication of leakage initiation. Therefore, it was concluded that defects induced during the manufacturing process caused the leakage on the pipe. Manufacturing errors included due to human error can be tackled through the use of automated filament winding equipment. The incorporation of the defective locations was performed in precise locations ensuring the exact fibre cut damage intended to be used. The use of scalpel provides good accuracy, however, the use of laser [161] and other automated equipment can eliminate the introduction of inclusions and human error with respect to the location of the defects and the cut damage applied. The attachment of end caps on the composite pipe, resembling the performance of a CPV [42, 44], was performed utilising adhesives providing high lap shear properties whilst ensuring even distribution and prevention of the creation of air channels through slow insertion of the caps.

Burst tests on an intact and a pipe with defects were carried out utilising a hydrostatic test rig. The occupation of the entire volume of the vessel with water led to the rapid increase of the pressure due to the small capacity of the vessel incommoding control of the fluid flow during the test due to the manual operation of the pressurisation system. Control of the fluid flow can be provided through hydraulic test rigs. The grip of the pressurised pipe ensured hoop and axial stresses to occur in a ratio of 2 to 1, respectively to resemble the function of CPVs. The identification of the exact location of the leak was carried out through bright coloured dye and video recording for safety reasons. However, the view of the camera was not able to record leak incidents at the lower part of the pipe. Therefore, the positioning of recording cameras should be such that the entire pipe is in view.

9.4 LBB concept validation

The LBB concept was validated on a composite pipe with fibre cut defects at damage of 87.5%. The comparison of the results from the experimental and simulation investigation for the indication of damage were in agreement and differed by 2%. The failure of leakage generation from the defective location is attributed to manufacturing defects at locations were leakage occurred leading to pressurisation relief, as well as to an early stage damage development associated with the 50% damage threshold at the locations were artificial defects were introduced. Having demonstrated that the prediction of the damage development on pipes around artificial defects is achievable, additional investigations for the identification of the damage threshold associated with the occurrence of leakage are required. An early conclusion is that this threshold corresponds to damage of more than 90%. Non-destructive evaluations such as C-scan and XCT were used for the validation and correlation of the damage mechanisms leading to failure. The use of C-scan before and after the pressurisation test did not show differences in the structure, which is the result of damage mechanisms being at their inception or due to the fact that matrix cracking and delamination close with the unloading of the structure. Illustration of structural damage can be possible for high damage values at stages where failure mechanisms have developed and propagated. The use of XCT provided details of the structure with regard to the failure mechanisms of fibre and matrix damage as well as delamination developing around the defects and of their interaction within the same or adjacent plies. XCT equipment usually corresponds to small dimension specimens in order to achieve high resolution images. Therefore, a trade-off relation exists between high resolution and area under study involving the risk that certain failure mechanisms might not be captured or might be interrupted, whilst in certain cases defects might be introduced by the cutting method.

10 Conclusions and suggestions for further investigation

10.1 Conclusions

The main conclusions of this research work are as follows:

1. The developed constitutive model based on the Ladevèze continuum damage model has been verified successfully through comparison of experimental and modelling results indicating a maximum error of 11.2 MPa for static tests and 5.3 MPa for cyclic tests.
2. The established methodology for the introduction of fibre cut discontinuities on $[0°]_{16}$ tensile specimens for the control of their failure was validated successfully at 20% fibre cut damage.
3. The incorporation of cut defects in the form of a concentrated square or circular area leads to the development of LBB behaviour, in which a first leakage occurs followed by a catastrophic failure. The increase of the fibre cut damage percentage as well as the incorporation of a patch leads to increased ability to discern between the first and ultimate failure pressure. The use of a two, four and eight layer patch around square fibre cut defective area leads to an increase of the second leak pressure plateau by about 20, 40 and 50%, respectively, compared to the case of defects without the patch. A circular compared to square fibre cut defective area leads to earlier separation between the initial and ultimate failure incidents. Pipe models with interlaminar weak bond areas and combination of those with fibre cut defective areas do not display substantial separation between the leak and damage failure occurrences.
4. The LBB behaviour did not occur from the area of the introduced weak points due to defects associated with the non-automated manufacturing process. However, the prediction of the LBB in terms of the initiation of damage from the introduced defects was successful with an error of 2% between experimental and simulation results.

5. A damage threshold of 90% is observed to be associated with the initiation of leakage against the assumed 50% damage threshold, which is found to be correlated to the initial stages of damage mechanisms development.

10.2 Suggestions for further investigation

Further investigation should be carried out for the expansion of this work as follows:

- Damage models with coupled in-plane and out-of-plane damage mechanisms can be utilised to account for the interaction developing between them during loading. This correlation is particularly significant for the examination of the interface, as matrix damage phenomena develop within it and lead to the occurrence of delamination damage. This can be utilised for the examination of the interfacial defects in combination with fibre cut defects on flat laminates as well as on CPV models.
- Further investigation on the pipe model can take place in order to include accurate interface properties between adjacent layers with the same offset orientation as well as of layers with opposite signs. This can take place through Mode I and Mode II out-of-plane testing.
- The simulation of the CPV utilising individual cylindrical shells to account for each layer can facilitate the development of the LBB concept through utilisation of a variety of design patterns through investigation of introduction of defects in different locations. An “S” type defect shape, similar to the one used for the validation of defect introduction methodology on flat specimens, can be potentially effective for gradual development of leak paths through the introduced defects, thus eliminating the use of reinforcing patch.
- Further examination on the size of defects and patch geometry with respect to the pipe diameter and containing pressure requirements can be performed for the identification of responses with development of first leakage at higher pressure values, whilst maintaining adequate delay against the occurrence of the second leakage event.

- Defects introduced during the manufacturing of the pipes were considered to be the cause of leakage in both control and fibre cut defective pipe test cases, thus incommoding the validation of the LBB concept in terms of the position of leakage incident. For elimination of this, filament winding utilisation for the manufacturing of composite pipes or CPVs is suggested. The minimisation of manufacturing defects can lead to identification of the maximum failure pressure in the cylindrical part of the vessel. Defective pipes produced with the minimum amount of manufacturing defects can be utilised for the accurate identification and correlation of the occurrence of leakage to the respective damage threshold, which in this work was considered possible to be above 90%.
- The consideration of the variability introduced due to the manufacturing process and introduction of defects and the identification of the defect types arising from these sources can be incorporated to the model for the development of more robust LBB designs. This can be used for the elimination of the defects introduced due to a certain source or to the consideration of their exact contribution to a failure response.
- The introduction of artificial fibre cut defects in the composite structure can be carried out through automated equipment (lasers, water cutting, knives, perforations). In this way, human error causing discrepancies in the amount of fibre cut damage introduced can be significantly reduced.
- The quantification of leakage can be performed through examination of the fluid flow through defects considered as porous media. The fluid flow can be investigated taking into account capillary effects and flow through porous media following Darcy's law.

References

[1] Rana S, Fangueiro R. Advanced Composite Materials for Aerospace Engineering. Elsevier; 2016. https://doi.org/10.1016/C2014-0-00846-5.

[2] Giurgiutiu V. Structural Health Monitoring of Aerospace Composites. Elsevier; 2016. https://doi.org/10.1016/C2012-0-07213-4.

[3] Barthélémy H. Hydrogen storage – Industrial prospectives. International Journal of Hydrogen Energy 2012;37:17364–72. https://doi.org/10.1016/j.ijhydene.2012.04.121.

[4] Dahl E, Becker JS, Mittelstedt C, Schürmann H. A new concept for a modular composite pressure vessel design. Composites Part A: Applied Science and Manufacturing 2019;124:105475. https://doi.org/10.1016/j.compositesa.2019.105475.

[5] Bouvier M, Guiheneuf V, Jean-marie A. Modeling and simulation of a composite high-pressure vessel made of sustainable and renewable alternative fibers. International Journal of Hydrogen Energy 2019;44:11970–8. https://doi.org/10.1016/j.ijhydene.2019.03.088.

[6] USLaunchReport. SpaceX - Static Fire Anomaly - AMOS-6 - 09-01-2016 2016.

[7] Gardiner G. SpaceX announces COPV's role in September rocket explosion. CompositesWorld 2017. https://www.compositesworld.com/blog/post/spacex-announces-copvs-role-in-sept-rocket-explosion.

[8] Swolfs Y, Meerten Y, Hine P, Ward I, Verpoest I, Gorbatikh L. Introducing ductility in hybrid carbon fibre/self-reinforced composites through control of the damage mechanisms. Composite Structures 2015;131:259–65. https://doi.org/10.1016/j.compstruct.2015.04.069.

[9] Sakai M, Matsuyama R, Miyajima T. The pull-out and failure of a fiber bundle in a carbon fiber reinforced carbon matrix composite. Carbon 2000;38:2123–31.

[10] Brunner AJ. Identification of damage mechanisms in fiber-reinforced polymer-matrix composites with Acoustic Emission and the challenge of assessing structural integrity and service-life. Construction and Building Materials 2018;173:629–37. https://doi.org/10.1016/j.conbuildmat.2018.04.084.

[11] Renard J, Thionnet A. Damage in composites: From physical mechanisms to modelling. Composites Science and Technology 2006;66:642–6. https://doi.org/10.1016/j.compscitech.2005.07.035.

[12] Hinton M, Soden PD. Predicting failure in composite laminates: the background to the exercise. Composites Science and Technology 1998;58:1001–10. https://doi.org/10.1016/S0266-3538(98)00074-8.

[13] Harik VM. Optimization of structural designs for a safe failure pattern: layered material systems. Materials & Design 2001;22:317–24. https://doi.org/10.1016/S0261-3069(00)00085-6.

[14] Harik VM. Control of Damage in Composite Laminates by Ply-Stacking Designs: Characteristic Failure Signatures and Safety Criteria. Journal of Engineering Materials and Technology 2003;125:385–93. https://doi.org/10.1115/1.1605771.

[15] Puck A, Schürmann H. Failure analysis of FRP laminates by means of physically based phenomenological models. Composites Science and Technology 2002;62:1633–62. https://doi.org/10.1016/S0266-3538(01)00208-1.

[16] Xie J, Waas AM. Predictions of Delamination Growth for Quasi-Static Loading of Composite Laminates. Journal of Applied Mechanics 2015;82:81004. https://doi.org/10.1115/1.4030684.

[17] Joosten MW. An enhanced ply damage model for failure prediction in unidirectional composite structures. Composite Structures 2019;207:752–63. https://doi.org/10.1016/j.compstruct.2018.09.039.

[18] Greve L, Pickett AK. Modelling damage and failure in carbon/epoxy non-crimp fabric composites including effects of fabric pre-shear. Composites Part A: Applied Science and Manufacturing 2006;37:1983–2001. https://doi.org/10.1016/j.compositesa.2005.12.012.

[19] Camanho PP, Maimí P, Dávila CG. Prediction of size effects in notched laminates using continuum damage mechanics. Composites Science and Technology 2007;67:2715–27. https://doi.org/10.1016/j.compscitech.2007.02.005.

[20] Larsen CE, Raju IS. Moving Aerospace Structural Design Practice to a Load and Resistance Factor Approach. 57th AIAA/ASCE/AHS/ASC Structures, Structural Dynamics, and Materials Conference, Reston, Virginia: American Institute of Aeronautics and Astronautics; 2016, p. 230. https://doi.org/10.2514/6.2016-0230.

[21] Charles E H, Starnes Jr JH, Mark J S. An assessment of the state-of-the-art in the design and manufacturing of large composite structures for aerospace vehicles 2001.

[22] Rafiee R, Torabi MA, Maleki S. Investigating structural failure of a filament-wound composite tube subjected to internal pressure: Experimental and theoretical evaluation. Polymer Testing 2018;67:322–30. https://doi.org/10.1016/j.polymertesting.2018.03.020.

[23] Martins LAL, Bastian FL, Netto TA. Structural and functional failure pressure of filament wound composite tubes. Materials & Design (1980-2015) 2012;36:779–87. https://doi.org/10.1016/j.matdes.2011.11.029.

[24] Wang L, Wang B, Wei S, Hong Y, Zheng C. Prediction of long-term fatigue life of CFRP composite hydrogen storage vessel based on micromechanics of failure. Composites Part B: Engineering 2016;97:274–81. https://doi.org/10.1016/j.compositesb.2016.05.012.

[25] Zheng C, Wang L, Li R, Wei Z, Zhou W. Fatigue test of carbon epoxy composite high pressure hydrogen storage vessel under hydrogen environment. Journal of Zhejiang University SCIENCE A 2013;14:393–400. https://doi.org/10.1631/jzus.A1200297.

[26] Cai B, Liu Y, Liu Z, Tian X, Ji R, Li H. Reliability-based load and resistance factor design of composite pressure vessel under external hydrostatic pressure. Composite Structures 2011;93:2844–52. https://doi.org/10.1016/j.compstruct.2011.05.020.

[27] Cho YS, Oh DH, Paik JK. An empirical formula for predicting the collapse strength of composite cylindrical-shell structures under external pressure loads. Ocean Engineering 2019;172:191–8. https://doi.org/10.1016/j.oceaneng.2018.11.028.

[28] Blanc-Vannet P. Burst pressure reduction of various thermoset composite pressure vessels after impact on the cylindrical part. Composite Structures 2017;160:706–11. https://doi.org/10.1016/j.compstruct.2016.10.099.

[29] Garcia MA, Davis BA, Miller JE. Hypervelocity impact testing of a pressurized composite overwrapped pressure vessel and comparison to numerical analysis. Procedia Engineering 2017;204:476–83. https://doi.org/10.1016/j.proeng.2017.09.744.

[30] Perillo G, Grytten F, Sørbø S, Delhaye V. Numerical/experimental impact events on filament wound composite pressure vessel. Composites Part B: Engineering 2015;69:406–17. https://doi.org/10.1016/j.compositesb.2014.10.030.

[31] Almeida JHS, Tonatto MLP, Ribeiro ML, Tita V, Amico SC. Buckling and post-buckling of filament wound composite tubes under axial compression: Linear, nonlinear, damage and experimental analyses. Composites Part B: Engineering 2018;149:227–39. https://doi.org/10.1016/j.compositesb.2018.05.004.

[32] Smerdov AA. A computational study in optimum formulations of optimization problems on laminated cylindrical shells for buckling I. Shells under axial compression. Composites Science and Technology 2000;60:2057–66. https://doi.org/10.1016/S0266-3538(00)00102-0.

[33] He J, Ren M, Sun S, Huang Q, Sun X. Failure prediction on advanced grid stiffened composite cylinder under axial compression. Composite

Structures 2011;93:1939–46. https://doi.org/10.1016/j.compstruct.2011.02.003.

[34] Halm D, Fouillen F, Lainé E, Gueguen M, Bertheau D, Van Eekelen T. Composite pressure vessels for hydrogen storage in fire conditions: Fire tests and burst simulation. International Journal of Hydrogen Energy 2017;42:20056–70. https://doi.org/10.1016/j.ijhydene.2017.06.088.

[35] Nash NH, Portela A, Bachour-Sirerol CI, Manolakis I, Comer AJ. Effect of environmental conditioning on the properties of thermosetting- and thermoplastic-matrix composite materials by resin infusion for marine applications. Composites Part B: Engineering 2019;177:107271. https://doi.org/10.1016/j.compositesb.2019.107271.

[36] Hong J-H, Han M-G, Chang S-H. Safety evaluation of 70 MPa-capacity type III hydrogen pressure vessel considering material degradation of composites due to temperature rise. Composite Structures 2014;113:127–33.

[37] Tuğcu P. Instability and ductile failure of thin cylindrical tubes under internal pressure impact. International Journal of Impact Engineering 2003;28:183–205.

[38] Wang L, Zheng C, Wei S, Wei Z. Micromechanics-based progressive failure analysis of carbon fiber/epoxy composite vessel under combined internal pressure and thermomechanical loading. Composites Part B: Engineering 2016;89:77–84.

[39] Uyaner M, Kara M, $\backslash$cSahin A. Fatigue behavior of filament wound E-glass/epoxy composite tubes damaged by low velocity impact. Composites Part B: Engineering 2014;61:358–364.

[40] BSI. 17339: 2018,Transportable gas cylinders. Fully Wrapped Composite Cylinders and Tubes for Hydrogen Use 2018.

[41] EN BS. BS EN 12245:2009+A1:2011. Fully Wrapped Composite Cylinders 2009.

[42] Martins LAL, Bastian FL, Netto TA. The effect of stress ratio on the fracture morphology of filament wound composite tubes. Materials & Design 2013;49:471–84.

[43] Meijer G, Ellyin F. A failure envelope for ±60° filament wound glass fibre reinforced epoxy tubulars. Composites Part A: Applied Science and Manufacturing 2008;39:555–64. https://doi.org/10.1016/j.compositesa.2007.11.002.

[44] Martins LAL, Bastian FL, Netto TA. Reviewing some design issues for filament wound composite tubes. Materials & Design 2014;55:242–9. https://doi.org/10.1016/j.matdes.2013.09.059.

[45] Abdalla FH, Sapuan SM, Hamdan MM, Sahari B. Internal Pressure Carrying Capacity for Different Loading Modes of Filament-Wound Pipes from Glass Fiber-reinforced Epoxy Composites. Polymer-Plastics Technology and Engineering 2008;47:802–8. https://doi.org/10.1080/03602550802188698.

[46] Farhood NH, Karuppanan S, Ya HH, Baharom MA. Burst pressure investigation of filament wound type IV composite pressure vessel. AIP Conference Proceedings, vol. 1901, 2017, p. 030017. https://doi.org/10.1063/1.5010482.

[47] Manoj Prabhakar M, Rajini N, Ayrilmis N, Mayandi K, Siengchin S, Senthilkumar K, Karthikeyan S, Ismail SO. An overview of burst, buckling, durability and corrosion analysis of lightweight FRP composite pipes and their applicability. Composite Structures 2019;230:111419. https://doi.org/10.1016/j.compstruct.2019.111419.

[48] Kara M, Uyaner M, Avci A, Akdemir A. Effect of non-penetrating impact damages of pre-stressed GRP tubes at low velocities on the burst strength. Composites Part B: Engineering 2014;60:507–14. https://doi.org/10.1016/j.compositesb.2014.01.003.

[49] Leh D, Saffré P, Francescato P, Arrieux R, Villalonga S. A progressive failure analysis of a 700-bar type IV hydrogen composite pressure vessel. International Journal of Hydrogen Energy 2015;40:13206–14. https://doi.org/10.1016/j.ijhydene.2015.05.061.

[50] Ramirez JPB, Halm D, Grandidier J-C, Villalonga S, Nony F. 700 bar type IV high pressure hydrogen storage vessel burst--Simulation and experimental validation. International Journal of Hydrogen Energy 2015;40:13183–92.

[51] Tapeinos IG, Zarouchas DS, Bergsma OK, Koussios S, Benedictus R. Evaluation of the mechanical performance of a composite multi-cell tank for cryogenic storage: Part I - Tank pressure window based on progressive failure analysis. International Journal of Hydrogen Energy 2019;44:3917–30. https://doi.org/10.1016/j.ijhydene.2018.12.118.

[52] Zhang M, Lv H, Kang H, Zhou W, Zhang C. A literature review of failure prediction and analysis methods for composite high-pressure hydrogen storage tanks. International Journal of Hydrogen Energy 2019;44:25777–99.

[53] Hamed AF, Khalid YA, Sapuan SM, Hamdan MM, Younis TS, Sahari BB. Effects of Winding Angles on the Strength of Filament Wound Composite Tubes Subjected to Different Loading Modes. Polymers and Polymer Composites 2007;15:199–206. https://doi.org/10.1177/096739110701500304.

[54] Rafiee R, Torabi MA. Stochastic prediction of burst pressure in composite pressure vessels. Composite Structures 2018;185:573–83.

[55] Bunsell AR, Barbier F, Thionnet A, Zejli H, Besançon B. Damage Accumulation and Lifetime Prediction of Carbon Fiber Composite Pressure Vessels. ASME 2010 Pressure Vessels and Piping Conference: Volume 6, Parts A and B, ASME; 2010, p. 303–10. https://doi.org/10.1115/PVP2010-25978.

[56] Blassiau S, Thionnet A, Bunsell AR. Micromechanisms of load transfer in a unidirectional carbon fibre-reinforced epoxy composite due to fibre failures: Part 3. Multiscale reconstruction of composite behaviour. Composite Structures 2008;83:312–23. https://doi.org/10.1016/j.compstruct.2007.05.004.

[57] Hull D, Legg MJ, Spencer B. Failure of glass/polyester filament wound pipe. Composites 1978;9:17–24. https://doi.org/10.1016/0010-4361(78)90513-X.

[58] Evans JT, Gibson AG. Composite angle ply laminates and netting analysis. Proceedings of the Royal Society of London Series A: Mathematical, Physical and Engineering Sciences 2002;458:3079–88. https://doi.org/10.1098/rspa.2002.1066.

[59] Onder A, Sayman O, Dogan T, Tarakcioglu N. Burst failure load of composite pressure vessels. Composite Structures 2009;89:159–66. https://doi.org/10.1016/j.compstruct.2008.06.021.

[60] Hocine A, Ghouaoula A, Achira FK, Medjdoub SM. Analysis of failure pressures of composite cylinders with a polymer liner of type IV CNG vessels. International Journal of Mechanical, Aerospace, Industrial , Mechatronic and Manufacturing Engineering 2013;7:148–52.

[61] Chou H-Y, Bunsell A, Mair G, Thionnet A. Effect of the Loading Rate on Failure of Composite Pressure Vessel. Volume 5: High-Pressure Technology; ASME NDE Division; Rudy Scavuzzo Student Paper Symposium, American Society of Mechanical Engineers; 2013, p. V005T05A002----V005T05A002. https://doi.org/10.1115/PVP2013-97159.

[62] Ellyin F, Carroll M, Kujawski D, Chiu AS. The behavior of multidirectional filament wound fibreglass/epoxy tubulars under biaxial loading. Composites Part A: Applied Science and Manufacturing 1997;28:781–90. https://doi.org/10.1016/S1359-835X(97)00021-3.

[63] Tapeinos IG, Rajabzadeh A, Zarouchas DS, Stief M, Groves RM, Koussios S, Benedictus R. Evaluation of the mechanical performance of a composite multi-cell tank for cryogenic storage: Part II – Experimental assessment. International Journal of Hydrogen Energy 2019;44:3931–43. https://doi.org/10.1016/j.ijhydene.2018.12.063.

[64] Gemi L, Tarakçioğlu N, Akdemir A, Şahin ÖS. Progressive fatigue failure behavior of glass/epoxy (±75)2 filament-wound pipes under pure internal pressure. Materials & Design 2009;30:4293–8. https://doi.org/10.1016/j.matdes.2009.04.025.

[65] Sayman O, Deniz ME, Dogan T, Yaylagan E. Failure pressures of composite cylinders with a plastic liner. Journal of Reinforced Plastics and Composites 2011;30:882–8. https://doi.org/10.1177/0731684411412225.

[66] Mertiny P, Juss K. Effect of Fiber-Reinforcement Material on the Leakage Failure in Polymer Composite Pressure Piping. Volume 3: Design and Analysis, ASME; 2008, p. 591–6. https://doi.org/10.1115/PVP2008-61540.

[67] Mertiny P, Gold A. Quantification of leakage damage in high-pressure fibre-reinforced polymer composite tubular vessels. Polymer Testing 2007;26:172–9. https://doi.org/10.1016/j.polymertesting.2006.09.009.

[68] Krishnan P, Abdul Majid MS, Afendi M, Gibson AG, Marzuki HFA. Effects of winding angle on the behaviour of glass/epoxy pipes under multiaxial cyclic loading. Materials & Design 2015;88:196–206. https://doi.org/10.1016/j.matdes.2015.08.153.

[69] Mertiny P, Ellyin F, Hothan A. An experimental investigation on the effect of multi-angle filament winding on the strength of tubular composite structures. Composites Science and Technology 2004;64:1–9. https://doi.org/10.1016/S0266-3538(03)00198-2.

[70] Majid MSA, Assaleh TA, Gibson AG, Hale JM, Fahrer A, Rookus CAP, Hekman M. Ultimate elastic wall stress (UEWS) test of glass fibre reinforced epoxy (GRE) pipe. Composites Part A: Applied Science and Manufacturing 2011;42:1500–8.

[71] Assaleh TA, Almagguz LA. Ultimate Elastic Wall Stress (UEWS) Test under Biaxial Loading for Glass-Fibre Reinforced Epoxy (GRE) Pipes. Advanced Materials Research 2014;974:188–94. https://doi.org/10.4028/www.scientific.net/AMR.974.188.

[72] Soden PD, Kitching R, Tse PC. Experimental failure stresses for ±55° filament wound glass fibre reinforced plastic tubes under biaxial loads. Composites 1989;20:125–35. https://doi.org/10.1016/0010-4361(89)90640-X.

[73] Swanson Sr, Christoforou AP. Response of Quasi-Isotropic Carbon/Epoxy Laminates to Biaxial Stress. Journal of Composite Materials 1986;20:457–71. https://doi.org/10.1177/002199838602000504.

[74] Salavatian M, Smith L. Matrix damage in composite pressure vessels with a bias fiber orientation. Journal of Composite Materials 2012;46:2793–802. https://doi.org/10.1177/0021998311432775.

[75] Foral R, Gilbreath D. Delamination Failure Modes in Filament-Wound Composite Tubes. Composite Materials: Fatigue and Fracture, Second Volume, 100 Barr Harbor Drive, PO Box C700, West Conshohocken, PA 19428-2959: ASTM International; 1989, p. 313-313–13. https://doi.org/10.1520/STP10422S.

[76] Tarakcioglu N, Gemi L, Yapici A. Fatigue failure behavior of glass/epoxy ±55 filament wound pipes under internal pressure. Composites Science and Technology 2005;65:703–8. https://doi.org/10.1016/j.compscitech.2004.10.002.

[77] Mertiny P. Leakage failure in fibre-reinforced polymer composite tubular vessels at elevated temperature. Polymer Testing 2012;31:25–30. https://doi.org/10.1016/j.polymertesting.2011.09.003.

[78] Hosseini SM, Shariati M. Experimental analysis of energy absorption capability of thin-walled composite cylindrical shells by quasi-static axial crushing test. Thin-Walled Structures 2018;125:259–68. https://doi.org/10.1016/j.tws.2018.01.026.

[79] Shi D, Xiao X. An enhanced continuum damage mechanics model for crash simulation of composites. Composite Structures 2018;185:774–85. https://doi.org/10.1016/j.compstruct.2017.10.084.

[80] Reddick Jr HK. Safe-life and damage-tolerant design approaches for helicopter structures. COMPOSITE MATERIALS, United States: United States; 1983, p. 129–51. https://doi.org/19830025690.

[81] Arjomandi K, Taheri F. Stability and post-buckling response of sandwich pipes under hydrostatic external pressure. International Journal of Pressure Vessels and Piping 2011;88:138–48. https://doi.org/10.1016/j.ijpvp.2011.02.002.

[82] Hou T, Pearce GMK, Prusty BG, Kelly DW, Thomson RS. Pressurised composite tubes as variable load energy absorbers. Composite Structures 2015;120:346–57. https://doi.org/10.1016/j.compstruct.2014.09.060.

[83] Hou T, Prusty BG, Pearce G, Kelly D, Thomson R. Experimental Investigation on Energy Absorbing Pressurised Composite Tubes. In: Suong Van Hoa PH, editor. 19TH INTERNATIONAL CONFERENCE ON COMPOSITE MATERIALS, Montréal: Concordia Centre for Composites, Department of Mechanical and Industrial Engineering, Concordia University, 1455 de Maisonneuve Blvd. West, Montreal, Quebec, Canada H3G1M8; 2013, p. 1–8.

[84] Hull D. A unified approach to progressive crushing of fibre-reinforced composite tubes. Composites Science and Technology 1991;40:377–421. https://doi.org/10.1016/0266-3538(91)90031-J.

[85] Mamalis AG, Robinson M, Manolakos DE, Demosthenous GA, Ioannidis MB, Carruthers J. Crashworthy capability of composite material structures. Composite Structures 1997;37:109–34. https://doi.org/10.1016/S0263-8223(97)80005-0.

[86] Hamada H, Ramakrishna S. Comparison of Static and Impact Energy Absorption of Carbon Fiber/PEEK Composite Tubes. Composite Materials: Testing and Design: Twelfth Volume, 100 Barr Harbor Drive, PO Box C700,

West Conshohocken, PA 19428-2959: ASTM International; 1996, p. 182-182–16. https://doi.org/10.1520/STP16545S.

[87] Supian ABM, Sapuan SM, Zuhri MYM, Zainudin ES, Ya HH. Hybrid reinforced thermoset polymer composite in energy absorption tube application: A review. Defence Technology 2018;14:291–305. https://doi.org/10.1016/j.dt.2018.04.004.

[88] Kim J-S, Yoon H-J, Shin K-B. A study on crushing behaviors of composite circular tubes with different reinforcing fibers. International Journal of Impact Engineering 2011;38:198–207.

[89] Pushparaja M, Balaganesan G, Velmurugan R, Gupta NK. Energy Absorption Characteristics of Carbon /Epoxy Nano Filler Dispersed Composites Subjected to Localized Impact Loading. Procedia Engineering 2017;173:175–81. https://doi.org/10.1016/j.proeng.2016.12.055.

[90] Tavassolimanesh A, Niknejad A, Assaee H. Effects of polyethylene and polyurethane Teflon-fillers on the energy absorption behavior of composite tubes during the flattening tests. Journal of Composite Materials 2015;49:2057–72. https://doi.org/10.1177/0021998314541568.

[91] Silva F, Njuguna J, Sachse S, Pielichowski K, Leszczynska A, Giacomelli M. The influence of multiscale fillers reinforcement into impact resistance and energy absorption properties of polyamide 6 and polypropylene nanocomposite structures. Materials & Design 2013;50:244–52.

[92] Hu D, Zhang C, Ma X, Song B. Effect of fiber orientation on energy absorption characteristics of glass cloth/epoxy composite tubes under axial quasi-static and impact crushing condition. Composites Part A: Applied Science and Manufacturing 2016;90:489–501. https://doi.org/10.1016/j.compositesa.2016.08.017.

[93] Ryzińska G, David M, Prusty G, Tarasiuk J, Wroński S. Effect of fibre architecture on the specific energy absorption in carbon epoxy composite tubes under progressive crushing. Composite Structures 2019;227:111292. https://doi.org/10.1016/j.compstruct.2019.111292.

[94] Yan L, Chouw N. Crashworthiness characteristics of flax fibre reinforced epoxy tubes for energy absorption application. Materials & Design 2013;51:629–40. https://doi.org/10.1016/j.matdes.2013.04.014.

[95] Xu J, Ma Y, Zhang Q, Sugahara T, Yang Y, Hamada H. Crashworthiness of carbon fiber hybrid composite tubes molded by filament winding. Composite Structures 2016;139:130–40. https://doi.org/10.1016/j.compstruct.2015.11.053.

[96] Abdewi EF, Sulaiman S, Hamouda AMS, Mahdi E. Effect of geometry on the crushing behaviour of laminated corrugated composite tubes. Journal of Materials Processing Technology 2006;172:394–9. https://doi.org/10.1016/j.jmatprotec.2005.07.017.

[97] Klaus M, Reimerdes H-G, Gupta NK. Experimental and numerical investigations of residual strength after impact of sandwich panels. International Journal of Impact Engineering 2012;44:50–8. https://doi.org/10.1016/j.ijimpeng.2012.01.001.

[98] Yang C, Xu P, Yao S, Xie S, Li Q, Peng Y. Optimization of honeycomb strength assignment for a composite energy-absorbing structure. Thin-Walled Structures 2018;127:741–55. https://doi.org/10.1016/j.tws.2018.03.014.

[99] Mahdi E, Sebaey TA. An experimental investigation into crushing behavior of radially stiffened GFRP composite tubes. Thin-Walled Structures 2014;76:8–13. https://doi.org/10.1016/j.tws.2013.10.018.

[100] Thornton PH. Energy Absorption in Composite Structures. Journal of Composite Materials 1979;13:247–62. https://doi.org/10.1177/002199837901300308.

[101] Thuis H, Metz VH. The influence of trigger configurations and laminate lay-up on the failure mode of composite crush cylinders. Composite Structures 1994;28:131–7.

[102] Oshkovr SA, Eshkoor RA, Taher ST, Ariffin AK, Azhari CH. Crashworthiness characteristics investigation of silk/epoxy composite square tubes. Composite Structures 2012;94:2337–42. https://doi.org/10.1016/j.compstruct.2012.03.031.

[103] Eshkoor RA, Ude AU, Sulong AB, Zulkifli R, Ariffin AK, Azhari CH. Energy absorption and load carrying capability of woven natural silk epoxy–triggered composite tubes. Composites Part B: Engineering 2015;77:10–8. https://doi.org/10.1016/j.compositesb.2015.03.017.

[104] Pitarresi G, Carruthers JJ, Robinson AM, Torre G, Kenny J, Ingleton S, Velecela O, Found MS. A comparative evaluation of crashworthy composite sandwich structures. Composite Structures 2007;78:34–44.

[105] Siromani D, Henderson G, Mikita D, Mirarchi K, Park R, Smolko J, Awerbuch J, Tan T-M. An experimental study on the effect of failure trigger mechanisms on the energy absorption capability of CFRP tubes under axial compression. Composites Part A: Applied Science and Manufacturing 2014;64:25–35. https://doi.org/10.1016/j.compositesa.2014.04.019.

[106] Stapleton SE, Adams DO. Crush Initiators for Increased Energy Absorption in Composite Sandwich Structures. Journal of Sandwich Structures & Materials 2008;10:331–54. https://doi.org/10.1177/1099636208091737.

[107] Othman A, Abdullah S, Ariffin AK, Mohamed NAN. Investigating the quasi-static axial crushing behavior of polymeric foam-filled composite pultrusion square tubes. Materials & Design 2014;63:446–59.

[108] Greve L, Pickett AK, Payen F. Experimental testing and phenomenological modelling of the fragmentation process of braided carbon/epoxy composite

tubes under axial and oblique impact. Composites Part B: Engineering 2008;39:1221–32. https://doi.org/10.1016/j.compositesb.2008.02.002.

[109] Patel S, Vusa VR, Guedes Soares C. Crashworthiness analysis of polymer composites under axial and oblique impact loading. International Journal of Mechanical Sciences 2019;156:221–34. https://doi.org/10.1016/j.ijmecsci.2019.03.038.

[110] Farley GL. Energy Absorption of Composite Materials. Journal of Composite Materials 1983;17:267–79. https://doi.org/10.1177/002199838301700307.

[111] Lavoie JA, Kellas S. Dynamic crush tests of energy-absorbing laminated composite plates. Composites Part A: Applied Science and Manufacturing 1996;27:467–75. https://doi.org/10.1016/1359-835X(95)00058-A.

[112] Joosten MW, Dutton S, Kelly D, Thomson R. Experimental evaluation of the crush energy absorption of triggered composite sandwich panels under quasi-static edgewise compressive loading. Composites Part A: Applied Science and Manufacturing 2010;41:1099–106. https://doi.org/10.1016/j.compositesa.2010.03.010.

[113] Hanagud S, Craig JI, Sriram P, Zhou W. Energy Absorption Behavior of Graphite Epoxy Composite Sine Webs. Journal of Composite Materials 1989;23:448–59. https://doi.org/10.1177/002199838902300502.

[114] Huang J, Wang X. On a new crush trigger for energy absorption of composite tubes. International Journal of Crashworthiness 2010;15:625–34. https://doi.org/10.1080/13588265.2010.484194.

[115] Mamalis AG, Manolakos DE, Viegelahn GL. Crashworthy Behaviour of Thin-Walled Tubes of Fibreglass Composite Materials Subjected to Axial Loading. Journal of Composite Materials 1990;24:72–91. https://doi.org/10.1177/002199839002400104.

[116] Farley GL, Jones RM. Crushing Characteristics of Continuous Fiber-Reinforced Composite Tubes. Journal of Composite Materials 1992;26:37–50. https://doi.org/10.1177/002199839202600103.

[117] Eshkoor RA, Ude AU, Oshkovr SA, Sulong AB, Zulkifli R, Ariffin AK, Azhari CH. Failure mechanism of woven natural silk/epoxy rectangular composite tubes under axial quasi-static crushing test using trigger mechanism. International Journal of Impact Engineering 2014;64:53–61. https://doi.org/10.1016/j.ijimpeng.2013.09.004.

[118] Priem C, Othman R, Rozycki P, Guillon D. Experimental investigation of the crash energy absorption of 2.5D-braided thermoplastic composite tubes. Composite Structures 2014;116:814–26. https://doi.org/10.1016/j.compstruct.2014.05.037.

[119] Cherniaev A, Butcher C, Montesano J. Predicting the axial crush response of CFRP tubes using three damage-based constitutive models. Thin-

Walled Structures 2018;129:349–64. https://doi.org/10.1016/j.tws.2018.05.003.

[120] Mamalis AG, Manolakos DE, Ioannidis MB, Papapostolou DP. Crashworthy characteristics of axially statically compressed thin-walled square CFRP composite tubes: experimental. Composite Structures 2004;63:347–60. https://doi.org/10.1016/S0263-8223(03)00183-1.

[121] Heidari-Rarani M, Kharratzadeh M. Buckling behavior of composite cylindrical shells with cutout considering geometric imperfection. Steel and Composite Structures 2019;30:305–13. https://doi.org/10.12989/scs.2019.30.5.305.

[122] Castro SGP, Zimmermann R, Arbelo MA, Khakimova R, Hilburger MW, Degenhardt R. Geometric imperfections and lower-bound methods used to calculate knock-down factors for axially compressed composite cylindrical shells. Thin-Walled Structures 2014;74:118–32. https://doi.org/10.1016/j.tws.2013.08.011.

[123] Kepple J, Herath MT, Pearce G, Prusty BG, Thomson R, Degenhardt R. Stochastic analysis of imperfection sensitive unstiffened composite cylinders using realistic imperfection models. Composite Structures 2015;126:159–73.

[124] Hilburger MW, Starnes JH. Effects of imperfections on the buckling response of compression-loaded composite shells. International Journal of Non-Linear Mechanics 2002;37:623–43. https://doi.org/10.1016/S0020-7462(01)00088-9.

[125] Schenk CA, Schuëller GI. Buckling analysis of cylindrical shells with random geometric imperfections. International Journal of Non-Linear Mechanics 2003;38:1119–32. https://doi.org/10.1016/S0020-7462(02)00057-4.

[126] Schenk CA, Schuëller GI. Buckling analysis of cylindrical shells with cutouts including random boundary and geometric imperfections. Computer Methods in Applied Mechanics and Engineering 2007;196:3424–34. https://doi.org/10.1016/j.cma.2007.03.014.

[127] Orifici AC, Bisagni C. Perturbation-based imperfection analysis for composite cylindrical shells buckling in compression. Composite Structures 2013;106:520–8. https://doi.org/10.1016/j.compstruct.2013.06.028.

[128] Taheri-Behrooz F, Omidi M. Buckling of axially compressed composite cylinders with geometric imperfections. Steel and Composite Structures 2018;29:557–67. https://doi.org/10.12989/scs.2018.29.4.557.

[129] Hao P, Wang B, Li G, Meng Z, Tian K, Zeng D, Tang X. Worst multiple perturbation load approach of stiffened shells with and without cutouts for improved knockdown factors. Thin-Walled Structures 2014;82:321–30.

[130] Wagner HNR, Hühne C. Robust knockdown factors for the design of cylindrical shells under axial compression: potentials, practical application and reliability analysis. International Journal of Mechanical Sciences 2018;135:410–30.

[131] Wang B, Du K, Hao P, Tian K, Chao YJ, Jiang L, Xu S, Zhang X. Experimental validation of cylindrical shells under axial compression for improved knockdown factors. International Journal of Solids and Structures 2019;164:37–51. https://doi.org/10.1016/j.ijsolstr.2019.01.001.

[132] Samanci A, Avci A, Tarakcioglu N, Şahin ÖS. Fatigue crack growth of filament wound GRP pipes with a surface crack under cyclic internal pressure. Journal of Materials Science 2008;43:5569–73. https://doi.org/10.1007/s10853-008-2820-x.

[133] Taşyürek M, Tarakçioğlu N. Enhanced fatigue behavior under internal pressure of CNT reinforced filament wound cracked pipes. Composites Part B: Engineering 2017;124:23–30. https://doi.org/10.1016/j.compositesb.2017.05.050.

[134] Samanci A, Tarakçioğlu N, Akdemir A. Fatigue failure analysis of surface-cracked (±45°) 3 filament-wound GRP pipes under internal pressure. Journal of Composite Materials 2012;46:1041–50. https://doi.org/10.1177/0021998311414945.

[135] Sahin ÖS, Akdemir A, Avci A, Gemi L. Fatigue Crack Growth Behavior of Filament Wound Composite Pipes in Corrosive Environment. Journal of Reinforced Plastics and Composites 2009;28:2957–70. https://doi.org/10.1177/0731684408094068.

[136] Buarque EN, D'Almeida JRM. The effect of cylindrical defects on the tensile strength of glass fiber/vinyl-ester matrix reinforced composite pipes. Composite Structures 2007;79:270–9. https://doi.org/10.1016/j.compstruct.2006.01.011.

[137] Arikan H. Failure analysis of (±55°)3 filament wound composite pipes with an inclined surface crack under static internal pressure. Composite Structures 2010;92:182–7. https://doi.org/10.1016/j.compstruct.2009.07.027.

[138] ISO 11119-3:2013. Gas cylinders — Refillable composite gas cylinders and tubes — Design, construction and testing — Part 3: Fully wrapped fibre reinforced composite gas cylinders and tubes up to 450L with non-load-sharing metallic or non-metallic liners. 2013.

[139] BS EN ISO 11439:2000. Gas cylinders. High pressure cylinders for the on-board storage of natural gas as a fuel for automotive vehicles. 2000.

[140] Chang J. Development of COPV-Related Standards. 48th AIAA/ASME/ASCE/AHS/ASC Structures, Structural Dynamics, and Materials Conference, Reston, Virigina: American Institute of Aeronautics and Astronautics; 2007. https://doi.org/10.2514/6.2007-2146.

[141] ISO/TS 17519:2019. Gas cylinders — Refillable permanently mounted composite tubes for transportation. n.d.

[142] Jingxuan H, Mingfa R, Qizhong H, Shanshan S, Haoran C. Buckling Behavior of Compression-loaded Advanced Grid Stiffened Composite Cylindrical Shells with Reinforced Cutouts. Polymers and Polymer Composites 2011;19:357–62. https://doi.org/10.1177/0967391111019004-516.

[143] Çelebi M, Gürdal Z, Tatting B, Blom-Schieber A, Rassaian M, Wanthal S, Türkmen HS. Bending of Composite Cylindrical Shells with Circular Cutouts: Buckling and Failure Analysis. Journal of Aircraft 2019;56:1551–64. https://doi.org/10.2514/1.C035246.

[144] Hilburger M, Waas A, Starnes Jr J. A numerical and experimental study of the response of selected compression-loaded composite shells with cutouts. 39th AIAA/ASME/ASCE/AHS/ASC Structures, Structural Dynamics, and Materials Conference and Exhibit, 1998, p. 1988.

[145] Starnes J, Hilburger M, Nemeth M. The Effects of Initial Imperfections on the Buckling of Composite Cylindrical Shells. Composite Structures: Theory and Practice, 100 Barr Harbor Drive, PO Box C700, West Conshohocken, PA 19428-2959: ASTM International; 2001, p. 529-529–22. https://doi.org/10.1520/STP14529S.

[146] Liu Q, Ma J, Xu X, Wu Y, Li Q. Load bearing and failure characteristics of perforated square CFRP tubes under axial crushing. Composite Structures 2017;160:23–35. https://doi.org/10.1016/j.compstruct.2016.10.032.

[147] Mamalis AG, Manolakos DE, Ioannidis MB, Papapostolou DP. The static and dynamic axial collapse of CFRP square tubes: finite element modelling. Composite Structures 2006;74:213–25.

[148] Hilburger M. Buckling and Failure of Compression-Loaded Composite Laminated Shells with Cutouts. 48th AIAA/ASME/ASCE/AHS/ASC Structures, Structural Dynamics, and Materials Conference, Reston, Virigina: American Institute of Aeronautics and Astronautics; 2007, p. 22–7. https://doi.org/10.2514/6.2007-2227.

[149] Shirkavand A, Taheri-Behrooz F, Omidi M. Orientation and size effect of a rectangle cutout on the buckling of composite cylinders. Aerospace Science and Technology 2019;87:488–97. https://doi.org/10.1016/j.ast.2019.02.042.

[150] Taheri-Behrooz F, Omidi M, Shokrieh MM. Experimental and numerical investigation of buckling behavior of composite cylinders with cutout. Thin-Walled Structures 2017;116:136–44. https://doi.org/10.1016/j.tws.2017.03.009.

[151] Wang W, Sheikh MN, Hadi MNS. Behaviour of perforated GFRP tubes under axial compression. Thin-Walled Structures 2015;95:88–100. https://doi.org/10.1016/j.tws.2015.06.019.

[152] Taheri-Behrooz F, Esmaeel RA, Taheri F. Response of perforated composite tubes subjected to axial compressive loading. Thin-Walled Structures 2012;50:174–81.

[153] Tafreshi A. Buckling and post-buckling analysis of composite cylindrical shells with cutouts subjected to internal pressure and axial compression loads. International Journal of Pressure Vessels and Piping 2002;79:351–9. https://doi.org/10.1016/S0308-0161(02)00026-1.

[154] Hilburger MW, Waas AM, Starnes JH. Response of composite shells with cutouts to internal pressure and compression loads. AIAA Journal 1999;37:232–7.

[155] Shi S, Sun Z, Ren M, Chen H, Hu X. Buckling response of advanced grid stiffened carbon–fiber composite cylindrical shells with reinforced cutouts. Composites Part B: Engineering 2013;44:26–33. https://doi.org/10.1016/j.compositesb.2012.07.044.

[156] Blom AW, Stickler PB, Gürdal Z. Optimization of a composite cylinder under bending by tailoring stiffness properties in circumferential direction. Composites Part B: Engineering 2010;41:157–65. https://doi.org/10.1016/j.compositesb.2009.10.004.

[157] Solis A, Barbero E, Sánchez-Sáez S. Analysis of damage and interlaminar stresses in laminate plates with interacting holes. International Journal of Mechanical Sciences 2020;165:105189. https://doi.org/10.1016/j.ijmecsci.2019.105189.

[158] Woo K, Nelson J, Cairns D, Riddle T. Effects of Defects: Part B—Progressive Damage Modeling of Fiberglass/Epoxy Composite Structures with Manufacturing Induced Flaws Utilizing Cohesive Zone Elements. 54th AIAA/ASME/ASCE/AHS/ASC Structures, Structural Dynamics, and Materials Conference, Reston, Virginia: American Institute of Aeronautics and Astronautics; 2013, p. 1628. https://doi.org/10.2514/6.2013-1628.

[159] Taketa I, Okabe T, Kitano A. Strength improvement in unidirectional arrayed chopped strands with interlaminar toughening. Composites Part A: Applied Science and Manufacturing 2009;40:1174–8.

[160] Li H, Wang W-X, Takao Y, Matsubara T. New designs of unidirectionally arrayed chopped strands by introducing discontinuous angled slits into prepreg. Composites Part A: Applied Science and Manufacturing 2013;45:127–33.

[161] Bullegas G, Pinho ST, Pimenta S. Engineering the translaminar fracture behaviour of thin-ply composites. Composites Science and Technology 2016;131:110–22. https://doi.org/10.1016/j.compscitech.2016.06.002.

[162] Taketa I, Okabe T, Matsutani H, Kitano A. Flowability of unidirectionally arrayed chopped strands in compression molding. Composites Part B: Engineering 2011;42:1764–9. https://doi.org/10.1016/j.compositesb.2011.01.021.

[163] Malkin R, Yasaee M, Bond IP, Trask RS. Ductility in composites: Influence of ply-cuts on the flexural behavior of carbon fibre reinforced polymer (CFRP). 2nd Joint US-Canada Conference on Composites-American Society for Composites, 26th Annual Technical Conference: Canadian Association for Composite Structures and Materials, 2011.

[164] Malkin R, Yasaee M, Trask RS, Bond IP. Bio-inspired laminate design exhibiting pseudo-ductile (graceful) failure during flexural loading. Composites Part A: Applied Science and Manufacturing 2013;54:107–16. https://doi.org/10.1016/j.compositesa.2013.07.008.

[165] Richards JM, Darby MI, Baggott R, Wosteim Holm GH, Yates B, Dorey G, Phillips LN. Effects of manufacturing defects on the mechanical properties of carbon fibre reinforced polyethersulphone laminates. Journal of Materials Science 1989;24:584–9. https://doi.org/10.1007/BF01107446.

[166] Brockmüller KM, Bernhardi O, Maier M. Determination of fracture stress and strain of highly oriented short fibre-reinforced composites using a fracture mechanics-based iterative finite-element method. Journal of Materials Science 1995;30:481–7. https://doi.org/10.1007/BF00354415.

[167] Huang H, Talreja R. Numerical simulation of matrix micro-cracking in short fiber reinforced polymer composites: initiation and propagation. Composites Science and Technology 2006;66:2743–57.

[168] Taketa I, Okabe T, Kitano A. A new compression-molding approach using unidirectionally arrayed chopped strands. Composites Part A: Applied Science and Manufacturing 2008;39:1884–90.

[169] Tang J, Swolfs Y, Yang M, Michielsen K, Ivens J, Lomov S V, Gorbatikh L. Discontinuities as a way to influence the failure mechanisms and tensile performance of hybrid carbon fiber/self-reinforced polypropylene composites. Composites Part A: Applied Science and Manufacturing 2018;107:354–65. https://doi.org/10.1016/j.compositesa.2018.01.020.

[170] Czél G, Pimenta S, Wisnom MR, Robinson P. Demonstration of pseudo-ductility in unidirectional discontinuous carbon fibre/epoxy prepreg composites. Composites Science and Technology 2015;106:110–9. https://doi.org/10.1016/j.compscitech.2014.10.022.

[171] Nakatani H, Nakaya K, Matsuba A, Kouno Y, Ogihara S. Effect of Prepreg Cut on the Mechanical Properties in CFRP Laminates. Journal of Solid Mechanics and Materials Engineering 2011;5:742–52. https://doi.org/10.1299/jmmp.5.742.

[172] Weicheng Cui, Wisnom MR, Jones M. An Experimental and Analytical Study of Delamination of Unidirectional Specimens with Cut Central Plies. Journal of Reinforced Plastics and Composites 1994;13:722–39. https://doi.org/10.1177/073168449401300804.

[173] Li H, Wang W-X, Matsubara T. Multiscale analysis of damage progression in newly designed UACS laminates. Composites Part A: Applied Science

and Manufacturing 2014;57:108–17. https://doi.org/10.1016/j.compositesa.2013.11.003.

[174] Olsson R, Iwarsson J, Melin LG, Sjögren A, Solti J. Experiments and analysis of laminates with artificial damage. Composites Science and Technology 2003;63:199–209. https://doi.org/10.1016/S0266-3538(02)00193-8.

[175] Lander JK, Kawashita LF, Allegri G, Hallett SR, Wisnom MR. A cut ply specimen for the determination of mixed-mode interlaminar fracture toughness. 14th European Conference on Composite Materials, 2010, p. 1–11.

[176] Charalambous G, Allegri G, Lander JK, Hallett SR. A cut-ply specimen for the mixed-mode fracture toughness and fatigue characterisation of FRPs. Composites Part A: Applied Science and Manufacturing 2015;74:77–87. https://doi.org/10.1016/j.compositesa.2015.02.020.

[177] Orifici AC, Wongwichit P, Wiwatanawongsa N. Embedded flaws for crack path control in composite laminates. Composites Part A: Applied Science and Manufacturing 2014;66:218–26. https://doi.org/10.1016/j.compositesa.2014.08.012.

[178] Yashiro S, Ogi K. Fracture behavior in CFRP cross-ply laminates with initially cut fibers. Composites Part A: Applied Science and Manufacturing 2009;40:938–47. https://doi.org/10.1016/j.compositesa.2009.04.023.

[179] Xue J, Wang W-X, Zhang J-Z, Wu S-J, Li H. Experimental and Numerical Study on the Tensile Behaviour of UACS/Al Fibre Metal Laminate. Applied Composite Materials 2015;22:489–505. https://doi.org/10.1007/s10443-014-9419-y.

[180] Xue J, Wang WX, Takao Y, Matsubara T. Thermal Residual Stress and Tensile Strength of UACS/Al Laminate with Different Slit Angles. Materials Science Forum 2013;750:204–7. https://doi.org/10.4028/www.scientific.net/MSF.750.204.

[181] Taketa I, Sato N, Kitano A, Nishikawa M, Okabe T. Enhancement of strength and uniformity in unidirectionally arrayed chopped strands with angled slits. Composites Part A: Applied Science and Manufacturing 2010;41:1639–46. https://doi.org/10.1016/j.compositesa.2010.07.010.

[182] Standard A. D5528/D5528--13. Standard Test Method for Mode I Interlaminar Fracture Toughness of Unidirectional Fiber-Reinforced Polymer Matrix Composites 2013.

[183] Standard A. D7905/D7905M--19. Standard Test Method for Determination of the Mode II Interlaminar Fracture Toughness of Unidirectional Fiber-Reinforced Polymer Matrix Composites 2019.

[184] Gillespie JW, Pipes RB. Compressive strength of composite laminates with interlaminar defects. Composite Structures 1984;2:49–69. https://doi.org/10.1016/0263-8223(84)90042-4.

[185] Hojo M, Matsuda S, Tanaka M, Ochiai S, Murakami A. Mode I delamination fatigue properties of interlayer-toughened CF/epoxy laminates. Composites Science and Technology 2006;66:665–75. https://doi.org/10.1016/j.compscitech.2005.07.038.

[186] Duarte A, Herszberg I, Paton R. Impact resistance and tolerance of interleaved tape laminates. Composite Structures 1999;47:753–8. https://doi.org/10.1016/S0263-8223(00)00049-0.

[187] Gao F, Jiao G, Lu Z, Ning R. Mode II Delamination and Damage Resistance of Carbon/Epoxy Composite Laminates Interleaved with Thermoplastic Particles. Journal of Composite Materials 2007;41:111–23. https://doi.org/10.1177/0021998306063356.

[188] Grail G, Pimenta S, Pinho ST, Robinson P. Exploring the potential of interleaving to delay catastrophic failure in unidirectional composites under tensile loading. Composites Science and Technology 2015;106:100–9. https://doi.org/10.1016/j.compscitech.2014.11.006.

[189] Chai H, Babcock CD, Knauss WG. One dimensional modelling of failure in laminated plates by delamination buckling. International Journal of Solids and Structures 1981;17:1069–83. https://doi.org/10.1016/0020-7683(81)90014-7.

[190] Kharghani N, Guedes Soares C. Behavior of composite laminates with embedded delaminations. Composite Structures 2016;150:226–39. https://doi.org/10.1016/j.compstruct.2016.04.042.

[191] Bottega WJ, Maewal A. Delamination Buckling and Growth in Laminates. Journal of Applied Mechanics 1983;50:184–9. https://doi.org/10.1115/1.3166988.

[192] Aslan Z, Daricik F. Effects of multiple delaminations on the compressive, tensile, flexural, and buckling behaviour of E-glass/epoxy composites. Composites Part B: Engineering 2016;100:186–96. https://doi.org/10.1016/j.compositesb.2016.06.069.

[193] Nilsson K-F, Asp LE, Alpman JE, Nystedt L. Delamination buckling and growth for delaminations at different depths in a slender composite panel. International Journal of Solids and Structures 2001;38:3039–71. https://doi.org/10.1016/S0020-7683(00)00189-X.

[194] Kutlu Z, Chang F-K. Composite panels containing multiple through-the-width delaminations and subjected to compression. Part II: Experiments & verification. Composite Structures 1995;31:297–314. https://doi.org/10.1016/0263-8223(95)00093-3.

[195] Wisnom MR. The role of delamination in failure of fibre-reinforced composites. Philosophical Transactions of the Royal Society A: Mathematical, Physical and Engineering Sciences 2012;370:1850–70. https://doi.org/10.1098/rsta.2011.0441.

[196] Aslan Z, Şahin M. Buckling behavior and compressive failure of composite laminates containing multiple large delaminations. Composite Structures 2009;89:382–90. https://doi.org/10.1016/j.compstruct.2008.08.011.

[197] Mohammadi B, Shahabi F. On computational modeling of postbuckling behavior of composite laminates containing single and multiple through-the-width delaminations using interface elements with cohesive law. Engineering Fracture Mechanics 2016;152:88–104. https://doi.org/10.1016/j.engfracmech.2015.04.005.

[198] Forghani A, Shahbazi M, Zobeiry N, Poursartip A, Vaziri R. An overview of continuum damage models used to simulate intralaminar failure mechanisms in advanced composite materials. Numerical Modelling of Failure in Advanced Composite Materials, Elsevier Inc.; 2015, p. 151–173. https://doi.org/10.1016/B978-0-08-100332-9.00006-2.

[199] Kachanov, L., Mohamed-Ali Rezgui, Mohamed-Toumi Nasri MA. Time of the rupture process under creep conditions. Materials Sciences and Applications 1958:26–31.

[200] Rabotnov Y. Creep rupture, 12 th Int. Congress of Applied mechanics. Stanford; 1968.

[201] Hinton M, Soden P, Kaddour A-S. Failure criteria in fibre reinforced polymer composites: the world-wide failure exercise. Elsevier; 2004.

[202] Kaddour A-S, Hinton MJ. Maturity of 3D failure criteria for fibre-reinforced composites: Comparison between theories and experiments: Part B of WWFE-II. Journal of Composite Materials 2013;47:925–966.

[203] Kaddour A, Hinton M, Smith P, Li S. The background to the third world-wide failure exercise. Journal of Composite Materials 2013;47:2417–2426.

[204] Herakovich CT. Mechanics of fibrous composites. John Wiley & Sons, Inc.; 1998.

[205] Reiner J, Vaziri R. Structural analysis of composites with finite element codes: An overview of commonly used computational methods 2018.

[206] Bazant ZP. Can multiscale-multiphysics methods predict softening damage and structural failure? International Journal for Multiscale Computational Engineering 2010;8.

[207] Drathi M, Ghosh A. Multiscale modeling of polymer-matrix composites. Computational Materials Science 2015;99:62–66.

[208] Ladevèze P, Néron D, Bainier H. A virtual testing approach for laminated composites based on micromechanics. The Structural Integrity of Carbon Fiber Composites, Springer; 2017, p. 667–698.

[209] Ladevèze P, Daghia F, Abisset E, Le Mauff C. A micromechanics-based interface mesomodel for virtual testing of laminated composites. Advanced Modeling and Simulation in Engineering Sciences 2014;1:7.

[210] Daghia F, Ladeveze P. Identification and validation of an enhanced mesomodel for laminated composites within the WWFE-III. Journal of Composite Materials 2013;47:2675–2693.

[211] Abisset E, Daghia F, Ladevèze P. On the validation of a damage mesomodel for laminated composites by means of open-hole tensile tests on quasi-isotropic laminates. Composites Part A: Applied Science and Manufacturing 2011;42:1515–1524.

[212] Wang L, Nygren G, Karkkainen RL, Yang Q. A multiscale approach for virtual testing of highly aligned short carbon fiber composites. Composite Structures 2019;230:111462.

[213] Tan W, Naya F, Yang L, Chang T, Falzon B, Zhan L, Molina-Aldareguía J, González C, Llorca J. The role of interfacial properties on the intralaminar and interlaminar damage behaviour of unidirectional composite laminates: experimental characterization and multiscale modelling. Composites Part B: Engineering 2018;138:206–221.

[214] Singh CV, Talreja R. A multiscale approach to modeling of composite damage. Modeling Damage, Fatigue and Failure of Composite Materials, Elsevier; 2016, p. 329–345.

[215] Feyel F, Chaboche J-L. FE2 multiscale approach for modelling the elastoviscoplastic behaviour of long fibre SiC/Ti composite materials. Computer Methods in Applied Mechanics and Engineering 2000;183:309–330.

[216] Bhattacharyya R, Basu PK. Multiscale progressive damage analysis of CFRP composites using a mechanics based constitutive relation. Composite Structures 2020;235:111759.

[217] Kaleel I, Petrolo M, Carrera E, Waas A. Computationally Efficient Concurrent Multiscale Framework for the Nonlinear Analysis of Composite Structures. AIAA Journal 2019;57:4029–4041.

[218] Lopes C, Sádaba S, González C, Llorca J, Camanho P. Physically-sound simulation of low-velocity impact on fiber reinforced laminates. International Journal of Impact Engineering 2016;92:3–17.

[219] Williams KV, Vaziri R, Poursartip A. A physically based continuum damage mechanics model for thin laminated composite structures. International Journal of Solids and Structures 2003;40:2267–2300.

[220] Pinho S, Iannucci L, Robinson P. Physically-based failure models and criteria for laminated fibre-reinforced composites with emphasis on fibre kinking: Part I: Development. Composites Part A: Applied Science and Manufacturing 2006;37:63–73.

[221] Pinho S, Iannucci L, Robinson P. Physically based failure models and criteria for laminated fibre-reinforced composites with emphasis on fibre kinking. Part II: FE implementation. Composites Part A: Applied Science and Manufacturing 2006;37:766–777.

[222] Raimondo L, Iannucci L, Robinson P, Pinho ST. A numerical material model for predicting the high velocity impact behaviour of polymer composites. Mechanical Response of Composites, Springer; 2008, p. 161–177.

[223] Ladevèze P. A damage computational method for composite structures. Computers and Structures 1992;44:79–87. https://doi.org/10.1016/0045-7949(92)90226-P.

[224] Ladevèze P, LeDantec E. Damage modelling of the elementary ply for laminated composites. Composites Science and Technology 1992;43:257–67. https://doi.org/10.1016/0266-3538(92)90097-M.

[225] Allix O, Ladevèze P. Interlaminar interface modelling for the prediction of delamination. Composite Structures 1992;22:235–242.

[226] Allix O, Ladevéze P, Corigliano A. Damage analysis of interlaminar fracture specimens. Composite Structures 1995;31:61–74. https://doi.org/10.1016/0263-8223(95)00002-X.

[227] Johnson AF, Pickett AK, Rozycki P. Computational methods for predicting impact damage in composite structures. Composites Science and Technology 2001;61:2183–92. https://doi.org/10.1016/S0266-3538(01)00111-7.

[228] Johnson A. Modelling impact damage in composite structural elements. Multi-Scale Modelling of Composite Material Systems, Elsevier; 2005, p. 401–429.

[229] Johnson AF, David M. Failure mechanisms in energy-absorbing composite structures. Philosophical Magazine 2010;90:4245–4261.

[230] Greve L, Pickett AK. Delamination testing and modelling for composite crash simulation. Composites Science and Technology 2006;66:816–26. https://doi.org/10.1016/j.compscitech.2004.12.042.

[231] Schueler D, Toso-Pentecôte N, Voggenreiter H. Simulation of high velocity impact on composite structures-model implementation and validation. Applied Composite Materials 2016;23:857–878.

[232] Le MQ, Bainier H, Néron D, Ha-Minh C, Ladevèze P. On matrix cracking and splits modeling in laminated composites. Composites Part A: Applied Science and Manufacturing 2018;115:294–301.

[233] Talreja R. A continuum mechanics characterization of damage in composite materials. Proceedings of the Royal Society of London A Mathematical and Physical Sciences 1985;399:195–216.

[234] Talreja R. Damage characterization. Composite Materials Series, vol. 4, Elsevier; 1991, p. 79–103.

[235] Talreja R. Damage mechanics of composite materials based on thermodynamics with internal variables. Durability of Polymer Based Composite Systems for Structural Applications 1990:65–79.

[236] Talreja R. Damage characterization by internal variables. Composite Materials Series 1994:53–53.

[237] Li S, Wang M, Jeanmeure L, Sitnikova E, Yu F, Pan Q, Zhou C, Talreja R. Damage related material constants in continuum damage mechanics for unidirectional composites with matrix cracks. International Journal of Damage Mechanics 2019;28:690–707.

[238] Matzenmiller A, Lubliner J, Taylor R. A constitutive model for anisotropic damage in fiber-composites. Mechanics of Materials 1995;20:125–152.

[239] Rabotnov YN. Creep problems in structural members. North-Holland; 1969.

[240] Krajcinovic D. Damage mechanics. Mechanics of Materials 1989;8:117–197.

[241] Bažant ZP, Oh BH. Crack band theory for fracture of concrete. Matériaux et Construction 1983;16:155–177.

[242] Cedolin L. Stability of Structures. New York: Oxford University Press; 1991.

[243] Belytschko T, Bažant ZP, Yul-Woong H, Ta-Peng C. Strain-softening materials and finite-element solutions. Computers & Structures 1986;23:163–180.

[244] Corporation LST. LS-DYNA keyword user's manual. Livermore Software Technology Corporation Livermore, CA; 2007.

[245] Williams KV, Vaziri R. Application of a damage mechanics model for predicting the impact response of composite materials. Computers & Structures 2001;79:997–1011.

[246] Maio L, Monaco E, Ricci F, Lecce L. Simulation of low velocity impact on composite laminates with progressive failure analysis. Composite Structures 2013;103:75–85.

[247] Xiao X. A coupled damage-plasticity model for energy absorption in composite. International Journal of Damage Mechanics 2010;19:727–751.

[248] Maimí P, Camanho PP, Mayugo J-A, Dávila CG. A thermodynamically consistent damage model for advanced composites 2006.

[249] Maimí P, Camanho PP, Mayugo JA, Dávila CG. A continuum damage model for composite laminates: Part I - Constitutive model. Mechanics of Materials 2007;39:897–908. https://doi.org/10.1016/j.mechmat.2007.03.005.

[250] Maimí P, Camanho PP, Mayugo J, Dávila C. A continuum damage model for composite laminates: Part II–Computational implementation and validation. Mechanics of Materials 2007;39:909–919.

[251] Soto A, González E, Maimí P, Mayugo J, Pasquali P, Camanho P. A methodology to simulate low velocity impact and compression after impact in large composite stiffened panels. Composite Structures 2018;204:223–238.

[252] González E, Maimí P, Camanho P, Turon A, Mayugo J. Simulation of drop-weight impact and compression after impact tests on composite laminates. Composite Structures 2012;94:3364–3378.

[253] Lopes C, Camanho P, Gürdal Z, Maimí P, González E. Low-velocity impact damage on dispersed stacking sequence laminates. Part II: Numerical simulations. Composites Science and Technology 2009;69:937–947.

[254] Systèmes D. Abaqus analysis user's manual. Simulia Corp Providence, RI, USA 2007.

[255] Pham DC, Cui X, Ren X, Lua J. A discrete crack informed 3D continuum damage model and its application for delamination migration in composite laminates. Composites Part B: Engineering 2019;165:554–562.

[256] Yun K, Kwak S, Wang Z, Chang M, Kim J, Liu J, Ri C. A Damage Model Reflecting the Interaction between Delamination and Intralaminar Crack for Failure Analysis of FRP Laminates. Applied Sciences 2019;9:314. https://doi.org/10.3390/app9020314.

[257] Hallett SR, Jiang W-G, Khan B, Wisnom MR. Modelling the interaction between matrix cracks and delamination damage in scaled quasi-isotropic specimens. Composites Science and Technology 2008;68:80–89.

[258] Bouvet C, Castanié B, Bizeul M, Barrau J-J. Low velocity impact modelling in laminate composite panels with discrete interface elements. International Journal of Solids and Structures 2009;46:2809–2821.

[259] Sun X, Wisnom M, Hallett S. Interaction of inter-and intralaminar damage in scaled quasi-static indentation tests: Part 2–Numerical simulation. Composite Structures 2016;136:727–742.

[260] Ostré B, Bouvet C, Minot C, Aboissière J. Finite element analysis of CFRP laminates subjected to compression after edge impact. Composite Structures 2016;153:478–489.

[261] Van der Meer F, Sluys L. Mesh-independent modeling of both distributed and discrete matrix cracking in interaction with delamination in composites. Engineering Fracture Mechanics 2010;77:719–735.

[262] Tay T, Sun X, Tan V. Recent efforts toward modeling interactions of matrix cracks and delaminations: an integrated XFEM-CE approach. Advanced Composite Materials 2014;23:391–408.

[263] Van der Meer F, Sluys L, Hallett S, Wisnom M. Computational modeling of complex failure mechanisms in laminates. Journal of Composite Materials 2012;46:603–623.

[264] Van der Meer FP, Dávila CG. Cohesive modeling of transverse cracking in laminates under in-plane loading with a single layer of elements per ply. International Journal of Solids and Structures 2013;50:3308–3318.

[265] Ling D, Yang Q, Cox B. An augmented finite element method for modeling arbitrary discontinuities in composite materials. International Journal of Fracture 2009;156:53–73.

[266] Fang X, Zhou Z, Cox B, Yang Q. High-fidelity simulations of multiple fracture processes in a laminated composite in tension. Journal of the Mechanics and Physics of Solids 2011;59:1355–1373.

[267] Chen B, Pinho S, De Carvalho N, Baiz P, Tay T. A floating node method for the modelling of discontinuities in composites. Engineering Fracture Mechanics 2014;127:104–134.

[268] De Carvalho N, Chen B, Pinho S, Ratcliffe J, Baiz P, Tay T-E. Modeling delamination migration in cross-ply tape laminates. Composites Part A: Applied Science and Manufacturing 2015;71:192–203.

[269] Fries T-P, Belytschko T. The extended/generalized finite element method: an overview of the method and its applications. International Journal for Numerical Methods in Engineering 2010;84:253–304.

[270] Moës N, Béchet E, Tourbier M. Imposing Dirichlet boundary conditions in the extended finite element method. International Journal for Numerical Methods in Engineering 2006;67:1641–1669.

[271] McGregor C, Vaziri R, Xiao X. Finite element modelling of the progressive crushing of braided composite tubes under axial impact. International Journal of Impact Engineering 2010;37:662–672.

[272] McGregor C, Zobeiry N, Vaziri R, Poursartip A, Xiao X. Calibration and validation of a continuum damage mechanics model in aid of axial crush simulation of braided composite tubes. Composites Part A: Applied Science and Manufacturing 2017;95:208–219.

[273] Forghani A, Zobeiry N, Poursartip A, Vaziri R. A structural modelling framework for prediction of damage development and failure of composite laminates. Journal of Composite Materials 2013;47:2553–2573.

[274] Zhou S, Sun Y, Muhammad R, Chen B, Tay T-E. Progressive damage simulation of scaling effects on open-hole composite laminates under compression. Journal of Reinforced Plastics and Composites 2017;36:1369–1383.

[275] Pam-Crash™. Virtual Performance 2008, Explicit Solver Notes Manual, ESI Group 2008.

[276] Allix O, Feissel P, Thévenet P. A delay damage mesomodel of laminates under dynamic loading: basic aspects and identification issues. Computers & Structures 2003;81:1177–91.

[277] Pickett AK, Fouinneteau MRC. Material characterisation and calibration of a meso-mechanical damage model for braid reinforced composites. Composites Part A: Applied Science and Manufacturing 2006;37:368–77. https://doi.org/10.1016/j.compositesa.2005.03.034.

[278] Lemaitre J, Chaboche J-L. Mechanics of solid materials. Cambridge: Cambridge University Press; 1990. https://doi.org/10.1017/CBO9781139167970.

[279] Ladevèze P, Allix O, Deü JF, Lévêque D. A mesomodel for localisation and damage computation in laminates. Computer Methods in Applied Mechanics and Engineering 2000;183:105–22. https://doi.org/10.1016/S0045-7825(99)00214-5.

[280] Ladevèze P, Lubineau G. An enhanced mesomodel for laminates based on micromechanics. Composites Science and Technology 2002;62:533–41.

[281] Voyiadjis GZ, Kattan PI, Taqieddin ZN. Continuum approach to damage mechanics of composite materials with fabric tensors. International Journal of Damage Mechanics 2007;16:301–29. https://doi.org/10.1177/1056789506064948.

[282] Fouinneteau MRC, Pickett AK. Shear mechanism modelling of heavy tow braided composites using a meso-mechanical damage model. Composites Part A: Applied Science and Manufacturing 2007;38:2294–306. https://doi.org/10.1016/j.compositesa.2006.12.006.

[283] Alfred Franklin V, Christopher T. Fracture Energy Estimation of DCB Specimens Made of Glass/Epoxy: An Experimental Study. Advances in Materials Science and Engineering 2013;2013:1–7. https://doi.org/10.1155/2013/412601.

[284] Olsson R. A simplified improved beam analysis of the DCB specimen. Composites Science and Technology 1992;43:329–38. https://doi.org/10.1016/0266-3538(92)90056-9.

[285] Arakawa K, Takahashi K. Interlaminar fracture analysis of composite DCB specimens. International Journal of Fracture 1996;74:277–87. https://doi.org/10.1007/BF00033831.

[286] Jumel J, Budzik MK, Ben Salem N, Shanahan MER. Instrumented End Notched Flexure – Crack propagation and process zone monitoring. Part I: Modelling and analysis. International Journal of Solids and Structures 2013;50:297–309. https://doi.org/10.1016/j.ijsolstr.2012.08.028.

[287] Szekrényes A. Delamination fracture analysis in the GII–GIII plane using prestressed transparent composite beams. International Journal of Solids and Structures 2007;44:3359–78. https://doi.org/10.1016/j.ijsolstr.2006.09.029.

[288] De Moura MFSF, Dourado N, Morais JJL, Pereira FAM. Numerical analysis of the ENF and ELS tests applied to mode II fracture characterization of cortical bone tissue. Fatigue & Fracture of Engineering Materials & Structures 2011;34:149–58. https://doi.org/10.1111/j.1460-2695.2010.01502.x.

[289] Gurit. SE84LV Low Temperature Cure Epoxy Prepreg. United Kingdom: 2017.

[290] PRF Composite Materials. RP507 Toughened Epoxy Prepreg system. United Kingdom: 2016.

[291] ChemTrend. Chemlease® PMR-90 EZ. 2017.

[292] Innovation. VACsealY-40. United Kingdom: 2018.

[293] Airtech. Bleeder Lease® B. Luxembourg: 2018.

[294] Airtech. A4000. Luxembourg: 2019.

[295] Airtech. Section Guide, Release films. Luxembourg: 2019.

[296] Airtech. Airweave®N-4. Luxembourg: 2015.

[297] Airtech. Ipplon®WN1500. Luxembourg: 2017.

[298] Polytetrafluoroethylene PTFE n.d.

[299] ASTM D5528-13. Standard test method for mode I interlaminar fracture toughness of unidirectional fiber-reinforced polymer matrix composites. ASTM International, United States; 2013. https://doi.org/10.1520/D5528-13.

[300] Huntsman. Araldite®2014-1. 2014.

[301] 3M. Scotch-Weld™ DP760. United Kingdom: 2009.

[302] Theplasticshop.co.uk. PTFE Virgin-FE1000. United Kingdom: 2014.

[303] East Coast Fiberglass Supplies. Shrink Tite Tape. United Kingdom: 2010.

[304] Binder. Data Sheet Model M240. Germany: 2019.

[305] ASTM D1599-18. Standard test method for resistance to short-time hydraulic pressure of plastic pipe, tubing and fittings. ASTM International, United States; 2018.

[306] ASTM D3039M-14. Standard test method for tensile properties of polymer matrix composite materials. ASTM International, United States; 2014.

[307] ASTM D3518/D3518M-13. Standard test method for in-plane shear response of polymer matrix composite materials. ASTM International, United States; 2013.

[308] ASTM D6641/D6641M-14. Standard test method for compressive properties of polymer matrix composite materials using a combined loading compression (CLC) test fixture. ASTM International, United States; 2014.

[309] ASTM D7905/D7905M-14. Standard test method for determination of the mode II interlaminar fracture toughness of unidirectional fiber-reinforced polymer matrix composites. ASTM International, United States; 2014.

[310] O'Higgins RM, McCarthy CT, McCarthy MA. Identification of Damage and Plasticity Parameters for Continuum Damage Mechanics Modelling of Carbon and Glass Fibre-Reinforced Composite Materials. Strain 2011;47:105–15. https://doi.org/10.1111/j.1475-1305.2009.00649.x.

[311] Boutaous A, Peseux B, Gornet L, Bélaidi A. A new modeling of plasticity coupled with the damage and identification for carbon fibre composite laminates. Composite Structures 2006;74:1–9. https://doi.org/10.1016/j.compstruct.2005.11.004.

[312] Bilal M, Masud S, Athar S. FPGA Design for Statistics-Inspired Approximate Sum-of-Squared-Error Computation in Multimedia Applications. IEEE Transactions on Circuits and Systems II: Express Briefs 2012;59:506–10. https://doi.org/10.1109/TCSII.2012.2204841.

[313] Rajee AM, Sagayaraj Francis F. A Study on Outlier distance and SSE with multidimensional datasets in K-means clustering. 2013 Fifth International Conference on Advanced Computing (ICoAC), IEEE; 2013, p. 33–6. https://doi.org/10.1109/ICoAC.2013.6921923.

[314] Fylstra D, Lasdon L, Watson J, Waren A. Design and Use of the Microsoft Excel Solver. Interfaces 1998;28:29–55. https://doi.org/10.1287/inte.28.5.29.

[315] Kemmer G, Keller S. Nonlinear least-squares data fitting in Excel spreadsheets. Nature Protocols 2010;5:267–81. https://doi.org/10.1038/nprot.2009.182.

[316] Harper PW, Hallett SR. Cohesive zone length in numerical simulations of composite delamination. Engineering Fracture Mechanics 2008;75:4774–92. https://doi.org/10.1016/j.engfracmech.2008.06.004.

[317] Chen BY, Tay TE, Baiz PM, Pinho ST. Numerical analysis of size effects on open-hole tensile composite laminates. Composites Part A: Applied Science and Manufacturing 2013;47:52–62. https://doi.org/10.1016/j.compositesa.2012.12.001.

[318] Ellul B, Camilleri D, Grech J, Muscat M. Filament Wound Composite Pressure Vessels and Pipes Subject to an Internal Pressure: An Experimental and Material Characterization Study. Journal of Pressure Vessel Technology 2016;138. https://doi.org/10.1115/1.4032506.

[319] Tang J, Swolfs Y, Longana ML, Yu H, Wisnom MR, Lomov S V., Gorbatikh L. Hybrid composites of aligned discontinuous carbon fibers and self-reinforced polypropylene under tensile loading. Composites Part A: Applied Science and Manufacturing 2019;123:97–107. https://doi.org/10.1016/j.compositesa.2019.05.003.

[320] Longana ML, Yu H, Lee J, Pozegic TR, Huntley S, Rendall T, Potter KD, Hamerton I. Quasi-Isotropic and Pseudo-Ductile Highly Aligned Discontinuous Fibre Composites Manufactured with the HiPerDiF (High Performance Discontinuous Fibre) Technology. Materials 2019;12:1794. https://doi.org/10.3390/ma12111794.

[321] Iarve E V., Kim R. Strength Prediction and Measurement in Model Multilayered Discontinuous Tow Reinforced Composites. Journal of Composite Materials 2004;38:5–18. https://doi.org/10.1177/0021998304038215.

[322] Iarve E V., Kim R. Three-Dimensional Fracture Analysis and Experimental Investigation of Model Unidirectional Discontinuous Tow Composite Laminates. Journal of Thermoplastic Composite Materials 2002;15:469–76. https://doi.org/10.1177/0892705702015006203.

[323] Salavatian M, Smith LV. An investigation of matrix damage in composite laminates using continuum damage mechanics. Composite Structures 2015;131:565–73. https://doi.org/10.1016/j.compstruct.2015.06.012.

[324] Long S, Yao X, Zhang X. Delamination prediction in composite laminates under low-velocity impact. Composite Structures 2015;132:290–8. https://doi.org/10.1016/j.compstruct.2015.05.037.

[325] Colombo C, Bhujangrao T, Libonati F, Vergani L. Effect of delamination on the fatigue life of GFRP: A thermographic and numerical study. Composite Structures 2019;218:152–61. https://doi.org/10.1016/j.compstruct.2019.03.023.

[326] Mahmoodabadi MJ, Nemati AR. A novel adaptive genetic algorithm for global optimization of mathematical test functions and real-world problems. Engineering Science and Technology, an International Journal 2016;19:2002–21. https://doi.org/10.1016/j.jestch.2016.10.012.

[327] Thakur M. A new genetic algorithm for global optimization of multimodal continuous functions. Journal of Computational Science 2014;5:298–311. https://doi.org/10.1016/j.jocs.2013.05.005.

[328] Mark McElroy, James G. Ratcliffe, Michael W. Czabaj, John Wang FY. A numerical and experimental study of damage growth in a composite laminate. Hampton, VA: 2014.

[329] Maimí P, Camanho PP, Mayugo JA, Turon A. Matrix cracking and delamination in laminated composites. Part II: Evolution of crack density and delamination. Mechanics of Materials 2011;43:194–211. https://doi.org/10.1016/j.mechmat.2011.01.002.

[330] Liu M, Suo S, Wu J, Gan Y, AH Hanaor D, Chen CQ. Tailoring porous media for controllable capillary flow. Journal of Colloid and Interface Science 2019;539:379–87. https://doi.org/10.1016/j.jcis.2018.12.068.

[331] Nishad CS, Karmakar T, Chandra A, Raja Sekhar GP. A non-primitive boundary integral formulation for modeling flow through composite porous channel. Engineering Analysis with Boundary Elements 2019;109:94–105. https://doi.org/10.1016/j.enganabound.2019.03.044.

Appendices

Appendix A Visual Basic code for in-plane properties

```
Function Y_12(G_12_0, E_2_0, b, d_12, d_22, sig_12, sig_22, Y_12_prev)

If d_12 < 1 And d_22 < 1 Then
   Y_12 = Sqr(sig_12 ^ 2 / (2 * G_12_0 * (1 - d_12) ^ 2) + _
   b * (max(sig_22, 0) ^ 2 / (2 * E_2_0 * (1 - d_22) ^ 2)))
   If Y_12 < Y_12_prev Then Y_12 = Y_12_prev
Else
   Y_12 = 1
End If

End Function

Function Y_22(E_2_0, d_22, sig_22, Y_22_prev)

If d_22 < 1 Then
   Y_22 = Sqr(max(sig_22, 0) ^ 2 / (2 * E_2_0 * (1 - d_22) ^ 2))
   If Y_22 < Y_22_prev Then Y_22 = Y_22_prev
Else
   Y_22 = 1
End If

End Function

Function d_12(Y_12, Y_12_0, Y_12_C, Y_12_U, Y_22, Y_22_U, dmax, d_12, epsrat_12)

Dim Ydyn_12_0 As Double, Ydyn_12_C As Double

Ydyn_12_0 = Y_12_0 * Sqr(1 + d_12 * Abs(epsrat_12))
Ydyn_12_C = Y_12_C * Sqr(1 + d_12 * Abs(epsrat_12))
If Y_12 < Y_12_U And Y_22 < Y_22_U Then d_12 = max(Y_12 - Ydyn_12_0, 0) / Ydyn_12_C
If Y_12 >= Y_12_U Or Y_22 >= Y_22_U Or d_12 > dmax Then d_12 = dmax

End Function

Function d_22(Y_12, Y_12_U, Y_22, Y_22_0, Y_22_C, Y_22_U, dmax, d_22, epsrat_22)

Dim Ydyn_22_0 As Double, Ydyn_22_C As Double
Ydyn_22_0 = Y_22_0 * Sqr(1 + d_22 * Abs(epsrat_22))
Ydyn_22_C = Y_22_C * Sqr(1 + d_22 * Abs(epsrat_22))
If Y_12 < Y_12_U And Y_22 < Y_22_U Then d_22 = max(Y_22 - Ydyn_22_0, 0) / Ydyn_22_C
If Y_12 >= Y_12_U Or Y_22 >= Y_22_U Or d_22 > dmax Then d_22 = dmax

End Function
```

```
Function sig_eps_12(G_12_0, d_12, d_12_prev, sig_12_prev, eps_12_p_prev, p_12_prev, _
epsrat_12, eps_12_e_prev, deps_12, _
            R_0, D_R, beta, m)

Dim dG_12 As Double, dsig_12 As Double, sig_12 As Double, eps_12_p As Double, _
   eps_12_e As Double, p_12 As Double
Dim R0dyn As Double, R As Double
Dim aux(1 To 4) As Variant

dG_12 = G_12(d_12, epsrat_12, G_12_0, d_12) - _
      G_12(d_12_prev, epsrat_12, G_12_0, d_12)
dsig_12 = deps_12 * G_12(d_12, epsrat_12, G_12_0, d_12) + _
                  2 * dG_12 * eps_12_e_prev
sig_12 = sig_12_prev + dsig_12
R0dyn = R_0 * (1 + D_R * Abs(epsrat_12))
R = R0dyn + beta * Abs(1 / 2 * p_12_prev) ^ m
If d_12 < 1 Then
   If Abs(sig_12 / (1 - d_12)) - R <= 0 Then
      eps_12_p = eps_12_p_prev
      p_12 = p_12_prev
      eps_12_e = sig_12 / G_12(d_12, epsrat_12 + deps_12, G_12_0, d_12) / 2
   Else
      eps_12_p = eps_12_p_prev + 2 * deps_12
      p_12 = p_12_prev + (1 - d_12) * deps_12
      sig_12 = Abs(epsrat_12) / epsrat_12 * (1 - d_12) * R
      eps_12_e = sig_12 / G_12(d_12, epsrat_12 + deps_12, G_12_0, d_12) / 2
   End If
Else
   eps_12_p = eps_12_p_prev + 2 * deps_12
   p_12 = p_12_prev + (1 - d_12) * deps_12
   sig_12 = Abs(epsrat_12) / epsrat_12 * (1 - d_12) * R
   If Abs(sig_12) > 0 Then
      eps_12_e = sig_12 / G_12(d_12, epsrat_12 + deps_12, G_12_0, d_12) / 2
   Else
      eps_12_e = 0
   End If
End If
aux(1) = sig_12
aux(2) = eps_12_p
aux(3) = eps_12_e
aux(4) = p_12
sig_eps_12 = aux

End Function
```

```
Function sig_eps_22(E_2_0, d_22, d22_prev, sig_22_prev, eps_22_p_prev, p_22_prev, _
epsrat_22, eps_22_e_prev, deps_22, _
            R_0, D_R, beta, m, a)

Dim dE_2 As Double, dsig_22 As Double, sig_22 As Double, eps_22_p As Double, _
   eps_22_e As Double, p_22 As Double
Dim R0dyn As Double, R As Double
Dim aux(1 To 4) As Variant

dE_2 = E_2(eps_22_e_prev, epsrat_22, d_22, E_2_0, d_22) - _
      E_2(eps_22_e_prev, epsrat_22, d22_prev, E_2_0, d_22)
dsig_22 = deps_22 * E_2(eps_22_e_prev, epsrat_22, d_22, E_2_0, d_22) + _
                  dE_2 * eps_22_e_prev
sig_22 = sig_22_prev + dsig_22
R0dyn = R_0 * (1 + D_R * Abs(epsrat_22))
R = R0dyn + beta * Abs(p_22_prev) ^ m
If d_22 < 1 Then
   If a ^ 2 * Abs(max(sig_22, 0) / (1 - d_22) + min(sig_22, 0)) - R <= 0 Then
      eps_22_p = eps_22_p_prev
      p_22 = p_22_prev
      eps_22_e = sig_22 / E_2(eps_22_e_prev, epsrat_22, d_22, E_2_0, d_22)
   Else
      eps_22_p = eps_22_p_prev + deps_22
      p_22 = p_22_prev + a * (1 - d_22) * deps_22
      sig_22 = Abs(epsrat_22) / epsrat_22 * (1 - d_22) * R / a ^ 2
      eps_22_e = sig_22 / E_2(eps_22_e_prev, epsrat_22, d_22, E_2_0, d_22)
   End If
Else
   eps_22_p = eps_22_p_prev + deps_22
   p_22 = p_22_prev + a * (1 - d_22) * deps_22
   sig_22 = Abs(epsrat_22) / epsrat_22 * (1 - d_22) * R / a ^ 2
   If Abs(sig_22) > 0 Then
      eps_22_e = sig_22 / E_2(eps_22_e_prev, epsrat_22, d_22, E_2_0, d_22)
   Else
      eps_22_e = 0
   End If
End If
aux(1) = sig_22
aux(2) = eps_22_p
aux(3) = eps_22_e
aux(4) = p_22
sig_eps_22 = aux

End Function
```

```
Function G_12(G_12_0, d_12, epsrat_12)

Dim G_12_s As Double

G_12_s = G_12_0 * (1 - d_12)
G_12 = G_12_s * (1 + d_12 * Abs(epsrat_12))

End Function

Function E_2(E_2_0, d_22, eps_22_e, epsrat_22)

Dim E_2_s As Double

If eps_22_e > 0 Then E_2_s = E_2_0
If eps_22_e <= 0 Then E_2_s = E_2_0 * (1 - d_22)
E_2 = E_2_s * (1 + d_22 * Abs(epsrat_22))

End Function

Function max(X1, X2)

max = X2
If X1 > X2 Then max = X1

End Function

Function min(X1, X2)

min = X2
If X1 < X2 Then min = X1

End Function
```